THE EPITAXIAL DEPOSITION OF SILICON

Thesis submitted for the degree of

Doctor of Philosophy

by

Michael Censlive

February, 1972.

Department of Metallurgy,
Imperial College of Science
and Technology,
University of London.

...

Abstract

This work describes studies of the structure and electrical properties of epitaxial layers of silicon deposited onto (111) oriented silicon single crystal substrates by evaporation in ultra high vacuum.

The structure of the layers has been investigated by electron diffraction and transmission electron microscopy. The variation of the minimum epitaxial growth temperature, with growth rate has been investigated and the results compared to those reported in the literature for epitaxial growth of silicon under similar conditions. The results are discussed with reference to a model based on the effects of ion bombardment. From the analysis, the activation energy for anneal of radiation damage in silicon is calculated and found to be in accord with published values. The electrical properties of the layers have been investigated and correlation found between the structure as determined by electron microscopy and resistivity profiles. The resistivity profiles have been found to be consistent with an isothermal damage anneal model which yields activation energies of the process in agreement with published data.

CONTENTS

	Page
Abstract.	2
Introduction.	8
Chapter 1. The Crystal Structure and Electron Diffraction.	10
1.1. The crystal structure of silicon.	10
1.2. Stacking in Face Centred Cubic and Diamond Lattices.	10
1.2.(1) Stacking fault defects	10
1.2.(2) Stacking Sequence of twins.	14
1.3. Electron Diffraction and Transmission Microscopy.	15
1.3.(1) Electron Diffraction	15
1.3.(2) Geometry of the diffraction pattern	17
1.3.(3) Geometry of the Kikuchi lines	17
1.3.(4) Effect of crystal imperfections on the diffraction pattern.	21
1.3.(5) Transmission Electron Microscopy: A brief review.	22
. . .	
Chapter 2. Literature Review.	24
2.1. Survey of chemical transport epitaxial growth techniques	24
2.1.(1) Effect of substrate orientation on growth rates	29
2.1.(2) Substrate preparation	31
2.1.(3) Defects in chemical vapour transport grown epitaxial layers	32
2.1.(4) Growth mechanisms in chemical transport epitaxy.	36
2.2. Growth of epitaxial layers of silicon by vacuum evaporation.	37
2.2.(1) Results of growth studies carried out at pressures $\geq 10^{-6}$ torr.	37
2.2.(2) Substrate surface cleaning methods	38
2.2.(3) Substrate surface contamination effects	39
2.2.(4) Variation of minimum epitaxial temperature with deposition rate and pressure.	40
2.2.(5) Defect content and variation in evaporated silicon layers.	41

2.2.(6) Nucleation and growth processes observed for deposition pressures $\geq 10^{-6}$ torr. 44

2.2.(7) Electrical properties of layers deposited at pressures $\geq 10^{-6}$ torr. 47

2.3. Results of growth studies carried out at pressures $< 10^{-8}$ torr. 48

2.3.(1) Introduction 48

2.3.(2) Results of studies of variation deposition rates and substrate temperatures for epitaxy 49

2.3.(3) Low energy electron diffraction studies of silicon surfaces and epitaxial growth. 51

2.3.(4) Variation of defect content with growth parameters 54

2.3.(5) Nucleation and growth processes observed for deposition pressures $< 10^{-8}$ torr. 54

2.3.(6) Electrical properties of layers grown at pressures $< 10^{-8}$ torr. 58

2.3.(7) Summary and analysis of reported epitaxial growth studies. 59

Chapter 3. Apparatus and experimental techniques. 65

3.1. Descritpion of the apparatus 65

3.1.(1) Vacuum system performance 65

3.1.(2) Silicon vapour source 67

3.1.(3) Source fabrication 67

3.1.(4) Furnace construction for U.H.V. use 69

3.1.(5) Operating conditions of the electron beam furnace 71

3.2. Substrate heating 71

3.2.(1) Assessment of the problem 71

3.2.(2) Radiation heating 72

3.2.(3) Substrate heater, design and construction 72

3.2.(4) Mounting of substrate heater 74

3.2.(5) Construction of substrate carrier assembly 76

3.2.(6) Substrate heater calibration 79

3.3. Substrate preparation 83

3.4. Procedure for deposition of layer 86

3.4.(1) Measurement of deposition rate 87

3.4.(2) Measurement of layer thickness 87

3.4.(3) Uniformity of layer thickness 87

3.5. Methods of examination of the structure of the layers 88

3.5.(1) Procedure for cutting 3 mm discs. 89

3.5.(2) Method of production of thin specimens for examination by transmission electron microscopy 91

3.6.(1) Experimental method for studies of nucleation and growth 92

3.6.(2) Replication method for studies of the growth surface. 93

Chapter 4. Results. 96

4.1. Variation of deposition rate and substrate temperature for epitaxy 96

4.2. The structure of the layers 96

4.2.(1) Visual appearance and topography 96

4.3. Analysis of the structure of the layers by transmission electron microscopy 99

4.3.(1) Analysis of the structure of group I 99

4.3.(2) Analysis of the structure of group II 103

4.3.(3) Orientation of stacking faults 109

4.3.(4) Variation of stacking fault density with growth parameters 112

4.3.(5) Examination of substrate layer interface 112

4.3.(6) Analysis of the stacking faults 115

4.4.(1) Variation of background defect content with growth parameters 121

4.4.(2) Contrast effect observed in transmission microscopy studies of the background defects 128

4.5. Nucleation and growth 131

4.5.(1) Investigation of the thermal treatment on the substrate surface 131

4.5.(2) Investigation of nucleation and growth processes. 135

Chapter 5. Discussion of Results. 143

5.1. Comparison of the results with the review data. 143

5.1.(1) Analysis of the relationship between the critical growth parameters R_c and T_c 144

5.1.(2) Comparison of the structure and quality of the layers grown in this present work, with published data. 148

5.2. Review of radiation damage in silicon 153

5.2.(1) Range energy relationships 153

5.2.(2) The natureof the radiation damage 157

5.2.(3) Variation of damage with dose: distribution of damage 158

5.2.(4) Variation of saturation dose with target temperature 160

5.2.(5) Annealing characteristics of the damage 160

5.3. Effect of the ion bombardment on the epitaxial growth process 163

5.4. Effect of the radiation damage on the structure of the layer 167

5.5. The nature of the defects produced by bombardment rates less than the saturation value 170

5.6. Investigation of the stacking faults 173

5.7. Nucleation and growth 177

5.7.(1) Analysis of the thermal cleaning process 177

5.7.(2) Analysis and discussion of the nucleation investigation. 179

Chapter 6. Electrical Measurements. 182

6.1. Experimental techniques 182

6.1.(1) Theory of the spreading resistance and construction and calibration of the 2 point probe. 183

6.1.(2) Bevel lapping procedure 185

6.1.(3) Summary of other electrical measurements 185

6.2. Results.

6.2.(1) Measurements of resistivity profiles 187

6.2.(2) Measurements of I-V characteristics of a P-N junction 190

6.2.(3) Scanning Electron Microscope investigation of a P-N junction. 192

6.3. Discussion of results. 194

6.3.(1) Analysis of resistivity profiles, and other electrical measurements. 196

Chapter 7. Suggestions for future work.

Appendix

A.I. Radiation heating 208

A.II. R.F. brazing technique 210

A.III. Structural modifications for reversal of furnace electrode polarity. 211

A.IV. Circuit of photo dectector used in jet thinning. 212

References. 213

Introduction.

The word epitaxy was first used by Royer (1932) to describe the growth of one crystalline material upon the surface of another, so that there was a unique relationship between their crystal axes.

The earliest studies in this field were limited to the study of orientation relationships between various combinations of materials whose crystallography could be found by visual inspection. This early work gave way to more detailed studies using electron diffraction techniques and transmission electron microscopy to examine the structures of thin films produced by vacuum evaporation onto crystalline substrates such as rock salt and mica. The basic techniques, and the results of the early studies on orientation, nucleation and growth and the defects observed, have been reviewed by Pashley (1956: 1965).

The fundamental points of interest may be briefly summarised, viz:-

(i) The effects of the different substrate crystal structures on the orientation and growth of the layers.

(ii) The mechanisms of nucleation and growth and their effe cts on the orientation and crystalline perfection of the deposit.

In cases where the deposit and the substrate are the same material, the process may be called auto-epitaxy. In this case there is no initial lattice mismatch, and the process may be considered as direct crystal growth from the vapour phase.

The intensive application of epitaxial growth techniques to semiconductor device manufacture, began in 1961, when it was shown that the epitaxial growth of silicon on a silicon substrate could produce new device geometries, and improve the characteristics of devices produced by standard diffusion techniques.

The basic advantage of epitaxial growth techniques over diffusion is the ability to grow a layer of high resistivity material upon a substrate of lower resistivity, or different doping type. This structure can then be used to produce devices by standard diffusion techniques.

Whilst it is in principle possible to produce a high resistivity layer, by diffusing in a dopant of the opposite type to that already present, the successive diffusions required to produce the active junction regions would then exceed the solid solubility limits. A detailed account of the techniques used in device manufacture is given in Runyan (1969).

The initial studies of the epitaxial growth of silicon were carried out using chemical vapour transport methods. These were developed from well-established processes used for the production and purification of silicon for the semiconductor device industry.

The majority of reported studies of the growth, defects and properties of epitaxial silicon layers have been carried out on layers deposited by chemical transport methods. Because of their wide-scale use in the present-day semiconductor industry, the chemical transport growth methods and results will be briefly reviewed. Before discussing the results obtained in the various studies of epitaxial silicon growth the crystallography of silicon and the diffraction techniques used in the study of the structure of epitaxial layers, will be briefly reviewed.

Chapter 1. Crystal Structure and Electron Diffraction.

1.1. The Crystal Structure of Silicon

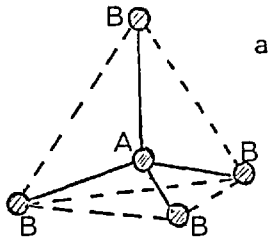
The silicon interatomic bonds are covalent, and the crystal structure is diamond cubic. Each atom A, is surrounded by the four nearest atoms B, arranged at the vertices of a tetrahedron. This arrangement is shown in Fig. (1.1a), and the position of such a tetrahedron in a face centered cubic (F.C.C.) space lattice of the diamond structure is shown in Fig. (1.1b). The diamond structure atom sites which lie on two F.C.C. sublattices, which are displaced so that the atom sites of one sublattice lie in the tetrahedral interstices of the other sublattice.

The diamond structure can then be described as an F.C.C. lattice, with a basis of 2 atoms per lattice site. The basis is oriented along the [111] direction and separated by $\frac{1}{4}$ the length of the unit cell diagonal. Because of the existence of the two sublattices; the (111) planes consist of pairs of planes, as shown in fig. (1.1c), the atoms of one plane of a pair belong to 1 sublattice and the others to the other sublattice. The lattice parameter of silicon is 5.429Å.

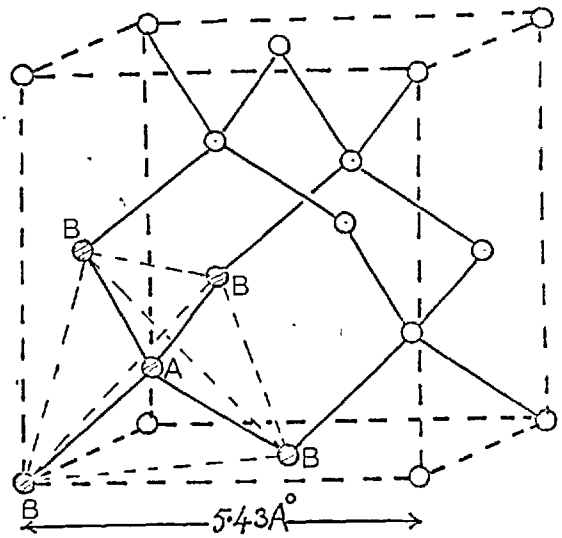
1.2. Stacking in Face Centred Cubic and Diamond Lattices.

1.2.(1) Stacking Fault Defects.

The F.C.C. unit cell has an atom at each corner and an atom at the centre of each face. This structure is close packed. If the atoms are regarded as hard spheres of equal diameters, arranged to give the cell structure, as shown in Fig. (1.2a), then it can be seen that the (111) planes consist of spheres in closd packed arrangement, ie. each touches its six neighbours in the plane. Thus the atoms of the next (111) layer must lie in the 'hollows' formed by the spheres of the initial layer, if the close packed structure is to be maintained: see Fig. (1.2b). There are two sets of 'hollows' which can be occupied: these may be designated B sites and C sites, the initial layer being designated A sites. By adding successive (111) planes in the site sequence ABC, ABC, ABC ... , the F.C.C. structure is obtained.

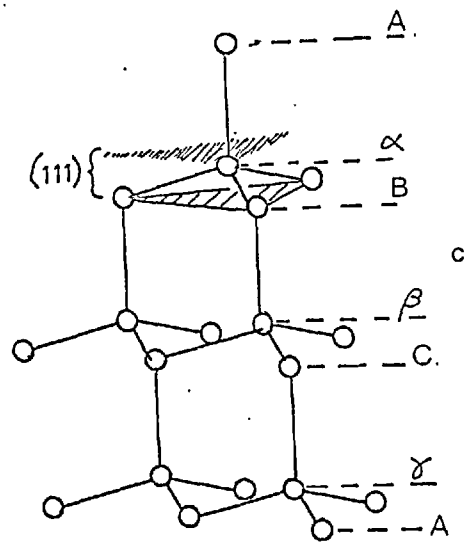


a THE TETRAHEDRAL ORIENTATION OF THE SILICON INTER-ATOMIC BONDS.



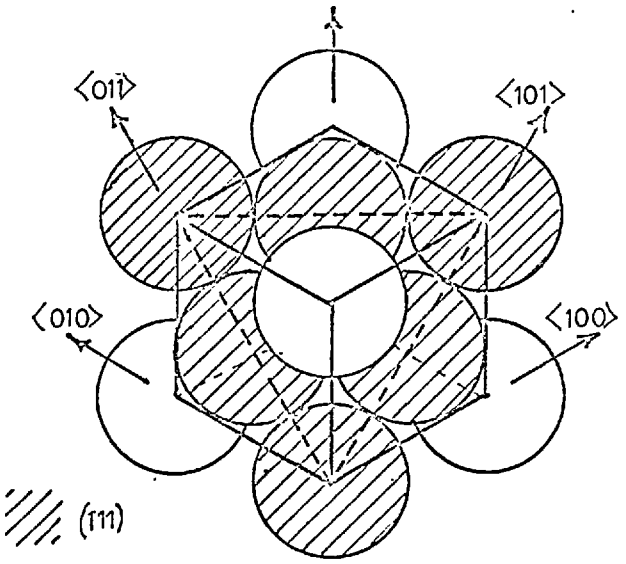
THE DIAMOND STRUCTURE UNIT CELL, SHOWING THE RELATION-SHIP WITH THE BOND TETRAHEDRON.

b



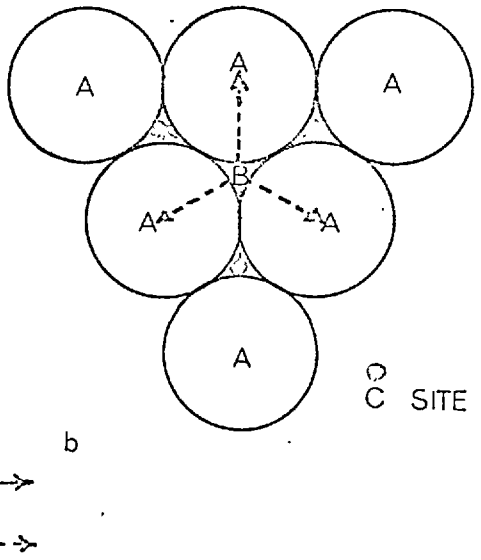
c THE GEOMETRY OF THE DOUBLE (111) PLANES IN THE DIAMOND STRUCTURE.

Fig. 1.1.



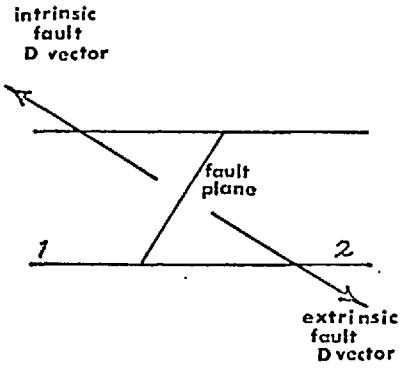
a

BALL MODEL OF THE F.C.C. STRUCTURE VIEWED ALONG A < 111 > DIRECTION.



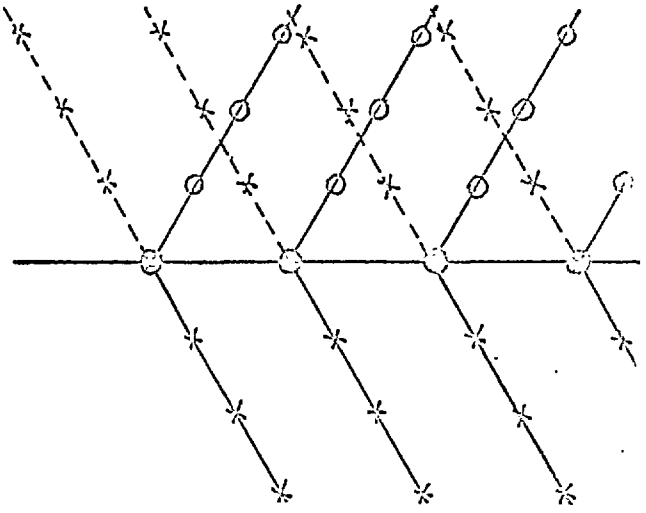
b

STACKING SITES AND SHEAR VECTORS ON A F.C.C. STRUCTURE (111) PLANE.



c

GEOMETRY OF FAULT DISPLACEMENT VECTORS.



× MATRIX SITE

o TWIN SITE

d

RELATIONSHIP BETWEEN TWIN AND MATRIX LATTICE SITES.

Fig. 1.2.

If in a region of the crystal, the site stacking sequence is ABC, ABC, BCA, BC, then the region is said to contain a stacking fault. Stacking faults may be produced in a number of ways: eg. a shear parallel to the fault plane, or by localised expansion or collapse of the lattice in a direction normal to the fault plane. For these various methods of fault formation, the partial dislocations which bound the faults will be different: Although the fault vector will be the same in each case. Frank (1953), has used a displacement vector $\underset{\sim}{D}$; normal to the fault plane; to describe the fault.

The crystal is considered to be divided into two sections, as shown in Fig. (1.2c). The displacement of section 2 relative to section 1 is the displacement vector of the fault. Thus for an extrinsic fault, the sections must be separated to accommodate the extra plane of atoms, and for an intrinsic fault, section 2 must be moved towards section 1, to close the gap caused by the removal of a plane of atoms. From this it is seen that the displacement vectors are of the form $\pm \frac{a}{3}[111]$.

Faults which arise from a shear mechanism in the fault plane will have fault vectors of the form $\frac{a}{6}[\bar{1}\bar{1}2]$. These vectors differ from $\frac{a}{3}[111]$ by a lattice translation vector; since $\frac{a}{6}[\bar{1}\bar{1}2] + \frac{a}{2}[\bar{1}\bar{1}0] = \frac{a}{3}[111]$ and $\frac{a}{2}[\bar{1}\bar{1}0]$ is a lattice translation vector. Thus $\frac{a}{3}[111]$ is an equivalent representation of the fault vector $\frac{a}{6}[\bar{1}\bar{1}2]$.

In the diamond structure it has been shown that the (111) planes consist of pairs of planes as shown in fig. (1.1c). The stacking sequence for these double planes is of the form $A\alpha$, $B\beta$, $c\gamma$, $A\alpha$, $B\beta$, $C\gamma$, etc. Where the planes are as denoted in Fig. (1.1c). $A\alpha$, $B\beta$ are the widely spaced planes, and γ, A; α B, β C, are the closely spaced planes whose spacing is $\frac{1}{3}$ that of the widely spaced planes.

In the diamond structure, stacking faults can be produced in similar ways as described above for the F.C.C. structure. An intrinsic fault is of the form $A\alpha$, $B\beta$, $A\alpha$, $B\beta$, $C\gamma$, ..., the pair of planes $C\gamma$, having been omitted. The dislocations and faults in the diamond structure have been reviewed by Hornstra (1958).

He has shown that the stacking faults in the diamond structure are analogous to those in the F.C.C. structure and so may be described by displacement vectors $\underset{\sim}{D}$ of the form $\pm < 111 >$.

1.2.(2) Stacking Sequence of Twins.

A defect commonly found in epitaxial films, is the twin. A twinned region is formed, when a portion of the lattice takes up a certain orientation relative to the rest of the lattice, the two portions of the lattice remaining in contact.

The twin may be regarded as formed by either a rotation of a portion of the structure relative to the rest, - the axis of rotation is then called the twin axis - or by the reflection of the lattice in a plane called the twin plane. Fig. (1.2d) shows the orientation relationship between a twin region and the parent lattice, the matrix. The stacking sequence across the twin boundary on a (111) plane is then A,B,C, A,B,C, B,A,C, B,A, The C sites indicated form the twin plane. This form of twin boundary in which there is one to one lattice site correspondance across the boundary is called a coherent twin boundary. Twinning on planes where there is no one to one lattice site correspondance across the boundary is called incoherent twinning.

An interesting form of twinning is often observed in epitaxial films of F.C.C. materials deposited onto F.C.C. substrates. If the substrate surface is considered as a set of A stacking sites, then the first layer of the deposit can occupy either 'B' stacking sites or 'C' stacking sites, since both sites have equal probabilities of occupancy. If in a region of the film, the stacking sequence ABC ACBACB..... is followed where the 'A' sites indicated are the substrate surface, then it is seen that the deposit is in F.C.C. stacking sequence, but is in twin orientation with respect to the substrate. This form of twinning is called double positioning, and has been investigated by Pashley and Stowell (1963) for epitaxial films of gold grown on (111) oriented rock-salt substrates.

1.3. Electron Diffraction and Transmission Microscopy.

The methods of structural investigation used in this work were electron diffraction and transmission microscopy. These subjects will be briefly reviewed to provide a background of terminology and techniques.

1.3.(1) Electron Diffraction

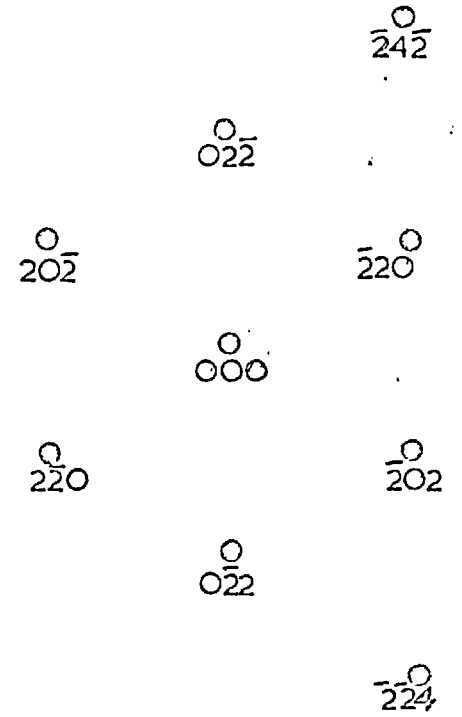
The analysis of the diffraction of electrons by a crystal lattice is most easily carried out using the concepts of the Ewald sphere, and reciprocal lattice, Rymer (1969); has shown that the diffraction pattern is those points in the reciprocal lattice which touch the Ewald sphere, and are allowed by the structure factor.

The crystal lattice determines the reciprocal lattice by the following relationship:

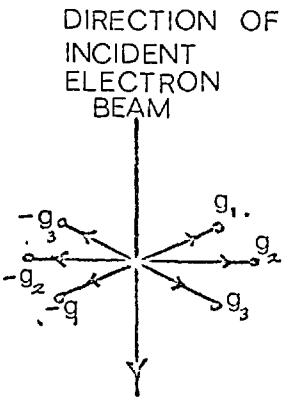
If a_i a_j a_k are the crystal lattice basis vectors, then the reciprocal lattice vectors, b_i b_j b_k are such that a_i $b_j = \delta_{ij}$. From this it is seen that $|b_j| = \frac{1}{|a_j|}$. If the crystal lattice basis is orthogonal, then b_i is parallel to a_i; b_j to a_j, and b_k to a_k. Also the reciprocal lattice vector $\underline{v} = hb_i + kb_j + lb_k$, is p rpendicular to the (hkl) planes of thc crystal lattice.

Each point in the reciprocal lattice represents a plane in the real lattice. For each point in the reciprocal which lies on the Ewald sphere, a diffracted beam will be produced by the planes in the real lattice, if the indices of the plane (which are also those of the reciprocal lattice point) satisfy the structure factor rules. For the diamond structure, the selection rules as given by Cullity (1953) are, as follows:- for allowed reflections the indices h,k,l are all even or all odd; and values of (h + k + l) which are equal to 2(2n + 1) where n is an integer, do not give rise to allowed reflections. Fig. (1.3a) shows the diffraction pattern for a silicon crystal oriented so that the incident electron beam is along the [111] direction.

The indices of the diffraction spots are assigned as follows. If $(UVW)^{*}$ is a lattice point in the reciprocal lattice L^{*}, then the condition for this point to lie in the reciprocal lattice plane $(HKL)^{*}$

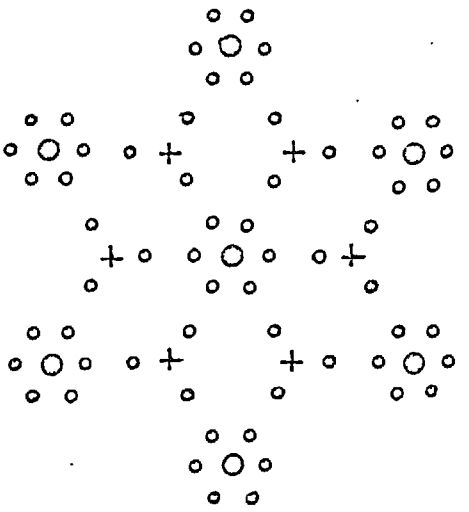


a (111) DIFFRACTION PATTERN FOR SILICON.



b

ORIENTATION OF THE DIFFRACTION PATTERN RELATIVE TO THE DIRECTION OF THE ELECTRON BEAM.



c

(111) DIFFRACTION PATTERN FOR SILICON SHOWING ADDITIONAL SPOTS DUE TO THE PRESENCE OF TWINS; AND DOUBLE DIFFRACTION EFFECTS.

- O REPRESENTS A MATRIX SPOT
- o REPRESENTS A TWIN SPOT
- ⊙ REPRESENTS A SPOT DUE TO DOUBLE DIFFRACTION BETWEEN MATRIX AND TWIN SPOTS PLOTTED IN THE FIGURE.
- \+ REPRESENTS SPOTS DUE TO DOUBLE DIFFRACTION BETWEEN MATRIX AND 'DOUBLE-POSITIONED' TWINS.

Fig. 1.3.

through the origin is $[h'k'l']^{\Xi}$. $(UVW)^{\Xi} = 0$. $[(h'k'l')^{\Xi}$ is the vector normal to the reciprocal lattice plane $(HKL)^{\Xi}$ and $(UVW)^{\Xi}$ is a vector defined by the origin and the coordinate points U, V, W, of the reciprocal lattice point.]

From the geometrical relationship between the reciprocal lattice L^{Ξ} and the real lattice L, when both are cubic.
$[h'k'l']^{\Xi} = [hkl]$.

Thus for the beam incident along the [111] direction the reciprocal lattice points which lie in the (111) reciprocal lattice plane are given by $(UVW)^{\Xi}$. $[111] = 0$, ie. all points of the form $U + V + W = 0$ and which are allowed by the structure factor, will be produced in the diffraction pattern. Fig. (1.3b) shows the orientation of the (111) diffraction pattern relative to the incident electron beam. If the direction of the electron beam is parallel to that of the positive [111] direction, andthe diffraction vectors are as indicated, then the positive [111] direction is parallel to the vector product $g_1 \wedge g_2$.

1.3.(2) Geometry of the Diffraction Pattern

Fig. (1.4) shows the formation of a diffracted beam D from a crystal with the (hkl) planes inclined at the Bragg angle to the incident electron beam I. If the specimen to screen distance is L and R is the radial distance of the diffracted beam, then from Fig. (1.4) $2\theta \simeq \frac{R}{L}$ radiens. From Bragg's Law, $2d_{hkl} \sin\theta \simeq \lambda$ where d_{hkl} is the interplanar spacing of the (hkl) planes. For small angles $2 \sin\theta \approx 2\theta$. Then $R_{hkl}\, d_{hkl} = \lambda L$. The quantity λL is called the camera constant, and is constant for a given geometry and electron lense currents. Thus from knowledge of λL, and R_{hkl}, d_{hkl} can be found.

1.3.(3) Geometry of Kikuchi Lines.

A prominent feature of the diffraction of electrons by crystalline material of good quality is the formation of Kikuchi lines: [Kikuchi (1928)].

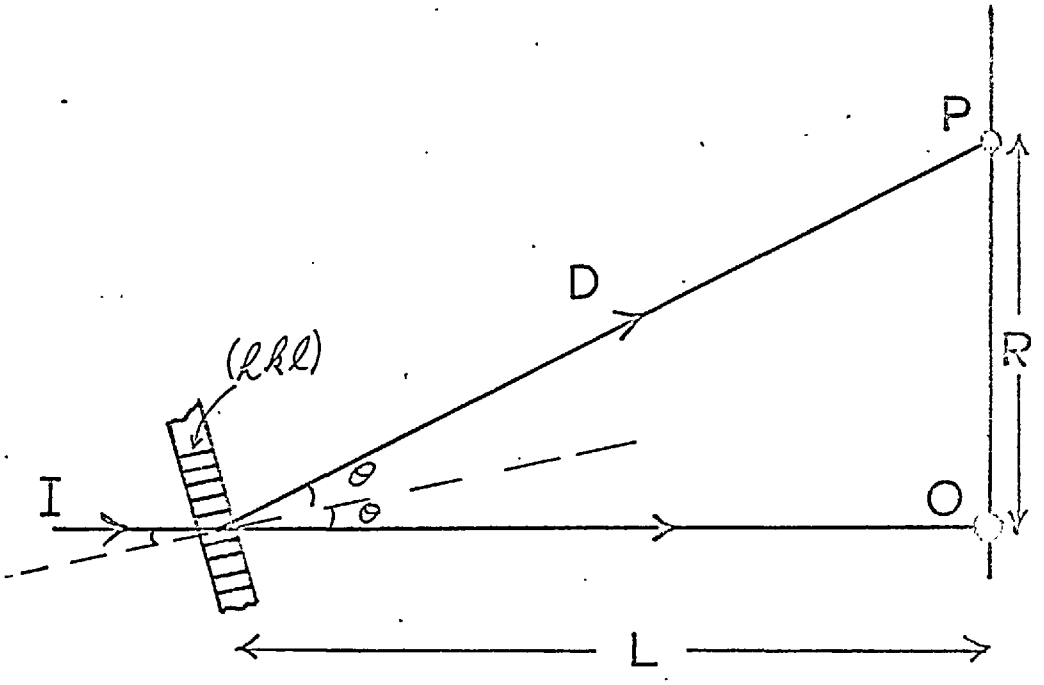


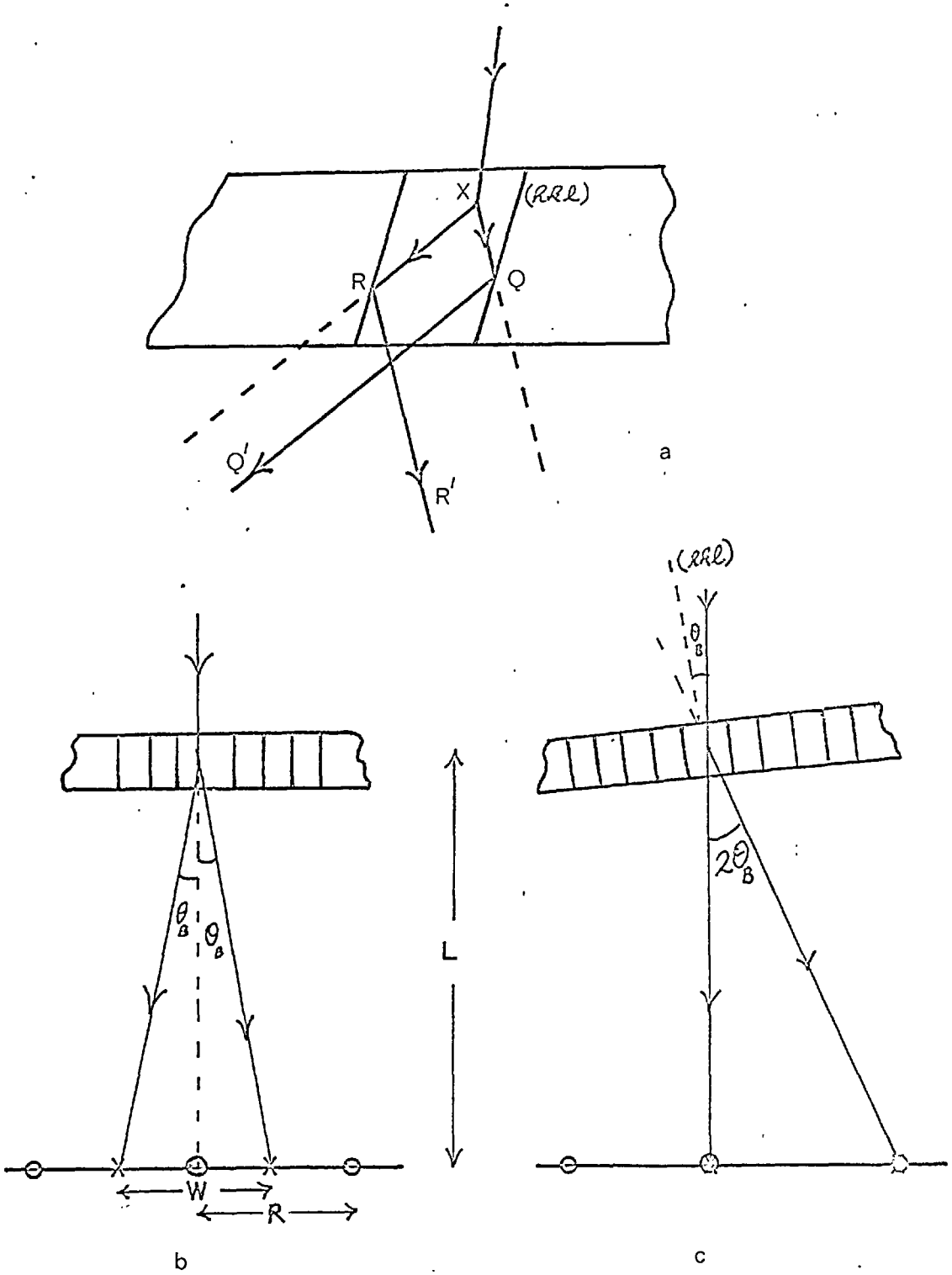
Fig. (1.4)
GEOMETRY OF THE DIFFRACTED BEAM.

In the formation of the diffraction pattern, the electrons are assumed to undergo one coherent scattering process; thus no energy is lost and Bragg's Law is obeyed.

In the formation of Kikuchi lines, the electrons are assumed to undergo at least two successive scattering interactions, the first, an inelastic scattering process which produces a small change in energy and hence wavelength; the second, a coherent scattering process, which obeys the Bragg equation. The distribution of intensity produced by the incoherent scattering process is favoured in the forwards direction. If the scattered rays travelling from X meet the crystal planes at the Bragg angle θ as shown in Fig. (1.5a), then the ray XQ is diffracted in the direction QQ' and the ray XR into the direction RR'. Since the intensity of scattered electrons is greater along XQ than along XR, the Bragg reflections cause a net transfer of intensity from XQ to XR.

The effect of all the reflection directions available from a set of crystal planes, is to produce two cones of rays of semivertical angles $(90-\theta)$. The inter section of these cones with the screen produce pairs of lines, one of which is brighter than the background and the other, corresponding to the loss of intensity, is darker than the background. Fig. (1.5b) shows the geometrical arrangement of the Kikuchi lines. From this diagram it is seen that $\frac{w}{2L} = \tan \theta_B$, where w is the distance between the Kikuchi lines. From Bragg's Law $2d_{hkl} \sin \theta_B = \lambda$, thus $w_{hkl} \cdot d_{hkl} = \lambda L$ since for small θ $\sin 2\theta \approx \tan 2\theta$. From comparison with the eqn. $R_{hkl} \cdot d_{hkl} = \lambda L$ it is seen that $R_{hkl} = w_{hkl}$. It is assumed that the small change in wavelength is negligible.

If the specimen is tilted so that the (hkl) planes are at the Bragg angle to the electron beam as shown in Fig. (1.5c) then from the geometry, it is seen that one of the Kikuchi lines corresponding to the (hkl) planes passes through the (hkl) diffraction spot, and the other line passes through the centre, or 000 spot. From this it is seen that by means of the Kikuchi lines, the specimen may be tilted so as to set any of the crystal planes at the exact Bragg angle, to the electron beam.



a FORMATION OF KIKUCHI LINE BY INELASTIC SCATTERING AT X.

b GEOMETRICAL RELATIONSHIP BETWEEN KIKUCHI LINES, [X] AND DIFFRACTED BEAMS [O].

c POSITION OF KIKUCHI LINES AND DIFFRACTED BEAMS FOR SPECIMEN TILTED INTO TWO BEAM CONDITION.

Fig.(1.5)

1.3.(4) Effect of Crystal Imperfections on the Diffraction Pattern.

(i) Twins.

A region of twinned material within the crystal will act as a crystal in a different though characteristic orientation with respect to the matrix. Thus it will produce a characteristic additional spot pattern in the diffraction pattern of the matrix. Pashley and Stowell (1963) have shown that for F.C.C. structure material the twin reciprocal lattice points lie along < 111 > directions passing through the matrix spots. Fig. (1.3c) shows the (111) diffraction pattern for silicon with twinned material present. As well as the twin spots indicated in the diagram additional spots produced by double diffraction effects are also shown. Double diffraction occurs when the electron beam is diffracted successively by crystalline material in different orientations. The additional spots can be indexed in terms of the indices of the matrix spots, for example, the spots indicated by X in Fig. (1.3c) can be seen to lie at radial distances of $\frac{1}{3}$ that of the matrix spots of the form $\{\bar{4}22\}$; thus these spots can be denoted by $\frac{n}{3}\{\bar{4}22\}$, where n takes values comensurate with increasing radial distance of the diffraction spot.

(ii) Polycrystaline Material

If the specimen consists of an assembly of small crystallites randomly oriented then the reciprocal lattice of the assembly consists of a set of reciprocal lattices, each corresponding to a crystallite, set at random orientations. This is equivalent to a set of spherical surfaces each of radius $\alpha \frac{1}{d_{hkl}}$, where d_{hkl} is the interplanar spacing of the (hkl) planes in the small crystals. The diffraction pattern of the polycrystalline array is a set of concentric circles formed by the intersection of the Ewald sphere, and the set of concentric spheres forming the reciprocal lattice of the assembly. The radii R_{hkl} of these rings are given by the equation $R_{hkl} \cdot d_{hkl} = \lambda L$, where d_{hkl} are the interplanar spacings of the (hkl) planes in the crystalites, and λL the camera constants. Thus a diffraction pattern consisting of spots is produced by material which is

predominantly a single crystal. A polycrystalline specimen will produce a diffraction pattern consisting of rings of angular radii characteristic of the material.

If the size of the crystallites is of the same order or larger than the electron beam diameter (usually of the order 1μ) then a single crystal spot pattern will be produced, but the pattern will change discontinuously as the specimen is moved through the beam, thus bringing differently oriented grains into the electron beam.

1.3.(5) Transmission Electron Microscopy: a brief review.

The study of the structure of the silicon layers by transmission electron microscopy, involves the examination of the variation of the intensity of the image. This intensity variation is termed constant. Contrast in transmission microscopy can arise from two effects; absorption contrast and diffraction contrast. For crystalline materials the latter mechanism is the more important. As the electron beam passes through a crystalline material, the beam is split into a direct beam, and beams diffracted from the various crystal planes. The directions of the diffracted beams depends on the crystal plane spacings as discussed above, section (1.3.(2)). If only the direct beam is used to produce an image by preventing the diffracted beams passing through the objective apperture, then the transmitted intensity depends on the difference between the incident intensity and that diffracted by the crystal. The intensity of the image then depends very sensitively on the crystallographic orientation of the foil with respect to the incident electron beam. Thus any form of localised lattice distortion or irregularity, gives rise to contrast variations in the image.

The investigation of the intensity variations have been carried out by Hirsch et al (1965) who have shown that if the foil is oriented with respect to the electron beam, so that the incident beam is reflected by only one set of the crystal lattice planes; the contrast effects produced by crystal defects could be calculated. The above diffracting condition is termed a two-beam diffracting condition, and occurs when a set of crystal lattice planes is at the exact Bragg angle

to the incident electron beam. From Fig. (1.5c) it can be seen that this condition can be established by the use of the Kikuchi lines to indicate the orientation of the specimen. The image produced by the use of the direct beam, is called the bright-field image. Imaging by use of a diffracted beam is called dark-field. It has the advantage of greater image contrast than the B.F. image.

There are two methods of producing dark-field images:

a) the low resolution, dark-field;

b) the high resolution dark-field.

a) Low resolution dark-field

In this method the objective aperture is simply displaced from the central directly transmitted beam position to allow the chosen diffracted beam to pass through to produce the image. Since the diffracted beam used is not close to the axis of the lenses, the large amount of spherical abberation which occurs limits the resolution.

b) High resolution dark-field

This is obtained by tilting the electron gun mechanically; or by tilting the beam, electrostatically or electromagnetically, so that the chosen diffracted beam passes down the lens axis, this eliminates spherical abberation effects. Thus, high magnifications can be used.

If the dark-field image is produced from a diffraction spot which is not a matrix spot, then the material producing this diffracted beam will appear in bright contrast, this is termed domain contrast. If a double diffraction spot were used; then only those regions whe e the beam can be successively diffracted by two or more different crystals will appear bright. These regions are the boundaries between the regions of different orientation. This gives rise to outline contrast in the image.

A full descritpion of the various analytical techniques used in transmission electron microscopy is given in Hirsch et al (1965),

Chapter 2. Review of Literature

2.1. Chemical Methods used in the Production of Epitaxial Silicon Layers.

This thesis is concerned with vacuum evaporated epitaxial layers of silicon; the most widely investigated and the most commercially important methods for the production of epitaxial silicon layers, however, are chemical transport techniques. For comparison, these methods will now be briefly reviewed.

The chemical reactions most commonly used are as follows:-

(i) Hydrogen reduction of volatile halides.

(ii) Disproportionation of halides.

(iii) Pyrolysis of hydrides.

The halides most commonly used are silicon tetrachloride or tetrabromide. These are both volatile liquids at room temperature. A typical chemical vapour transport system is shown in fig. (2.1). Purified hydrogen is passed over a temperature-controlled bath of the halide. The amount of halide picked up is determined by the hydrogen flow rate and vapour pressure of the halide at the bath temperature. The mixture of the gases is led over the substrates which are heated by radiation from an inductively heated susceptor. The tilted substrate support shown in fig. (2.1) ensures that each substrate sees an undepleted gas stream. All connecting pipes are made of inert materials to avoid contaminating the layers with reaction products. The arrangement described above is typical of most systems in use at the present time. A more detailed description of chemical transport systems is given by Li (1966).

The reaction which occurs using $SiCl_4$ is as follows: $SiCl_4 + 2H_2 \rightleftarrows Si + 4HCl$. This reaction was studied by Sedgwick (1964) and Lever (1964) who showed that it proceeds in two steps.

1. $SiCl_4 + H_2 \rightarrow SiHCl_3 + HCl$
2. $SiHCl_3 + H_2 \rightarrow Si + 3HCl$.

The deposition rate and layer quality were investigated by several workers: Theurer (1961), Bylander (1962) and Steinmeyer (1963). They found the rate and quality were determined by the substrate temperature, the $SiCl_4/H_2$ ratio, the flow rates, and the system geometries.

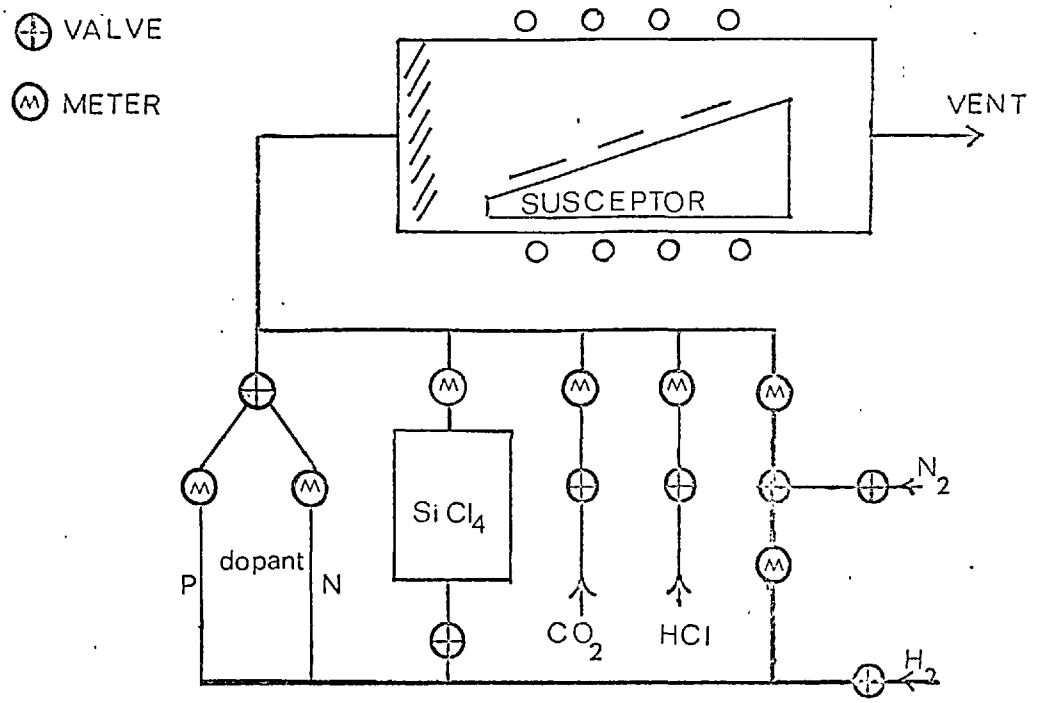


Fig. (2.1)
A CHEMICAL VAPOUR TRANSPORT SYSTEM WITH FACILITIES FOR HCl GAS PHASE ETCHING, VAPOUR PHASE DOPING, AND OXIDE GROWTH.

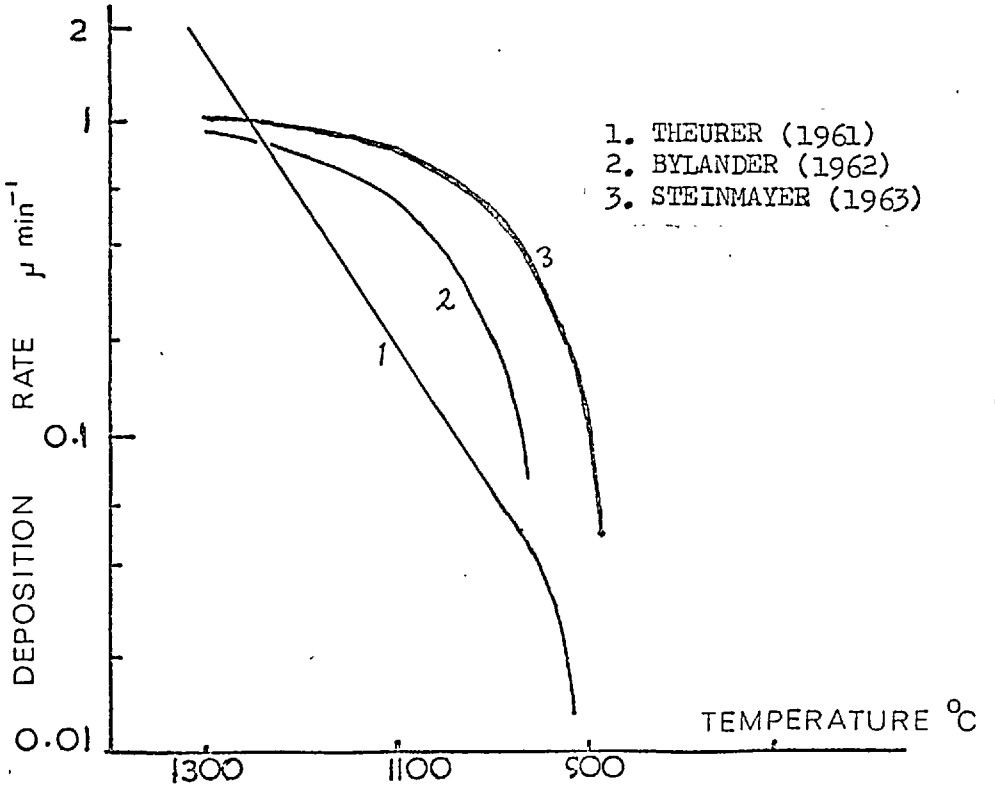


Fig. (2.2)
VARIATION OF EPITAXIAL GROWTH RATE WITH SUBSTRATE TEMPERATURE FOR THE REDUCTION OF $SiCl_4$.

The results of the above workers are summarised in fig. (2.2). From these results it is seen that to obtain layers of good crystallinity, high growth temperatures are required. At these high growth temperatures, usually of the order of 1200°C, dopant diffusion between substrate and layer occurs. This effect reduces the sharpness of the doping profile. The magnitude of this effect is illustrated in fig. (2.3) which shows the impurity profile of a layer grown at 1275°C for 20 minutes on a substrate of low resistivity. The profile shows that the dopant diffusion effect extends over 2μ into the layer. (Data from Grove et al (1966).)

In order to minimise this diffusion effect, reactor operating conditions of gas flow-rate and reactant vapour concentrations are chosen to give the highest growth rate giving good quality at the temperature used, to reduce the time spent at the high growth temperatures. However, in practice, inter-diffusion effects limit the sharpness of resistivity profiles, and therefore the minimum usable thickness of the epitaxial layer. In order to avoid the effects of the doping gradients at the interface, the epitaxial layers are usually $\gtrsim 10\mu$ thick and the device active regions are limited to the top 5μ.

In attempts to reduce the growth temperature and hence the diffusion effect, other reactions and silicon compounds have been used. Miller and Grieco (1963) used the reduction of $SiBr_4$, since the Si - Br bond has an energy of 3 ev, compared with the Si - Cl bond energy of 3.7 ev. They found that the hydrogen reduction could be carried out at temperatures of the order of 1050°C. However, the growth rate obtained at this temperature was of the order of 0.06μ per minute. Thus because of the lower growth rates, the small decrease in growth temperature was not very beneficial because a longer growth time had to be used.

Trichloro-Silane, $SiHCl_3$, has also been used by various workers, because of the simpler reaction mechanism suggested by the results of Sidgwick and Lever on studies of $SiCl_4$ reduction. Glang and Wajda (1962), and Rundle (1968) found that using $SiHCl_3$ the deposition rates were independent of substrate temperature for certain reactant flow rates.

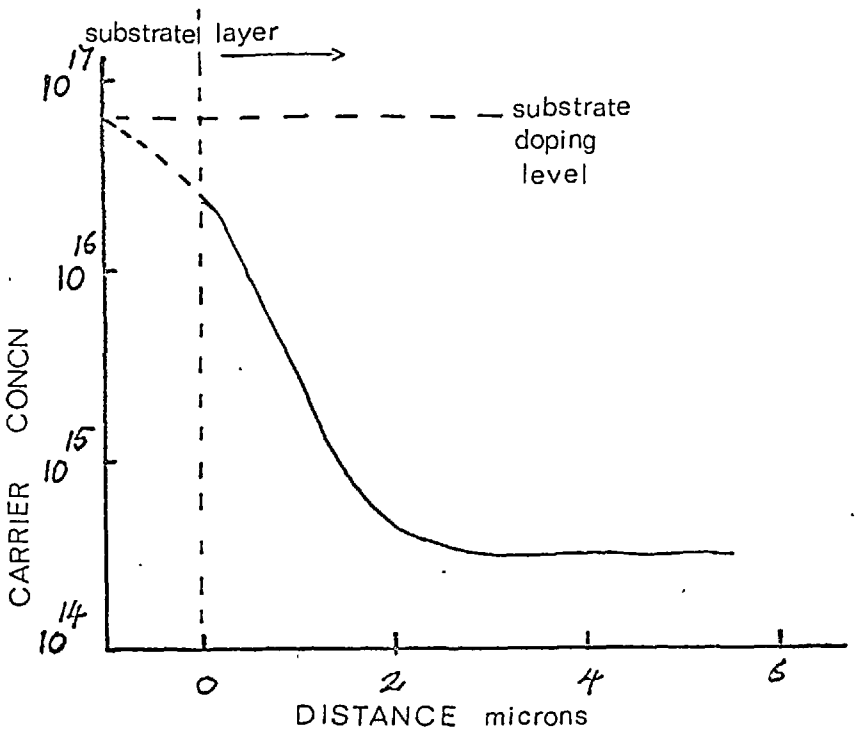


Fig. (2.3)
EFFECT OF DOPENT DIFFUSION DURING THE GROWTH OF AN EPITAXIAL LAYER.
GROWTH TEMPERATURE 1100°C; DURATION 10 mins.
[AFTER GROVE ET AL 1966].

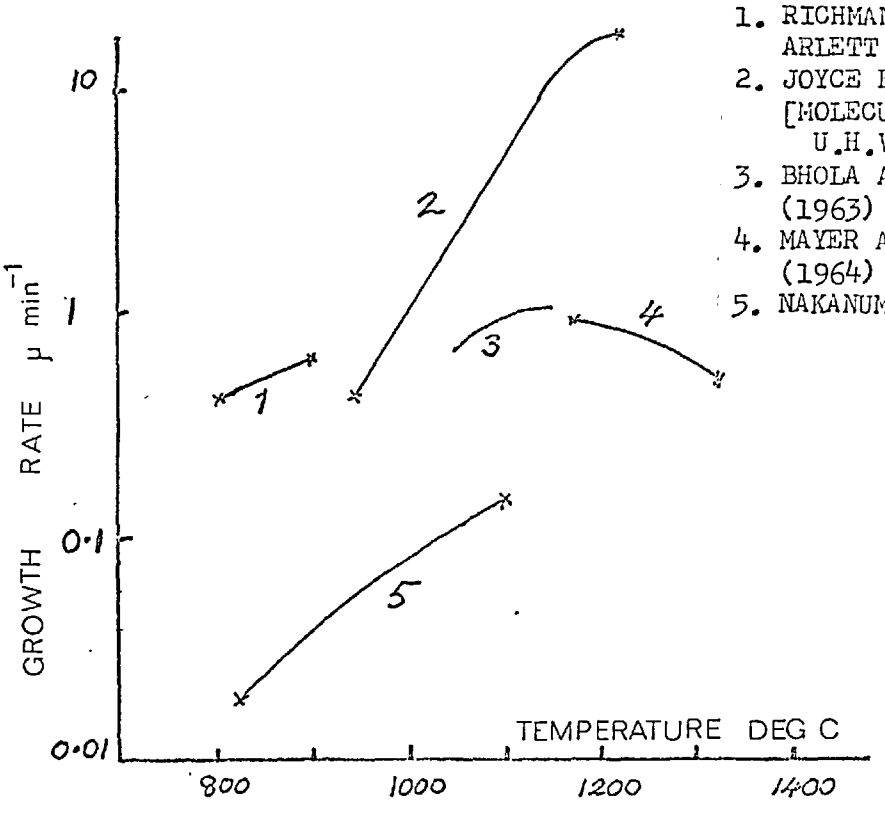


Fig. (2.4)
GROWTH RATES ACHIEVED WITH SILANE.

This result was confirmed by Sutton (1969) using very high reactant flow rates. This effect favours uniformity of growth in the presence of small temperature fluctuations which are inevitable in a gas flow system.

However, though the reaction mechanism is simpler, the temperature and growth rates are of the same order of magnitude as observed for the reduction of $SiCl_4$, ie. $\sim 1200^{\circ}C$ and, 0.5 - 1μ per minute. Joyce and Charig (1962) report that for substrate temperatures $< 1000^{\circ}C$ the growth is polycrystalline.

The disproportionation of silicon iodide had been used by Litton and Anderson (1954); to produce the high-purity starting material for device manufacture. This reaction was used by Wajda et al (1960) and May (1965) to deposit epitaxial layers. The method used was to insert the source material, substrate and iodine in a sealed quartz tube under reduced pressure of hydrogen. The tube is placed in a two zone furnace. For high pressures of iodine; source material temperatures of $\sim 1100^{\circ}C$ and substrate temperatures of 800° - $900^{\circ}C$, growth rates of 5μ per hour were achieved.

The growth temperature is extremely low, but because a closed system is used, reaction products cannot easily be removed. These tend to congregate at the interface and may cause imperfections. Arizumi et al (1968) observed this behaviour in the growth of epitaxial germanium, and attributed it to excess GeI_4, absorbed on to the substrate at the beginning of the deposition.

A technique for obtaining high quality layers using $SiCl_4$ and a growth temperature of $900^{\circ}C$ was reported by Nakanuma (1966). In this method, the epitaxial growth is commenced at $1200^{\circ}C$, and after sufficient time to grow several monolayers of Si, the substrate temperature is reduced to $900^{\circ}C$ whilst maintaining the initial growth rate by keeping the reactant flow constant.

Because of its unstable nature, Silane, SiH_4, should be decomposable at low temperatures. However, because of handling difficulties, little work had been done, until it was found that concentrations of 5% SiH_4 in an inert gas were relatively safe. Kagdis (1962), using reduced pressures of the order 2 - 10 torr of Silane, obtained epitaxy on (111) oriented silicon substrate material at $960^{\circ}C$.

Mayer and Shea (1964) diluted silane with hydrogen and investigated the growth rates and temperatures as functions of the SiH_4/H_2 ratio. They found that single crystal layers could be grown in the temperature range 1175° - 1210°C. However, the layer quality as deduced from electrical measurements was relatively poor, compared with layers produced by the standard $SiCl_4$ process.

This work was extended by Bhola and Mayer (1963), who also investigated doping effects using arsine and borane. They found that for growth temperatures $< 1000°C$ the layers were polycrystalline. This conflicts with the findings of Kagdis (1962) which were confirmed by the results of Joyce and Bradley (1963) who obtained epitaxy over the entire range of temperatures - 900°C to 1260°C using a silane molecular beam technique. Joyce and Bradley's analysis of the reaction kinetics of the silane decomposition reaction -

$$SiH_4 \rightleftarrows Si + 2H_2$$

showed that the rapid decrease of growth rate at temperatures less than 1000°C was due to the rate limit of the removal of hydrogen from the substrate surface. Using this result, Richman and Arlett (1969) diluted the silane with helium and achieved growth rates of 0.6μ per minute at temperatures of 900°C.

The results of various workers using silane are presented in fig. (2.4) for convenience in comparisons.

From these results it is seen that epitaxial growth can be achieved at low temperatures with silane, but with the exception of the work of Richman and Arlett, the low temperature growth rates obtained are very low. The use of silane has not enabled high quality epitaxial layers to be grown at temperatures less than 1000°C.

2.1.(1) Effect of Substrate Orientation on Growth Rates.

Tung (1965) investigated the variation of growth rate with substrate orientation using the hydrogen reduction of silicon tetrachloride. His results are shown in fig. (2.5a). These variations are followed in form by the other chemical reactions though with some differences in rates. Tung also found that there was a critical rate, above which large numbers of pyramidal growth defects were observed. This

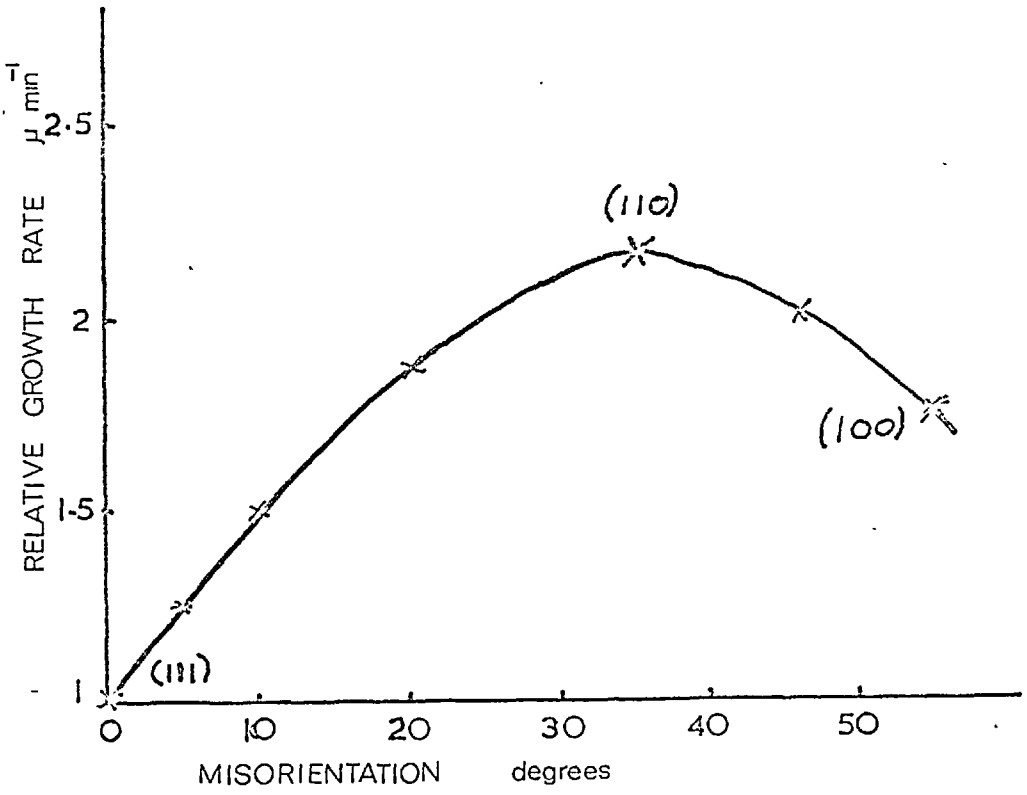


Fig. (2.5)(a)
VARIATION OF RELATIVE GROWTH RATE WITH MISORIENTATION OF GROWTH FACE FROM THE (111) ORIENTATION.
[AFTER TUNG 1965].

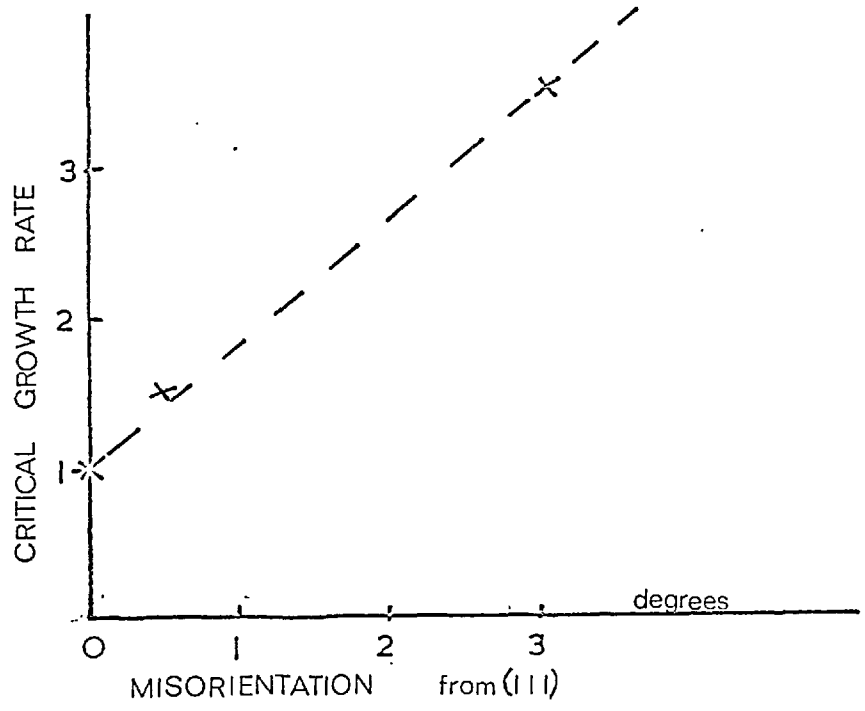


Fig. (2.5)(b)
GRAPH SHOWING VARIATION OF CRITICAL GROWTH RATE WITH MISORIENTATION FROM THE (111).
[AFTER TUNG (1965)]

critical rate was also found to be dependent on substrate orientation as shown in fig. (2.5b). These results suggest that rate effects on a given surface can produce regions of different orientation by the following possible saturation effect. If the rate of supply of material exceeds the maximum growth rate of the surface orientation at that temperature, then the excess could grow in other orientations. The variation of growth rate with misorientation could be explained as follows: for growth on an exact (111) surface, the rate would be controlled by production of steps or growth fronts by condensation. For misoriented surfaces these active regions would already exist. Thus, higher growth rates are possible on vicinal surfaces.

From fig. (2.5a) it is seen that the (111) orientation has the lowest epitaxial growth rate. The reason for the predominate use of (111) oriented material is mainly the ease with which large defect-free crystals of this orientation can be grown for substrate production. Bean and Gleim (1969) have also shown that the (111) oriented material, chipping during cleaving is much less severe than for other orientations. This is believed to be due to differences in the Young's moduli for the various directions: the < 111 > having the highest modulus.

< 100 > 1.3×10^{12} dynes per sq. cm.

< 110 > 1.7×10^{12} dynes per sq. cm.

< 111 > 1.9×10^{12} dynes per sq. cm.

From the findings of Tung (1965) the substrates used for epitaxial growth are misoriented by 1 to 2 degrees, to avoid defects being produced at high rates of growth.

2.1.(2) Substrate Preparation for Chemical Epitaxial Growth

Substrate wafers are produced by slicing the single crystal rods. This initial slicing controls the orientation. The wafers are then lapped to remove the saw damage, with a succession of diminishing sizes of lapping compound. Each lapping removes the damage of the preceding stage. One face of the wafer is then polished to produce an optically flat surface. The last layer of damage is then removed by a chemical polishing method which does not affect the surface finish of the wafer.

The effect of surface imperfection on the growth process is discussed in the section on defects.

2.1.(3) Defects in Silicon Epitaxial Layers

Crystal imperfections and defects play an important part in controlling the electrical properties of semiconducting materials. The main result of increasing defect densities in general is a reduction in the carrier mobility and life-time.

The main defects found in epitaxial silicon layers are stacking faults and dislocations. In addition to these faults twinned regions in the form of tripyramidal defects or micro twin lamelae are also found; however, these latter defects are only found in films grown in the presence of contamination, especially hydro-carbon material as was shown by Miller et al (1963). Lawrence (1965) has shown that tripyramidal defects can also be produced by the presence on the substrate surface of small fragments of silicon.

Stacking faults have been investigated in great detail by etching techniques, and optical microscopy; Chu and Gaveler (1963); and by transmission electron microscopy; by Booker (1964).

The stacking sequence for (111) planes in the diamond structure was shown in section 1, and the causes of stacking faults, such as a shear process, or collapse of vacency clusters, were discussed. In epitaxial growth of silicon, it has been found that stacking faults may be grown into the crystal during the deposition process. The fact that the faults grow with the crystal is a consequence of the covalent nature of the bond, which gives a low fault energy. Amelinckx et al (1962) have estimated the fault energy to be of the order of 50 ergs per cm^2. The stacking faults lie on (111) planes and so have characteristic geometrical forms which depend on the orientation of the (111) planes with respect to the growth geometry. For the (111) growth surface, it is seen that the $\{111\}$ planes form a tetrahedron; one of whose faces is the growing surface, and the opposite vertex is at the substrate. Thus if a fault were nucleated at this vertex, a stacking fault would be propagated along the 3 inclined faces forming the tetrahedron. The mechanism of fault initiation will be discussed later. Fig. (2.6) shows the geometry of the fault tetrahedra, produced if faults propagate along all three $\{111\}$ planes. It is possible for the faults to be propagated

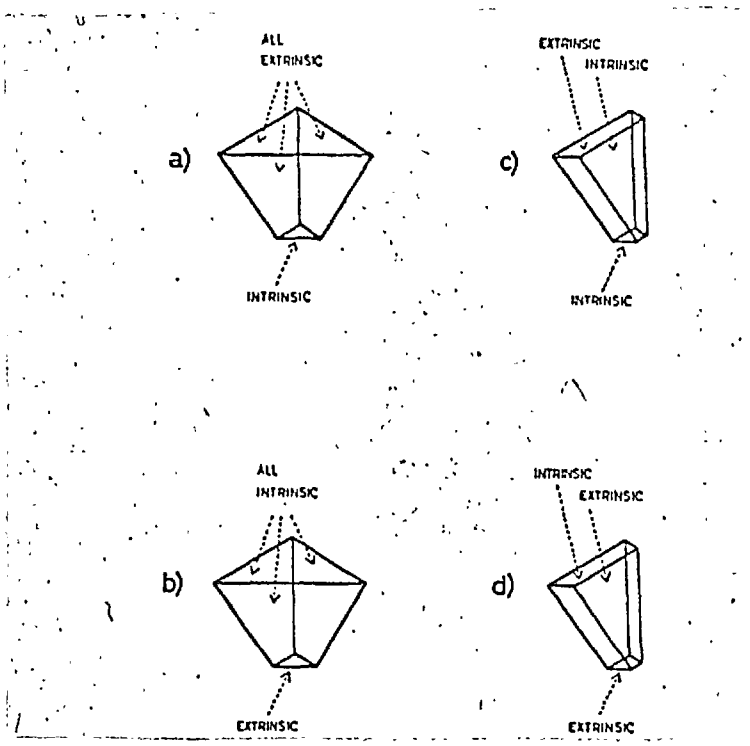


Fig. (2.6)
GEOMETRY OF STACKING FAULTS IN (111) ORIENTED SILICON.
[AFTER BOOKER 1964]
a,b TETRAHEDRAL DEFECTS
c,d CLOSED POLYGON PAIR DEFECTS.

along two close parallel (111) planes. This will give rise to the geometry of fig. (2.6c,d). The fault consisting of a close pair of line faults.

If only one face of the tetrahedron propagates with growth as a fault, a single line fault is produced.

Since the faults have the characteristic geometry, it is seen that the length of the trace of the fault in the growth surface is related to the depth of the point of origin of the fault by a geometrical factor. for (111) growth the depth of the origin point = 0.81 x [the length of the trace in the surface] (Mendelson (1964).

As well as the single geometric forms discussed above, interaction during the growth of the layer, may produce different geometric forms.

Finch et al (1963), Queisser et al (1962), Mendelson (1964) and Schwuttke and Sils (1963) investigated the causes of stacking faults in layers grown by chemical transport methods. They found that localised surface stresses, mechanical damage and surface oxide patches, were among the main causes of stacking faults.

Batsford and Thomas (1964) showed that washing the substrate in 'tap water' before depositions also caused large numbers of faults in subsequent growth. This effect was also found by Pomerantz (1967), who assumed it to be due to the presence of heavy-metal ions. Chu and Gavaler (1963) used etching techniques and found that the dislocations at the ends of the two forms of fault whown in fig. (2.6 a,b) and (c,d) were of two different types. On etching those at the ends of the line faults produced etch-pits, whilst the same etch did not produce pits at the vertices of the triangular stacking faults.

This difference was confirmed by the X-ray diffraction work of Schwuttke (1963), who found that the partial dislocations associated with the line defects had Burgers vectors of the form $\frac{a}{6} < 112 >$ whereas triangular faults had dislocations with $< 110 >$ Burgers vectors.

To account for these varied effects many models for fault nucleation have been proposed. Jaccodine (1963) proposed a process based on the collapse of vacancy clusters at the growth interface. This mechanism was used by Silcox and Hirsch (1959) to account for the

small tetrahedral faults seen in quenched gold. The results of Notis and Conard (1963) support this mechanism; however, as shown by Mendelson (1964) this model is incapable of accounting for the geometric forms of the line faults.

Booker and Stickler (1962) proposed a model for stacking fault nucleation, based on the local mismatch of the initial growth nuclei. The geometrical shape being determined by the shape of the initial mismatch boundary. These studies were continued by Booker and Howie (1963) and Booker and Stickler (1963). These results confirmed the model, and Booker and Stickler (1963) showed that the nature of the initiating mismatch area could be deduced from the nature of the stacking fault produced in subsequent growth. The relationship between the various faults is as follows:

If a pair of faults with a common partial dislocation are at an acute angle to each other, then they are of the same type, ie. both intrinsic or extrinsic.

If the angle is obtuse then, the faults are of opposite types, ie. intrinsic, extrinsic or vice versa. The various arrangements are shown in Fig.(2.6)

The model suggested by Booker et al discussed above, is similar to that suggested by Mendelson (1964), in which the mismatch takes the form of a partial dislocation at the layer substrate interface.

Whilst the exact process of defect nucleation is not certain, methods for the elimination of stacking faults has been evolved by various workers. Batsford and Thomas (1964) have shown that pre-annealing the substrate at 1200°C for 15 minutes in a current of purified hydrogen will reduce the fault density in subsequent growth, by several orders of magnitude.

The effect of the state of the surface was studied by Henderson and Whitton (1969), who found that removal of the top half micron of substrate surface by a gas-phase etch reduced the fault density in subsequent growth from 10^5 to 10^2 per sq. cm. The etching technique used was that devised by Lang and Stavish (1963) using anhydrous HCl at a substrate temperature of 1200°C. This gives a featureless surface, superior to that produced by wet chemical polishing.

The reaction which occurs is the reverse of the deposition reaction, ie. $Si + 3\,HCl \rightarrow SiHCl_3 + H_2$. The findings of Henderson and Whitton are confirmed by the work of Chu and Tallman (1964) using water vapour as an etchant.

2.1.(4) The Growth Mechanism in Chemical Epitaxy

The mechanism involved is not yet completely understood. However, some simplified models have been produced for various reactions based on studies of the thermodynamics and reaction kinetics. Theurer (1961), Charig and Joyce (1962) and Bylander (1962) have studied the reduction of $SiCl_4$ and $SiHCl_3$ and have concluded that the silicon is formed on the substrate by a surface-controlled reaction. Burton and Cabrera (1949), Frank (1949), Burton et al (1951) and Cabrera and Vermilyea (1958) have produced general theories of growth from the liquid and vapour phase based on the existence of steps of ledges in the surface.

The formation of these steps has been discussed in great detail by Cabrera and Vermilyea (1958) and Frank (1958), and much experimental evidence exists confirming the effect of steps on surface phenomena. These theories suggest that the rate of growth is proportional to the surface step density. This is confirmed by the work of Tung (loc cit). Thus the substrates produced commercially for epitaxial growth are misoriented by up to 2° from the (111) direction to produce a high step density on the surface. If the surface steps are active in the growth then the growth mode should be that of lateral growth by extension of these surface steps.

Transmission microscopy studies by Charig and Joyce (1962) using hydrogen reduction of $SiHCl_3$ have shown that the initial growth takes the form of discrete islands or clusters of atoms, the smallest observed being of the order 500Å in diameter. Three dimensional growth centres were also found by Rawlins and Brosselard (1966) in studies of the initial growth mechanism, using the reduction of $SiCl_4$. Their findings are similar to those of Charig and Joyce (opus cit) in that the nuclei were not crystallographically shaped. These results indicate that the surface steps are not active during the initial growth.

The growth, after coalescence of the nuclei has occurred probably proceeds by a step-flow mechanism. This result is suggested by the work of Resvez and Evans (1964) who studied the surface topography of continuous layers grown by reduction of $SiCl_4$. Using replication methods they found on (111) surfaces, fine striations along the $< 110 >$ directions and rows of low ridges normal to $< \bar{1}\bar{1}2 >$ directions. These latter features were interpreted as surface growth-fronts.

Summary

From this review of the chemical growth processes, it is seen that the processes in present use have the disadvantage of high growth temperatures. These in turn limit the resistivity profile which can be obtained because of the dopent diffusion effects.

2.2. Vacuum Evaporation.

The investigations of the epitaxial growth of silicon by vacuum evaporation may be divided into two groups.

I Those experiments carried out in high vacuum conditions, ie. those of working pressures greater than 10^{-7} torr.

II Those studies carried out in ultra high vacuum, in working pressures in the range 10^{-8} to 10^{-10} torr.

2.2.(1) Results of Growth Studies Carried out at Pressures $\geq 10^{-7}$ torr.

Because of the great chemical reactivity of silicon, the use of crucibles of refractory oxides or metals results in the deposition of contaminated layers: Hale (1963). Also at the high temperature required about 1500°C, the rate of attack of the crucible is rapid.

Thus in order to deposit contaminant-free material, the main method used was that of electron bombardment. Hale (1963) used a piece of silicon, melted on a water-cooled hearth. This method had been superceded by that of Unvala (1963) who mounted the source into a recess in the hearth, which improved the cooling and stability, and allowed the silicon to act as its own crucible, with only the focus zone being molten.

Substrate Preparation

The substrates used were mainly of the (111) orientation, and were produced by the standard methods of sawing and lapping, and chemical polishing to remove the lapping damage. The exact orientations used by the various workers are not given, but may be assumed to be 1^{o} - 2^{o} off the (111) orientation as used in chemical epitaxy processes. Before use the substrates were polished in standard chemical polishing solutions, and before deposition they were cleaned by heating. Since the thermal treatment is of importance in controlling the state of the surface, we shall review the effects of thermal treatment on silicon surfaces in some detail.

2.2.(2) Substrate Surface Cleaning Methods.

The state of the substrate surface has been shown to have a great influence on the quality of layers grown by chemical transport methods. Consequently elaborate chemical cleaning procedures have been devised as discussed in part I of the review. The chemical methods used cannot be used in vacuum systems because of corrosion effects.

Apart from traces of greases caused by exposure to the atmosphere or handling, the main contaminant on the surface is a thin layer of silicon dioxide. This oxide layer forms on any clean silicon surface when exposed to the air. The thickness of the oxide layer has been estimated by Archer (1957) to be of the order of 20Å, for oxide films formed on a freshly etched silicon surface exposed to the air.

Allen et al, (1959) and Hagstrum, (1961) have shown that this thin oxide coating can be removed by heating the silicon to temperatures of the order 1200^{o} - $1300^{o}C$, for periods of 3 - 5 seconds in vacua of 10^{-9} torr. The oxide is removed by a reaction of the form $SiO_2 + Si \rightarrow 2SiO$. The SiO is volatile at high temperatures. Toombs and Welch (1952) give values for the vapour pressure of SiO, which show that for temperatures of the order $1200^{o}C$, $P_{SiO} \approx 10^{-3}$ torr and at $30^{o}C$, $P_{SiO} \approx 10^{-11}$ torr.

Lander and Morrison (1962) examined the state of heat treated silicon surfaces using low energy electron diffraction techniques (L.E.E.D.) which are sensitive to the top few atomic layers at a surface.

They investigated the oxide coverage of silicon surfaces at various temperatures and pressures of oxygen. Their results show that for a given pressure of oxygen, there exists a certain temperature, above which the silicon surface will remain oxide-free.

The rate of recontamination of a cleaned surface depends on the pressure and composition of the residual gases. The surface temperature is also important since the sticking coefficients of the components of the residual gases will vary with temperature. Also reactions may occur to produce volatile or non-volatile surface compounds. The maximum background pressure which can be tolerated depends on the ratio of the activation time of the process being investigated to the time for the absorption of a monolayer of gas on the surface.

Table (I) gives the values of monolayer absorbate formation times for various values of pressure.

2.2.(3) Substrate Surface Contamination Effects

The effects of the thermal treatments given to the substrates by various workers showed significant differences. Unvala (1963), heating substrates to 1200°C in vacua of the order 10^{-5} torr, observed no traces of silicon carbide on the surface, nor in the layer grown subsequently. Thomas (1966), although working at pressures of 10^{-7} torr, observed large quantities of silicon carbide after heating the substrate to 1200°C. In some cases, the silicon carbide was found to be epitaxially oriented with respect to the substrate.

Both Unvala and Thomas reported the presence of large numbers of etch pits in the surface after heating. For pressures $\leq 10^{-6}$ torr, the pits were observed to be well-formed triangles, with edges in $<110>$ directions. These pits have been observed in many studies of annealed silicon surfaces: eg. Batdorf and Smits (1959), Newman and Wakefield (1959). The pits are caused by the localised chemical attack by reactive gases, such as O_2 or H_2O, in the ambient vacuum. Reactions of the form $Si + O_2 \rightarrow 2SiO$ occur at localised points and the SiO, as was noted, is highly volatile at the temperatures used. The removal of the SiO_2 exposes a fresh silicon surface, thus producing a pit. Farnsworth (1959); (1960) showed that both $\{111\}$ and $\{311\}$ planes are exposed by this process which is given the name thermal etching.

The results of Unvala and Thomas suggest that the composition of the residual gases is important, especially the relative amounts of hydrocarbons, water vapour and oxygen. Excess of one or other of these could account for the finding of no silicon carbide by Unvala, whereas Thomas finds the surface to be covered with a layer, or assembly of grains of silicon carbide.

From these results we see that under the conditions of vacua of the order 10^{-5} torr to 10^{-7} torr, the annealed silicon substrate surface contains large numbers of etch pits, traces of oxide, and possibly traces, or large amounts of silicon carbide, depending on the hydrocarbon content of the residual gases.

2.2.(4) Variation of Minimum Epitaxial Temperature with deposition rate and Pressure.

The minimum epitaxial temperature is a useful parameter in comparing the results obtained by the various workers, under differing conditions. In the work described in group I of the review, the depositions were carried out in a pressure range 10^{-5} - 10^{-7} torr, using oil diffusion pumped vacuum systems. The high working pressures reported are a direct consequence of the high temperatures required for evaporation and substrate heating, and the resulting general outgassing effects. Hale (1963) obtained epitaxy at a substrate temperature of 1200°C, at an evaporation pressure of 10^{-6} torr. Unvala and ~~Beeker~~ (1963), at a pressure of 10^{-5} torr, found a minimum epitaxy temperature of 1100°C. At 10^{-7} torr, Gasson (1962) found a minimum temperature of 950°C; and Thomas (1966), also working at 10^{-7} torr, obtained epitaxy at 800°C.

In the work of Hale, the deposition rate was of the order of 0.5μ per minute, whereas Unvala used rates of the order 1μ per minute. In the cases of Thomas and Gasson, at pressures of 10^{-7} torr the deposition rates were 0.5μ per minute and $< 0.1\mu$ per minute, respectively, but despite this large difference in rates, the difference in the epitaxial temperatures found by Thomas and Gasson is only 150°C.

From these results it is seen that the epitaxial temperature is reduced for lower evaporation pressures and for the deposition pressures used by the above mentioned workers, it is seen that the epitaxial temperatures are more sensitive to the deposition pressures

than to large variations of deposition rates. This finding is in accord with most published results of epitaxial studies of various materials. The presence of the large amounts of silicon carbide observed by Thomas did not affect the epitaxial process. This point will be discussed later. Unvala and Booker (1963) found that increasing the deposition rate required an increase in substrate temperature to maintain epitaxial growth. Their results are shown in fig. (2.7).

The increase in minimum epitaxial substrate temperature with deposition rate has been observed in most reported studies of epitaxial growth: as reviewed by Hasse and Thun (1969).

Sloope and Tiller (1962; 1965) studied the variation of the epitaxial temperatures with deposition rate for germanium deposited on to (111) oriented CaF_2, over a wide range of pressures, 10^{-5} - 10^{-9} torr. They found that for deposition pressures less than 10^{-6} torr, their results could be expressed as linear plots of log (deposition rate) versus the reciprocal of the minimum epitaxial substrate temperature. The slopes of these lines were interpreted as representing the surface diffusion activation energy. For deposition pressures $< 10^{-6}$ torr, the values of these activation energies did not vary with deposition pressure. For pressures $> 10^{-6}$ torr, variations from linearity were found. These were ascribed by Sloope and Tiller to a contamination effect probably produced by the residual gases. A similar effect can be seen in the results of Booker and Unvala shown in fig. (2.7).

2.2.(5) Variation of defect content of Evaporated Silicon Layers.

Defects in Evaporated Silicon Layers

The defects found in evaporated silicon films have been investigated in detail by Unvala and Booker (1966), and found to be identical to those observed in layers grown by the chemical vapour transport methods. The geometry and origins of these faults has been discussed in Section 2.1.(3) of this review.

Hale (1963), using optical microscopy and etching techniques, and Thomas (1964), using transmission electron microscopy, reported the presence of large numbers of stacking faults and dislocations in their layers.

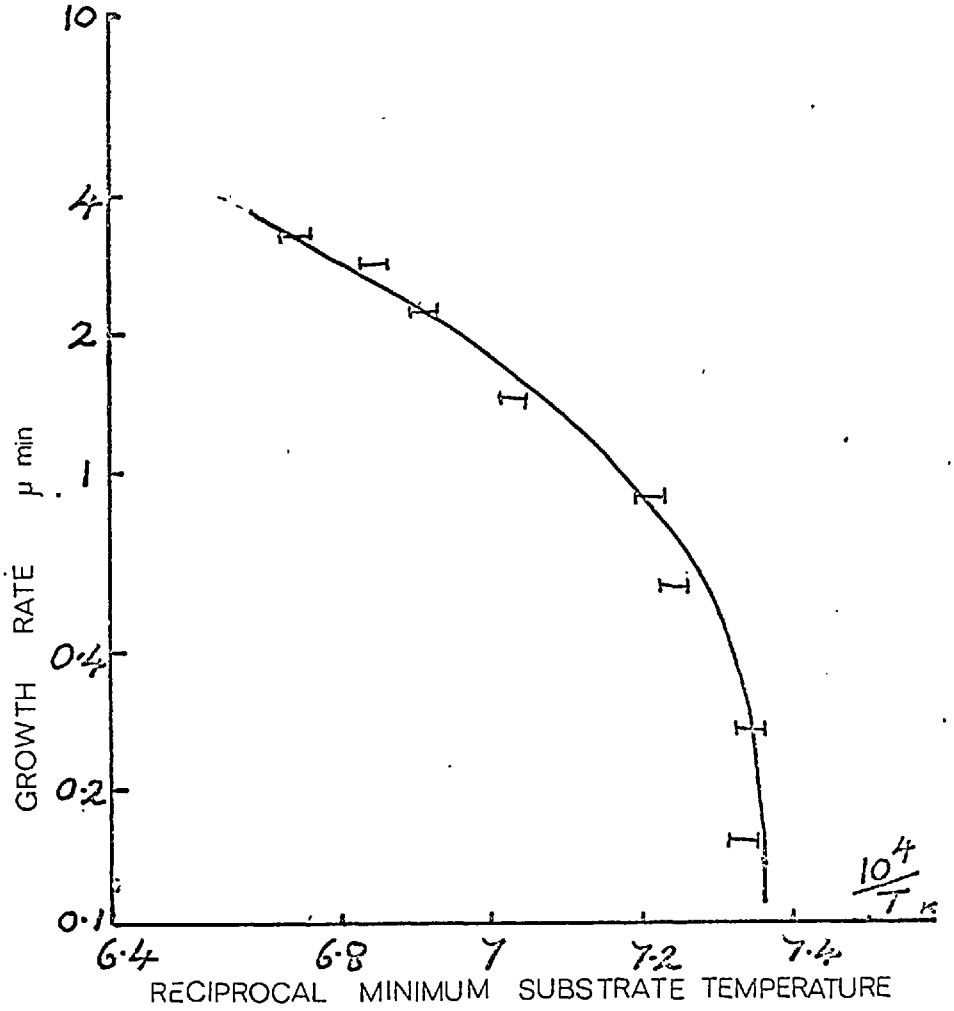


Fig. (2.7)
GRAPH OF MINIMUM EPITAXIAL TEMPERATURE VERSUS GROWTH RATE. PLOTTED AS LOG RATE VERSUS $10^4/T_{MIN}$

[DATA FROM BOOKER AND UNVALA 1963]

Thomas (1964) found that the densities of both dislocations and stacking faults decreased with increasing substrate temperature, but increased with increasing deposition rate. At a growth temperature of 1200°C and deposition rate of 0.5μ per minute the stacking faults could not be eliminated. Thomas also observed large numbers of tripyramidal defects in all the layers grown. These were due to silicon carbide contamination as was shown by Miller (1963).

Unvala and Booker (1964) found that by increasing the deposition rate above a certain value, they could eliminate the stacking fault defects completely, for substrate temperatures in the range 1200°C to 1100°C.

This critical rate was found to vary with the pressure at which the evaporation was performed, being $\sim 0.3\mu$ per minute for pressures of 10^{-7} torr increasing to 1μ per minute for pressure of 10^{-6} torr. This effect was interpreted by Unvala as the gettering of residual traces of oxide on the substrate surface by the impinging silicon vapour. A confirmation of this effect is Hale's (1963) observation that oxide mask regions on the substrate could be removed by evaporating silicon onto the substrate held at temperatures of the order 1200°C, which is the value used by Unvala. Unvala further showed that the introduction of oxygen during evaporation caused the formation of large numbers of stacking faults. This result confirms the model of Finch et al (1963) for the nucleation of faults by oxide particles.

Unvala also demonstrated the effect of hydro-carbons in producing tripyramidial defects by the admission of coal-gas into the vacuum system.

Miller, (1963) points out that the tripyramidal defect is only found if both oxygen and hydrocarbon contamination are present simultaneously. Thus the hydrocarbon content of the residual vacuum in the case of Thomas must have been quite high, since in all layers grown he found the tripyramidial defects.

The effect of carbon in producing the tripyramidal defect was confirmed in the work of Nielson and Rich (1964). They exposed the substrates at 1200°C to toluene vapour immediately before deposition.

Subsequent growth produced large numbers of the tripyramidal defects. They also found that if after the toluene exposure, the substrate was heated to 1200°C for 30 minutes in a good vacuum, ($\leq 10^{-7}$ torr) the number of tripyramidial defects produced in subsequent growth was very much smaller. This indicated apparently that the carbide compound was absorbed by the substrate, the carbon possibly going into solid solution. Silicon carbide dissociates only at temperatures $\gtrsim$ 1700°C.

Nielson and Rich (1964) also observed the effects of deposition pressures on the stacking fault densities. They found that for layers grown at pressures of 5×10^{-8} torr, all the faults were of the same size and had nucleated at the substrate-layer interface. Layers grown at the same rate and substrate temperature, but at a pressure of $\geq 10^{-5}$ torr, had higher fault densities, and faults of different sizes were observed. This latter observation indicated that some faults had been initiated during the growth, possibly by the formation of patches of oxide on the surface or by the absorption of residual gas.

2.2.(6) Nucleation and Growth Processes observed in Layers Deposited at Pressures of 10^{-6} torr.

The formation of the epitaxial layer can be divided into three stages.

1. The initial nucleation.
2. The growth of the nuclei.
3. The coalescence stage: formation of the continuous layer.

These stages were investigated by Hale (1963) using optical microscopy, and by Thomas (1966) and Unvala and Booker (1964) using transmission electron microscopy.

Hale (1963) observed island growth in which the depositing silicon formed small well-oriented islands of triangular shapes on (111) oriented substrates. The islands enlarged and coalesced to form a continuous layer. Hale (1963) estimated the coalescence thickness to be 3μ. The coalescence thickness is an indication of the amount of contamination of the surface. Booker and Unvala (1964), and Thomas (1964) also observed island growth and found that the nuclei formed only in etch pits, on either the sides, or in the bottoms.

Thomas (1966) observed that the growth continues in the etch pits until they are filled. Further growth then occurred by lateral extension of the nuclei until coalescence. During this stage no new nuclei were seen on the surface. All the nuclei that Thomas (1966) observed were of the same size. This indicated that they were all formed at the same time, and grew at the same rate. In contrast to the observations of Hale the shapes of the nuclei were not crystallographic.

All the nuclei observed by Thomas (1964) contained large numbers of defects. However, their growth and coalescence did not increase the defect density. Thus the defect content of the layer was controlled by the initial nucleation rather than by the growth process. In contradiction to this observation, Newman and Wakefield (1964) observed their initial nuclei to be almost defect-free. The defects in their films were produced during the coalescence stage. This result was similar to findings by Matthews (1959), and Jacobs et al (1961) in studies of nucleation and growth process in metal films grown on rock salt and on molybdenite substrates. In these metal films the stacking faults were produced as a result of the mismatch between the deposit and substrate lattices. This was discussed in detail by Matthews (1959). This explanation cannot be applied to the case of silicon deposited on silicon substrates since there is then no lattice mismatch. A possible explanation may be that the stacking faults nucleate at debris swept up by the growth fronts of the nuclei, and entrained at coalescence.

Unvala and Booker (1964) observed a strong rate dependence of the nucleation process. At very high deposition rates, $\geq 1\mu$ per minute, no nuclei were seen using optical microscopy. (Thus the size of any nuclei present would have to be $\leq 1\mu$ diam.). At low deposition rates $< 0.5\mu$ large nuclei of various sizes and non-crystallographic shapes were observed using optical microscopy. (The size of the nuclei in this case would then be $\geq 2\mu$ in diameter.)

As in the work of Thomas (1966) the nuclei were found to contain large numbers of stacking faults and dislocations, when examined by transmission microscopy. The layer formation occurred by lateral growth and eventual coalescence. Unvala also found, as had the

previously mentioned workers, that coalescence did not increase the fault density. The coalescence thickness for low deposition rates was estimated by Unvala (1964) to be of the order of 2 - 3μ. This value is very close to that of Hale (1963) and is probably due to the effect of absorbed contamination due to the high working pressure of the order 10^{-5} torr, similar to Hale's.

The rate dependence of the nucleation process was interpreted by BOOKER & Unvala (1964) to be the result of the removal of surface contamination by a chemical reaction. This is exhibited in the variation of nuclei sizes, which indicates that growth commenced at the various points at different times, due to the various regions on the substrate surface becoming clean at different times during the initial growth period.

The contamination responsible was investigated by electron diffraction and deduced to be silicon dioxide, in the form of an amorphous layer.

The nucleation rate dependence was thus determined by the effect of contamination and its rate of removal by the incident silicon. Comparison of this observation with Thomas's findings of nuclei of uniform size indicated that the contamination found by Thomas was not removed by the gettering process postulated by Unvala. This again confirmed the difference between the surface contaminants found by Unvala and Thomas. This difference was probably due to differences in the composition of the residual gases.

After the coalescence process had occurred, the subsequent growth occurred by a different mechanism, since no nuclei were reported observed by the above workers on the surface of a freshly deposited layer. This latter observation was similar to the results of Revsez and Evans, cited earlier in this review.

The results reviewed above, are evidence that the growth medhanism in the post-coalescence stage of growth, is a two-dimensional process of lateral growth of possibly monolayer steps.

2.2.(7) Electrical Properties of High Vacuum Evaporated Silicon Layers

Of the works cited, only Unvala, Booker (1964) and Hale (1963) investigated the electrical properties of the layers in any detail.

Resistivity

The resistivity of the layer is a measure of the net amount of dopant in the layer. The sources of the dopants are:

(i) Diffusion from the substrate.

(ii) Contamination effects from the ambient gases.

(iii) Coevaporation of the dopants in the source.

At the high growth temperatures that he used, Hale (1963) found that dopant diffusion from the substrate was the dominant transfer mechanism. He also observed variation in resistivity of various specimens due to the preferential evaporation of dopants from the source, and also substrate surface depletion effects caused by the high temperatures used to clean the substrate. By evaporating dopant from an ancillary crucible, Hale (1963) also produced PN junctions. These had very soft breakdown characteristics at low reverse bias voltages. These poor quality I-V characteristics reflected the high defect content of the layers.

Booker and Unvala (1964) carried out a similar programme of measurements on resistivities and junction properties using much better quality layers. They found that for low resistivity source material the layer resistivity was the same as that of the source, to within measurement errors.

However, for high resistivity sources the layers had much higher resistivities than the source and had a tendency to be P type, even for N type source material. This could be due to contamination either by electrically active materials or by preferential evaporation of the dopants used in the source. Booker and Unvala (1964) obtained max. values of 15 Ω cm for P-type material and of 3 Ω cm for N-type material.

The diode junctions grown by Unvala and Booker (1964) exhibited sharp reverse biase breakdowns at between 30 and 40 volts for ~ 0.1 Ω cm N-type layers on 5-10 Ω cms P-type substrates.

The sharp breakdown is characteristic of good crystal structure, although studies by Quiesser et al (1963) have shown that breakdowns remain sharp for stacking fault defect densities up to 10^5 per sq. cm.

Summary

From these results, it is clear that by using vacuum evaporation epitaxial growth has been carried out at lower temperatures than by means of the chemical processes. However, the growth characteristics and quality of the layers produced by vacuum evaporation were often dominated by contamination effects and chemical reactions caused by poor vacuum conditions.

2.3. Results of Studies of Epitaxial Growth of Silicon carried out in Ultra High Vacuum Conditions.

2.3.(1) Introduction; Sublimation Sources.

In sublimation, the material passes directly from the solid to the vapour state, without the production of any liquid phase. This type of source can only be used for materials which have high vapour pressures in the solid state.

Honig (1954) gives a value of vapour pressure of 10^{-4} torr for silicon at 1300°C. (m.p. Silicon $\simeq$ 1410°C)

A typical form of sublimation source consists of a rod of silicon clamped between two electrodes. The rod is usually 'necked' at the centre to give a local 'hot zone' which is maintained at temperatures around 1350°C by passing a current through the rod. This type of source has the advantage of simplicity and consequently high reliability.

The main disadvantage of sublimation sources is the very low deposition rate. This requires the substrate to be mounted very close to the source to obtain useful deposition rates. The deposition rate, and layer uniformity, can be improved by using an array of source rods close together, thus forming a 'large area' source. Since the deposition process is carried out at pressures of the order 10^{-9} torr, surfaces remain clean for a time which is long, relative to the deposition rates used.

The time to form a monolayer of absorbed gases at a pressure of 10^{-9} torr is given in table (I).

With very low deposition rates, the rate of surface coverage by residual gas absorptions may become significant. The effects will depend to a great extent on the composition of the residual gases.

2.3.(2) Growth Parameters for Epitaxy in UHV Conditions

One of the earliest studies of growth in ultra-high vacuum conditions was that of Nannichi (1963). Using an ion-pumped system he obtained epitaxy at substrate temperatures of 830°C, using a very low sublimation rate of $10^{-4}\mu$ per minute (as estimated by the author) at a pressure of 10^{-8} to 10^{-9} torr.

In a vacuum of the same order, Handelman and Povilonis (1964) grew layers at a rate of 0.3μ per minute, at substrate temperatures of 1100°C, also using an ion pumped system.

This growth temperature was a consequence of the experimental arrangement used, (the substrate being mounted very close to, and heated by radiation from, the sublimation source) and so may not represent the minimum substrate temperature for this growth-rate, and vacuum conditions used.

Handelman and Povilonis (1964) found a high degree of uniformity and reproducibility in the perfection of the layers. They also observed a variation of layer quality with deposition pressure. Layers grown at higher pressures; of the order 10^{-7} torr contained large numbers of included grains of various sizes.

Widmer (1964) improved the vacuum conditions and was able to sublimate at a pressure of 10^{-10} torr, using an oil-free system. He investigated the epitaxy and defect content for (111) oriented substrates using two deposition techniques. In one, which shall be called 'direct', the silicon substrate was cleaned by heating to $\sim$ 1200°C for several minutes. This removed the oxide, as discussed previously. The substrate temperature was then reduced to that for deposition, which was then commenced.

In the second method, silicon was 'predeposited' on to the substrate, whilst at the above cleaning temperature. The substrate temperature was then reduced after a few minutes to that of growth without interrupting the deposition rate (cf. the experiments of Nakanuma and Unvala discussed earlier). Using the direct method, Widmer found that layers grown at 0.03μ per minute, at temperatures of 320°C, contained a mixture of large polycrystalline regions in an amorphous or finely polycrystalline matrix. For growth temperatures of 550°C at the above rate; the layers were single crystal, with large numbers of defects. Layers grown at 800°C, were defect-free.

From these results it is seen that the low temperature limit for epitaxy lies between 550°C and 320°C; for the rate used.

Using the pre-deposition method; layers grown at 320°C, though polycrystalline, contained large grains with no amorphour region. Layers grown at 550°C were defect-free.

These results confirm the general findings that the initial growth and the substrate surface control the layer quality, since in this pre-deposition case contamination from the residual vacuum was negligible.

Weisberg (1967) showed the effect on the epitaxial process of oxygen contaminant from the source material. By using as a source oxygen-free material - (trade name Lopex; produced by Texas Instruments Limited, nominal oxygen content $O_2 < 10^{17}$ ppm) - he obtained epitaxy for (111) oriented substrates at a minimum epitaxial growth temperature of 450°C at 0.01 to 0.02μ min^{-1} at a pressure of 3×10^{-8} torr. This minimum temperature is in accord with the results of Widmer, who used a higher rate and a better vacuum.

Comparison of this result with that of Widmer suggests that the deposition rate dependence effect is small compared with the contamination effect. This effect could explain the result of Nannichi (1963), who reported a minimum temperature of 830°C at an almost zero-rate of deposition. In this case, the growth rate was probably equal to or less than the surface recontamination rate by the residual gases, and the minimum temperature of growth found was that for maintenance of a clean surface.

As well as the direct method (defined above) Wiesberg (1967) also used the pre-deposition method as used by Widmer, using a starting temperature of 800°C. Layers grown by this method were again single crystal at 450°C, but polycrystalline at 380°C. This latter value is near to that found by Widmer for polycrystalline growth also using a pre-deposition method. Wiesberg also used (100) oriented substrates, and using the pre-deposition method, found layers grown at 380°C were strongly oriented, though with definite traces of twinned regions, as detected by reflection-diffraction techniques.

This showed that the epitaxial temperature for (100) surfaces was lower than that for (111) surfaces. This is probably due to the different structures of the surfaces, as can be seen in table (II). This effect was indicated in the work of Tung, reviewed in the previous section (2.1.(1)).

2.3.(3) Low Energy Electron Diffraction Studies of Surfaces and Epitaxial Growth.

The sensitivity of low energy electron diffraction effects to the first few atomic planes at the surface makes this technique ideal for the study of surface phenomena. The initial studies of the surface structure of silicon by L.E.E.D. were carried out by Farnsworth et al (1957/59/61). These studies were extended by Lander and Morrison (1962,63), who showed that distinct surface structures could be associated with the different diffraction patterns obtained. These patterns were designated by a nomenclature introduced by Lander and Morrison (1962) and extended by Wood (1964). The surface was given the name of the L.E.E.D. diffraction pattern it produced.

These studies showed that silicon surfaces had definite structures related to but differing from the underlying bulk material, and that various surface structures could be produced in the same material by different thermal treatments.

In the case of silicon, Lander and Morrison (1962) found that the (111) oriented surface of silicon gave two distinct, different, diffraction patterns depending on the heat treatment given to the specimen.

After high temperature ($\gtrsim 1000^{\circ}C$) annealing and rapid cooling, a pattern designated the Si(111)-7 was observed. If the specimen was cooled very slowly or annealed at 600° to $700^{\circ}C$ for a period of 15 - 20 mins. then a different pattern was observed. This latter pattern was designated Si(111)-5 by Lander and Morrison (1963). The retention of the (111)-7 pattern after rapid cooling indicates the 'freezing in' of this surface structure.

The existence of these two distinct patterns indicates the presence of two distinct surface structures, each with its own temperature range of existence. While the exact atomic surface structures that the diffraction patterns represent are difficult to deduce, the diffraction patterns show that the structures of annealed silicon surfaces are different from that of the bulk. This is termed reconstruction.

Thomas and Francombe (1967a) used L.E.E.D. techniques to examine the structure of silicon layers sublimed on to thermally cleaned silicon surfaces at different deposition temperatures, at a fixed deposition rate of $0.03\mu\ min^{-1}$. They found that for layers grown on a (111)-7 surface at temperatures in the range $1000^{\circ}C$ to $600^{\circ}C$, no change in the L.E.E.D. pattern was detected on cooling and re-examination.

For growth temperatures below $600^{\circ}C$ the initial (111)-7 pattern was found to have changed to give a pattern interpreted as a superimposition of the (111)-7 and (111)-5 patterns. This composit pattern was interpreted as indicating the presence of domains of (111)-7 and (111)-5 structures in the surface. Also, the constancy of the relative pattern intensities observed before and after a given deposition indicated that the domains were stable during growth.

It was also observed that as the growth temperature was raised towards $600^{\circ}C$ the relative intensity of the (111)-5 pattern decreased, showing that the concentration of (111)-5 domains had decreased. Layers grown at temperatures below $300^{\circ}C$ were either amorphous or finely polycrystalline, since it was difficult to distinguish between these two states by L.E.E.D.

Growth on a (100)-2 surface gave similar results; the initial (100)-2 L.E.E.D. pattern was unchanged after depositions at growth temperatures from $1000^{\circ}C$ to $650^{\circ}C$. For deposition at temperatures

between 650° and 300°C, modifications to the (100)-2 pattern were seen in the form of extra spots. And for depositions below 250°C no spot pattern was observed, this latter indicating that the surface and hence the layers were again amorphous or finely polycrystalline.

The limits on epitaxial temperature found by Thomas and Francombe using L.E.E.D. data are in agreement with the lower limit indicated by Widner's results, obtained at almost identical pressures and deposition rates. There is also good agreement with the lower limit found by Wiesberg (1967) at a vacuum two orders of magnitude worse. From these results it would seem that the lowest possible temperature for epitaxy under zero deposition rate conditions was between 350° and 400°C for a clean (111) oriented surface. The anomalously high temperature reported by Nanichi is therefore suggested to be a contamination effect.

This conclusion was reinforced by the detailed work of Jona (1968), who examined dynamic L.E.E.D. patterns produced during growth experiments using very low deposition rates ($< 10^{-4}\mu$ per minute, a value similar to that used by Nannichi). Jona found the minimum temperature for epitaxy on a clean (111) oriented silicon surface to be 400°C. For deposition at 340°C, the L.E.E.D. pattern indicated a surface which, though not amorphous, was highly disordered.

This minimum value found by Jona may be taken to be the zero deposition rate minimum epitaxial temperature, and is in full accord with the findings reviewed above of Widmer, Wiesberg, Thomas and Francombe, for (111) oriented silicon surfaces.

For a silicon (100)-2 surface, Jona (1968) found a minimum temperature for epitaxy of 240°C. He also found that deposition on a (100)-2 surface at room temperature produced a L.E.E.D. pattern indicating an ordered surface structure. However, there were differences between this (100)-2 room temperature growth pattern and that from layers deposited at 240°C, onto a (100)-2 surface.

These results on the (100) surface showed the same trends as the results of Weisberg (1967) Francombe and Thomas (1967a) and demonstrated the marked effect of the difference in surface structure of the (111) and (100) surfaces. (cf. Tung. loc cit.) as can be seen in Table (II).

Jona also investigated the annealing characteristics of very thin amorphous layers deposited on to the clean (111) oriented substrate surface. He observed that the crystallization process of these layers occurred via two different surface structures before the Si(111)-7 surface structure was formed. The activation energy of this crystallisation process was estimated as 2.6 ev. This value is of the same order as the silicon-silicon bond energy as given in Table V.

2.3.(4) Variation of Defect Content with Growth Parameters.

Handelman and Povilonis (1964) found large numbers of stacking faults in all layers grown. Annealing the substrate at 1200°C for periods up to 10 minutes before deposition did not affect the fault density in subsequent growth. The growth parameters used - 1100°C and 0.3μ per minute - were the same values as those found by Unvala (1963) to eliminate stacking faults at a deposition pressure of 10^{-6} torr in an oil-pumped vacuum system as opposed to the value of 10^{-8} torr in an oil-free system used by Handelman and Povilonis. This suggested the presence of some form of contamination which was stable at 1200°C, and was most probably silicon carbide. The presence of silicon carbide in a nominally oil-free ion pumped system might have been due to the use of wax to seal the quartz sublimation chamber to the metal pump manifold.

Widmer (1964) found that the layers grown by the direct method at a substrate temperature of 800°C and deposition rate of 0.03μ per minute were defect-free, whilst those grown at the same rate at 550°C had fault densities of the order 10^{7} per sq. cm. Using the pre-deposition technique, layers grown at 550°C were found to be fault-free by Transmission Electron Microscopy.

Thomas and Francombe (1967b) were able to correlate the results of their L.E.E.D. studies with transmission electron microscope studies of the structure of the layers. They found that for growth temperatures greater than 600°C, where the (111)-7 structure was maintained by the growing layer surface, the layer contained very few stacking faults. Densities of the order 10^{3} per sq. cm. were found.

Layers grown at substrate temperatures in the range 600°C to 400°C, where the mixed surface structure develops, were found to contain high fault densities. The fault density was found to increase with decreasing temperature reaching levels of the order 10^{10} per sq. cm. at substrate temperatures of about 400°C.

These results indicated that stacking faults may be caused by the growth and interaction of the two surface structures, or, by the presence of impurities, which were present at too low a concentration to be detected by L.E.E.D.

2.3.(5) Nucleation and Growth Processes in U.H.V.

Abbink et al (1968) investigated the nucleation process by an in-situ replication technique capable of high resolution. They used substrates oriented so that the direction [111] was inclined by about two degrees to the $[\bar{1}\bar{1}2]$ direction lying in the substrate surface. They found that substrate surfaces thermally processed at 900°C for 1 hour to give the (111)-7 L.E.E.D. diffraction pattern contained large numbers of surface steps. The steps were found to be oriented so that the normal to the riser was in $< 112 >$ directions. The steps were found to be either about 3Å in height, or multiples of this height. They also found large numbers of particles in the surface. These were extracted by the replicas and found to be silicon carbide.

Silicon was sublimed onto substrate surfaces prepared as above, at rates of 0.01μ per minute and substrate temperature of 800°C. Examination of the initial growth on the substrate surface by Abbink et al, showed that this growth occurred in large islands which were irregularly shaped. The formation of islands showed that the steps on the annealed substrate surface had been inoperative during the initial growth. Subsequent growth on a freshly deposited silicon layer was found to take place by a step-flow mechanism no islands being observed. The freshly deposited surface also contained large numbers of silicon carbide particles.

The source of the carbon was unknown. Since the deposition pressure was of the order of 10^{-9} torr, the residual gases could not have contributed sufficient carbon to account for the high density of carbide particles observed.

The initial growth process was also investigated by Booker and Joyce (1966) and Joyce et al (1967), using the pyrolysis of a molecular beam of silane, in ultra high vacuum conditions. Using very low deposition rates of the order 1 to 0.1Å per second and a substrate temperature of 800°C, they found the initial growth on a thermally cleaned silicon surface took place by island growth. On (111) oriented surfaces the islands were well-formed triangles of uniform size and distribution. The flank faces of the nuclei were found to be $\{311\}$ planes.

It was found that the presence of a surface oxide layer on the substrate inhibited the formation of the islands. This accounted for the induction period observed, during which the oxide was assumed to be removed by a gettering process similar to that suggested by Booker and Unvala (1964).

The shapes of the islands differ from those found by Abbink et al (1968), who observed the islands to be non-crystallographically shaped. This may be due to traces of oxide on the surface in the case of Joyce et al (1967), since they did not use a high temperature cleaning treatment. However, Joyce et al (1967) cite the absence of stacking faults in the nuclei as indicating the absence of oxide on the initial substrate surface.

Joyce et al (1967) also carried out quantitative measurements of the nucleation process. They found that for a given substrate temperature, a saturation density of nuclei formed. A power law rela ionship was found for this saturation density and the molecular beam intensity viz, $N_s = CI^{1 \cdot 25}$, where N_s is the saturation density of nuclei,, and I is the beam intensity expressed as the number of silane molecules incident per second on the substrate. The saturation density was also found to be exponentially dependent on the substrate temperature, following an equation of the form, $N_s = C_{exp}\left[-\frac{E}{KT}\right]$. Where E is the activation energy of the process. From the analysis of the nucleation density, Joyce et al (1967) derived a value for the activation energy of surface diffusion. The value obtained lies between 1.77 and 2.5 ev. These results were found to be in agreement with a nucleation equation derived by Lewis and Campbell (1966).

Later work by Joyce et al (1969) and parallel work using L.E.E.D. and Auger spectrometry by Charig and Skinner (1969) extended the studies of silicon surfaces and nucleation mechanisms.

Using the silane molecular beam on (111) oriented substrates, Joyce et al (1969) found that for a constant substrate temperature, the height to width ratio of the nuclei varied with substrate pre-growth thermal treatment. The number of nuclei per unit area remained constant for a given substrate temperature however, as found previously.

As both the substrate annealing duration and temperature were varied, the morphology of the nuclei was observed to change. Well-defined triangles were obtained after a two minute pre-growth anneal at 1000°C. Thin irregular 'sheets' were found after a two minute pre-growth anneal at 1150°C. After a ten minute anneal at 1200°C no nuclei were seen (within the resolving power of the electron microscope) in the subsequent growth. Thus two-dimensional or layer growth had occurred. The parallel observations by Charig and Skinner (1969) showed that after the pre-insertion chemical cleaning procedures used by Joyce et al, the silicon surface showed strong oxygen and carbon peaks, before any annealing treatment in vacuo. They found that after 15 seconds at 1200°C the carbon and oxygen "auger signals" from the substrate had disappeared.

This result is similar to the observations of Nielson and Rich (1964), on the formation of tripyramidial defects following exposure of the substrate to toluene, in that, post-exposure heating to 1200°C caused the removal of the carbide contamination.

The above results indicate that the impurity responsible for island growth is carbon. The form of the carbon, whether as free carbon or combined with silicon as silicon carbide, is uncertain, although from the temperatures used, silicon carbide is more likely.

This effect of carbon is confirmed by the experiments of Joyce et al (1969) in which contamination of a cleaned silicon surface by exposure to ethylene at low pressures caused the appearance of growth nuclei on subsequent deposition. Heating an ethylene-contaminated surface to the temperatures given above restored the laminar growth mode.

The source of the carbon surface contamination has been suggested by various workers, - Bonsels and Lambert (1969), and Schink (1965) to be carbon in solid solution in the substrate silicon. Concentrations of the order 10^{18} - 10^{19} atoms of carbon per cc of silicon have been found by the above workers using chemical analysis techniques.

The carbon containing gases present in U.H.V. residual gases, such as CO, CO_2, CH_4 have been shown by Kahn and Summergrad (1967) not to yeild carbide on contact with heated silicon. However, Russel and Haneman (1969), using E.S.R. have detected traces of silicon carbide on silicon surfaces heated in U.H.V., this they suggested is caused by the cracking of methane CH_4. This, however, would produce ammounts of carbon, too small to account for the observed effects.

2.3.(6) Electrical Properties of Layers Grown in U.H.V.

Handelman and Povilonis (1964) investigated the dopant transfer mechanism during sublimation. They found for boron-doped sources the initial layer resistivities were greater than that of the source, but after long source use the resistivities became equal to within measurement errors. They showed that this behaviour was the result of initial preferential evaporation of the silicon from the source. This left a boron-rich surface layer which eventually caused a steady state dopant transfer. Measurements on N-doped layers indicated a similar behaviour. The high growth temperature used - 1100°C is reflected in the substrate out-diffusion effects, especially for N-type layers, because of the high volatility of group V elements such as phosphorus and arsenic.

Thomas and Francombe (1969) observed a similar dopant transfer mechanism: they found that the steady state was not achieved until at least half the source array of heated bars had been sublimed. Very uniform transfer of both P and N dopants from both high and low resistivity sources was then observed. Using (100) oriented substrates and a growth temperature of 550°C ensured high quality layers as discussed earlier. P-N junctions were produced by subliming the oppositely doped material on to P and N substrates. However, the use of a 1200°C, five minute anneal to prepare the substrate surface led to detectable out diffusion of the substrate dopant.

Thus the junctions were not as sharp as the low growth temperature should produce. Junctions produced by depositing P-type material on N substrates gave better characteristics than those produced by deposition of N-type material on P substrates.

By sequentially depositing P-type and then N-type material on to P-type substrates, better diodes were produced. Since the junction was then between two regions, both grown at 550°C, the substrate acting only as a mechanical support and epitaxially orienting initial crystal. Thus the dopant out-diffusion effect caused by annealing did not affect the junction properties.

These electrical measurements showed that the sublimation method was capable of better control and uniformity than was evidenced by the results of the evaporation studies reviewed, and was capable of producing layers of controlled resistivity reproducibly.

2.3.(7) Analysis of the Epitaxial Growth Data.

Table III summarises the reported results of epitaxial growth temperatures, rates and deposition pressures. Table IV summarises the reported variations of defect density with deposition parameters.

Fig. (2.8) is a plot of the log. (deposition rate) versus reciprocal minimum epitaxial substrate temperature for the results given in Table II. As can be seen, the data falls on to straight line plots: AB the results of workers of the group mentioned in section 2.2.(1) of the review; and CD and DE the results of growth experiments carried out in ultra-high vacuum. It is interesting to note that the results of Nannichi and Handelman and Povilonis, although carried out under nominal U.H.V. conditions, fall on the line AB, thus confirming the effect of residual gas contamination, and the result of Thomas lies close to the line DE.

The slope of line AB, fig. (2.8) gives an activation energy of 3.3 ev. This value is in good agreement with the values of the silicon inter-atomic bond energy of which various values have been found: these are tabulated in Table V.

TABLE III

VARIATION OF EPITAXIAL RATES AND TEMPERATURES FOR (111) ORIENTED SUBSTRATES.

Deposition Rate microns $min.^{-1}$	Deposition Temperature Deg. C	Deposition Pressure torr	Reference
$\sim 1 \times 10^{-4}$ ※	320°	4.10^{-10}	Jona (1969)
0.036	320°	10^{-10}	Widmer (1964)
0.02	350°	10^{-9}	Thomas and Francombe (1967)
0.1	420°	10^{-9}	Thomas and Francombe (1969) ※※
$\times 10^{-4}$	830°	10^{-8}	Nannichi (1963)
0.01	450°	10^{-8}	Wiesberg (1967)
0.3	1100°	10^{-8}	Handelman and Povilonis (1964)
1	1125°	10^{-6}	Hale (1963)
0.01	950°	10^{-7}	Gasson (1962)
0.5	800°	10^{-7}	Thomas (1966)
2.8	1200°	10^{-5}	Unvala and Booker (1965) ※※※

※ Deposition Rate quoted as $\frac{1}{3}$ monolayer per min; equivalent to $\sim 1 \times 10^{-4}$ μ if 1 monolayer assumed to be 1Å.

※※ Private communication; M.H. Francombe.

※※※ See also fig. 2.7.

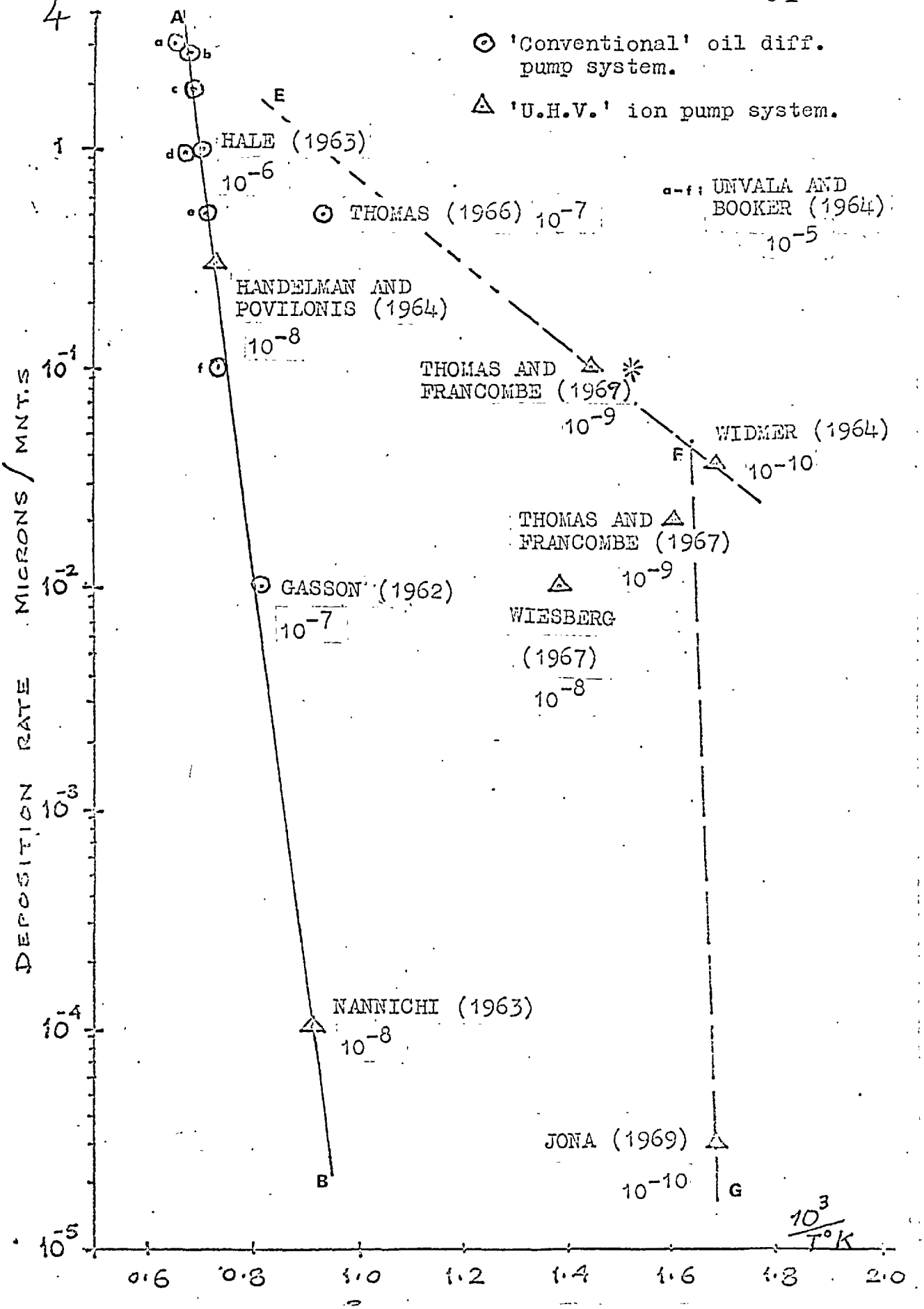


Fig. (2.8)
PLOT OF REPORTED MINIMUM EPITAXIAL TEMPERATURE - RATE DATA TABULATED IN TABLE III. DATA PLOTTED AS LOG RATE VERSUS $\frac{10^3}{T°K}$

* PRIVATE COMMUNICATION M.H. FRANCOMBE

TABLE IV

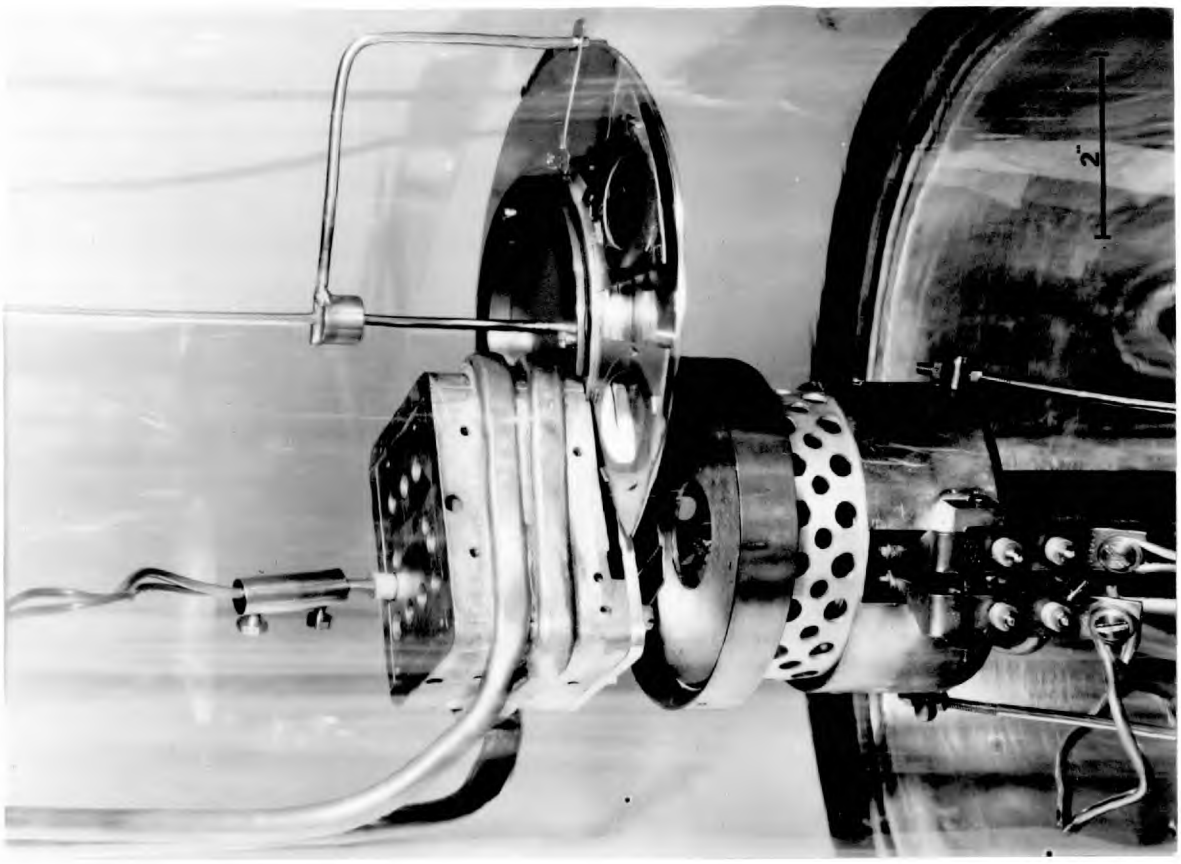
VARIATION OF STACKING FAULT DENSITY WITH DEPOSITION PARAMETERS

Deposition Rate microns $min.^{-1}$	Substrate Temperature Deg. C	Deposition Pressure torr	Fault Density sq. cm.	Reference
0.036	550°	10^{-10}	10^{7}	Widmer (1964)
0.036	800°	10^{-10}	0[*]	Widmer (1964)
0.02	650°	10^{-9}	$\sim 10^{3}$	Thomas and Francombe (1967)
0.02	400°	10^{-9}	$\geq 10^{10}$	Thomas and Francombe (1967)
0.3	1200°	10^{-7}	0[*]	Unvala and Booker (1964)
1.0	1200°	10^{-6}	0[*]	Unvala and Booker (1964)

[*] Nominally zero as given in reference.

From fig. (2.8) it is also seen that with the two exceptions noted above, the results of growth studies in U.H.V. form two straight lines, CD and DE. Since the ordinates for the section CD are almost equal, the slope is not determinable.

This may be interpreted as indicating that there is no strong rate dependence of the epitaxial process over this range of deposition parameters. The portion DE has a slope of 2.08, indicating a process activation energy of 0.41 ev.



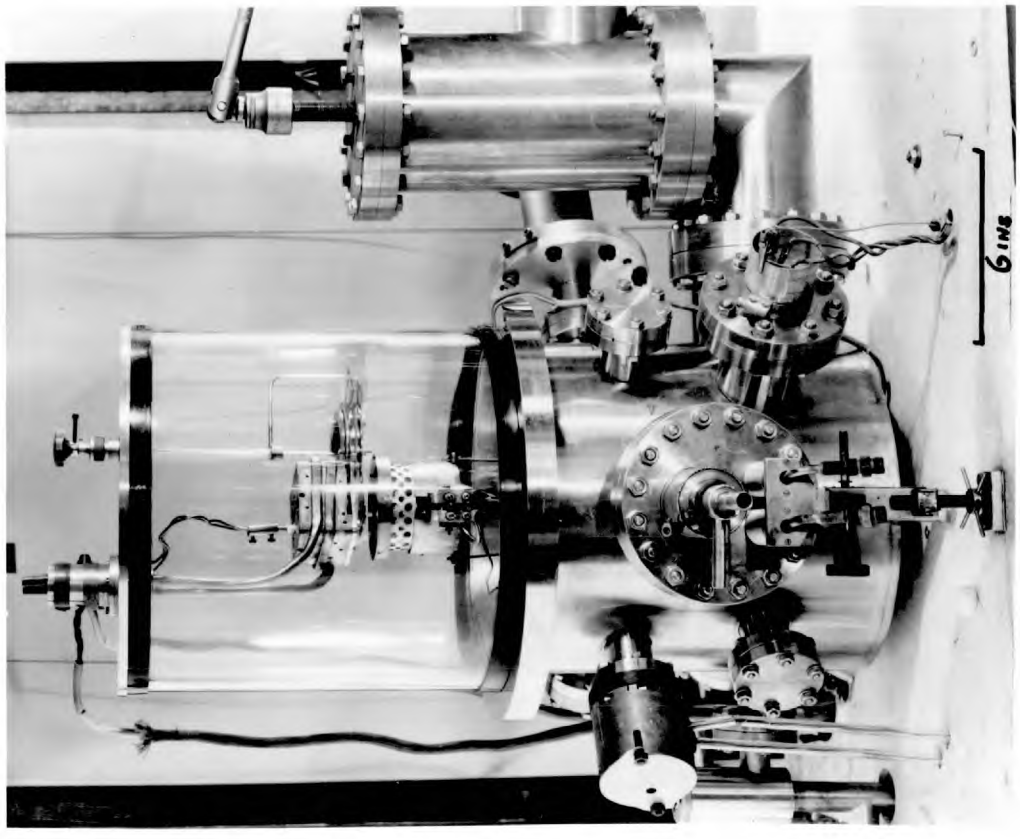


FIG. (3.1) a. THE VACUUM CHAMBER

b. THE SUBSTRATE HEATER AND CARRIER ASSEMBLY

3. Apparatus and Experimental Techniques.

3.(1) General Description of Apparatus

The vacuum chamber consists of a twelve inch diameter stainless steel cylindrical well fitted with ports to accommodate various feed-through assemblies. The vacuum seals on the ports are of the Varian 'conflat' type using annealed copper gaskets.

The system is rough-pumped by sorption pumps using molecular sieve, (10Å pore size) cooled by liquid nitrogen. This method of roughing avoids any possible hydrocarbon contamination such as could come from back-streaming of rotary-pump oil vapour. The main pump is a diode ion-pump rated at 140 litres per second.

The ion pump is connected to the well through a 4" all-metal valve, which allows the ion-pump to be isolated when the system is let up to atmospheric pressure. The pumping speed in the well is considerably reduced by the valve and the associated pipe-work, and is probably of the order of 70 - 80 litres per second. The well is also fitted with a titanium sublimation pump, with a water-cooled collar.

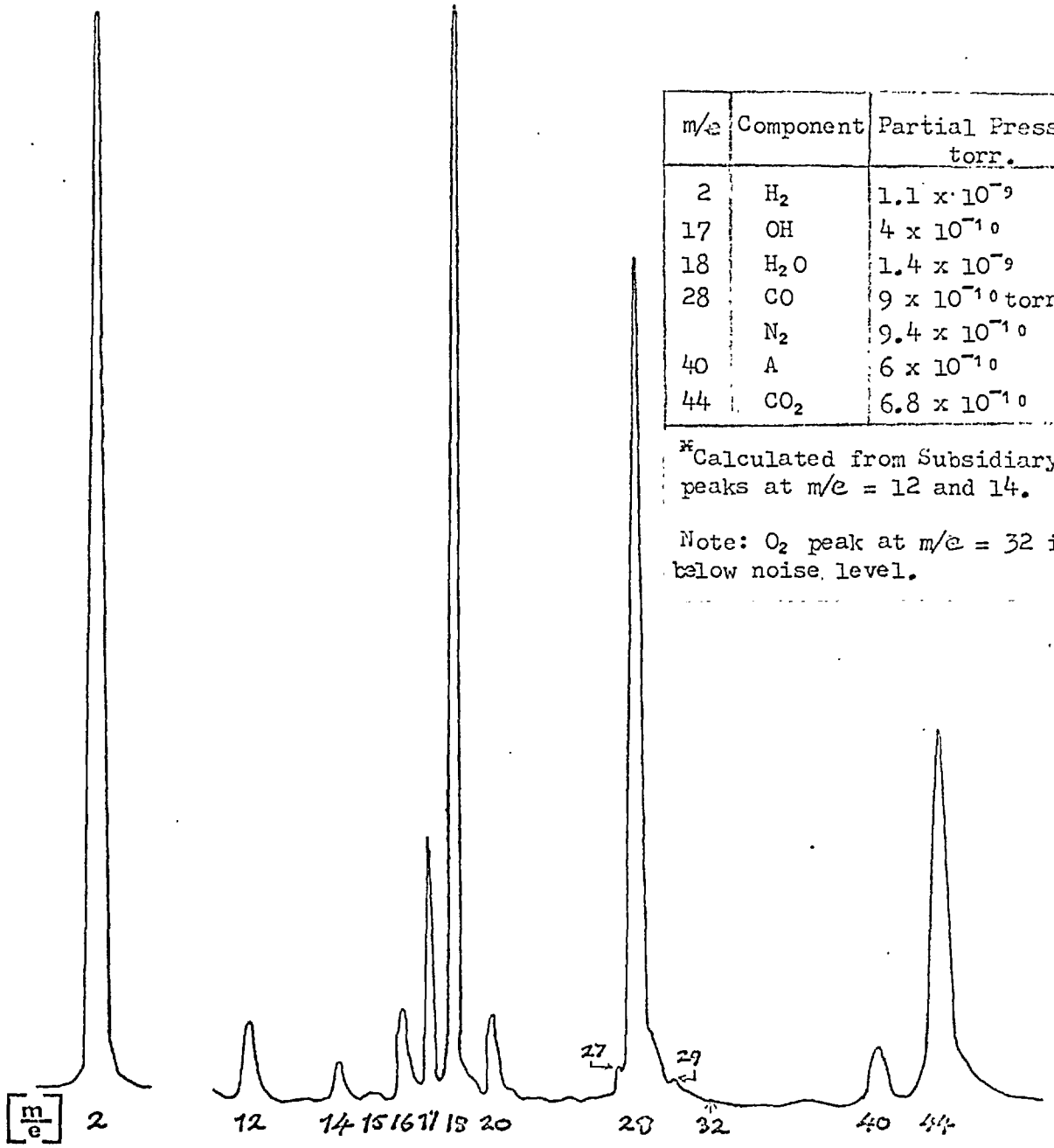
The electron-beam furnace, ion-gauge, and electrical feed-throughs are mounted on the various ports.

The system was also fitted with a mass spectrometer: [an AEI model MS 10]. Initially a twelve inch diameter Pyrex bell jar was used, to enable an external radiation-heater to be used. This was later replaced by a glass cylinder and top-plate assembly. The general arrangement is shown in Fig. (3.1a).

The cylinder, top plate and well are sealed with 'L' shaped Viton 'B' gaskets. The use of Viton gaskets allows easy demounting of the cylinder from the well for substrate loading, but limits the bake-out temperature to 150°C. Bake-out is accomplished by enclosing the well and valve in an oven. The oven temperature is controlled by a thermocouple attached to the top plate. This ensures that the Viton seals are not over-heated.

3.1.(1) Vacuum System Performance

After a 24 hour bake-out at 150°C base pressures of the order of $2 \sim 4.10^{-9}$ torr are obtained. Fig. (3.2) shows a 'typical' mass spectrum trace of the residual gases.



m/e	Component	Partial Pressure torr.
2	H_2	1.1×10^{-9}
17	OH	4×10^{-10}
18	H_2O	1.4×10^{-9}
28	CO	9×10^{-10} torr*
	N_2	9.4×10^{-10} *
40	A	6×10^{-10}
44	CO_2	6.8×10^{-10}

*Calculated from Subsidiary peaks at m/e = 12 and 14.

Note: O_2 peak at m/e = 32 is below noise level.

Fig. (3.2)
MASS SPECTRUM OF THE RESIDUAL GASES AFTER BAKE OUT OF SYSTEM AT 150°C FOR 15 HOURS. PARTIAL PRESSURES OF COMPONENT GASES CALCULATED FROM DATA IN MS10 HANDBOOK.

3.1.(2) Silicon Vapour Source

The electron beam furnace is based on that designed by UNVALA (opus cit). In this furnace a beam of electrons is electrostatically focussed on to a silicon block mounted in a recess, in a water-cooled pedestal.

The effect of heating in this manner is to produce a molten pool contained in the centre of the silicon block. This method of heating, where the material acts as its own crucible, is called auto-crucible or skull melting. Since molton silicon is very reactive, this method of containment has the great advantage of avoiding a crucible, and hence any contamination which could occur from its use. Fig. (3.3a) shows the basic arrangement of the furnace electrode system and the position of the filament which ensures line of sight protection for the source.

The filament used was a 0.02 inch diameter tungsten wire bent to a circle, whose diameter is just equal to that of the rim of electrode E'. This ensures no direct line of sight between the filament and the source, thus preventing contamination, and uneven heating of the sides of the source.

Source Fabrication

Efficient cooling of the silicon source is most important in obtaining a good auto-crucible effect. Thermal contact between the source and base of the recess is poor and so the main heat loss is by conduction through the walls of the recess. For the cooling to be effective, the source must be a very tight fit in the recess, to give good thermal contact over the limited area available. If the source were ground so that it was a tight fit at room temperature, it was found that expansion on heating caused the source to fracture.

By experiment it was found that the optimum 'fit' was that which would just allow smooth rotation of the source in the pedestal recess, when both were at room temperature.

Source Dimensions

The diameter of the source is the same as the o.d. of the pedestal to give the correct electrostatic field shape. The length l, fig. (3.3b), is determined by the maximum power input, the effectiveness of the cooling,

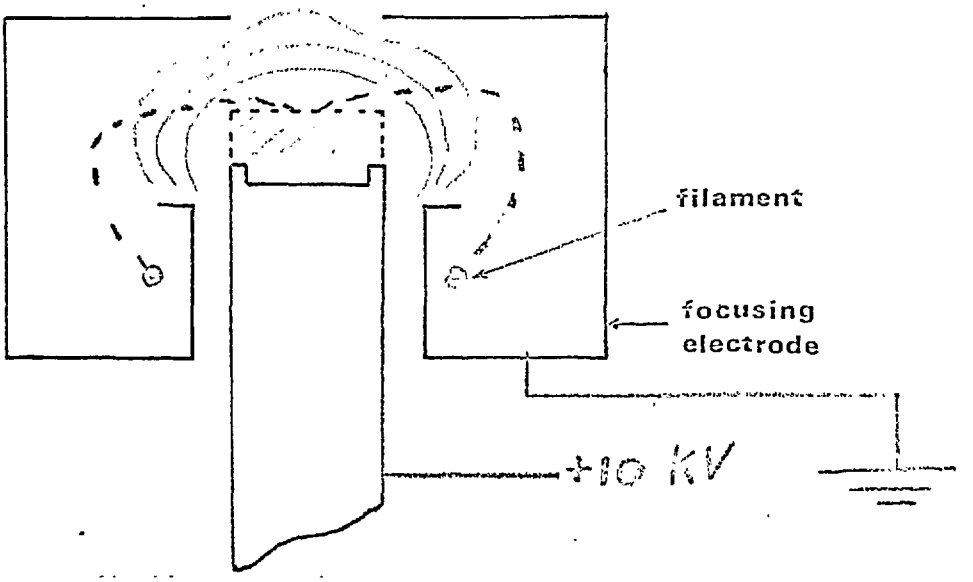


Fig. (3.3a)
ARRANGEMENT OF ELECTRODES IN ELECTRON BEAM FURNACE.

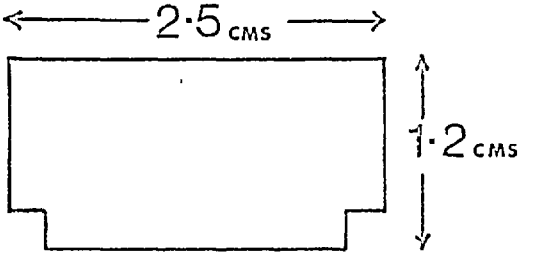


Fig. (3.3b)
DIMENSIONS OF SILICON SOURCE.

and the thermal conductivity of silicon. From experiments it was found that a length ℓ of 1.2 cms. was suitable.

3.1.(4) Furnace Construction for U.H.V. use

For use in U.H.V. the basic furnace design of Unvala (loc cit) was modified to allow water cooling of heated areas to reduce outgassing. Fig. (3.4) shows the arrangement.

The electrode E' was made from a nickel cylinder, and is a tight fit in the hollow annular section S.

This section S is linked to a loop of steel pipe P, which supports the electrode E. This electrode E is made of $\frac{1}{8}$" thick copper sheet, and was tightly clamped to the pipe P, by the clamp C.

The other part of the electrode E consisted of a sheet of copper tightly clamped to the outer side of S. The system of electrodes is supported by the pipes P'P', which are mounted on the focussing assembly F, through the bellows B, to allow motion, as shown in Fig. (3.4). Water is circulated through Pipes P' and S to cool the electrodes.

Electrode E' is closest to the filament and receives most of the radiant heat. It is cooled by conduction into S. The cooling of electrode E is probably marginal, since there is only a very small contact area between it and the pipe P. This arrangement, however, does allow easy removal of this electrode for cleaning and maintenance. It is seen from Fig. (3.4) that the major part of the evaporated silicon condenses on the inside of electrode E. Thus, to prevent contamination caused by flakes of silicon falling into the source, the electrode E was periodically cleaned by abrasion.

In order to use 'tap-water' to cool the focussing electrode system EE', to reduce outgassing, the polarity of the beam furnace is inverted relative to the original system as used by Unvala (..1964). The filament and focussing electrodes are at ground potential, and the source pedestal is held at a high positive potential. Water cooling of the source was achieved by the use of a closed-circuit deionised water circulator.

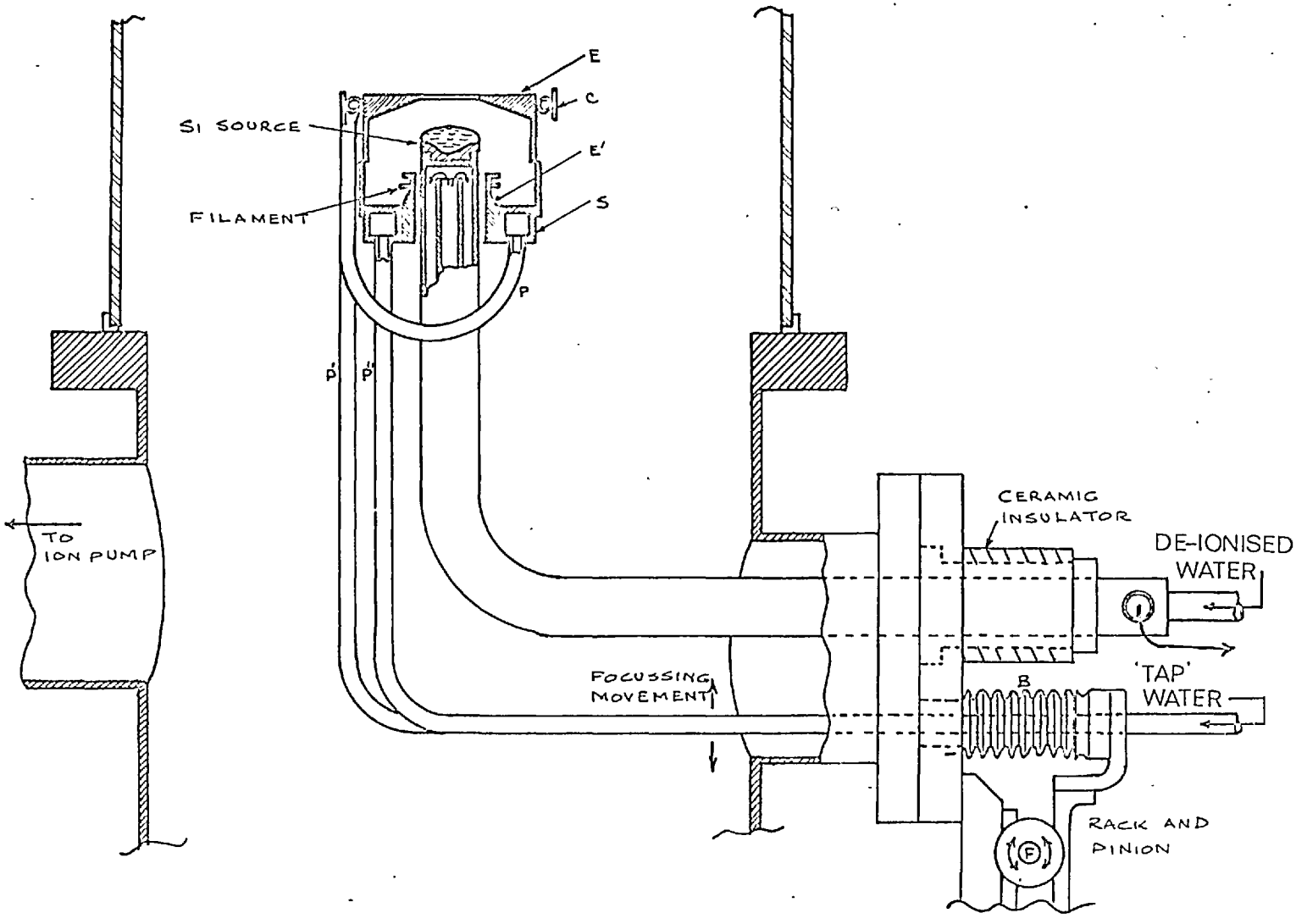


Fig. (3.4)
DIAGRAM OF ELECTRON BEAM FURNACE SHOWING CONSTRUCTION
OF WATER COOLED ELECTRODES EE', FOCUSSING MECHANISM

3.1.(5) Operating Conditions of the Electron Beam Furnace

Because of the large cooling effects of the auto-crucible method, high furnace powers are required to melt and evaporate the silicon. It was observed that a power input of the order of 500 watts was required to just heat the focal point of the source to red-heat (700 - 800°C). A high operating voltage has the advantage of suppressing space-charge repulsion, which tends to defocus the beam at the currents used which were of the order 100 m.A.

For safety reasons, and also for relative ease of insulation, the voltage used was limited to 10 KV. (Any X-rays produced will be absorbed by the walls of the vacuum system.)

The furnace power is controlled by variation of the filament temperature and hence the emitted current, keeping the voltage constant at 10 KV. This control was accomplished by feeding the filament transformer from a 'variac'. This method also has the advantage that the filament is run at the minimum temperature that will give the required beam current. Using this control mode, as opposed to saturated emission mode, the stability of the beam furnace depends largely on the filament current stability and the filament condition. In use, the stability, as judged by variations observed in electron beam current, was found to be very good. Only slight variations of the order of 2 m.A. in a standing value of 60 m.A. were observed. Manual control was therefore considered to be adequate to maintain a constant value of furnace current, and hence evaporation rate. The electron beam is focussed on to the source by moving the electrode system EE' relative to the pedestal by means of the rack and pinion shown in fig. (3.4).

3.(2) Substrate Heating

3.2.(1) Assessment of the Problem and Methods

The main factors influencing the choice of method of substrate heating were as follows:-

(i) The nature and properties of the substrate material.

(ii) Uniformity of heating over the substrate area, and control and stability of temperature.

(iii) The temperature likely to be required.

(iv) The need to prevent stray radiation heating effects in order to maintain as low a working pressure as possible.

. . . Substrate Heating Methods

The methods which are available for use are as follows: Electron bombardment, Joule heating, R.F. Induction heating, Radiation heating.

The substrates used are in the form of circular wafers, $1\frac{1}{4}$" diameter and 8 - 10 thou. thick. Thus the shape and fragility precludes the joule heating method because of the difficulty of attaching conductors.

Electron bombardment and R.F. heating would be cumbersome and also would produce a higher working pressure due to outgassing.

3.2.(2) Radiation Heating

Initial Experiments

The first radiation heater used consisted of an elliptical reflector, at one of whose focii was mounted a 1 KW projector lamp (AEI A1/59). The reflector was mounted over the bell-jar so that the substrate was at the other focus.

This method had the advantage that the radiation source was completely outside the vacuum system. Thus no contamination would be caused. It was found, however, that for substrate diameters $> \frac{1}{2}$" the heating was non-uniform. This was due to the construction of the lamp filament assembly and its position relative to the focus of the reflector.

3.2.(3) Substrate heater

The basis of the design consists of a plane radiator separated by a short distance from the substrate.

The detailed calculations of the radiation exchange between the radiator and the substrate are given in the appendix.

Construction of the Substrate Heater

The heater consists of six tungsten strips, each $2\frac{1}{4}$" long, 0.2" wide and 0.005" thick. The strips are bent into the shape shown in

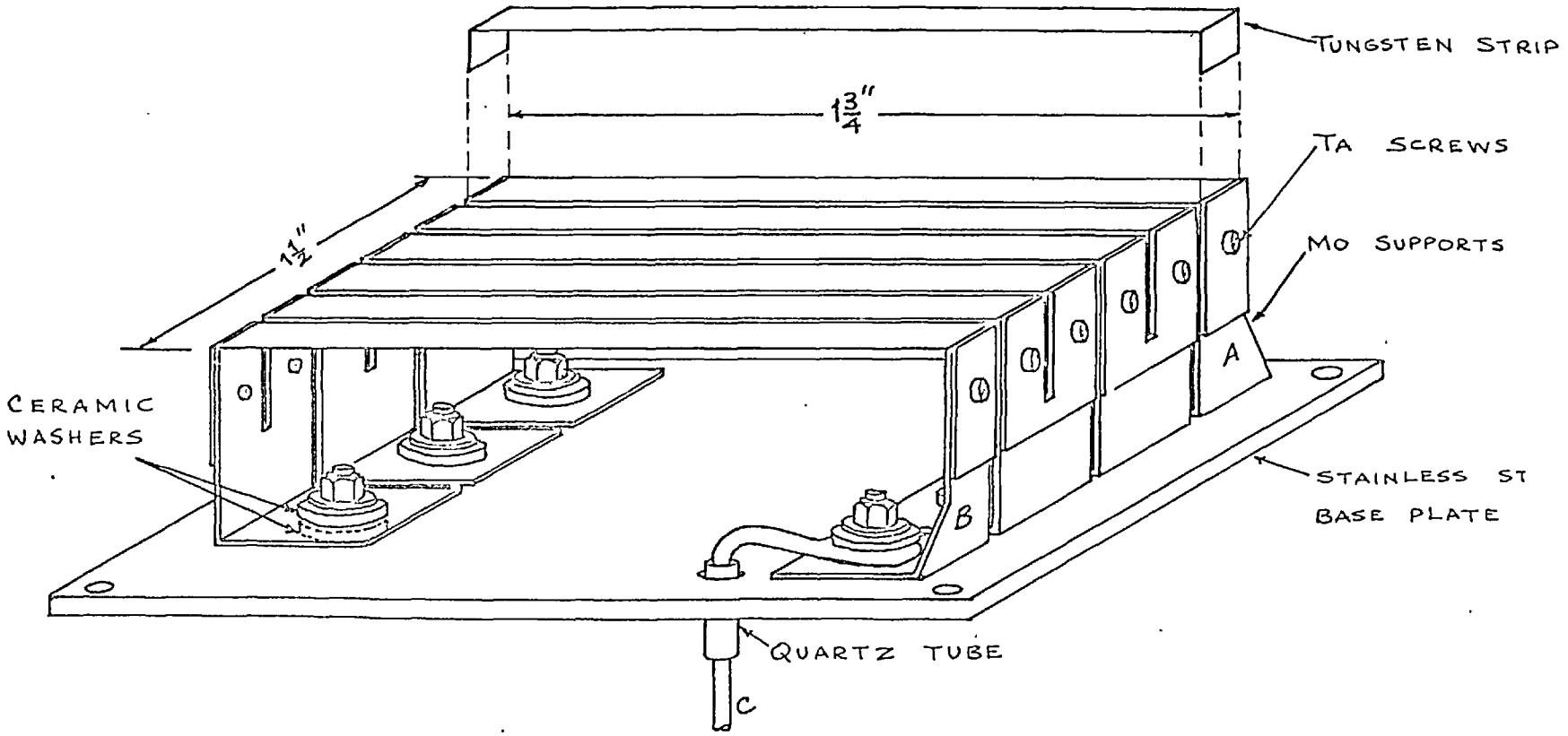


Fig. (3.5)
DIAGRAM SHOWING THE ARRANGEMENT OF TUNGSTEN STRIPS IN THE SUBSTRATE HEATER.

Fig. (3.5). (Tungsten can be easily bent without cracking if heated above 300°C.)

The heater strips are mounted between support strips, as shown in Fig. (3.5), and clamped to them by small molybdenum plates secured by 8BA screws.

The support strips are made of molybdenum, 0.04" thick, tapped to receive the clamping screws.

These support strips are mounted on a small steel base-plate, using small ceramic washers as shown in Fig. (3.5). These washers insulate the strips from the base plate; thus the tungsten strips are electrically connected in series, via the support strips. This arrangement requires a much lower current than would a single strip of tungsten of the same area. The strips A and B shown in Fig. (3.6) act as current leads. A is connected to the base plate, B is connected to an insulated copper rod C.

Experiments with this heater array showed that the radiation caused a large amount of outgassing.

Since for a heat shield of emissivity 1, the 'temperature drop' is only $\sim 300^{\circ}C$, radiation screening by heat shields alone would be difficult, requiring 3 - 4 heat shields, with the attendant difficulties of outgassing and the long times taken to reach equilibrium.

This problem was solved by use of a water-cooled radiation screen. Details of the construction of this are given in the appendix.

The small steel base-plate carrying the heater strips was bolted into the box. Holes were drilled in the top to give clearance for the bolts holding the support strips, and to allow the electrical connection C through the box wall. Some small holes were drilled in random places through the walls of the box to allow the enclosed volume to outgass. Fig. (3.1b) shows the general arrangement of the substrate heater, and its position over the electron beam furnace.

3.2(4). The Mounting of the Substrate Heater

The 3" copper rod was taken through a hole in the top plate and sealed by compressing a Viton 'O' ring as shown in Fig. (3.6a). The tubular extension and jubilee clip prevent any lateral motion which

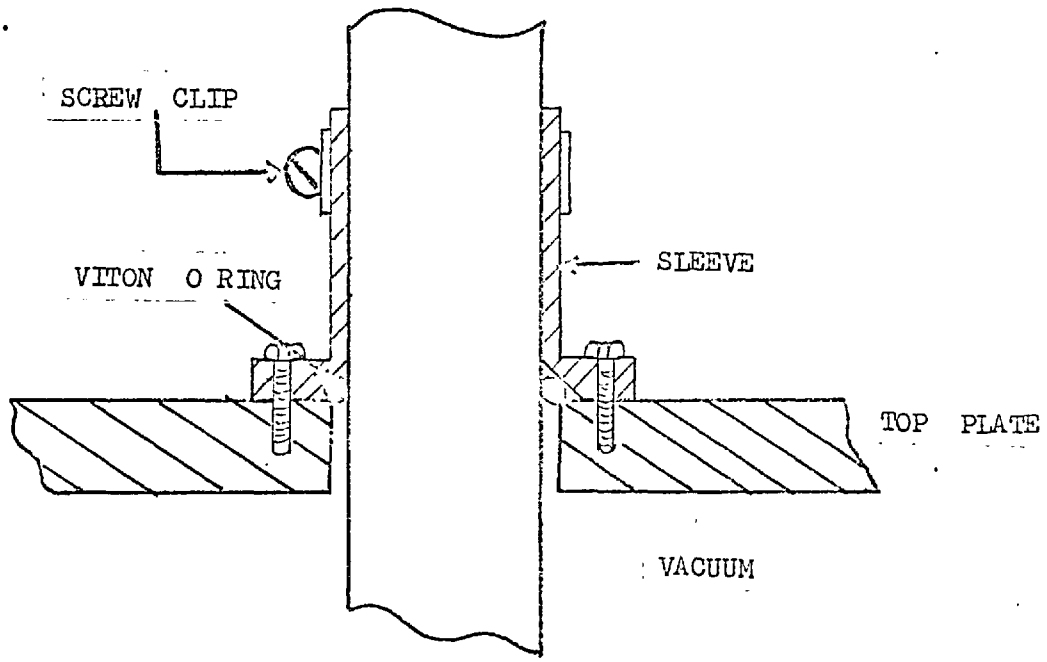


Fig. (3.6) a:
SUBSTRATE HEATER MOUNTING WHICH ENABLES VARIATION OF SOURCE TO SUBSTRATE DISTANCE.

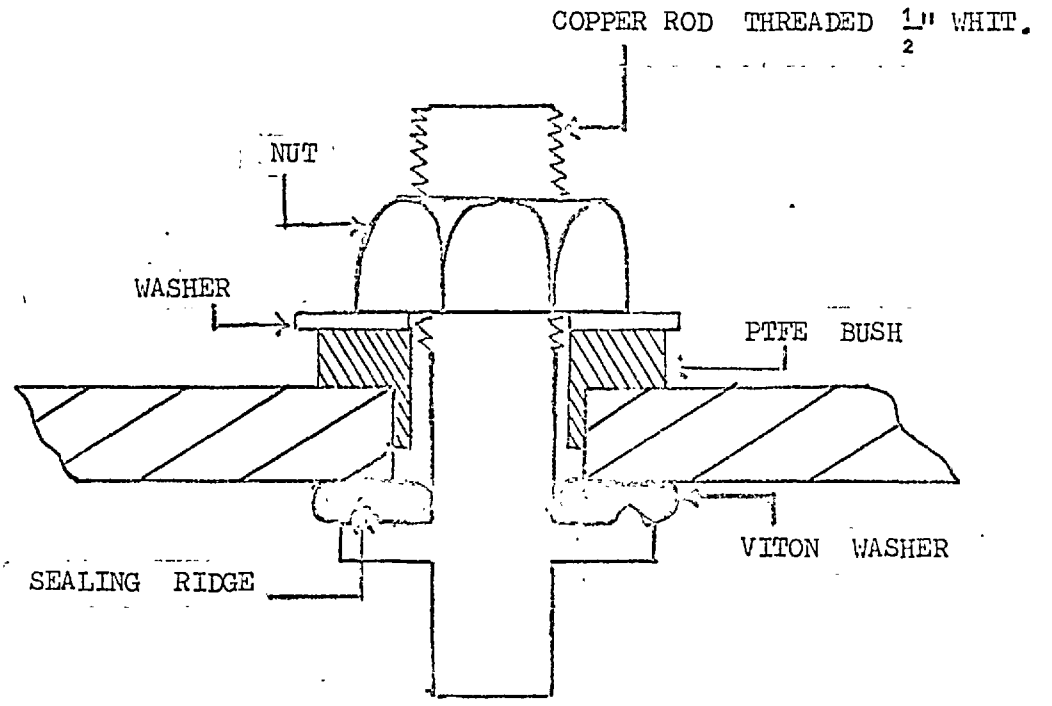


Fig. (3.6) b:
DIAGRAM SHOWING CONSTRUCTION OF A SIMPLE U.H.V. HIGH CURRENT LOW VOLTAGE FEED-THROUGH.

would cause leaks. By loosening the clip, sliding the rod up or down and re-sealing, the distance between source and substrate can be varied very easily. From Fig. (3.6) it is seen that the top plate is in electrical connection with the heater array via the copper box, and so can be used as one of the electrical connections. This requires the other connection to be insulated from the top plate on which it was mounted. Since the maximum operating voltage of the heater is of the order of 20 volts, electrical insulation and vacuum sealing are obtained by using a Viton washer in the arrangement shown in Fig. (3.6b). The P.T.F.E. bush prevents the shank touching the inside of the hole in the top plate, and insulates the nut from the top-face of the plate.

The tungsten heater strips are heated by passing alternating current through them using a high current transformer. The heater temperature is controlled by varying the voltage applied to the primary of the transformer by means of a variac. The primary voltage is measured by means of a 1 m.A. f.s.d. meter in a bridge circuit across the primary.

The details of the calibration of the heater and substrate temperatures against the meter scale are given in the experimental methods, section (3.2.6.)

3.2.(5) Substrate Carrier Assembly

In view of the long cycle-time, the ability to deposit more than one layer per pump-down is a great advantage.

The substrate carrier consists of five trays mounted on a stainless steel ring R. The trays are of molybdenum, 20 thou. thick with a central hole $\frac{7}{8}$" in diameter. The substrates are located over the holes by three small pieces of tungsten wire spot welded to the tray. Fig. (3.7) shows the arrangement of the tray and substrate. Each tray is secured to R by a 10 BA counter-sunk screw. The matching of the curvature of the edge of the tray to R ensures that each tray is accurately located, yet has enough lateral play to allow for thermal expansion. The use of the single screw fixing also avoids any expansion stress which would be caused by the use of two screws or the spot-welding of the tray to the ring. This method also allows interchange of trays to permit the use of various sized substrates.

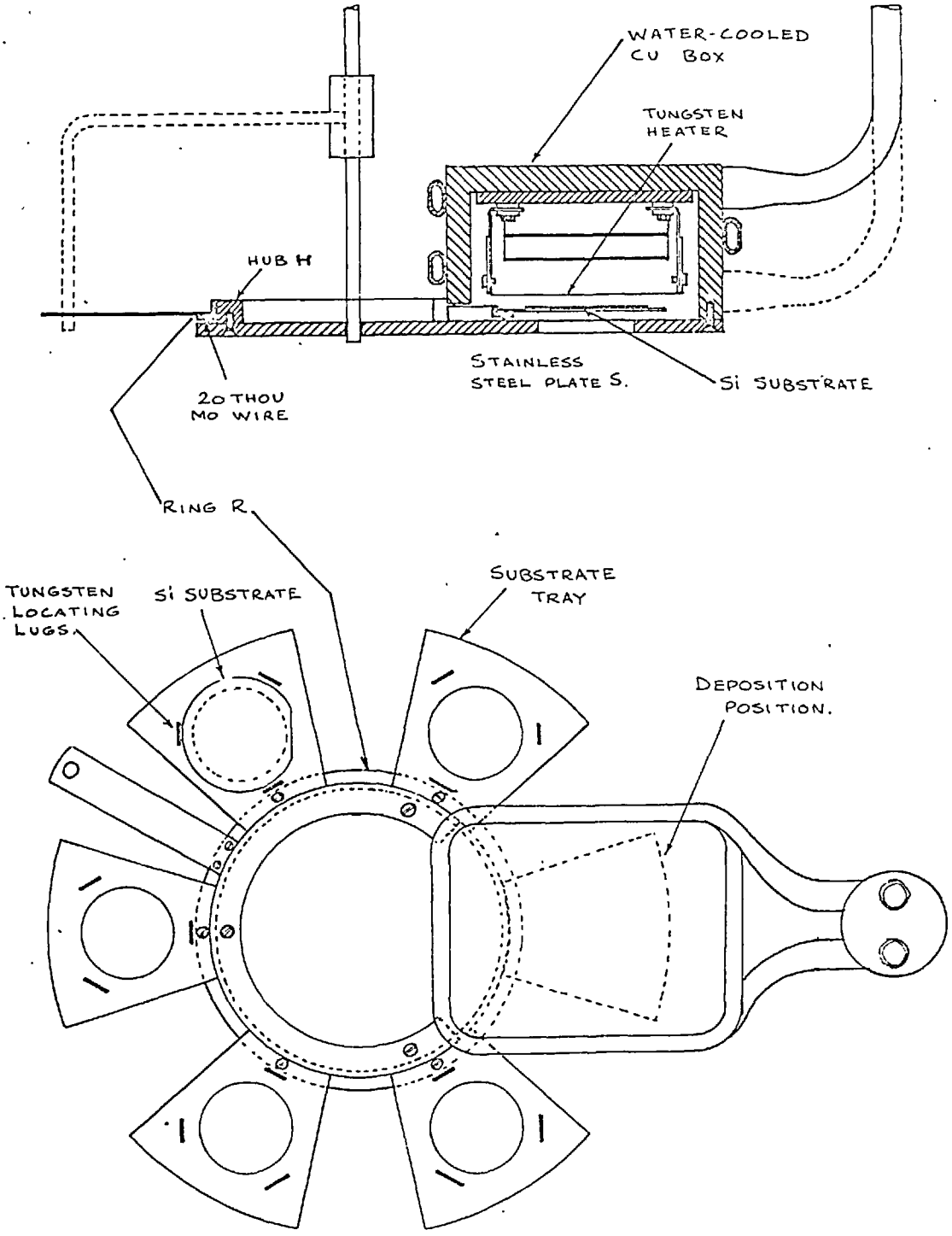


Fig. (3.7)
DIAGRAM SHOWING THE ARRANGEMENT OF SUBSTRATE HEATER, WATER COOLED SHIELD AND MULTIPLE SUBSTRATE CARRIER ASSEMBLY.

The ring R is carried on a steel plate S, and is located by the sector H, which acts as a bearing as shown in Fig. (3.7).

To avoid cold-welding which can occur between like moving metals in contact in U.H.V., a 0.02" diameter molybdenum wire was spot-welded around the edge of S, to act as a bearing surface. Also the locating hub H was made from a high carbon steel, and made 0.01" smaller than the internal diameter of R, to prevent binding.

The plate S is bolted to the open side of the copper 'box' and has a $1\frac{1}{4}$" diameter hole to allow the evaporating silicon through.

The shutter used to control the evaporation is mounted below 'S' using one of the bolts securing 'H' as a spindle. A soft iron 'bob' allows a magnet to be used to control the shutter from outside the vacuum system. Because it is indirectly operated, stops are fitted to restrict the shutter travel.

When a loaded tray is in position in the heater, the tungsten heater strips are completely shielded from the evaporating silicon, thus preventing any attack (through the formation of a silicide). A circular plate was bolted below S, to shield the other substrates from evaporating silicon, during deposition.

The substrate carrier ring R is rotated by means of a crank-arm mounted on the shaft of a rotary feed-through fitted to the top-plate. The lower end of the shaft is housed in a hole in the plate S. The arrangement of the crank-arm and carrier ring R, can be seen in Fig. (3.1b).

The rotary feed-through used was an 'Edwards' ordinary high vacuum type. It was modified for U.H.V. use by removing the vacuum-side needle bearing and replacing the 2 neoprene 'O' rings normally fitted, by 3 viton 'O' rings.

With these modifications, it was possible to maintain vacua of the order 10^{-9} torr whilst rotating the carrier. Because they are used unlubricated and are frequently baked to the maximum permissible temperature, the 'O' rings in the rotary feed-through degenerate with use. To maintain optimum performance, they were periodically replaced.

3.2.(6) Substrate Heater Calibration

A series of experiments was carried out to measure the substrate temperature as a function of the heater temperature, and to calibrate these temperatures against the reading of the meter in the heater transformer primary.

For temperatures in the range 750°C to 1700°C for the heater and 750°C to 1200°C for the substrate, a Leeds and Northrup optical pyrometer was used. This was a disappearing filament-type (model No. 8622 C) fitted with a 0.65μ filter.

In use, an accuracy of $\sim \pm 5$°C could be obtained.

Corrections to Pyrometer Readings

The corrections made to the pyrometer readings were as follows:

The emissivities of the heater strips and the silicon substrates vary both with temperature and surface finish.

The value of 0.6 [Allen (1957)] was used for silicon and 0.45 was used for tungsten [Blau and Fisher (1962)].

A correction was also applied for radiation absorption by the bell-jar wall. This was estimated by sighting on the liquid-solid boundary of the molten source, and assuming this to be at 1420°C (m.p. of Si). The difference was then assumed to be due to absorption. (This absorption effect was assumed to be linear with temperature, since no data was available.)

For the temperature range $\sim$ 200°C to $\sim$ 850°C, a thermocouple junction was used. Thus in the range 750° to 850° the pyrometer and thermocouple measurements could be compared for consistency.

For effective use, the thermocouple junction must be in intimate contact with the silicon substrate. Two methods were used to achieve the thermal contact required.

(i) A thermocouple junction was 'brazed' to a silicon substrate.

(ii) A silicon slab was ground to the shape shown in Fig. (3.8b) and a thermocouple junction inserted in the cavity, which acts as a 'black-body' enclosure.

The thermocouple voltages were measured with a Cropico (Model 6C) potentiometer. This has a direct-reading scale for the thermocouple used:- Chromel; Alumel.

A cold-junction correction is provided by a scale displacement which is pre-set to room temperature.

Thermocouple Junction Fabrication

The junctions used were made in the following way: the thermocouple wires (7 thou. diameter) were fused together in a flame to give a small bead about 1 mm. diameter.

The junctions made this way were tested by plotting cooling curves for molten aluminium. These measurements showed that the junctions so made, were reproducible and accurate to within the limit of the Cropico potentiometer, which is ± 2°C.

Method of Attachment of the thermocouple junction to the silicon wafer.

A flat was ground on the thermocouple junction bead to give a clean metal surface and large contact area.

The thermocouple and silicon wafer were mounted in a jig with the 'bead' lightly sprung against the wafer. Between the wafer and the bead was placed a piece of aluminium foil about 0.1" square and 0.002" thick. The jigged assembly was mounted in a vacuum system and, the wafer was radiation heated until the aluminium foil was seen to melt and wet the silicon and the bead. The temperature was then reduced over a period of 3 minutes to avoid any stress.

The jigged assembly was then mounted under the substrate heater and the calibration carried out. With this arrangement, the substrate temperature as a function of heater temperature was measured for different distances from heater to substrate.

The measurements made with the 'brazed' thermocouple were repeated with the slab shown in fig. (3.8) to check if the junction had been affected by the brazing process. The results of these experiments are summarised in figs. (3.8a) and (3.8b).

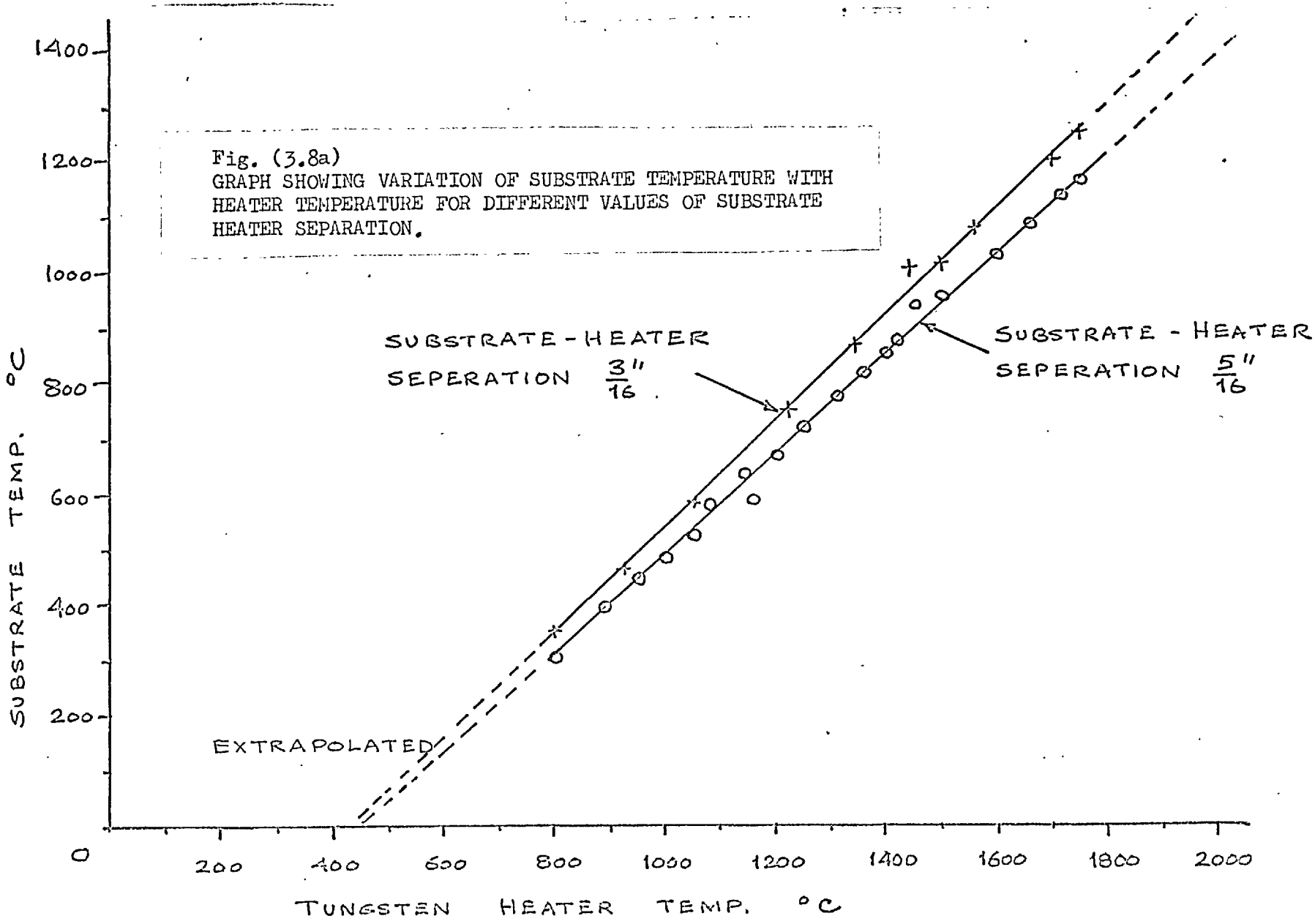


Fig. (3.8a)
GRAPH SHOWING VARIATION OF SUBSTRATE TEMPERATURE WITH HEATER TEMPERATURE FOR DIFFERENT VALUES OF SUBSTRATE HEATER SEPARATION.

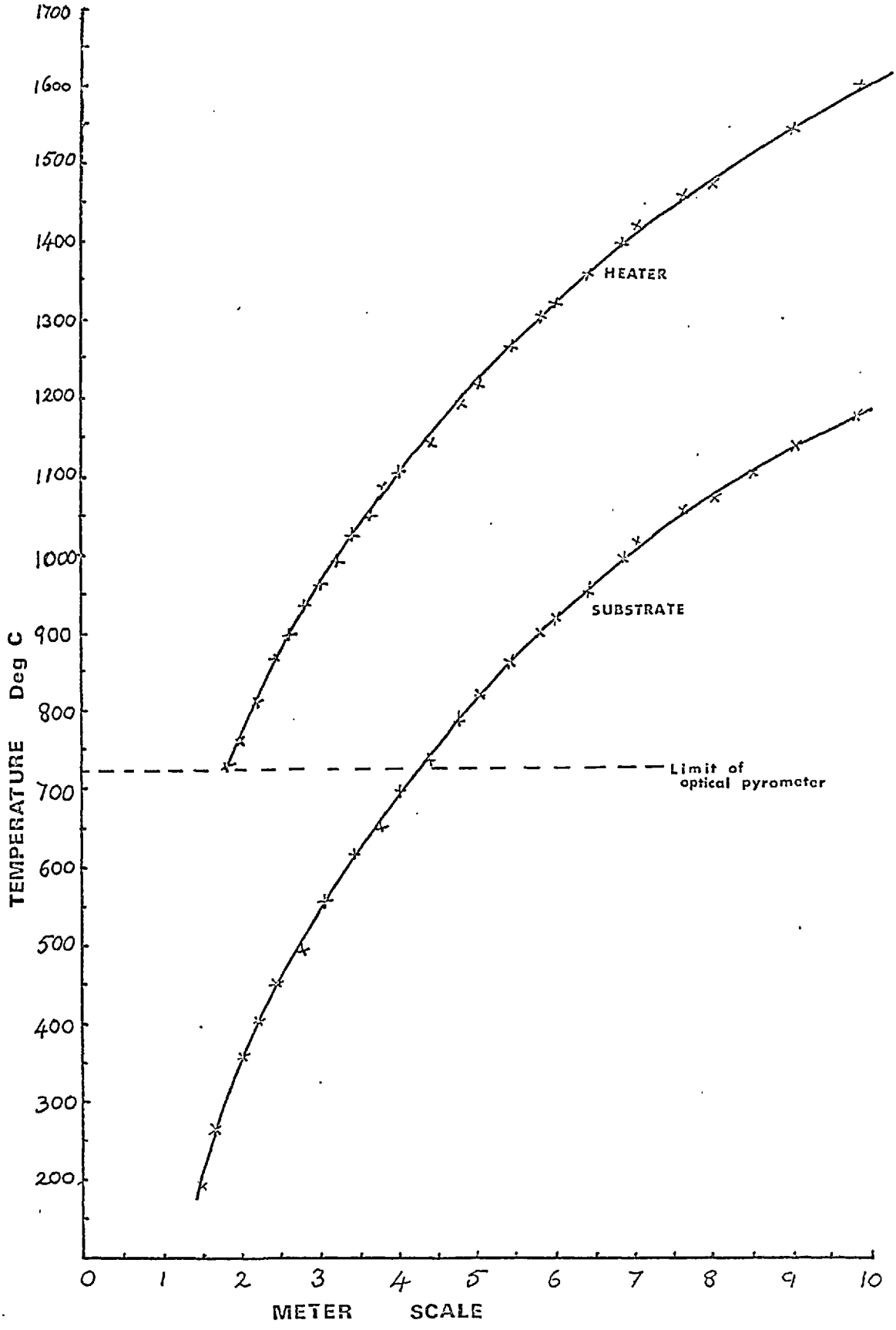
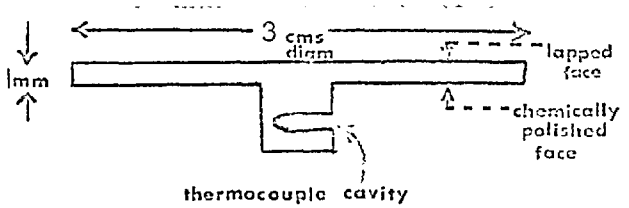


Fig. (3.8b)
GRAPH OF SUBSTRATE AND HEATER TEMPERATURES VERSUS METER SCALE READING.



SILICON SLAB USED FOR THERMOCOUPLE MEASUREMENTS.

The graph of substrate temperature versus heater temperature is linear as predicted by equations derived in the appendix. It is seen from fig. (3.8b) that departures from proportionality occur at high temperatures. This is probably due to the shift of the colour temperature of the heater towards the 'yellow' region: hence the approximations used in the appendix do not apply.

Uniformity of Substrate Temperature

The temperature distribution across the substrate was investigated using the pyrometer. A small decrease in temperature - $\sim 5^{\circ}C$ - was seen near the edge of the aperture in the carrier tray.

Temperature Variations during Deposition

During the deposition the substrate temperature could vary. These variations could be caused by:-

(i) Variation of heater current.

(ii) Change of emissivity of surface due to deposition.

(iii) Effect of radiation from the furnace.

(iv) Contribution of the latent heat of condensation of silicon.

Of these, (iii) and (iv) were estimated and found to be small: $\leq 5^{\circ}C$. The main effect would be due to fluctuations in heater current.

In an experiment, during which a deposition was carried out, the substrate and heater temperatures were measured over a period of 30 minutes, and no large variations were detected, using an optical pyrometer. Thus any fluctuations of temperature would be of the order $5^{\circ}C$ - the limit of pyrometer accuracy - and can be ignored.

3.3. Substrate Preparation

The substrates used were standard epitaxy substrates, purchased from various manufacturers from their standard ranges. The substrates are in the form of circular wafers of silicon 1" to $1\frac{1}{4}$" diameter, 8 - 10 thou. thick, depending on type and supplier . In the 'as-received' state one face is polished to an optical flat finish, the other is finely lapped or etched.

The orientation of the faces is 1 - 2 degrees off an exact [111] direction: (the reasons for misorientation were discussed in the review).

Both N type and P type substrates were used, the N type being antimony-doped of resistivity 0.005Ω cm. and the P type boron-doped, resistivity 30 - 35Ω cms. The economics of purchasing did not allow investigation of a complete range of dopings and resistivities.

The use of commercial substrates had several advantages: it avoided the need for slicing and polishing operations; which, without the use of special machinery would have resulted in high wastage; the quality and uniformity of the surface finish were better; and because the substrates would be those used for commercial layers and devices, a comparison could be made between the layers grown in this investigation and those produced commercially.

3.3.(1) Cleaning Procedures

The aim of all cleaning procedures used is to produce a surface free from foreign materials.

As discussed in the review, the most serious contaminants have been found to be:

(a) Hydrocarbons, present as either an absorbed surface layer or in the ambient gases.

(b) Oxide on the substrate surface, or traces of oxygen or water vapour in the ambient gases.

(c) Mechanical damage such as surface scratches, or particles of dust on the surface.

The cleaning procedures adopted were divided into two parts.

(i) The pre-loading cleaning.

(ii) Treatment in vacuo.

(i) Pre-loading Cleaning Procedure

The substrates were ultra-sonically cleaned in two changes of trichlorethylene for 5 minutes to remove any traces of grease. The trichlorethylene was then flushed away with ethyl alcohol, with which it is miscible.

The wafer was removed from the alcohol, and whilst still covered with a film of alcohol, placed in a beaker of hot concentrated nitric acid.

A vigorous effervescence occurs, which aids the removal of any traces of organic materials. The wafer is heated for twenty minutes in the acid, then removed and washed free of any traces of acid with deionised water.

The substrate is then chemically polished using a non-preferential etch of concentrated nitric acid, acetic acid and hydrofluric acid in the proportions by volume, 15:5:3.

Polishing Procedure

The substrate was placed in a plastic beaker, polished face uppermost and covered to a depth of $\frac{1}{2}$" with the polishing solution. The beaker was gently agitated for about 1 minute, care being taken not to expose the silicon surface to the air. The etch was quenched by adding excess acetic acid until the reaction ceases; then the etch was displaced with deionised water.

The polishing time was limited to 1 minute, to prevent degradation of the surface. (Polishing for longer than 1 minute gives an 'orange peel' surface.)

After polishing, the wafer was soaked in hydrofluric acid for 5 minutes to remove any oxide, then washed free of acid in deionised water. The wafer was then washed in a recirculating bath of deionised water fitted to allow the conductivities of in-flow and out-flow to be measured. These readings were taken as a measure of the cleanliness of the substrate. When the 'out-flow' conductivity was equal to that of the 'in-flow', the wafer was then assumed to be free of any contaminant.

The wafer was withdrawn from the deionised water, edgeways, so that any droplets adhering, are at the edge, where deposition does not occur; blown dry in a current of hot air, then loaded immediately into the vacuum system.

(ii) Heat Treatment in Vacuum

The substrates were cleaned in vacuum by heating to 1200°C for 20 seconds immediately before deposition. This treatment had been shown by various workers to produce clean silicon surfaces. This has been discussed in the review.

During this thermal cleaning process, variations in the partial pressures of the ambient gases were observed. These observations will be discussed at a later place.

3.4. Method of Deposition of Layers

After the bake-out and outgassing procedures described, the vacuum is of the order of $2 - 4 \times 10^{-9}$ torr.

The water cooling pipes are connected to all the units and the furnace is run at 500 watts to outgas the source. This causes the pressure to rise to $10^{-8} \sim 10^{-7}$ torr.

This outgassing is continued for $30 \sim 40$ minutes during which time the pressure returns to the $10^{-9} \sim 10^{-8}$ torr range.

Increasing furnace power to 900 - 1000 watts causes a brief gas surge, the pressure then falling to a low 10^{-8} torr reading, which remains steady.

The substrate heater is then outgassed by heating to approximately 1500°C for 3 minutes; this causes the pressure to rise to 10^{-7} torr range briefly, then falling to a value close to the previous steady reading.

The furnace is then set to the power required for the rate of deposition desired. A substrate is rotated into the heater and centred over the aperture. The substrate is heated for 20 seconds at 1200°C, then the temperature reduced to that of deposition.

The substrate is held at the deposition temperature for 4 seconds to stabilise the temperature and then the shutter is opened.

Deposition is terminated by closing the shutter. The substrate is held at the deposition temperature for a further 3 minutes, then the heater current is reduced to zero over a 3 minute interval.

The substrate is allowed to cool for a further 15 minutes. This procedure was used for all the depositions to standardise the growth procedure.

3.4.(1) Measurement of Deposition Rate

There are two basic requirements:

(i) The determination of the rate of deposition.

(ii) The indication of any variation of the rate during the deposition time, which could be up to 30 minutes.

Initial experiments had shown that the furnace electron beam current was stable over long periods, and it was therefore assumed that the deposition rate would be as stable.

The deposition rate was found from the measurement of the thickness of the deposit and the duration of the evaporation. The rate is then $R = \frac{\text{thickness}}{\text{time}}$. Since the vapour pressure of silicon at temperatures of 1100 to 1200°C is given by Honig (1954) as 10^{-7} torr, re-evaporation is negligible at the substrate temperatures used, $\sim \leq 1000^{\circ}C$ compared with the deposition rate.

3.4.(2) Measurement of Layer Thickness

The thickness of the deposited silicon layer was measured by a mechanical profiling technique using a 'Talysurf' to track across the step produced by the edge of the hole in the tray. This method of measurement had the advantages of requiring no sample preparation, of having good accuracy over a large range of thicknesses, and of only needing part of the sample, providing that it included a portion of the undeposited substrate. The accuracy is of the order of $\leq 2\%$. The use of the 'Talysurf' also enables measurements to be made easily on the 'orange peel' surfaces, where confusion would arise with the use of an interferometric method.

3.4.(3) Uniformity of the Thickness

Holland (1956) has reviewed the theoretical distributions of vapours for various source geometries. For the small area emitter, as is the case here, the evaporation rate $R \propto \frac{\cos^2\theta}{r^2}$ where r is the

radius vector and θ the angle between the normal to a plane receiver and r. If t_o is the thickness for normal incidence then the thickness t_x at a point dist x from the axis

$$\frac{t_x}{t_o} \approx \frac{1}{[1 + (\frac{x}{h})^2]^2}$$ where x is the radial distance in the receiving plane, and h is the distance of the source. For substrate-source separations of the order of 6 cm. and substrate diameters of 2 cms.

$$\frac{t_e}{t_o} \simeq \frac{1}{[1 + (\frac{1}{6})^2]^2} \approx 0.94$$ where t_e is the thickness at edge of the layer.

Therefore the errors produced in measuring the thickness at the edge of the layer are negligible compared with the overall experimental errors.

3.5. ; Methods of Examination of the Structure of the Layers

The main method used was transmission electron microscopy, together with transmission electron diffraction.

In order to study the structure of a material by transmission electron microscopy, it must be thin enough to allow transmission of the electron beam. The transmission thickness limit varies for different materials, being inversely proportional to the atomic weight. For silicon; Atomic wt. 28 the transparency thickness limit is approximately 6000Å (for electrons of 100 KV energy). At this thickness the silicon is transparent to visible light and this effect is used to control the thickness. The electron microscope used was an AEI E.M.6.B whose specimen holders are designed for 3 mm. diameter specimens.

The 3 mm. discs were cut from the layer using an ultrasonic trepanning technique. The cutting tool consists of a short length $\sim \frac{1}{2}$", of $\frac{1}{8}$" nominal bore, thin-wall steel tube, brazed, together with a nut to the end of a 4 B.A. bolt.

The tube used was 'cryogenic' tubing supplied as a sample by Oxford Cryogenics Ltd.

3.5.(1) Method of cutting the 3 mm. Discs

A glass slide was heated sufficiently just to melt some black wax, which was spread out to give a thin layer on the slide. The silicon specimen was pressed into the 'just molten' wax with the deposited surface uppermost. (Pressing the slice into the wax ensures that there will be no unsupported areas, which would crack during the cutting; also the cut discs do not come loose and break up.) The glass slide was allowed to cool. A thin layer of 'acetone collodion' was then painted over the silicon surface. This protects the deposited layer surface from abrasion, and being transparent allows the selection of a particular specimen area. The discs are cut using a slurry of 3F grade carborundum in water to which a little detergent has been added. The addition of the detergent helps the slurry to flow into the cut. After the discs have been cut, the silicon carbide particles are washed off the slide, and the collodion layer is stripped off.

The discs are taken from the slide by heating it very gently to just remelt the wax, and removing the discs with tweezers.

The discs are cleaned by boiling in two changes of trichloroethylene which dissolves any of the wax adhering to the discs.

For studies where knowledge of the relative position of the discs in the substrate was needed; after heating the slide, each disc was removed and cleaned individually. The cleaned discs were stored in labelled containers.

3.5.(2) Method of producing thin regions for Transmission Microscopy.

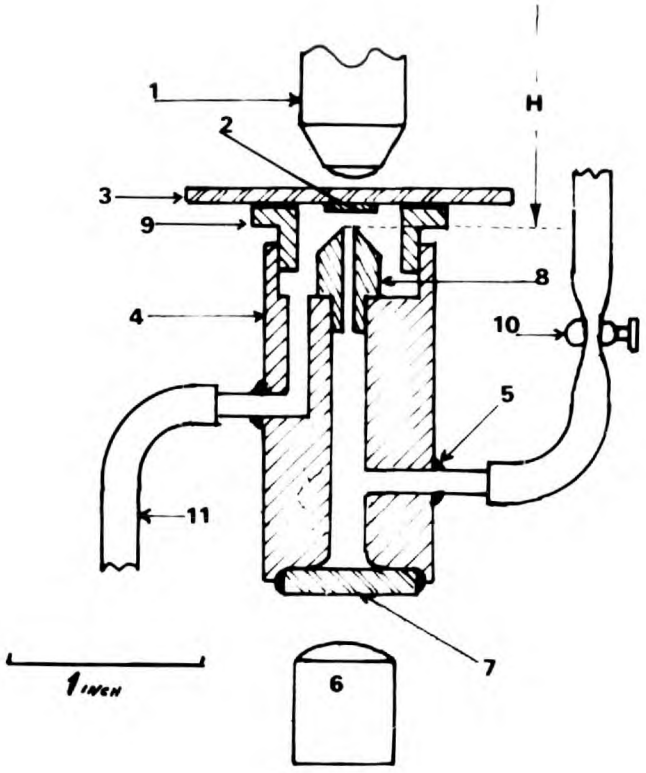
The method of thinning is based on that of Booker and Stickler (1962). The 'jet thinner' used is shown in fig. (3.10). It is constructed from P.V.C., this being resistant to the etch used. The etch is a mixture of 10 parts to 1 part by volume of concentrated nitric and hydrofluric acids.

The criteria for good thinning are:

(i) Formation of a large thin area;

(ii) The production of a 'dimple' with a smooth polished surface.

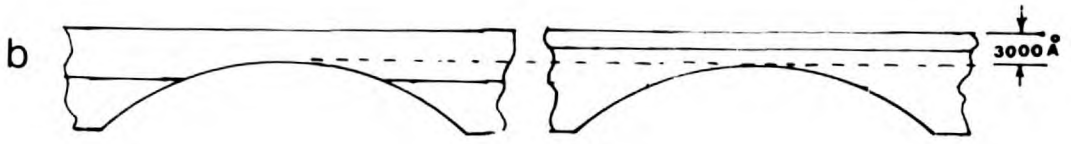
The smoothness of the dimple surface can be seen in Fig. (3.10b).



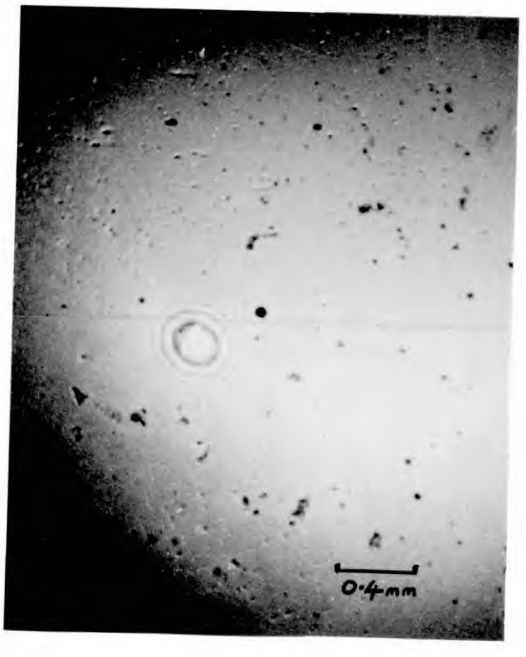
a

1. MICROSCOPE
2. 3mm. DIAM. SILICON DISC
3. GLASS SLIDE
4. P.V.C. BODY
5. JOINTS CEMENTED WITH BLACK WAX
6. LAMP
7. P.V.C. WINDOW
8. DEMOUNTABLE P.T.F.E. JET, 1mm. BORE
9. ADJUSTABLE COLLAR
10. FLOW RATE CONTROL
11. P.V.C. TUBE

H RESERVOIR HEAD



b



c

FIG. (3.9)

a. JET THINNING APPARATUS

b. GEOMETRY OF THE THINNED AREA

c. INTERFEROGRAPH OF THE THIN AREA USING SODIUM LIGHT

From experiments it was found that the thinning process depended critically on the flow rate, jet diameter and jet to sample distance. The jet thinner was designed so that these parameters could be varied and optimised. For the 1 mm. jet bore used the following settings gave reproducible, good results:

Head ~ 20 cms.

Flow rate ~ 3 - 5 'drops per sec' (2 ccs/min)

Jet-sample separation ~ 1 mm.

The 3 mm. discs were cleaned by immersion in carbon tetrachloride, then rinsed in ethyl alcohol, and then allowed to dry on a filter paper.

A clean glass slide was coated with a thin layer of acetone collodion which was then dried under a lamp. When this coating had dried another thin layer was applied on the first, and while this layer was still 'wet' a disc was placed in it, with the 'deposited-layer' side down. This was done carefully to avoid any trapped air bubbles.

The slide was replaced under the lamp, to dry the collodion. Then using a low-powered stereo-microscope, a layer of 'Lacomit' (acid-resistant varnish) was 'painted' around the disc to cover the collodion, and to seal the edge of the disc to prevent under-cutting attack by the etch. After painting with 'Lacomit', the slide was replaced under the lamp to dry.

The jet thinner is set up so that on looking through the microscope, the illuminated hole in the jet is central in the field of view. The etch flow-rate and head are set to the values given, and the glass slide carrying the mounted specimen placed over the jet, as shown in fig. (3.10) and positioned so that the 3 mm. disc is central in the field of view. This ensures that the thin region will be more or less central in the disc by virtue of the initial setting-up procedure. At the low flow-rates used, the thinning process takes between 10 and 15 minutes. A photo-electric detector was used to monitor the thinning: the circuit is given in the Appendix.

When silicon is approximately 5μ thick it is transparent to 'red' light and the thin region appears as a dull red patch in the

field of view. As the region gets thinner, the red patch changes colour through yellow, to a pale straw colour just before perforation. The photo-electric detector was set to detect the 'red transparent' stage. The transition from 'red' to 'straw' is relatively slow, taking on average 30 - 40 seconds and was monitored by 'eye'. At the 'straw' stage the glass slide was removed and plunged into a beaker of water to quench the etch. It was often found afterwards that during the transfer of the slide to the water, the residual droplet of etch created a small hole in the silicon. In these cases of perforation, the collodion undercoat prevents the acid from flowing over the surface of the layer and attacking it. After washing the specimen for a few minutes in a very gentle flow of water, the glass slide is immersed in a dish of warm water and allowed to soak for 10 - 15 minutes. This causes the collodion to swell and detach itself from the slide, freeing the silicon disc. The thinned disc needs no further cleaning and can be examined or stored.

Fig. (3.9b) shows the dimensions of the thinned region. It can be seen that only the top 3000Å is left in the thin region. Thus in order to study the substrate layer interface, either very thin layers must be grown, of thickness $\leq$ 4000Å, or thinning carried out from each side in turn.

3.6.(1) Experimental Method for Nucleation Studies

Since the initial growth process has a profound effect on the structure of the layer, some experiments were carried out to investigate the nucleation and growth stages.

The basic technique used in most nucleation studies as reported in the literature is to grow a series of discontinuous layers by exposing the substrate to a constant deposition rate for different times. This method was tried by scanning the shutter slowly across the substrate, thus exposing it for a varying time. However, because of the high deposition rates used, the results were in most cases not satisfactory. [In most reported studies of the nucleation process the rates used are of the order 1 - 50Å per minute. This low rate allows good control of the deposition durations.] In this work, however, the rates used are an order of magnitude greater. The method used was to create a zone of varying rate. A strip of molybdenum 3 mms.

wide was mounted below the deposition aperture in plate S so that it was 3 ~ 4 mms. below the substrate. Because of the finite source area, a penumbra zone, in which the deposition rate varies, is produced on the substrate: the experimental arrangement is shown in fig. (3.10). From this figure it is seen that three zones are produced.

(i) A zone at the centre which is completely masked, designated the mask zone; or M.Z.

(ii) Two regions, one each side of the M.Z. in which the rate of deposition varies, increasing as one moves away from the M.Z.: these are called Nucleation Zones or N.Z.

(iii) The regions outside the penumbra, where 'normal' deposition occurs, designated continues layer of C.Z. regions.

These regions were investigated by replication techniques and transmission electron microscopy.

3.6.(2) Replication Method

In the standard method of production of shadowed replicas, Bradley (1959), the replica is freed by dissolution of the specimen. This method was modified to enable the specimen to be recovered so that transmission microscopy studies of the same area could be carried out. The specimen, in the form of a standard 3 mm. diameter disc, was cleaned ultrasonically to remove any particles of dirt, and then a thin layer, 20 - 40 Å, of aluminium deposited onto the surface. A carbon layer about 150 Å thick was then evaporated on top of the aluminium layer, at normal incidence.

The thickness of the carbon layer is of importance, since if it is too thick, the intensity transmitted will be small, and detail will be lost. If the carbon layer is very thin, it will be very fragile and difficult to handle.

To monitor the thickness of the carbon deposit, a piece of 'shiney' aluminium foil was placed alongside the specimen, and carbon evaporation was stopped when the aluminium foil surface was a violet-blue colour. This corresponds to a thickness of carbon of 100 to 200 Å.

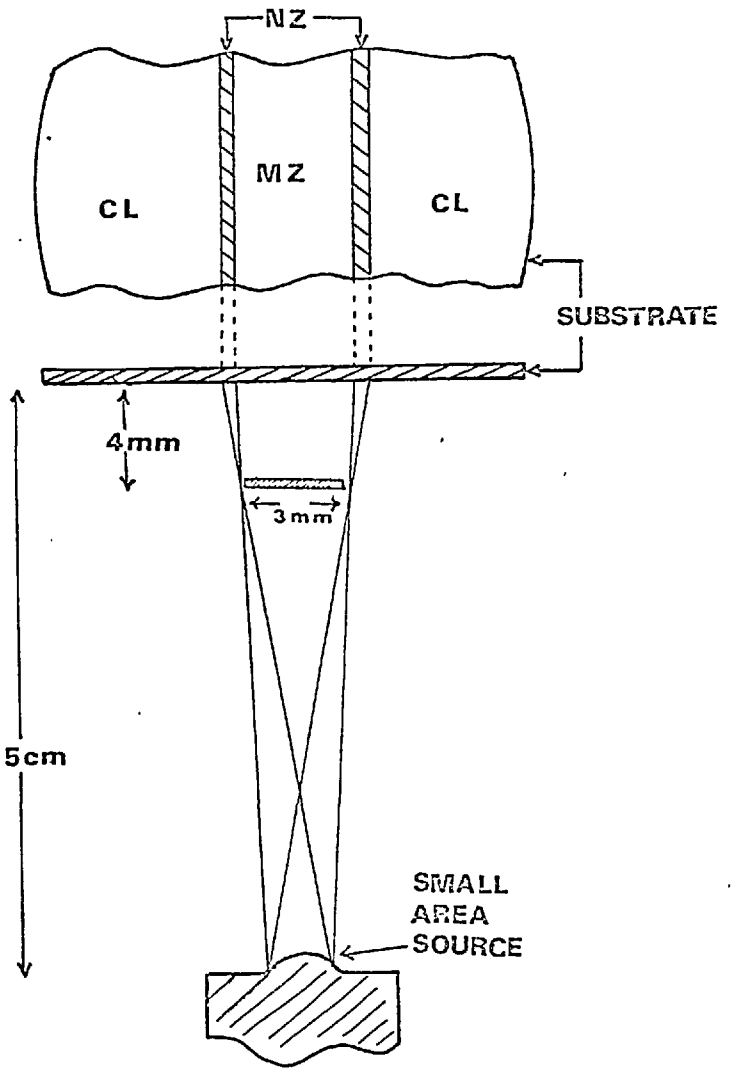


Fig. (3.10)
DIAGRAM SHOWING THE SHADOWING ARRANGEMENT USED TO PRODUCE NUCLEATION ZONES.
MZ = MASKED ZONE
NZ = NUCLEATION ZONE
CL = CONTINUOUS LAYER.

The specimen was then tilted and shadowed by the evaporation of heavy metals. Angles of approximately 70° and 30° to the specimen surface normal were used. The metals used for shadowing were gold, platinum and gold/palladium alloy, as they come to hand. The shadowing metals used a high atomic weight, to give good contrast.

The replica was removed from the specimen by slowly inserting it replicated face upermost; at a slight angle, into a shallow dish of dilute hydrochloric acid (1 vol. acid to 5 vols. water).

The aluminium dissolves and the replica floats off onto the surface of the acid. The acid does not attack the specimen, the replica, or the shadowing metals. The replicas were removed, and floated on to a shallow dish of water to remove the acid, then picked up on 3 mm. grids, and stored.

Chapter 4. Results.

4.1. Growth Conditions for Epitaxy

The layers were deposited at various rates and growth temperatures in the manner described in the experimental techniques section. The layers were examined by electron diffraction and transmission microscopy, to determine the conditions for the transition from epitaxial to non-epitaxial growth. The presence of a ring diffraction pattern was taken to indicate non-epitaxial growth, and the presence of a spot pattern to indicate epitaxial growth.

The values of the growth parameters, R_c and T_c - growth rate and temperature - for the transition, were found as follows. The values of growth parameters corresponding to single crystalline and to polycrystalline growth were plotted and the points corresponding to the transition were found by interpolation. The curve through these points then represented the variation of critical growth rate and temperature, R_c, T_c. Fig. (4.1) shows the graph so obtained.

It was also found that for growth temperatures below 380 ~ 400°C epitaxial growth could not be obtained for any deposition rate. This indicated 380°C to be the zero-rate minimum epitaxial temperature for the (111) oriented silicon substrates.

4.2. The Structure of the Layers

4.2.(1) Visual Appearance and Topography

Layers grown on optically polished substrates were also optically flat, whether epitaxial or polycrystalline.

Interferometric measurements showed the surfaces to be smooth as shown in fig. 4.2b, with no trace of faceting or steps, through the entire range of growth parameters investigated.

The overall smoothness of the surface is shown in the streaking of the diffraction spots and presence of Kikuchi bands as shown in fig. (4.2). This suggests that the layer surfaces are atomically smooth: Pashley (1965).

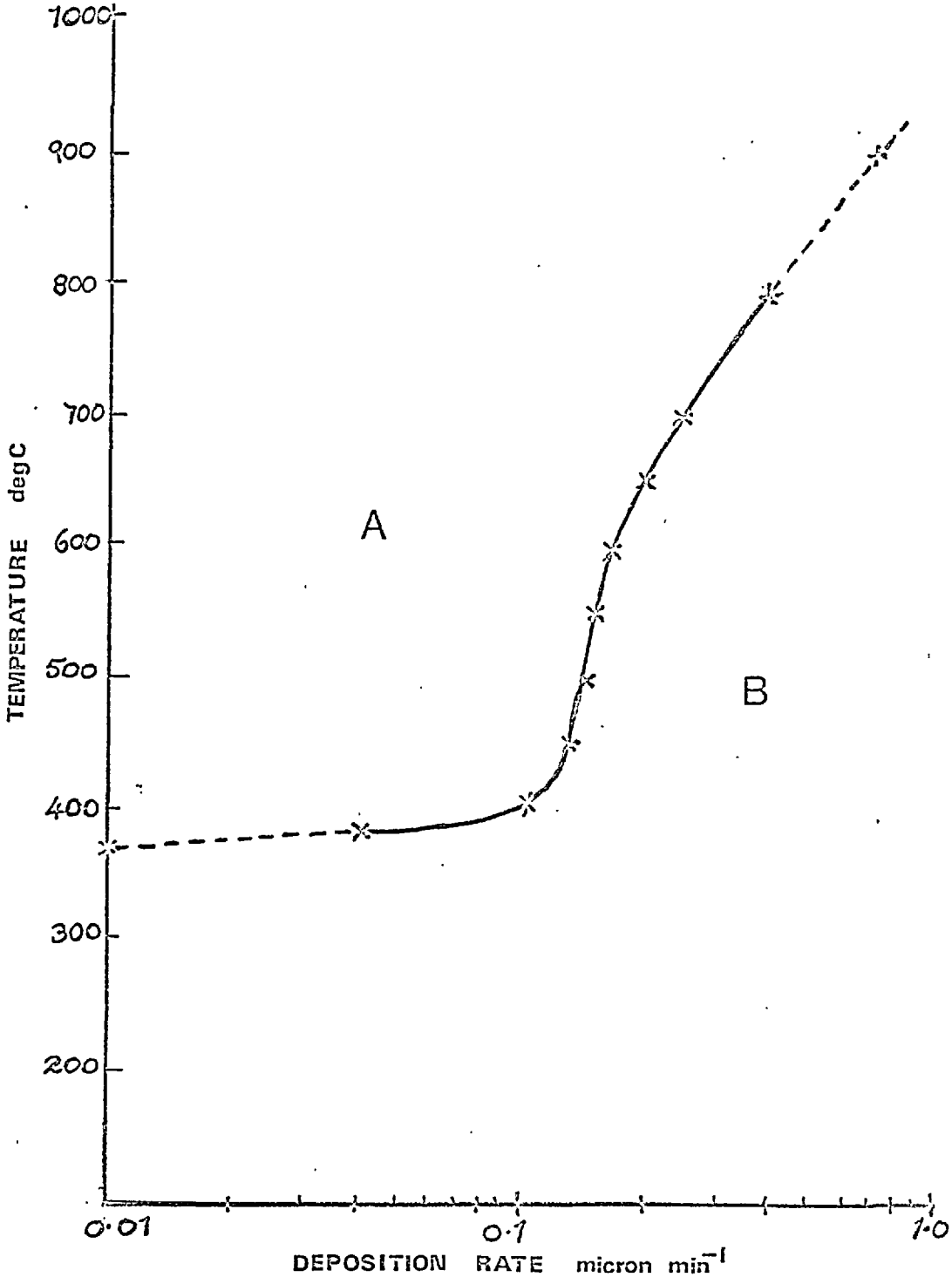
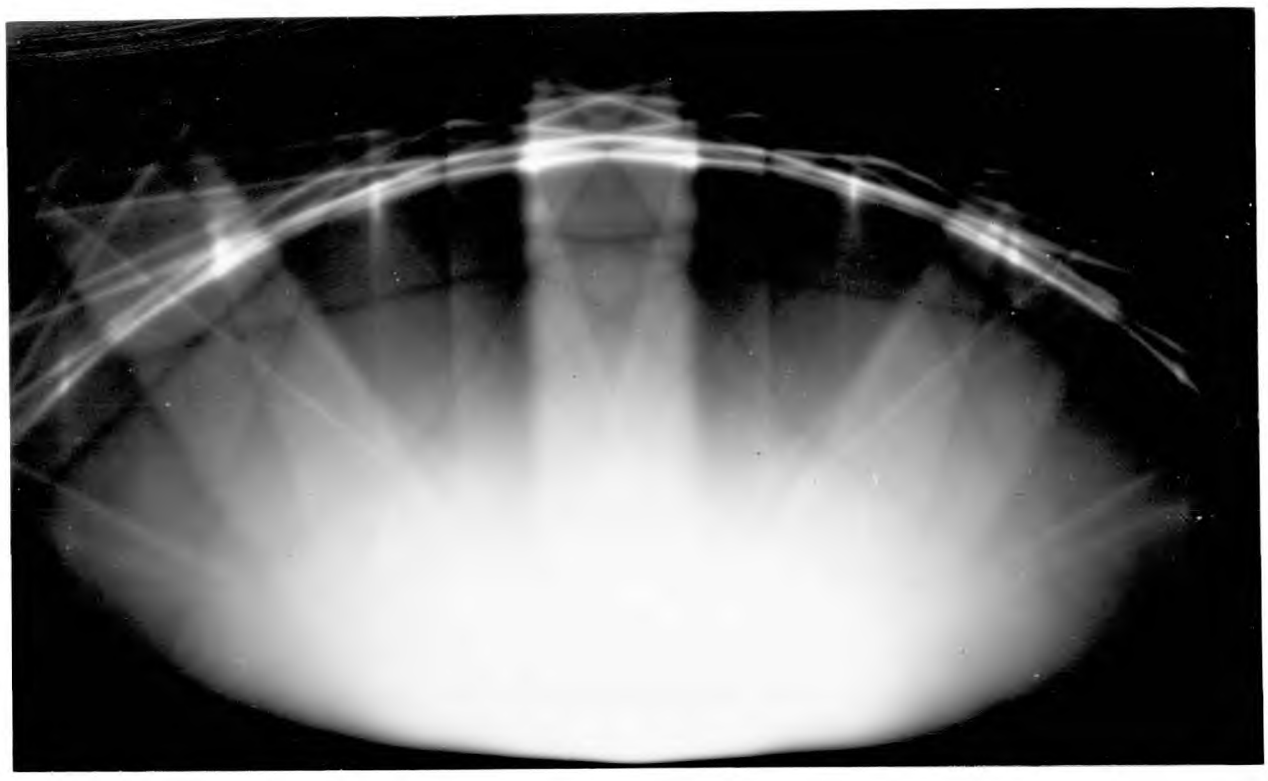
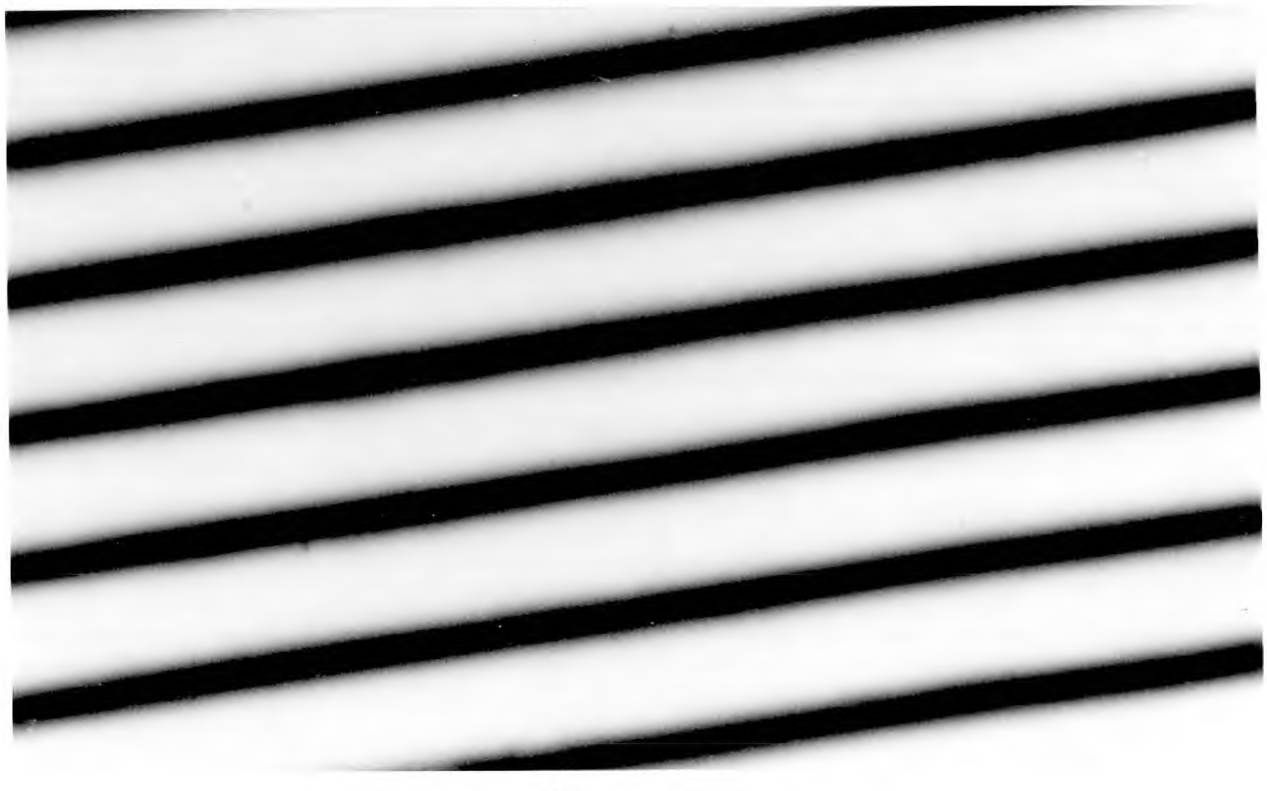


Fig. (4.1)
PLOT OF MINIMUM EPITAXIAL TEMPERATURE VERSUS DEPOSITION RATE.
A = INDICATES THE DOMAIN OF GROWTH PARAMETERS R,T: FOR WHICH EPITAXIAL GROWTH WAS POSSIBLE.
B = INDICATES THE DOMAIN OF GROWTH PARAMETERS R,T: FOR WHICH EPITAXIAL GROWTH WAS NOT POSSIBLE.



a



b

FIG. (4.2)

a. GLANCING ANGLE REFLECTION DIFFRACTION PATTERN FROM THE SURFACE OF A LAYER

b. WEDGE FRINGES SHOWING THE FLATNESS OF THE LAYER SURFACE

4.3. Analysis of the Structure of the Layers by Transmission Electron Microscopy.

Introduction

The layers grown for values of deposition parameters which gave epitaxial growth conditions showed large variations in structure, quality and defect content.

In analysing and presenting these results, it was found convenient to divide the layers into two groups. The division is based on the observed structure as follows:

Group I — Those layers which consisted mainly of twinned material.

Group II — Those layers which were well oriented, and contained stacking fault defects.

For this latter group, the fault density was taken as a measure of layer quality.

4.3.(1) Analysis of the Structure of Layers of Group I

It was found that the layers in this group were those grown in the temperature range 400°C to 600°C and at rates $\geq$ 0.1μ per minute.

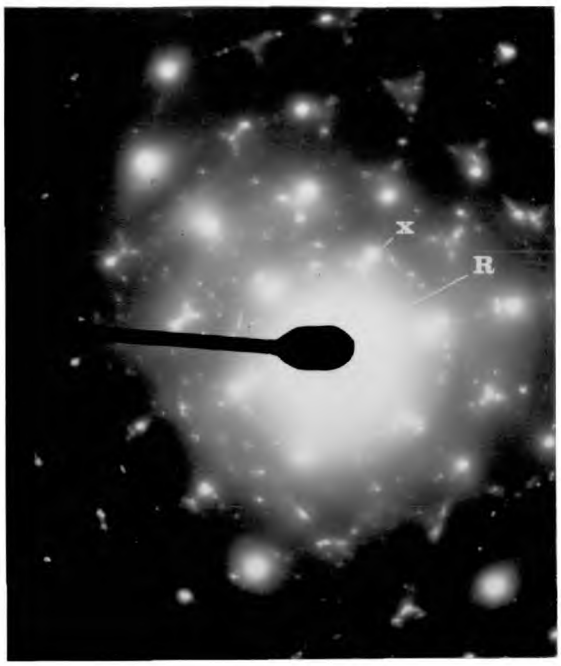
Within this group, variation of quality with deposition parameters was observed, as seen from the following examples.

Fig. (4.3) shows the diffraction pattern, bright-field and dark-field micrographs of a layer 3μ thick grown at 0.1μ per minute at a substrate temperature of 460°C.

As can be seen from the diffraction pattern, fig. (4.3a), the layer is epitaxial but the presence of the extra spots and a ring marked R indicate the presence of considerable disorder.

This is confirmed in the bright-field micrograph, fig. (4.3b). The presence of the extra spots around the $\{\bar{2}20\}$ matrix spots indicates the presence of twinned material.

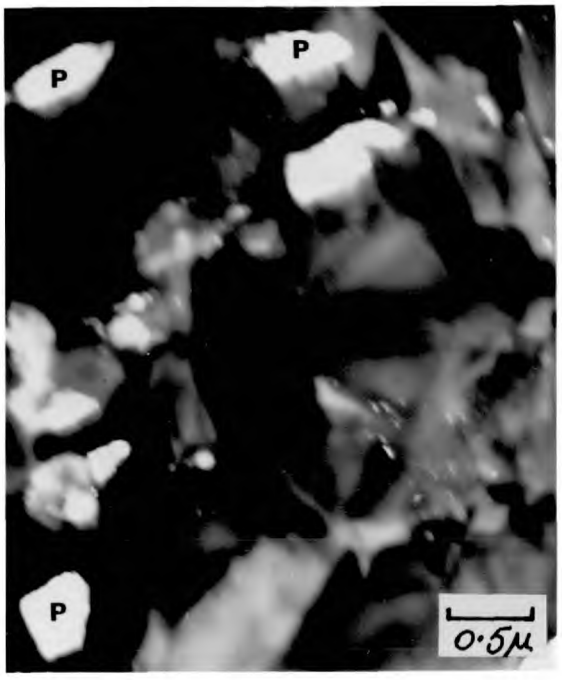
The dark-field micrograph, fig. (4.3d), taken using the diffraction spot indicated in fig. (4.3a), shows the twinned regions in bright contrast. This is an example of domain contrast discussed in section (1.35). The presence of the ring R in the diffraction pattern indicates the presence of polycrystalline material.



a



b



c



d

FIG (4.3) TRANSMISSION ELECTRON MICROGRAPHS OF A LAYER DEPOSITED AT 460° C: 0.1μ min^{-1}

a. GENERAL AREA DIFFRACTION PATTERN

b. BRIGHT FIELD MICROGRAPH

c. DARK FIELD MICROGRAPH USING R

d. DARK FIELD MICROGRAPH USING TWIN SPOT

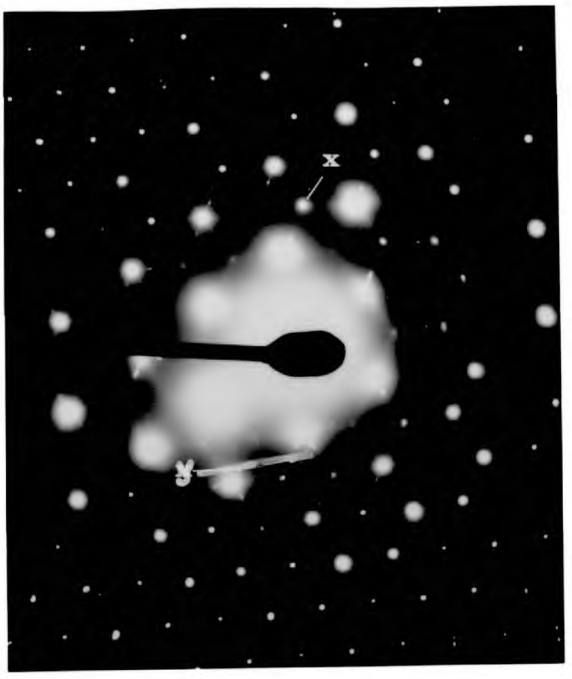
X in .a 100 KV

The ring R can be seen to be resolved into individual spots, showing that the polycrystalline regions are large, relative to the diameter of the electron beam, (estimated to be 1μ). This is confirmed by the dark-field micrograph fig. (4.3c), taken using a spot in the ring to form the image. This micrograph shows some of the grains, marked P in the micrograph, in bright contrast. The diffraction pattern of figure (4.3a) also shows the presence of faint spots and streaks lying along the < 110 > directions. These spots and streaks are caused by diffraction effects at the twin boundaries and indicate that the twins may be in the form of 'stacks' of laminae. Some twinned regions in the form of stacked laminae can be seen at S, fig. (4.3b and d). From these micrographs it can be seen that the layer consists mainly of twinned material with some polycrystalline grains. Thus although epitaxial, the quality of the layer is very poor.

The effect of increasing the deposition temperature at approximately the same growth rate can be seen in fig. (4.4), which shows the diffraction pattern; bright field and dark field micrographs of regions in a layer 2μ thick, grown at 0.1μ per minute at a substrate temperature of 600°C.

The diffraction pattern fig. (4.4a) has a more ordered appearance and there is no trace of rings. Extra spots are visible, for example at X in fig.(4.4a). These spots can be indexed as $\frac{1}{3}$ ($\bar{4}22$) relative to the matrix spots [they lie along the [$\bar{4}22$] directions and are $\frac{1}{3}$ the distance of the ($\bar{4}22$) spots from the origin.]

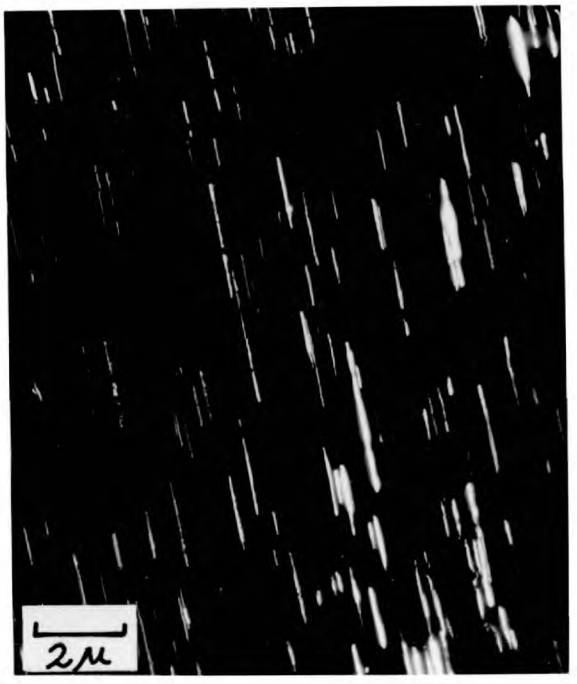
The diffraction pattern also shows prominent streaking along < 211 > directions. These streaks may lie in the plane of the pattern, or be produced by the interaction of the Ewald sphere with reciprocal lattice spikes which do not lie in the (111) reciprocal lattice plane. The formation of the $\frac{1}{3}$ ($\bar{4}22$) spots has been investigated in detail by Pashley and Stowell (1963); for films of gold, on F.C.C. material grown on (111) faces of NaCl, which also has an F.C.C. lattice. They found that these diffraction spots could be produced by double diffraction of the electron beam at the boundaries between doubly positioned twins. The stacking sequence for double positioned twins was discussed in the review, section 1.



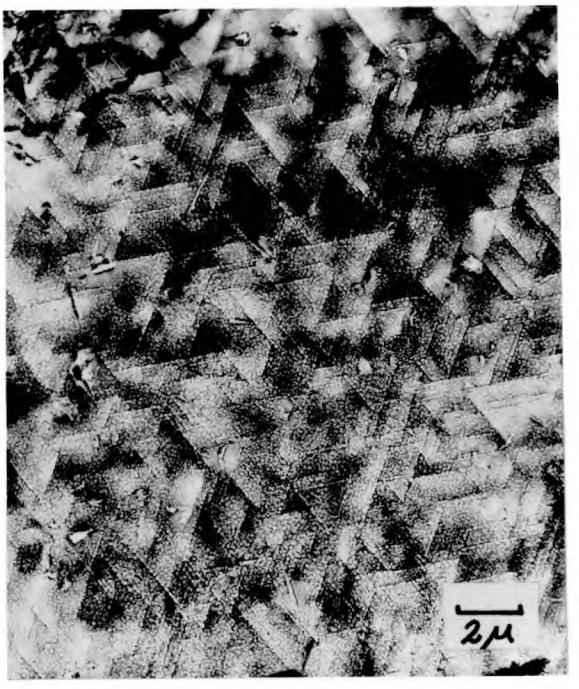
a



b



c



d

FIG. (4.4) TRANSMISSION ELECTRON MICROGRAPHS OF A LAYER DEPOSITED AT 600° C; 0.1μ $min.^{-1}$

a. GENERAL AREA DIFFRACTION PATTERN

b. BRIGHT FIELD MICROGRAPH

c. DARK FIELD MICROGRAPH ON DOUBLE DIFFRACTION SPOT X

d. DARK FIELD MICROGRAPH ON ALLOWED TWIN SPOTS Y

Fig. (4.4c) is a dark-field micrograph taken on the double diffraction spot X indicated in fig. (4.4a). The boundaries of the twin regions are seen in bright contrast, as was discussed in the review. From the microscope rotation callibrationm these boundaries are found to lie parallel to the $\{211\}$ planes normal to the foil plane as was found in the case of Au on NaCl, by Pashley and Stowell, (1963). Fig. (4.4d) is a dark field of an area of the specimen using the diffraction spot Y a $\{\bar{1}11\}$ twin spot indicated in fig. (4.4a). This micrograph shows triangular shaped areas which are composed of small spots in bright contrast. From the rotation calibration the sides of these triangles were found to lie parallel to the double position boundaries discussed above, thus it is probable that the boundaries of these triangular areas, are the double positioned twin boundaries. This is confirmed by the correlation between the lengths of the triangles, and the double positioned boundaries.

It is also seen that the small bright regions are not visible in the bright field micrograph (4.4b), but it is seen that some of the bright regions in fig. (4.4c) are composed of small bright spots.

4.3(2.) Structure of Layers in Group II

Introduction

The layers in this group had good crystalline perfection as judged by the presence of Kikuchi lines in the diffraction patterns: Pinsker (1953); Pashley (1965). The defects found in the layers were stacking faults, dislocations and a uniform distribution of small defects which had the appearance of either a fine grain backgrouns, or a distribution of black spots, in the micrographs. This defect content was observed to vary with both deposition rate and substrate temperature.

Investigation of the Defects

I Stacking Faults

Hirsch et al (1965) have shown that under two-beam diffraction conditions, an imperfection in a crystal introduces an additional phase factor $e^{-i\alpha}$; into the intensity of the diffracted wave:

$\alpha = 2\pi\, \underset{\sim}{g}.\underset{\sim}{R}$, where $\underset{\sim}{g}$ is the operating diffraction vector, and $\underset{\sim}{R}$ is the displacement vector of the imperfection. At a stacking fault, both parts of the crystal, above and below the fault, are identical in structure, but are translated relative to each other by the fault shear vector R. Thus the relative phase of the diffracted wave changes discontinuously across the fault by the amount α; where α is given by $\alpha = 2\pi\, \underset{\sim}{g}.\underset{\sim}{R}$. (Since α is periodic we need only consider $-\pi < \alpha < \pi$, and Arg $(\alpha + 2n\pi)$ = Arg α for integral n.)

In section (1.2) the shear vectors for stacking faults were shown to be of the form $\pm \frac{a}{6} < 112 >$, and for the faults on the $\{111\}$ planes it was shown that these fault vectors could be represented by displacement vectors of the form $\pm \frac{a}{3} < 111 >$.

For $\alpha = 2m\pi$; where m is an integer or zero, the contrast factor $e^{-i\alpha}$, is unity. Thus the fault will be invisible, and the contrast observed will be that of a perfect crystal. Since $\alpha = 2\pi\, \underset{\sim}{g}.\underset{\sim}{D}$, the condition for fault invisibility is $\underset{\sim}{g}.\underset{\sim}{D} = 0$, or an integer that is, $\underset{\sim}{g}$ is parallel to $\underset{\sim}{D}$. This rule applies regardless of the sign of $\underset{\sim}{D}$; i.e. for both extrinsic and intrinsic faults.

Thus if $\underset{\sim}{g}.\underset{\sim}{D} = 0$, or an integer, the fault will be 'out of contrast', i.e. invisible. Thus it is seen that a fault on the $(11\bar{1})$ plane for which $\underset{\sim}{b} = \pm \frac{a}{6}(11\bar{1})$ will be out of contrast for a $[\bar{2}20]$ diffraction vector, but in contrast for a $[20\bar{2}]$ diffraction vector. It is also seen that faults on the (111) plane, ie. the planes parallel to the substrate surface, are out of contrast for all $\{2\bar{2}0\}$ type diffraction vectors, and hence invisible.

The contrast produced by the stacking fault in two-beam diffracting conditions was shown by Hirsch et al (1965) to consist of fringes parallel to line of intersection of the fault plane with the foil surfaces.

Fig. (4.5) shows a series of micrographs of a group of stacking faults under different two-beam diffracting conditions. The faults are out of contrast when the operating diffraction vector $\underset{\sim}{g}$ is parallel (or anti-parallel) to the line of intersection of the fault plane and foil surfaces. This latter fact follows from the rule derived above. The condition $\underset{\sim}{g}.\underset{\sim}{D} = 0$, means that the vector $\underset{\sim}{g}$ is

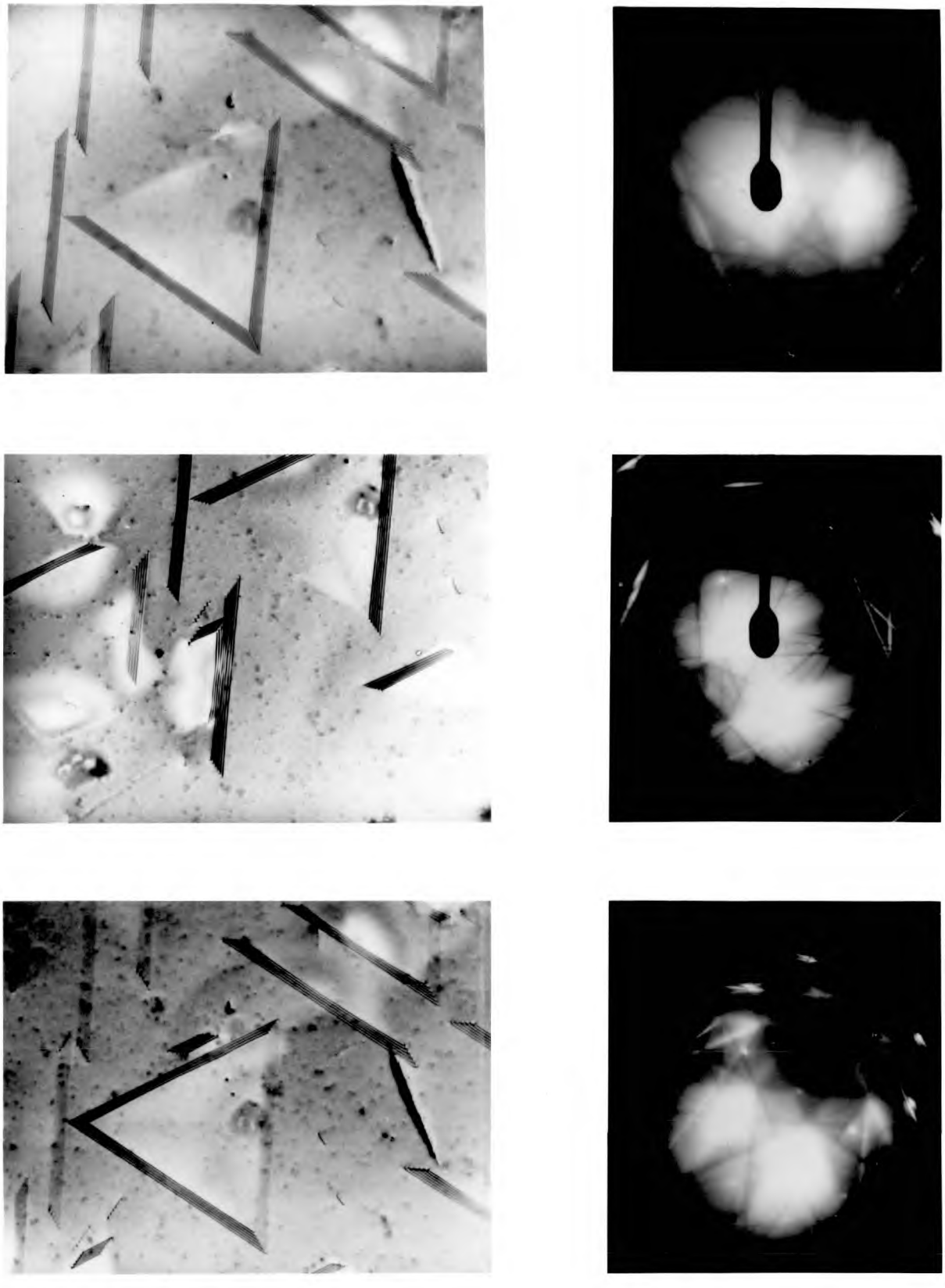


FIG. (4.5) TRANSMISSION ELECTRON MICROGRAPHS OF A GROUP OF STACKING FAULT DEFECTS SHOWING CONTRAST VARIATION UNDER DIFFERENT DIFFRACTION CONDITIONS

perpendicular to $\underset{\sim}{D}$; or the component of $\underset{\sim}{D}$ in the plane of the foil.

It was also shown by Hirsch et al (1965) that under two-beam diffracting conditions, the stacking fault fringe periodicity is $\frac{Eg}{2}$ where Eg is the extinction distance of the operating diffracted beam. For a $\{\bar{2}20\}$ diffraction vector in silicon; $Eg \approx 750$Å (Hirsch et al). Thus the fringe periodicity is 375Å in a direction parallel to the electron beam.

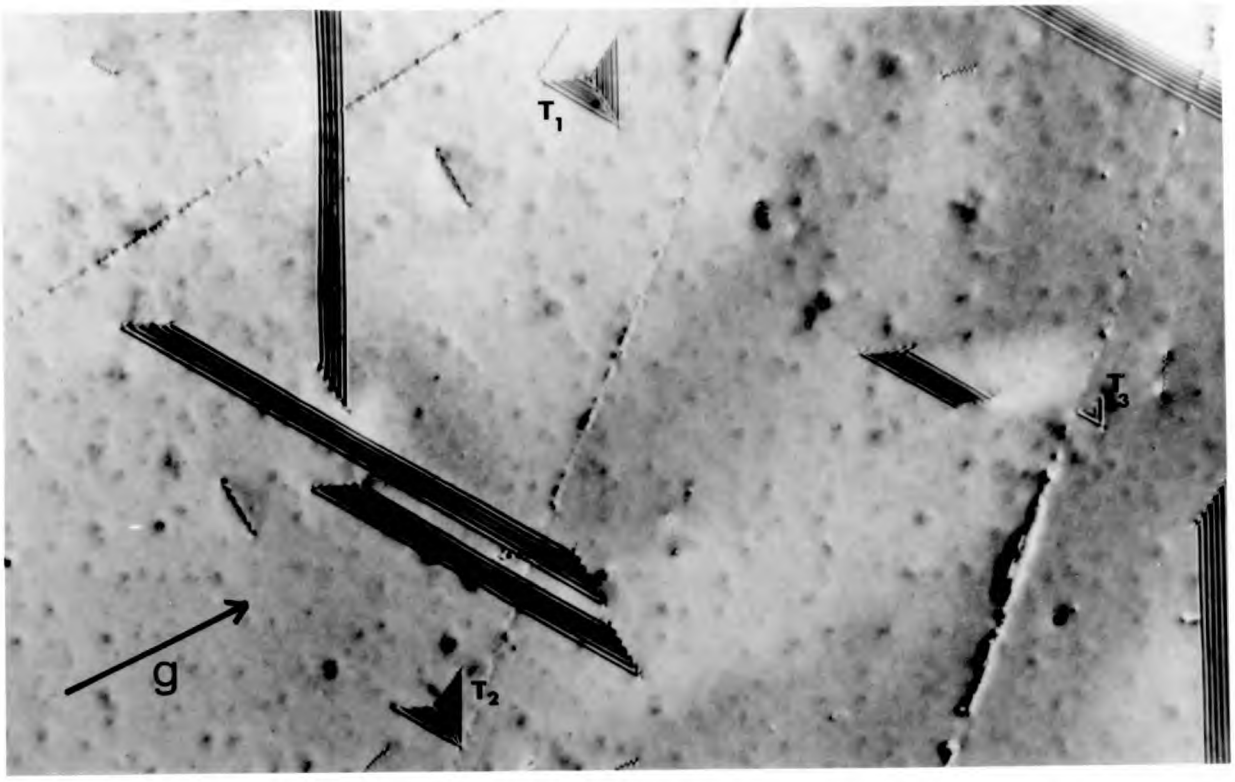
The selected area diffraction patterns of the faults do not show extra spots, thus confirming the features to be stacking faults as opposed to micro-twin lamellae which can also give fringe contrast. The stacking faults observed in the layers were similar in form to those found by the various workers whose results have been reviewed.

It was found that for all the layers in group II, the 'line' form of stacking fault predominated, and various sizes of faults were observed.

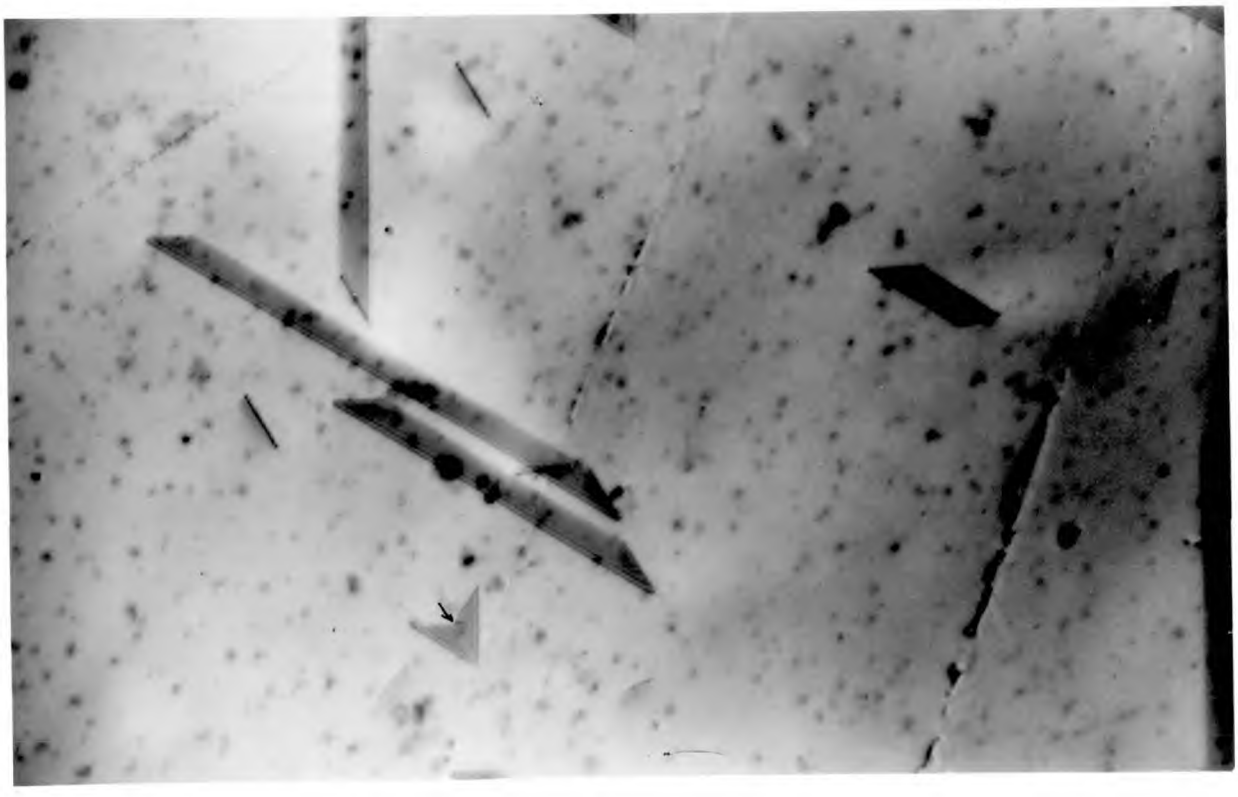
Fig. (4.6) is a micrograph of a layer grown at 800°C, at a rate of 0.07μ per minute. The micrograph was taken under two-beam conditions using a reflection of the $\{2\bar{2}0\}$ form. It is seen that the line-form faults were of dissimilar lengths, and also that the triangular faults T_1, T_2 and T_3 were of different sizes.

From the geometry of the stacking fault, the length l of the trace in the surface of the layer, fig. (4.7), is given by $l = 1.22 \times d$; Booker and Stickler (1962) where d is the depth to the point of origin of the fault. Thus a variation of lengths of fault indidates that the faults have been nucleated at different depths; since the layer thickness is the same for a given specimen. The longest faults were those nucleated at the interface. These had a length proportional to the layer thickness, which we shall call l_D, the characteristic length.

As shown in fig. (3.9c), the thinning process for transmission microscope specimen preparation leaves only the top 5000Å of the layer. Thus for layers of thickness greater than 5000Å the interface region is removed. In fig. (4.6a) it is seen that the whole of the triangular faults, including the lower vertex, can be seen. Their extension into the layer can be estimated from the number of fringes visible in the fault.



a



b

FIG. (4.6)

a. BRIGHT FIELD MICROGRAPH OF A LAYER DEPOSITED AT 800° C; 0.07 μ min.$^{-1}$

b. LOW RESOLUTION DARK FIELD MICROGRAPH OF AREA SHOWN IN a.

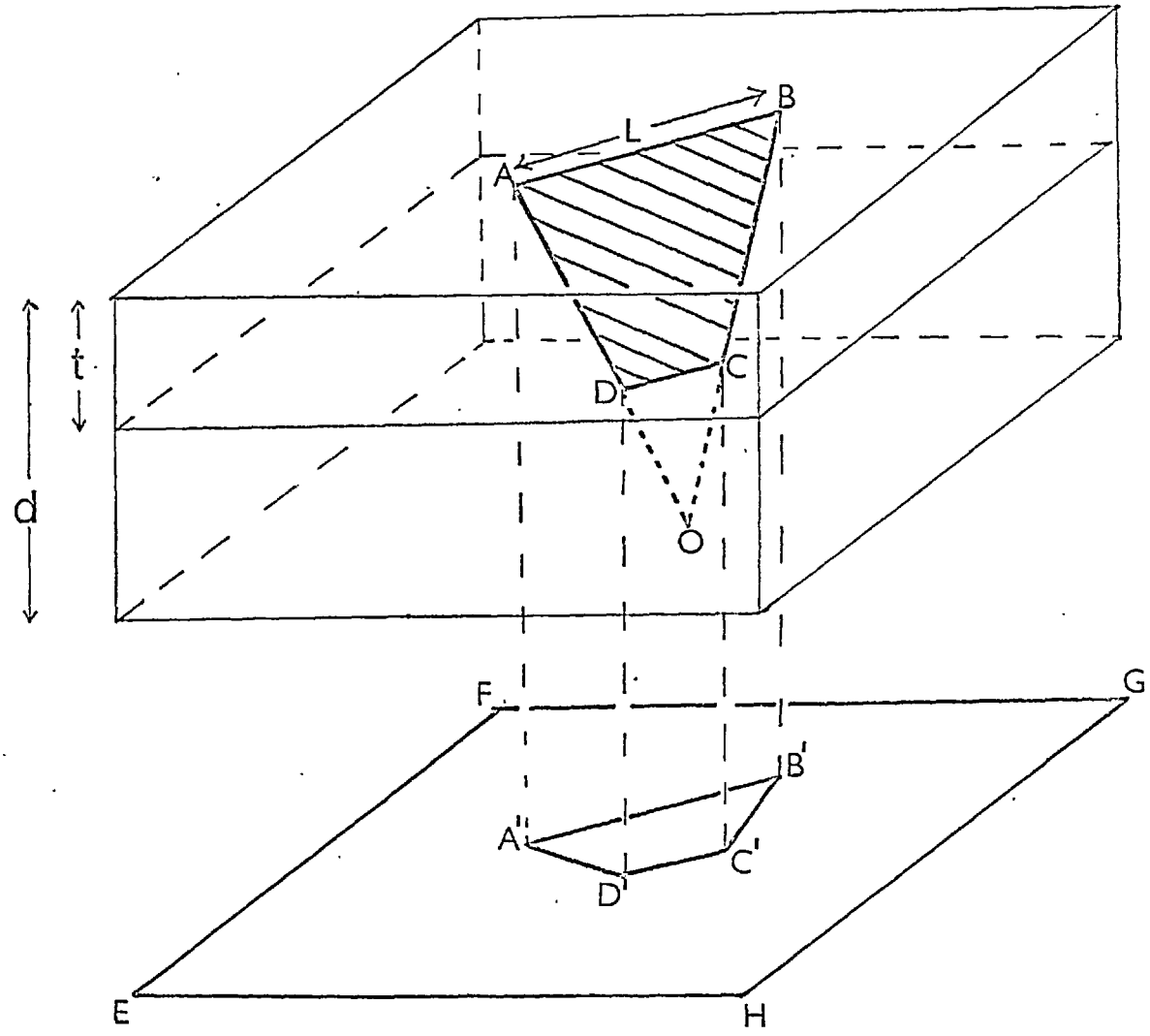


Fig. (4.7)
GEOMETRY OF THE STACKING FAULT, AND THE TRANSMISSION MICROSCOPE IMAGE, ABCD IS THE FAULT; ORIGIN O. t IS THE THICKNESS OF THE TRANSMISSION MICROSCOPE SPECIMEN d IS THE THICKNESS OF THE LAYER. A'B'C'D' IS THE IMAGE OF THE FAULT.

For reflections of the form $\{\bar{2}20\}$ in silicon, Eg is 750Å (Hirsch et al (1965)). From this the depth of the point of origin of T_1, which had 4 fringes visible, was approximately 1500Å, and T_3, which had 2 fringes visible, had a point of origin approximately 750Å below the surface. The small variation in the number of fringes visible in the line faults is due to the thin region of the specimen being slightly wedge-shaped, due to the thinning method. The differences in numbers of fringes also confirms that the triangular faults have not been produced by growth and interaction of the line type faults since if this was the case, the triangle and line faults would all have the same number of fringes visible.

In films grown at higher deposition temperatures, the triangular faults were more numerous and had sides of length l_D as shown in fig. (4.8a) which is a micrograph of a layer grown at 900°C and 0.1μ per minute.

A similar effect was observed for very low deposition rates, as shown in fig. (4.8b) which is a micrograph of a layer grown at 0.05μ per minute at a temperature of 650°C.

4.3.(3) The Orientation of the Triangular Stacking Faults

The triangular stacking faults were always found to be similarly oriented. Fig. (4.9a) is a micrograph showing two triangular faults beginning to interact. Some etch pits E_1 E_2 ... are visible: it can be seen that the etch pits are oriented anti-parallel to the faults. The etch pits were found to lie on the substrate side of the thinned foil, and were caused by local preferential etching during the thinning.

Fig. (4.9b) is a diagrammatic representation of a section through the foil. ABCD represents the etch pit and EF, FG, GE are the traces in the upper surface, of the plane forming the etch pit. It is seen that EFG is in parallel orientation to the trace of the stacking fault, IJK.

If the etch pits are tetrahedra formed by the exposure of $\{111\}$ planes, then the vertex will point in a $\langle\bar{2}11\rangle$. It is seen from fig. (4.9) that the fault vertices point in $[\bar{2}11]$ type directions.



a



b



c

FIG. (4.8)

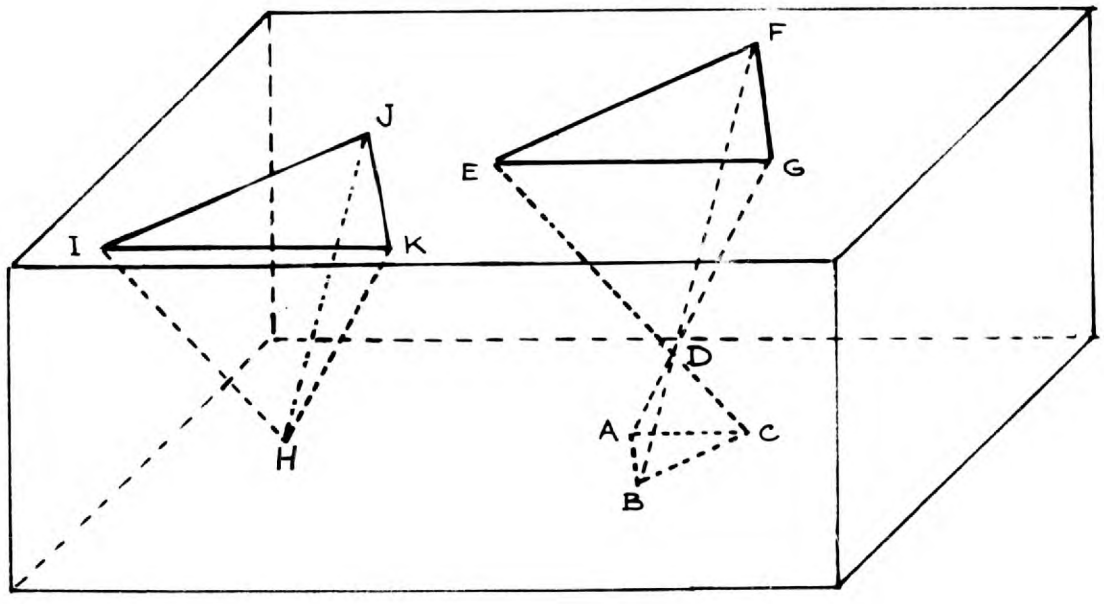
a. TRANSMISSION MICROGRAPH OF A LAYER DEPOSITED AT 900° C: 0.1μ min.$^{-1}$

b. TRANSMISSION MICROGRAPH OF A LAYER DEPOSITED AT 650° C: 0.05μ min.$^{-1}$

c. TRANSMISSION MICROGRAPH OF A LAYER DEPOSITED AT 1000° C; 0.04μ min.$^{-1}$



a



b

FIG. (4.9)

a. TRANSMISSION MICROGRAPH SHOWING ETCH PITS E_1 E_2 ... AND STACKING FAULT F.

b. DIAGRAMMATIC REPRESENTATION OF A SECTION THROUGH THE FOIL

4.3.(4) Measurement of Stacking Fault Density

For the layers of Group II, the stacking fault density was used as a measure of the quality of the layers. The density expressed as number of faults per square centimetre of layer, was determined by counting the number of faults visible in the field of view, with the specimen tilted into a two-beam condition. This procedure was repeated for several fields of view and for up to three thinned discs taken at random from the layer. Since in a given two-beam condition we may assume $\frac{1}{3}$ of all the faults present will be out of contrast, the counts obtained may be assumed to represent $\lesssim \frac{2}{3}$ the number of faults present; thus the counts obtained were multiplied by $\frac{3}{2}$. Fig. (4.10) shows the results obtained. The large spread in the 420°C plot is due to the difficulty of counting the individual faults because of overlapping.

The results show that for a given substrate temperature, the fault density increases with growth rate. The estimated spreads could preclude the observation of a non-linear dependence, however, a growth rate dependence is clearly seen.

4.3.(5) Examination of Substrate-layer Interface

Fig. (4.11) shows a portion of the substrate-layer interface of a thin layer deposited at about 700°C. This layer was produced by opening the shutter for approximately 2 minutes and was estimated to be about $3 \sim 5000$Å thick. It is seen that each stacking fault has a small black spot, at the point from which the fault originates.

It is also seen that, whilst all the faults have the black spots at the origin points, not all the black spots have stacking faults associated with them.

The exact nature of these black spot defects could not be determined but as can be seen from fig. (4.11c) some have regular and some irregular shapes. Also, the regions appear very much darker than the surrounding silicon, and therefore may have a high absorption for electrons. Fig.(4.11c) also shows line features similar to those shown in fig. (4.8b, and c). It is also seen in fig.(4.11) that these line features appear to originate from the black spots discussed above.

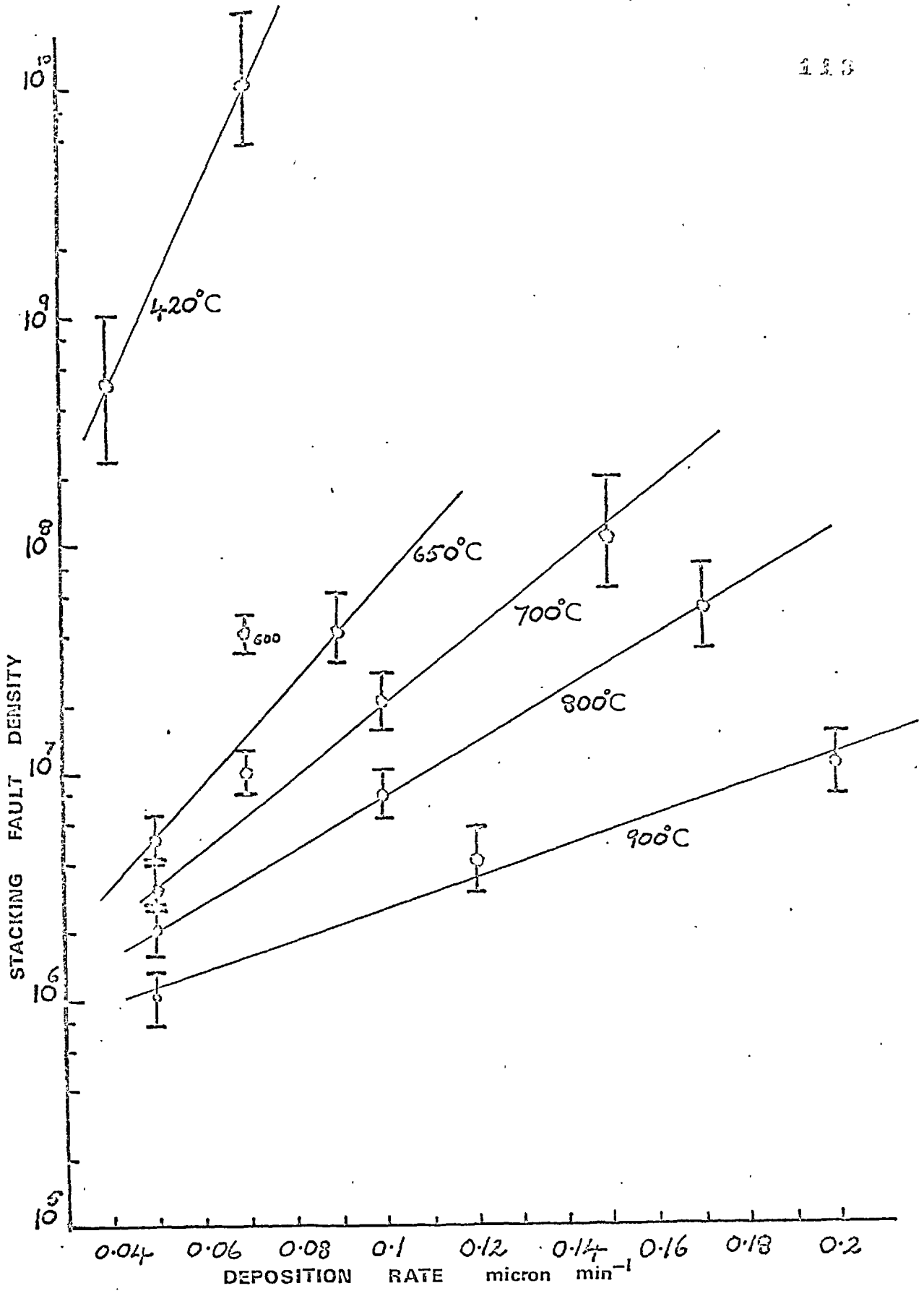
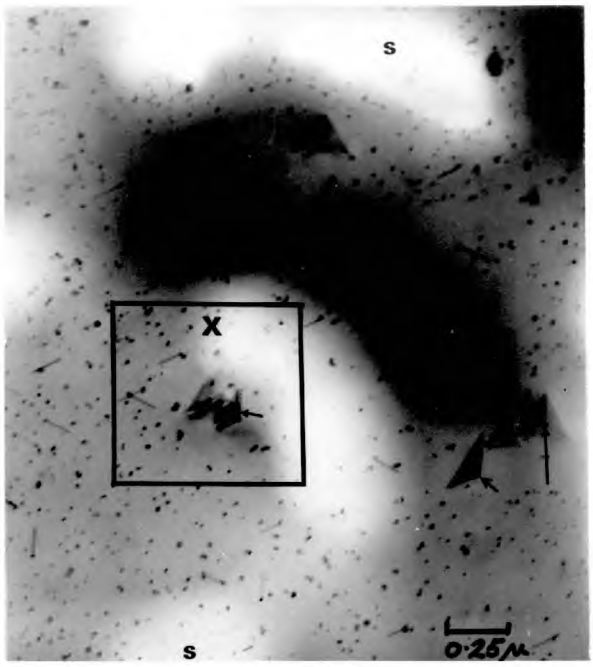
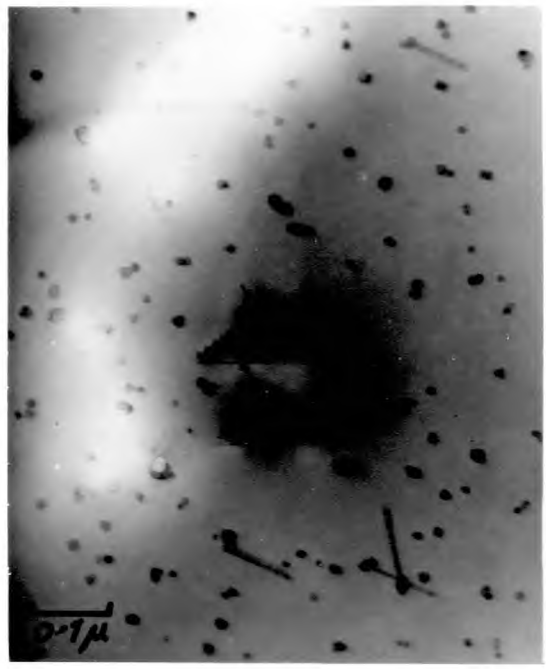


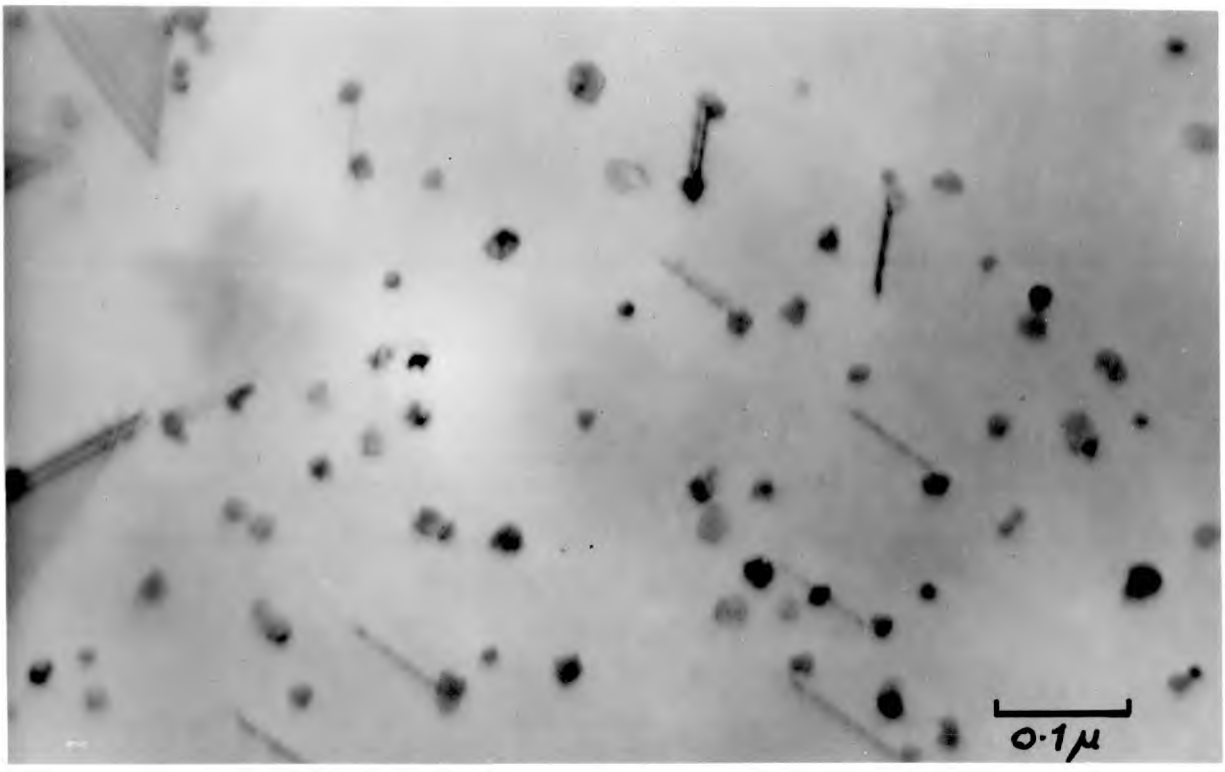
Fig. (4.10)
PLOT OF STACKING FAULT DENSITY VERSUS DEPOSITION RATE FOR VARIOUS SUBSTRATE TEMPERATURES.



a



b



c

FIG. (4.11)

a. A REGION OF THE LAYER SUBSTRATE INTERFACE

b. AREA SHOWN AT X AT HIGHER MAGNIFICATION

c. INTERFACE AREA AT HIGH MAGNIFICATION

4.3.(6) Analysis of Stacking Faults

As discussed in the review, section (1.2.(1)), stacking faults may be of two types - extrinsic and intrinsic.

Hirsch et al (1965) have shown that for two-beam diffracting conditions the phase shift introduced by a stacking fault is α, where $\alpha = 2\pi\, \underset{\sim}{g}.\underset{\sim}{D}$., $\underset{\sim}{g}$ being the operating diffraction vector, and $\underset{\sim}{D}$ the displacement vector of the fault. ($\underset{\sim}{D}$ is defined in section (1.2.(1)).) It was shown by Arts et al (1963) that the value of the phase shift α could be found from the contrast of the outermost edge fringes in the bright field micrograph of the fault. If on a positive print, both the outermost edge fringes are in bright contrast, then α is positive. If the outermost edge fringes are dark, then α is negative.

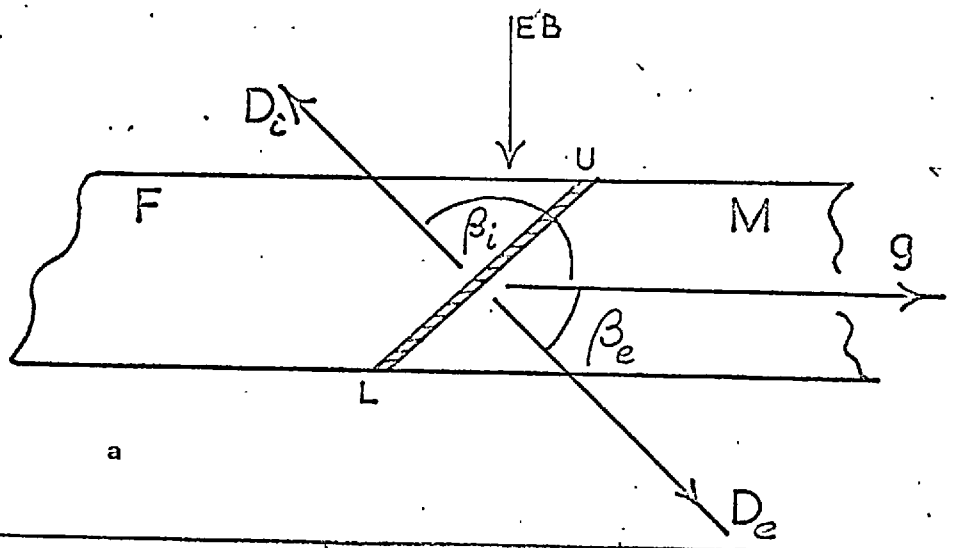
It was also found by the above workers that for foils thick enough to produce absorption effects, the dark-field image of the fault is pseudo-complementary to the bright field image in that the fault fringe contrast reverses only for the edge fringe on the exit side of the foil. From these results Gevers et al (1963) have shown how the nature of the fault can be found.

Following the analysis of Arts et al (1963) we can write $\alpha = 2\pi|D|.|g|\cos\beta$, where β is the angle between the vectors $\underset{\sim}{D}$ and $\underset{\sim}{g}$. For $\{111\}$ planes, $\underset{\sim}{D} = \pm\frac{a}{3}\langle 111\rangle$ so $|D| = \frac{a}{3}\sqrt{3}$ and from the definition of reciprocal lattice vectors $|g_{hkl}| = \left|\frac{1}{d_{hkl}}\right|$; which is $\frac{\sqrt{h^2 + k^2 + l^2}}{a}$ for cubic lattices. Thus for $\underset{\sim}{g}$ vectors of the form $\{2\bar{2}0\}$, $|g| = \frac{2\sqrt{2}}{a}$, (taking the positive sign for $\sqrt{}$ in the above.)

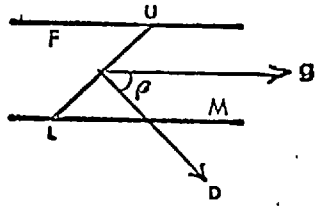
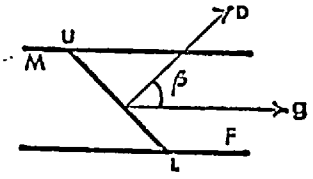
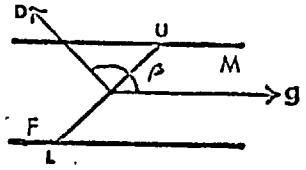
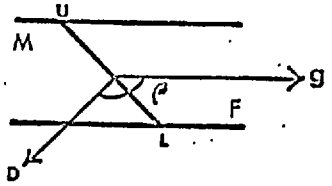
Thus $\alpha = \frac{2\pi.2\sqrt{6}.}{3}\cos\beta$

Arts et al (1963) have shown that for the $\underset{\sim}{g}$ vectors of the form $\{2\bar{2}0\}$ α is positive for β acute. Thus the sign of $\cos\beta$ depends on the sign of α.

In fig. (4.12a) the stacking fault is shown as produced by the displacement of a portion of the crystal in the manner discussed in Section (1.2.1). F is the fixed portion and M the moved portion of the crystal. It is assumed that the electron beam enters the crystal through the fixed portion. Then it is seen for the given direction of g that there are two possible values for β, corresponding to the two



a

GEOMETRY	BRIGHT FIELD FRINGE CONTRAST		COS β	DARK FIELD FRINGE CONTRAST		FAULT
	U	L		U	L	
	B	B	>0	B	D	EXT
	B	B	>0	B	D	INT
	D	D	<0	D	B	INT
	D	D	<0	D	B	EXT

b

Fig. (4.12).

a GEOMETRICAL RELATIONSHIP BETWEEN FAULT DISPLACEMENT VECTOR D_i DIFFRACTION VECTOR g AND ANGLE β.

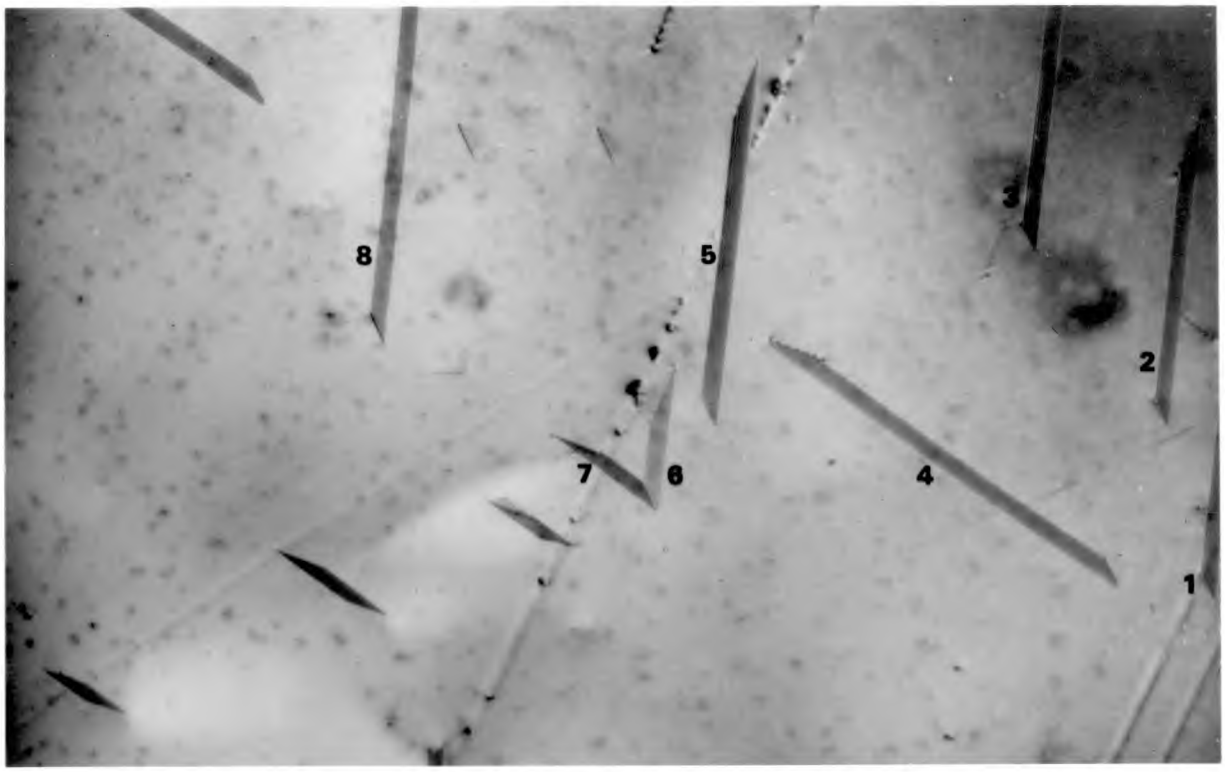
b EDGE FRINGE CONTRAST OF FAULT CONFIGURATIONS

senses of the stacking fault displacement vector $\underset{\sim}{D}$, as shown in the diagram.

From the definitions of the $\underset{\sim}{D}$ Vectors, Section (1.2.(1)), it is seen that $\underset{\sim}{D}_e$ is the extrinsic fault displacement and $\underset{\sim}{D}_i$ is the intrinsic fault displacement. Since the fault inclination may also be opposite to that shown in Fig. (4.12a), it is seen that there are four cases to be considered. These are shown diagrammatically in fig. (4.12b) with the edge fringe contrasts to be expected in bright-field, (BF) and dark-field, (DF) micrographs. U and L are the edge fringes on the beam entrance and exit faces of the foil. From comparison between the DF and BF micrographs, the sense of inclination of the fault to the beam can be found using the contrast reversal at the beam exit face, and the sign of α can be found from the BF edge fringe contrast. Hence, the value of β, acute or obtuse, can be found, and so the nature of the fault determined.

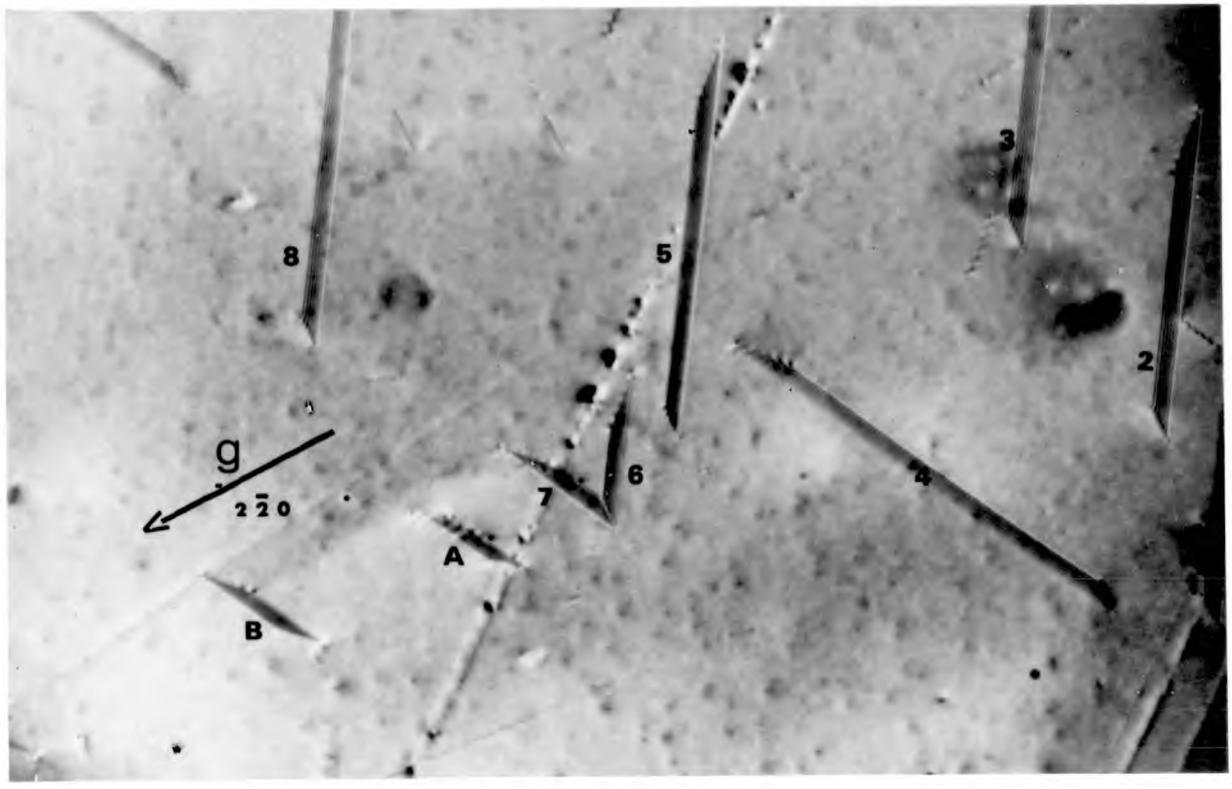
From fig. (4.12b) it is seen that the nature of the fault can be found from the dark-field image alone; as has been shown by Gevers et al (1963), if the origin of the $\underset{\sim}{g}$ vector is marked at the centre of the dark field fault image, then the direction of the $\underset{\sim}{g}$ vector is away from a bright edge fringe if the fault is intrinsic, and towards a bright edge fringe if the fault is extrinsic, regardless of the sense of inclination of the fault to the beam. This rule applies also for directions of $\underset{\sim}{g}$ not perpendicular to the line of intersection of the fault plane and foil surfaces.

The direction of the operating $\underset{\sim}{g}$ vector relative to the image, can be found from the selected area diffraction pattern, provided that the rotation correction for the magnification range used be applied. Fig. (4.13a,b,) shows the bright field and dark field micrographs of a group of stacking faults. The images appear as trapezia as shown in fig. (4.7). For the faults shown in fig. (4.13) the parallel sides of the trapezia are denoted by L - long; and S - short in the accompanying table which gives the edge fringe contrasts observed. Thus from the preceding analysis, faults 1, 2, 3, 4, 5, 8 are intrinsic, and 6, 7 extrinsic. Faults 6, 7 are two of the three faults forming a tetrahedral defect, the third fault being out of contrast in the micrographs.



a

0·5 μ



b

FIG. (4.13)

a. BRIGHT FIELD MICROGRAPH OF A GROUP OF STACKING FAULT DEFECTS

b. HIGH RESOLUTION DARK FIELD MICROGRAPH OF THE SAME AREA

Table IV. Stacking Fault Fringe Contrasts Observed in Fig. (4.13 a,b)

Fault Number	Bright Field Edge Fringe Contrast		Dark Field Edge Fringe Contrast		Comp Edge	α	β
	L	S	L	S			
1	B	B	B	D	S	+	acute
2	B	B	B	D	S	+	acute
3	B	B	-	-	-	+	acute
4	D	D	D	B	S	-	obtuse
5	B	B	B	D	S	+	acute
6	D	D	D	B	S	-	obtuse
7	B	B	B	D	S	+	acute
8	B	B	B	D	S	+	acute

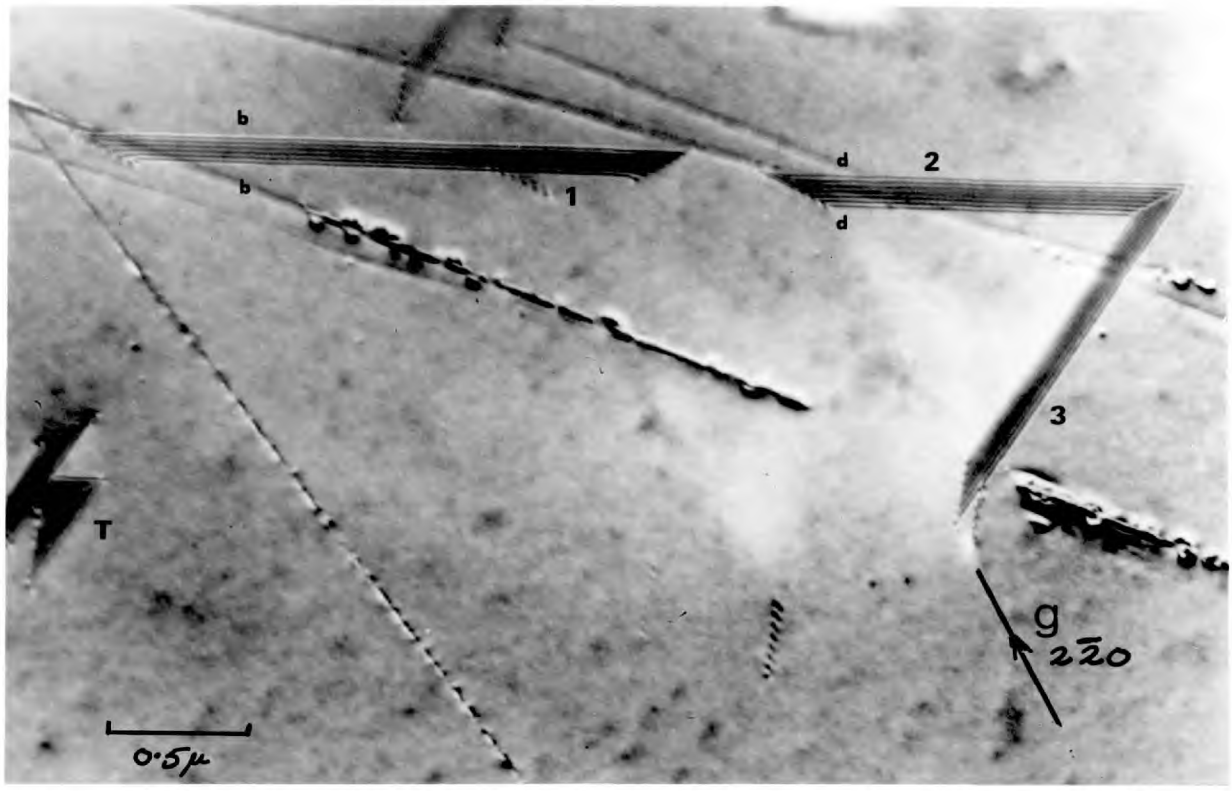


FIG. (4.14)

BRIGHT FIELD MICROGRAPH

Fig. (4.13) also shows features at A, B, which give stacking fault fringe contrast, but do not have the characteristic trapezoidal shape, as shown by the other faults. The exact nature of these features is not known, but from analysis of the edge fringe contrast they are extrinsic in nature.

The difference in nature between the triangle and line faults is confirmed in fig. (4.14) which is a bright field micrograph of a layer deposited at 800°C and 0.06 μ min^{-1}.

From their geometrical forms, faults 1 and 2 lie on parallel $\{111\}$ planes. As can be seen, the edge fringes of fault 1 are bright, whereas those of fault 2 are dark. The edge fringes of fault 3 are bright, indicating that it is of the same nature as fault 2. It is also seen that the small triangular fault T has similar edge fringe contrasts to faults 2 and 3 indicating that the nature of these three faults is the same.

4.4.(1) Variation of Background Defect Content with Growth Parameters

In this section micrographs and diffraction patterns of layers grown at various values of deposition rate and substrate temperature, are shown in order to compare the defect contents.

Fig. (4.15) shows the diffraction pattern, bright-field and dark-field micrograph of a layer deposited at 0.14μ per minute at a substrate temperature of 700°C. The diffraction pattern fig. (4.15a) shows the presence of several fine rings, indicated by R_1 R_2 R_3 in the figure. These can also be seen in the form of broad diffuse halos passing through the $\{\bar{2}20\}$ and $\{\bar{4}22\}$ matrix spots. The assymetry of the diffraction spot sizes, is caused by the foil being tilted from the symmetric orientation relative to the beam.

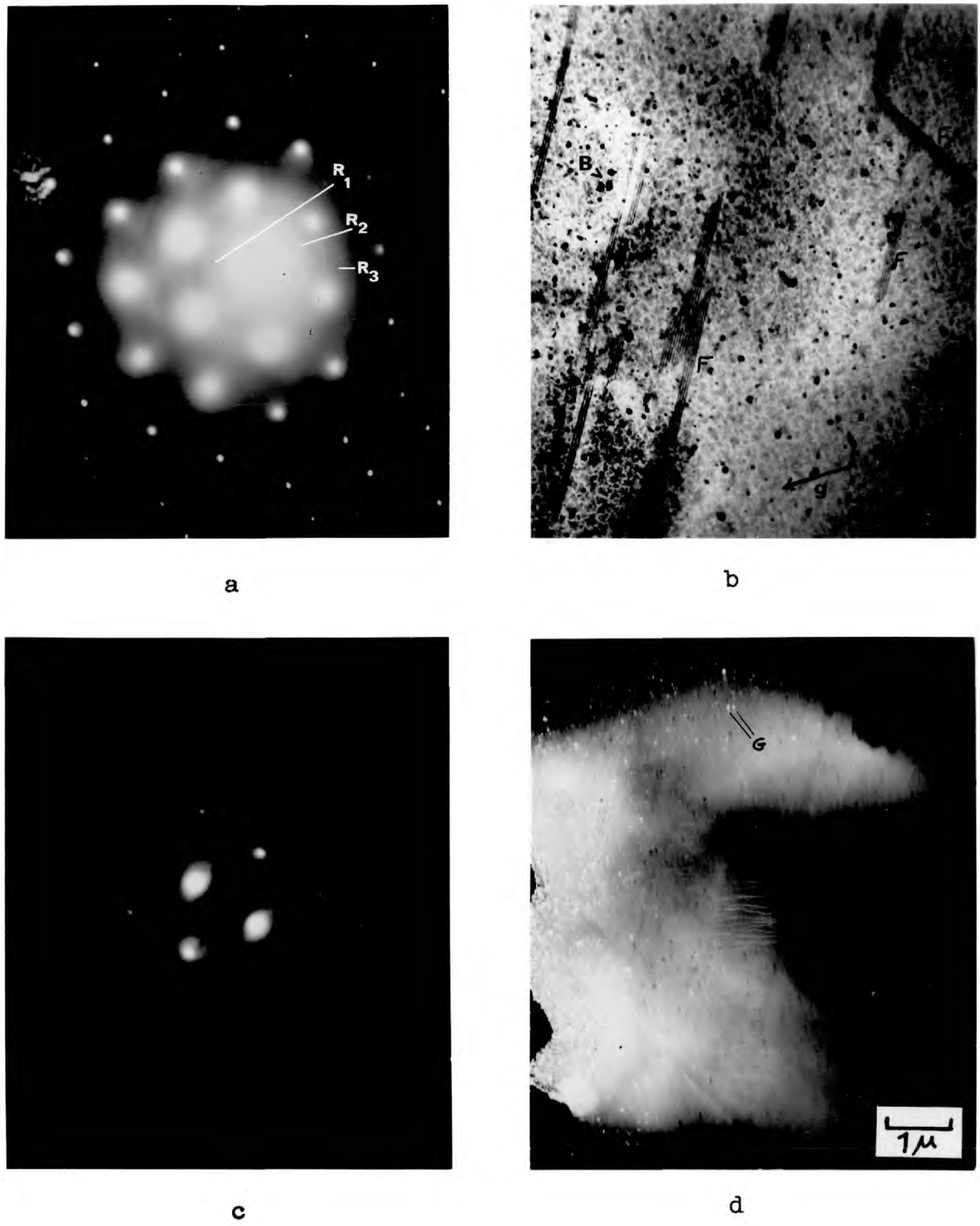
From measurements of the diffraction pattern, we have:

Diameter of Ring R_1 1.1 cms

Diameter of Ring R_2 1.2 cms

Diameter of $\{\bar{2}20\}$ diffraction spot circle 1.8 cms

Diameter of $\{\bar{4}22\}$ diffraction spot circle 3.1 cms



a b

c d

FIG. (4.15) TRANSMISSION MICROGRAPHS OF A LAYER GROWN AT 700° C; 0.14 μ $min.^{-1}$

a. GENERAL AREA DIFFRACTION PATTERN

b. BRIGHT FIELD MICROGRAPH

c. SELECTED AREA DIFFRACTION PATTERN OF AREA b.

d. D.F. MICROGRAPH TAKEN ON RING R_2, IN a.

Using the equation derived in section $R_{hkl} \cdot d_{hkl} = \lambda L$; the radius of the $\{\bar{2}20\}$ spot circle; and the lattice constant of silicon 5.43Å, we have

$$\lambda L = \frac{R\bar{2}20 \quad 5.43}{\sqrt{2^2 + \bar{2}^2 + 0^2}}$$

Using this value of λL, the silicon $\{111\}$ diffraction ring radius was calculated to be 0.61 cms, this value is in agfeement with the measured radius of R_2; 0.6 cms. The radius of R_1 is measured as 0.55 cms, this value is close to the radial distance of diffraction spots of the form $\frac{1}{3}\{\bar{4}22\}$, which is calculated to be 0.52 cms; using the value of λL given above. The spots of the form $\frac{1}{3}\{\bar{4}22\}$, could be produced by double diffraction at double positioned twin boundaries as was discussed earlier.

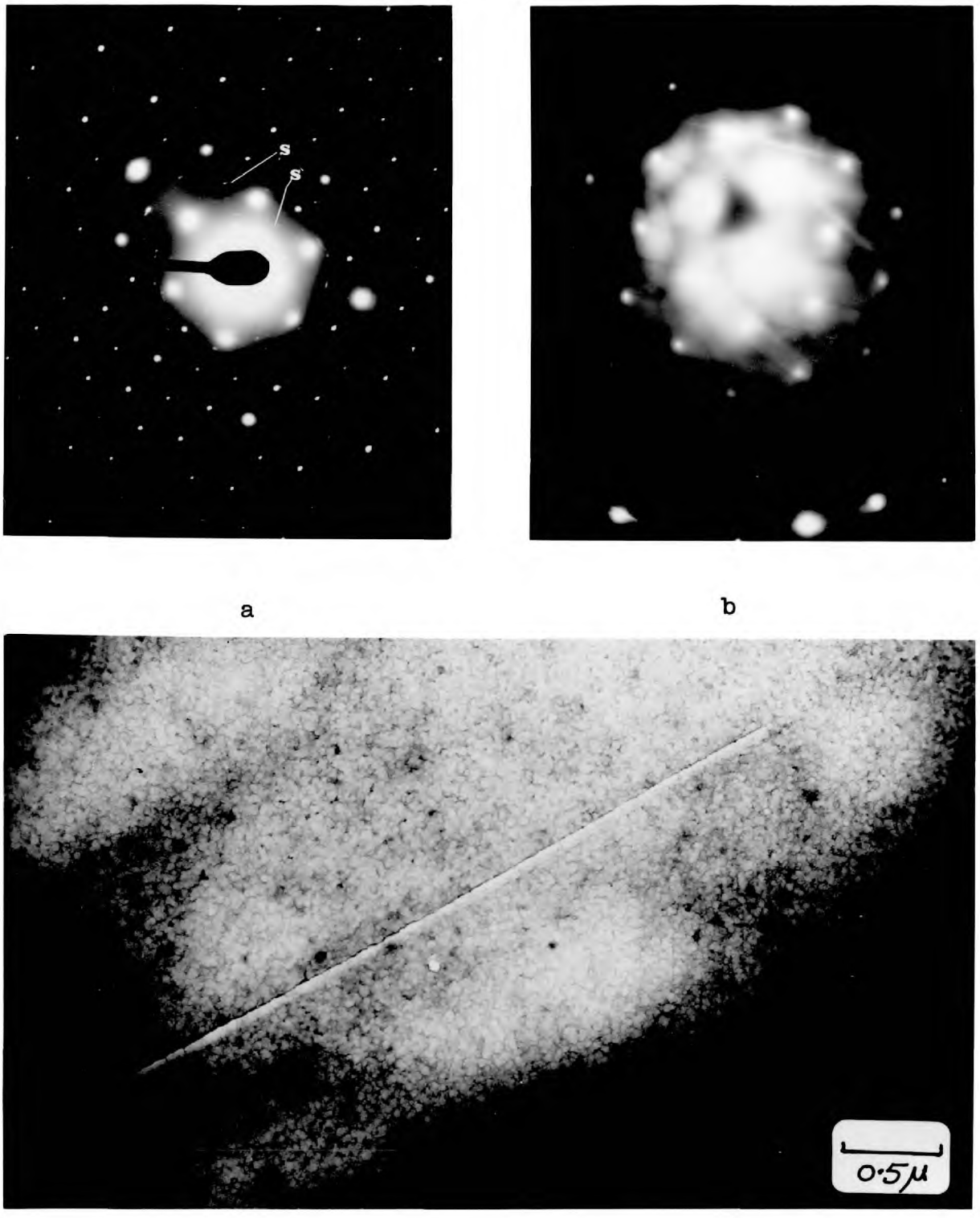
In this case the existence of a ring in this position may indicate the presence of grains which are in double positioned arrangement with respect to the matrix.

The presence of polycrystaline material indicated by the rings R_1, R_2, R_3 discussed above, is confirmed by the dark field micrograph fig. (4.15c) taken on ring R_2. It shows the polycrystalline material G in bright contrast. The edge region of the foil is also in bright contrast due to the spiking through of the $\{111\}$ reciprocal lattice points.

Fig (4.15b), a bright field micrograph, shows the presence of stacking faults and a distribution of granular regions. The stacking fault defects indicated at F are usually only found in relatively Good quality epitaxial material. The small black 'blobs' visible in this micrograph were due to contamination during the preparation of this specimen.

The coexistance of the ring diffraction pattern and kikuchi lines in the micrograph taken from the same specimen, can be interpreted as indicating the presence of polycrystalline regions in an essentially well-oriented single crystal matrix.

Fig. (4.16) shows micrographs of a layer deposited at the rate of 0.1μ per minute at a substrate temperature of 700°C. The ring structures seen in fig. (4.15a) have given way to fine arced streaks



a

b

c

FIG. (4.16) TRANSMISSION MICROGRAPHS OF A PORTION OF A LAYER GROWN AT 700° C; 0.1μ min.$^{-1}$

a. GENERAL AREA DIFFRACTION PATTERN

b. SELECTED AREA DIFFRACTION PATTERN OF AREA IN c.

c. BRIGHT FIELD MICROGRAPH

indicated at S, some of which pass through the $\frac{1}{3}(\bar{4}22)$ points. The centre spot is again seen to be surrounded by a broad halo and traces of diffuse halos are also seen round the $\{2\bar{2}0\}$ and $\{\bar{4}22\}$ matrix spots. The halos, are less prominent than those seen in fig. (4.15a).

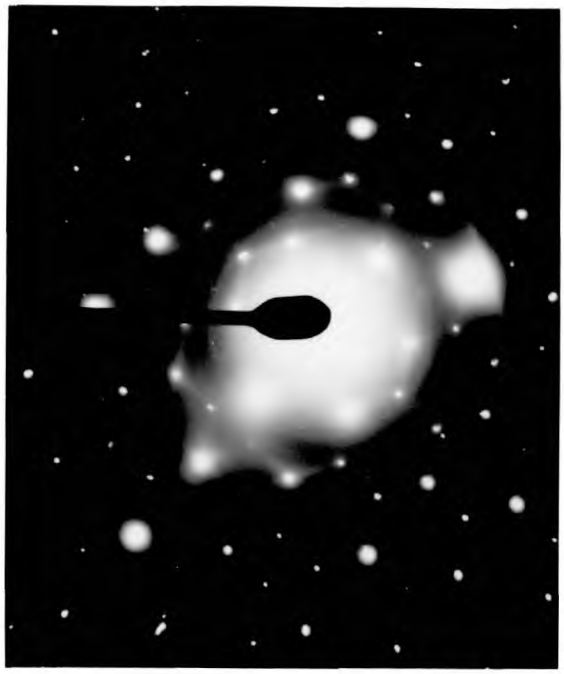
The bright field micrograph fig. (4.16c) shows a microstructure similar to fig. (4.4c). The selected area diffraction pattern in fig. (4.16b) shows prominent Kikuchi lines.

Fig. (4.17) shows micrographs and a diffraction pattern of a layer deposited at 0.15μ per minute at 850°C. The granular background can still be seen, though it is less prominent than fig. (4.16b). In fig. (4.17b) thickness extinction fringes are seen at the edge of the foil. The granular background is seen as bright contrast areas on the dark fringes.

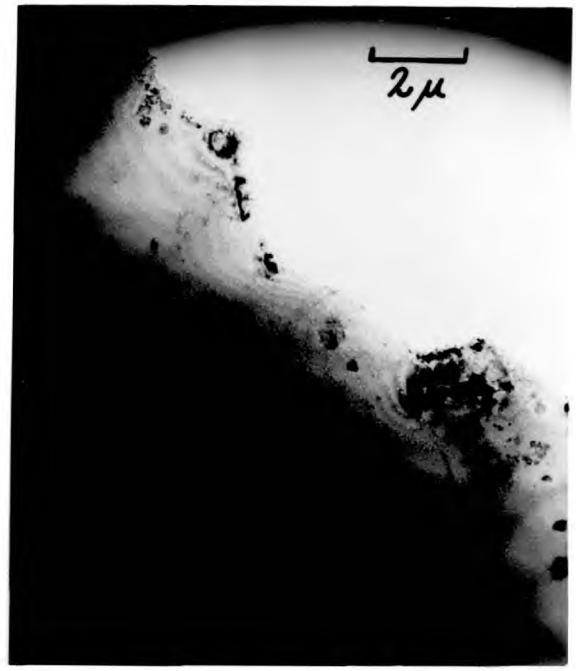
The diffraction pattern fig. (4.17a) shows a broad halo surrounding the centre spot, and a diffuse halo can also be seen running through the $\{\bar{2}20\}$ and $\{\bar{4}22\}$ spots.

The diffraction pattern also shows streaking in <110> directions which may be due to the presence of stacking faults or the associated lattice strain. Fig. (4.17c,d) is a stereo-pair of a region near the edge of the foil. From the stereo-pair, it is seen that the small bright-contrast regions are distributed throughout the entire foil thickness.

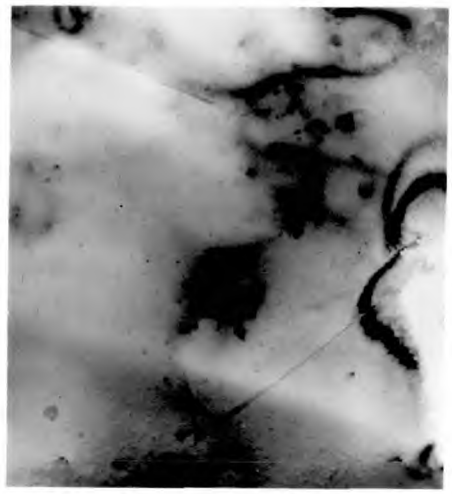
Fig. (4.18) shows micrographs of a layer deposited at 900°C and 0.2μ per minute. The diffraction pattern shows no trace of ring structure. The bright field micrograph fig. (4.18b) shows a similar microstructure to fig. (4.16b). Fig. (4.18d) shows part of the region in fig. (4.18b) at higher magnification; from this the regions are seen to have diameters of the order 300Å. In fig. (4.18b) strong contrast variation is seen on either side of the stacking fault at P and Q. Along the line of the stacking fault, the foil is in an exact two-beam condition as shown by the selected area diffraction pattern, fig. (4.18c). On either side curvature of the foil causes departure from the exact Bragg condition, and the bright contrast of the micro-regions at P reverses to dark contrast at Q. A contrast variation similar to that observed in fig. (4.17c) is seen at the



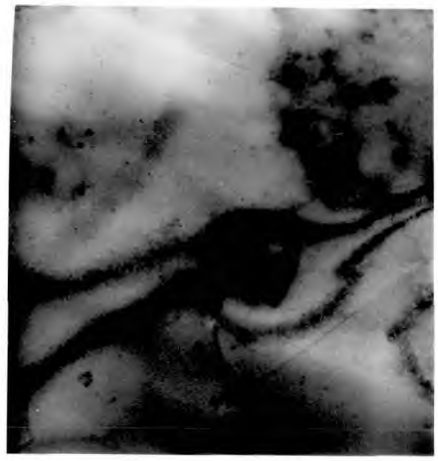
a



b



c



d

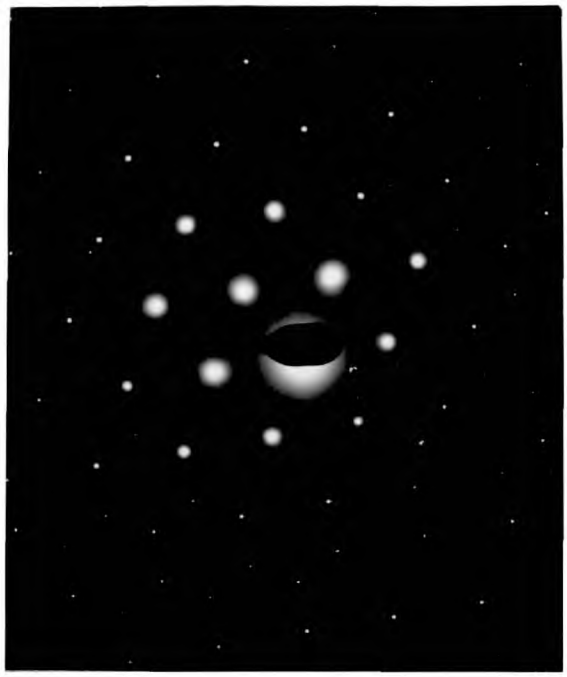
1μ

FIG. (4.17) TRANSMISSION MICROGRAPHS OF A LAYER GROWN AT 850° C; 0.15μ $min.^{-1}$

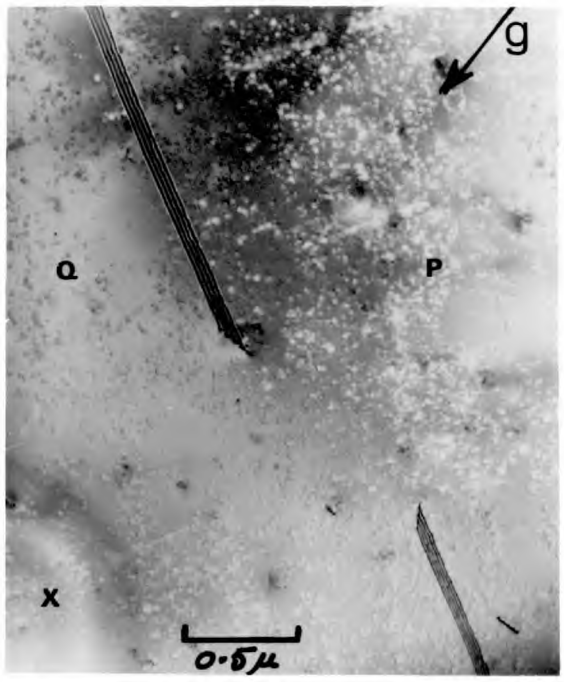
a. GENERAL AREA DIFFRACTION PATTERN

b. BRIGHT FIELD IMAGE OF THE EDGE OF THE THINNED AREA

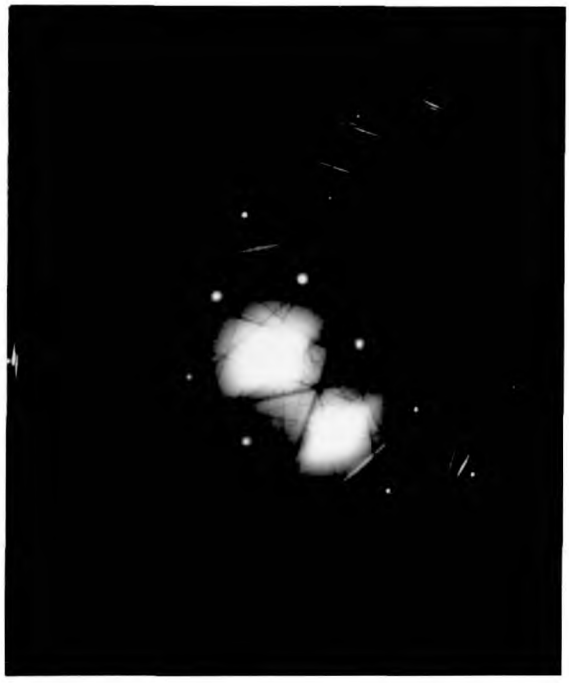
c.
d. } STEREO-PAIR OF PART OF THE LAYER



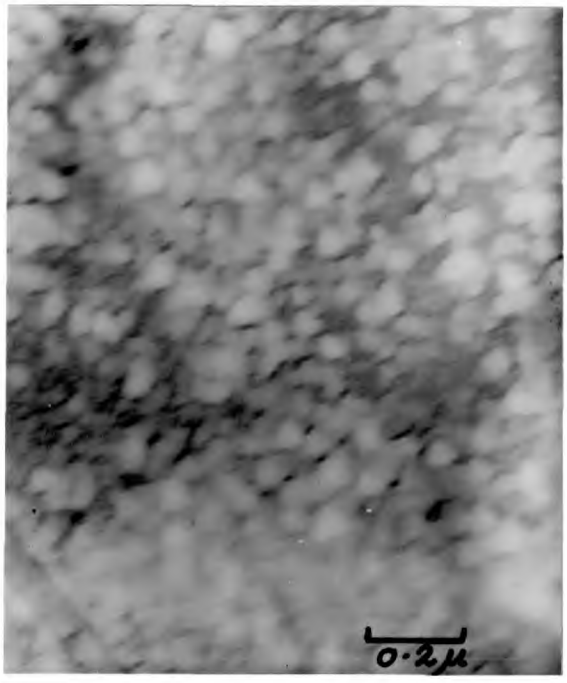
a



b



c



d

FIG. (4.18) TRANSMISSION MICROGRAPHS OF A LAYER GROWN AT 900° C; 0.2 μ $min.^{-1}$

a. GENERAL AREA DIFFRACTION PATTERN

b. BRIGHT FIELD MICROGRAPH

c. SELECTED AREA DIFFRACTION PATTERN OF b.

d. PORTION OF AREA SHOWN IN b. AT HIGHER MAGNIFICATION

thickness contours produced by the locally thin region at X in fig. (4.18b).

In contrast to the background structure seen in figs. (4.16) (4.17) and (4.18), fig. (4.8c) shows a micrograph of a layer grown at 1000°C; 0.04μ per minute. It is seen that the background is similar to that in fig. (4.6). Though the black spots are still present, the density is much less than in fig. (4.7) but a number of < 112 > oriented line defects is seen.

From these results it is seen that for layers grown at deposition rates > 0.1μ per minute, the bright field micrographs show a contrast variation which has the form of a granulated appearance. For growth rates $\leq$ 0.1μ per minute the layer has large numbers of black spot defects, as can be seen in fig. (4.18a,e); and there is no granular structure in evidence.

It is also seen that the density of black spots varies with the deposition rate.

4.4.(2) Contrast Effects Observed in the Background Defects

From the previous results of variation of defect content with growth parameters it is seen that we may subdivide the layers of group II into two sub-groups, viz:

IIa: those layers grown at deposition rates $\gtrapprox$ 0.1μ per minute

IIb: those grown at deposition rates $\lesssim$ 0.1μ per minute.

Group IIa. Films grown at deposition rates > 0.1μ microns per minute

From figs. (4.17) and (4.18) the main contrast effect observed is the contrast reversal of the small regions across extinction contours. In Fig. (4.17) the contrast reversal occurs across a bend extinction contour, and in fig. (4.18) the change in contrast can be seen at the thickness fringes at the edge of the foil. This form of contrast variation is termed structure factor contrast, and was originally observed in specimens containing precipitates of a different phase or structure.

Structure factor contrast effects were investigated by Ashby and Brown (1963), who showed that if an inclusion of thickness dt and extinction distance Eg^i is in a foil of thickness t, then the net effect is to increase the effective foil thickness by the amount $dt.\left[\frac{Eg - Eg^i}{EgEg^i}\right]$ where Eg is the extinction distance of the matrix.

From Hirsch et al (1965), this change in effective thickness gives rise to a change in diffracted intensity of dI, which for an exact two-beam diffracting condition is given by the equation

$$dI = -2\pi dt\left[\frac{Eg - Eg^i}{Eg.Eg^i}\right] \operatorname{Sin}\left(\frac{\pi t}{Eg}\right). \operatorname{Cos}\left(\frac{\pi t}{Eg}\right) \qquad 4.4.(1)$$

where dt is $\ll Eg$.

At the two-beam diffracting condition, the intensity variation dI is independent of the position of the inclusion in the foil.

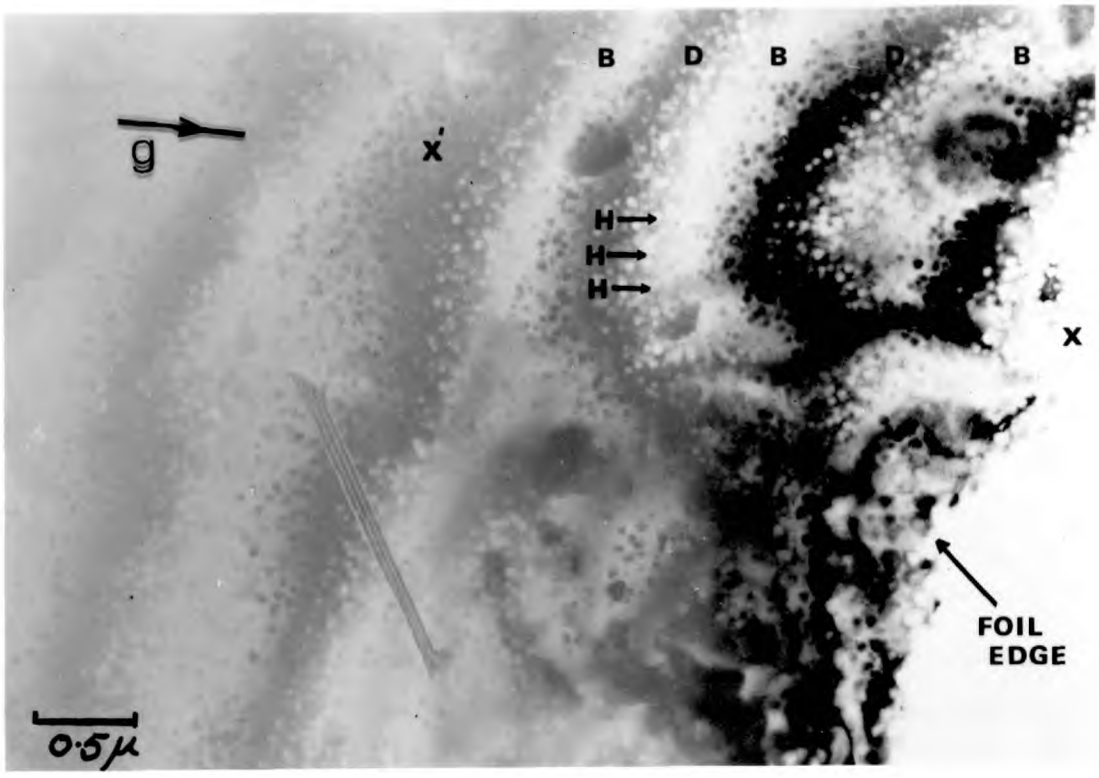
For deviations from the exact Bragg condition, the contrast observed will vary with the position of the inclusion within the foil. Fig. (4.19a) shows a region of the edge of the foil shown in fig. (4.17b) at higher magnification, it can be seen that there are small regions, H, in bright contrast on that side of the dark fringe which is towards the edge of the foil.

At a bright fringe, the foil thickness t, is an integral number of extinction distances, ie. $t = nEg$. Then for the two adjacent dark fringes, $t = (n \pm \frac{1}{2})Eg$.

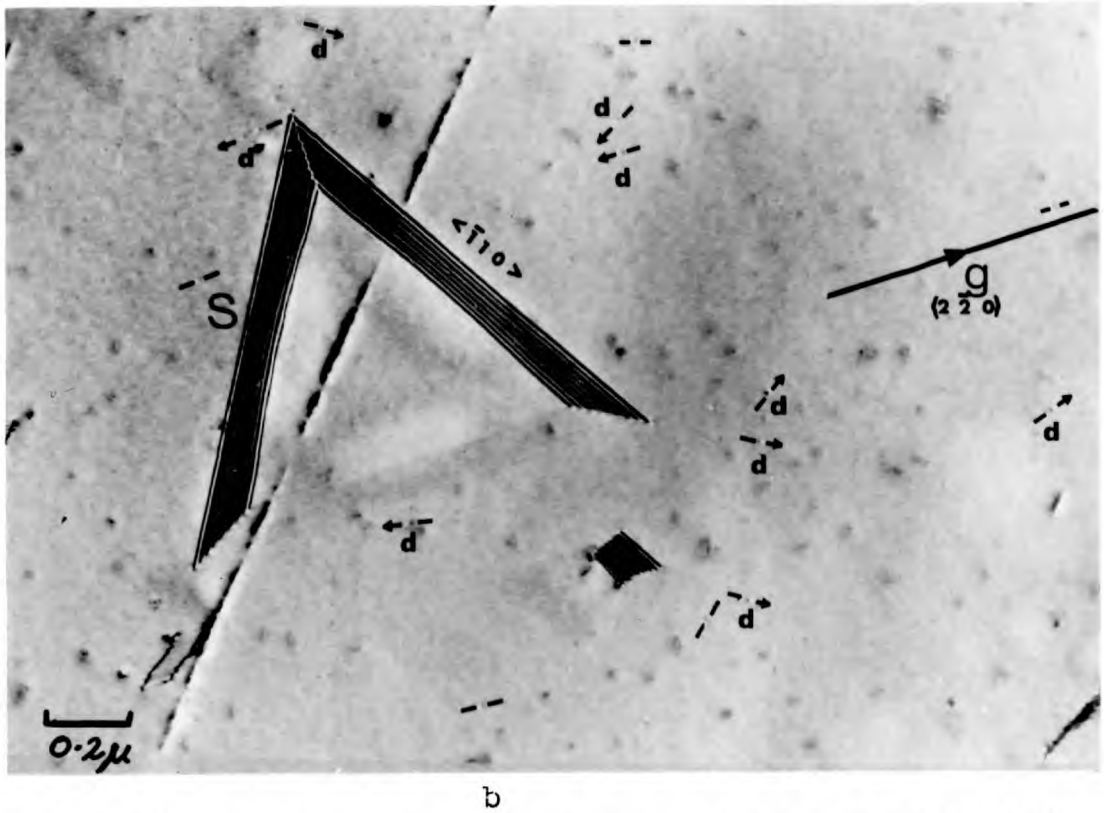
From the equation for dI given above, it is seen that dI varies with t. For $t = \frac{Eg}{4}; \frac{3\,Eg}{4}; \frac{5\,Eg}{4}$; ie. $t = \frac{(2n + 1)Eg}{4}$.

$|dI|$ is a maximum.

In the direction of increasing foil thickness, ie. X to X, in fig. (4.19a) the foil thickness increases from nEg at a bright fringe to $(n + \frac{1}{2})Eg$ at the adjacent dark fringe. It is seen that the regions indicated at H, are at positions corresponding approximately to foil thicknesses of $(n + \frac{1}{4})Eg$. ie. $(n + \frac{1}{2})Eg > t_H > nEg$; where t_H is the foil thickness at the regions H.



a



b

FIG. (4.19) a. TRANSMISSION MICROGRAPH OF THE FOIL EDGE SHOWN IN FIG. (4.17b).
THICKNESS EXTINCTION CONTOURS ARE INDICATED: B = BRIGHT FRINGE, D = DARK FRINGE. H INDICATES REGIONS IN BRIGHT CONTRAST; g IS THE OPERATING DIFFRACTION VECTOR

b. TRANSMISSION MICROGRAPH OF A LAYER DEPOSITED AT 800° C; 0.05 μ $min.^{-1}$. g IS THE DIFFRACTION VECTOR; d IS THE CONTRAST VECTOR OF THE BLACK SPOT DEFECTS.

Since the regions H are in bright contrast; dI is positive; thus in the equation quoted above, Eg^i must be greater than Eg. Since equation 4.4(1)i can be written as

$$dI = -\pi dt\left[\frac{Eg - Eg^i}{Eg\,Eg^i}\right] . \operatorname{Sin}\left(\frac{2\pi t}{Eg}\right)$$

and for $t = (n + \frac{1}{4})Eg$, with integral n

$$\operatorname{Sin}\left(\frac{2\pi t}{Eg}\right) = +1.$$

Thus from this result it is seen that the small regions have a different structure factor to the silicon matrix material and the extinction distance of this structure is greater than that of silicon.

Group IIb: Films grown at deposition rates < 0.1 microns per minute

In general the prevalent background defect, the large black spots, did not show any strong variation with different g vectors, as can be seen from figs. (4.5) and (4.13). However, in many cases very small black dots giving strong contrast effects were observed.

Fig. (4.19b) is a micrograph of part of a layer grown at 800°C at 0.05μ per minute. As can be seen, there are large numbers of small spots, showing strong contrast effects. The direction of the acting g vector is given by the line of the out of contrast side of the stacking fault, S.

The black spot contrast vector, d, is defined as the direction of the black to white contrast as indicated in fig. (4.19b). As can be seen, whilst several of the d vectors lie parallel (or anti-parallel) to g, the operating diffraction vector, the majority are at an angle of approximately 30° to the line of g.

4.5. Nucleation and Growth.

4.5.(1) Investigation of the effects of the thermal treatment on the Substrate Surface

The predeposition cleaning process involved rapidly heating the chemically polished substrate to 1200°C for 20 seconds, then reducing

the temperature to that of the deposition. The pressure changes observed during the heating of substrates were investigated with the mass-spectrometer. The results obtained are shown diagrammatically in fig. (4.20), which shows the behaviour of the peak found at $[\frac{m}{e}] = 44$. It is seen that the "44 peak" rises and falls during a period less than the total duration of the heat treatment given. It was also found that the hydrogen peak increased rapidly during the heating.

In order to investigate these processes in more detail, a substrate was heated slowly from room temperature to 1200°C. over a period of five minutes. It was found that both the "44" peak and the hydrogen peak began to increase rapidly at substrate temperatures of approximately 800°C. These experiments using both rapid heating and slow heating were repeated on a substrate which had been oxidised to produce a layer of oxide $\simeq 1\mu$ thick. In this case no increase in the 44 or hydrogen peaks was observed.

The oxidised substrate was also held at 1200°C for five minutes, during which period no rapid increase of any peak heights was observed. On recovering the oxidised slice, it was found that the oxide layer was still present.

Fig. (4.21) shows micrographs and diffraction patterns of surface regions of chemically polished substrates which have been thermally processed as follows. Fig. (4.21a,b,c) shows the micrographs and diffraction patterns of an area in the mask-zone, [see fig. (3.10)] which had been heated to 1200°C for 20 seconds, then held at 800°C for 30 mins. Fig. (4.21 d,e) shows micrographs and diffraction patterns of a region of substrate which had been heated to 800°C for 30 mins. The vacuum in both cases was of the order $6 - 8\ 10^{-8}$ torr.

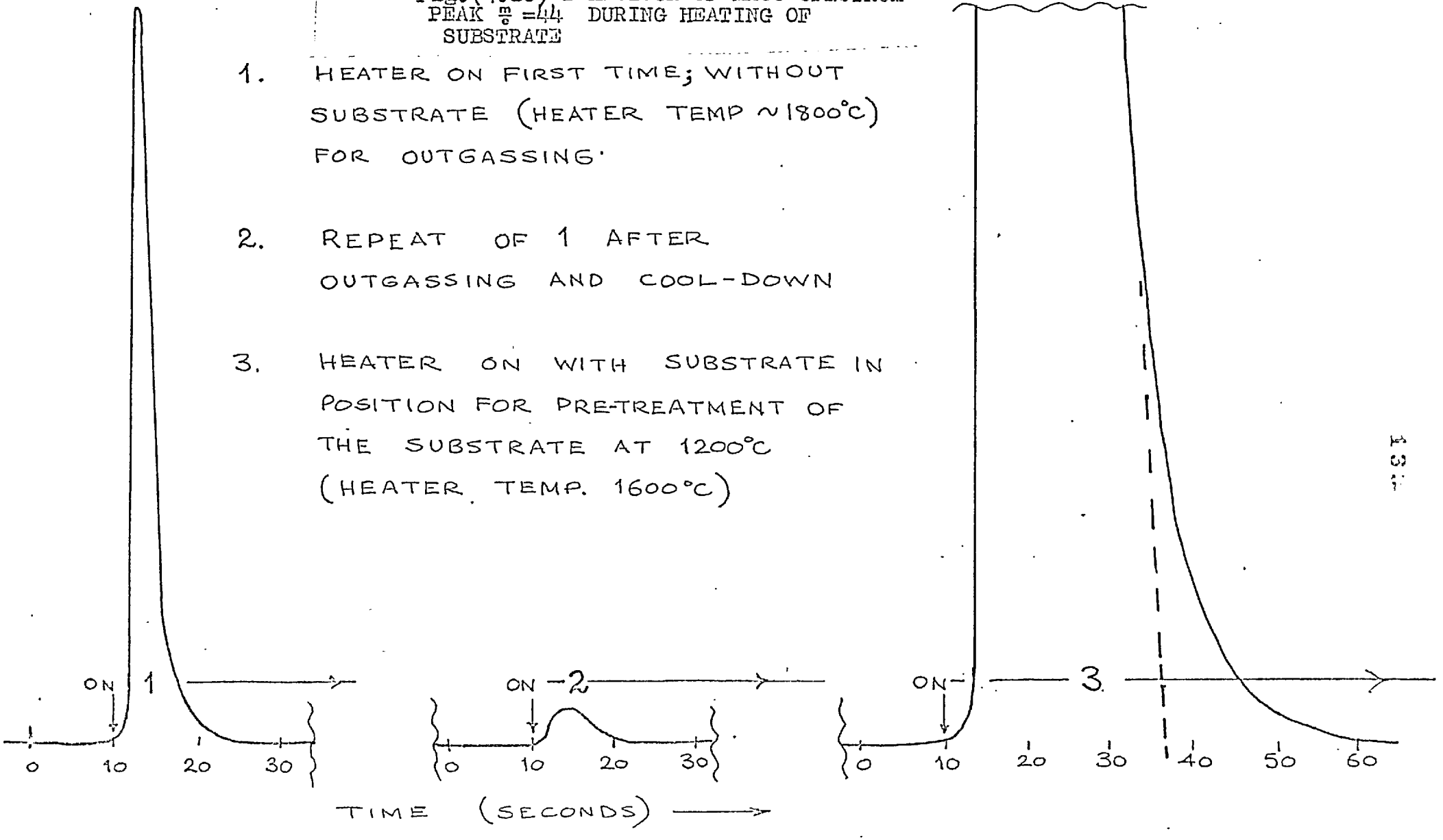
In the diffraction pattern fig. (4.21c) extra spots are visible indicated at x and y. They lie along $< \bar{1}10 >$ directions. Measurements from the plate showed that the $\{2\bar{2}0\}$ silicon diffraction spots lie at a radius of 1.00 cms from the undiffracted beam and the spots x and y lie at a radius of ~ 1.25 cms. From the equation derived in section (1.3(4)we have $R_1 d_2 = R_2 d_2 = \lambda L$. Then $d_x \simeq \frac{1.00.5.43}{1.25\sqrt{8}}$;

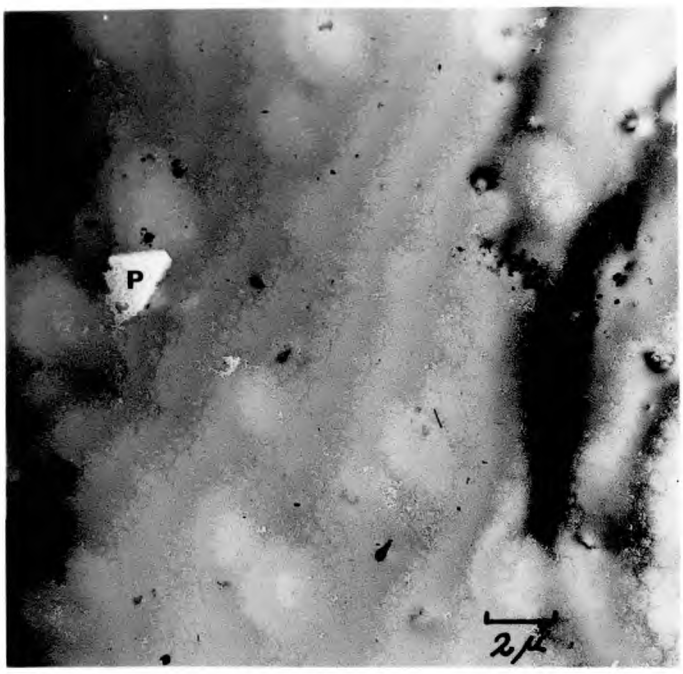
Fig. (4.20) BEHAVIOUR OF MASS SPECTRUM PEAK $\frac{m}{e}$ =44 DURING HEATING OF SUBSTRATE

1. HEATER ON FIRST TIME; WITHOUT SUBSTRATE (HEATER TEMP ~1800°C) FOR OUTGASSING.

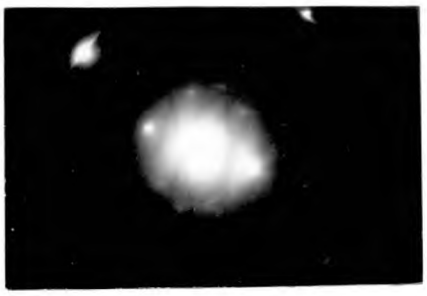
2. REPEAT OF 1 AFTER OUTGASSING AND COOL-DOWN

3. HEATER ON WITH SUBSTRATE IN POSITION FOR PRE-TREATMENT OF THE SUBSTRATE AT 1200°C (HEATER TEMP. 1600°C)





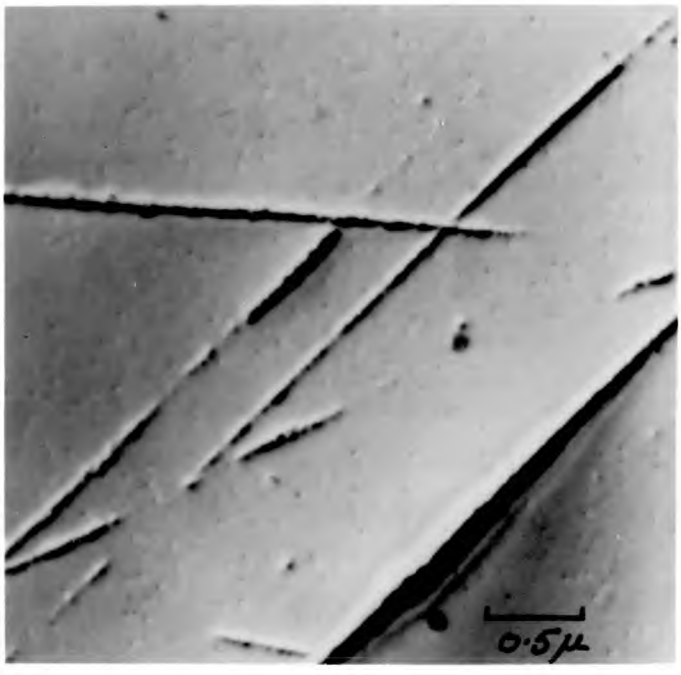
a



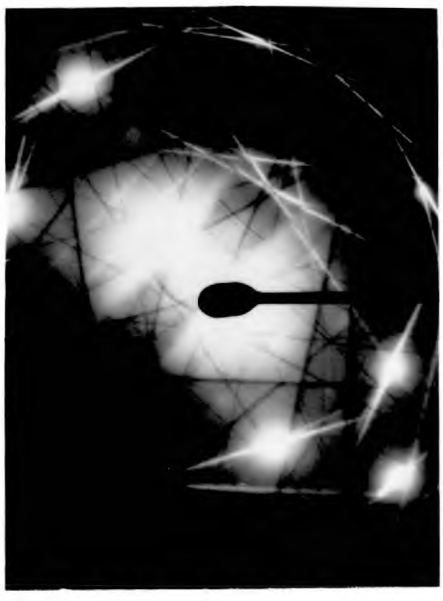
b



c



d



e

FIG. (4.21)

a. TRANSMISSION MICROGRAPH OF AN AREA IN THE MASK ZONE

b. SELECTED AREA DIFFRACTION PATTERN OF THE ETCH-PIT INTERIOR

c. SELECTED AREA DIFFRACTION PATTERN OF AREA AROUND THE ETCH-PIT *p*

d. TRANSMISSION MICROGRAPH OF AREA OF SUBSTRATE HEATED TO 800° C

e. SELECTED AREA DIFFRACTION PATTERN OF AREA IN d.

where d_x is the inter-planar spacing of the material responsible for the diffraction spots x, y. Thus $d_x \simeq 1.81$Å. This value is in good agreement with the $\{220\}$ interplanar spacing of β silicon carbode, for which the value 1.82Å is given by Toombs et al (1965).

From this result it may be concluded that silicon carbide is present on the surface of the specimen which had been heated to 1200°C. From the orientation of the carbide diffraction pattern it appears that it is crystalline and epitaxial on the (111) silicon surface. From fig. (4.21b) it is seen that the etch pit interior is relatively free from silicon carbide since the additional spots do not appear in the selected area diffraction pattern of the interior of the etch pits.

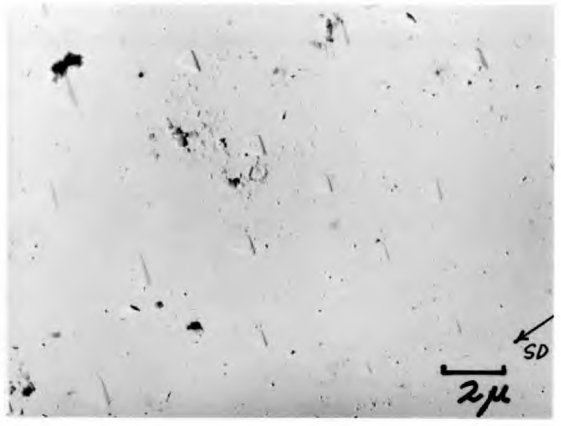
4.5.(2) Nucleation and Growth

Fig. (4.22) shows a series of replica micrographs of the nucleation zone of a layer deposited at 800°C at a pressure of 10^{-6} torr. S.D. indicates the replica shadowing direction. The nuclei are seen to be well oriented triangular pyramids, with one edge blended into the substrate surface. The edges were found to be oriented along $< 1\bar{1}0 >$ directions and the apices in $< 211 >$ directions in the (111) plane. Fig. (4.23a) shows that the faceting on the highest apex of some of the nuclei indicated in the figure at P is similar to that seen in the etch pits at P, shown in Fig. (4.23b).

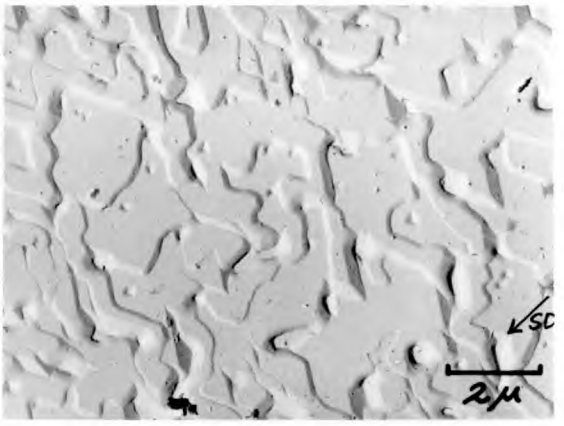
The transmission micrographs of the etch pits shown in fig. (4.23b) were taken under kinematic, ie. "many beam", diffracting conditions, to produce a better pit-shape delineation by the fringes, since the etch pits are very shallow.

The tilt of the nuclei relative to the substrate surface can be estimated from the transmission micrographs in fig. (4.24 a,b,c). These micrographs were taken from the same specimen as the replica micrographs of fig. (4.22) and are of similar; though not identical areas of the nucleation zone.

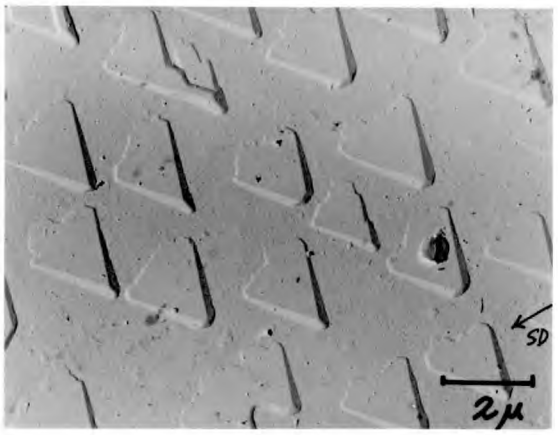
These micrographs show the nuclei in two-beam diffracting conditions; the thickness extinction contour fringes are clearly visible at t_1; t_2.



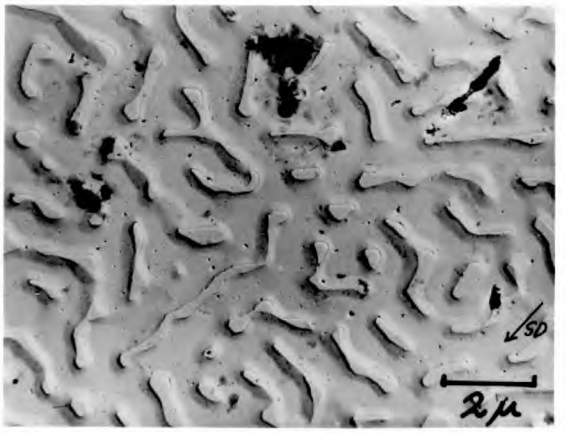
a



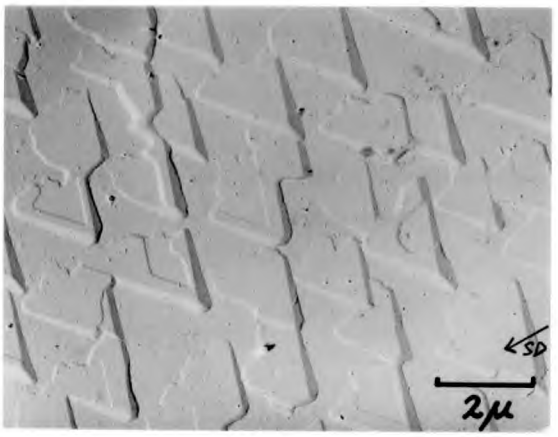
e



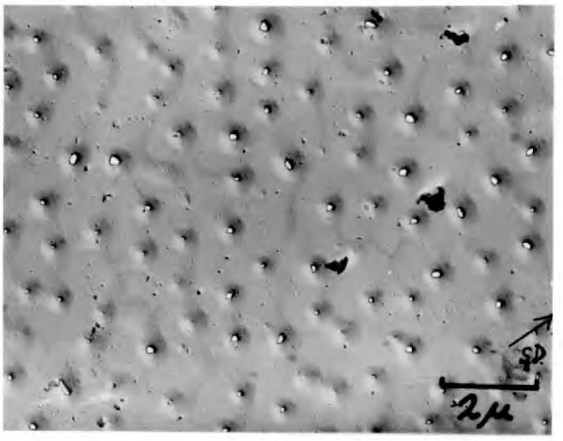
b



f



c



g

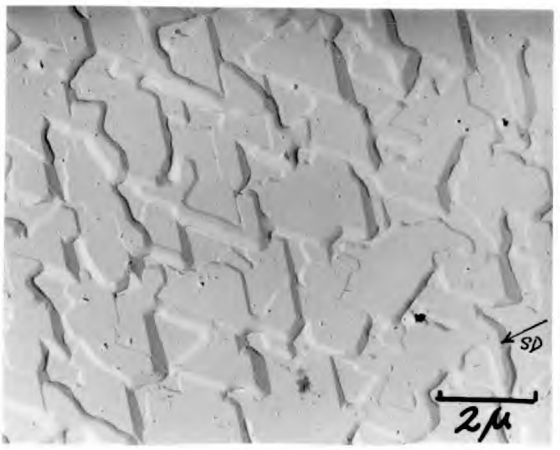
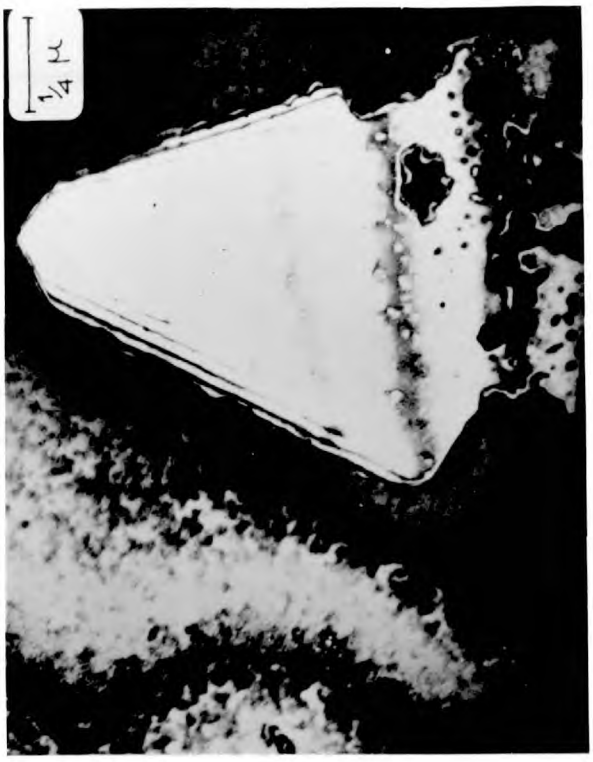
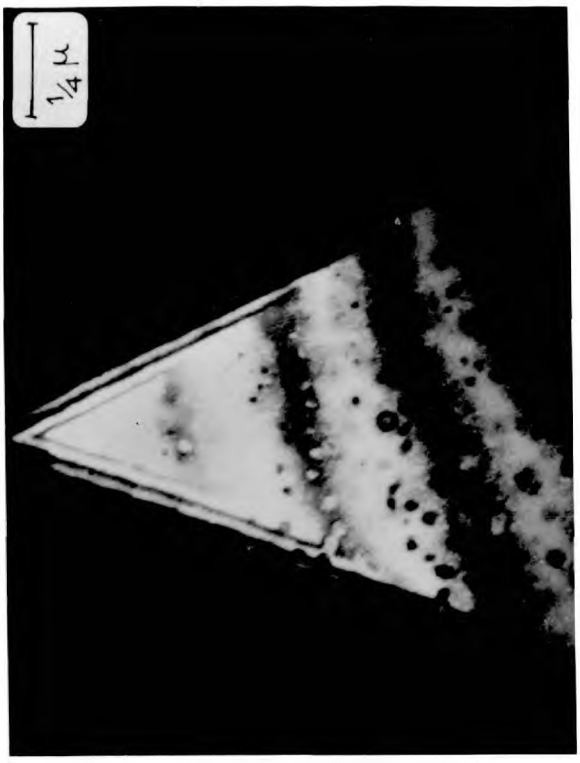


FIG. (4.22) a,b,c,d,e,f,g IS A SERIES OF REPLICA MICROGRAPHS OF REGIONS IN THE NUCLEATION ZONE OF A LAYER DEPOSITED AT A SUBSTRATE TEMPERATURE OF 800^{0} C AT A PRESSURE OF 1×10^{-6} TORR.

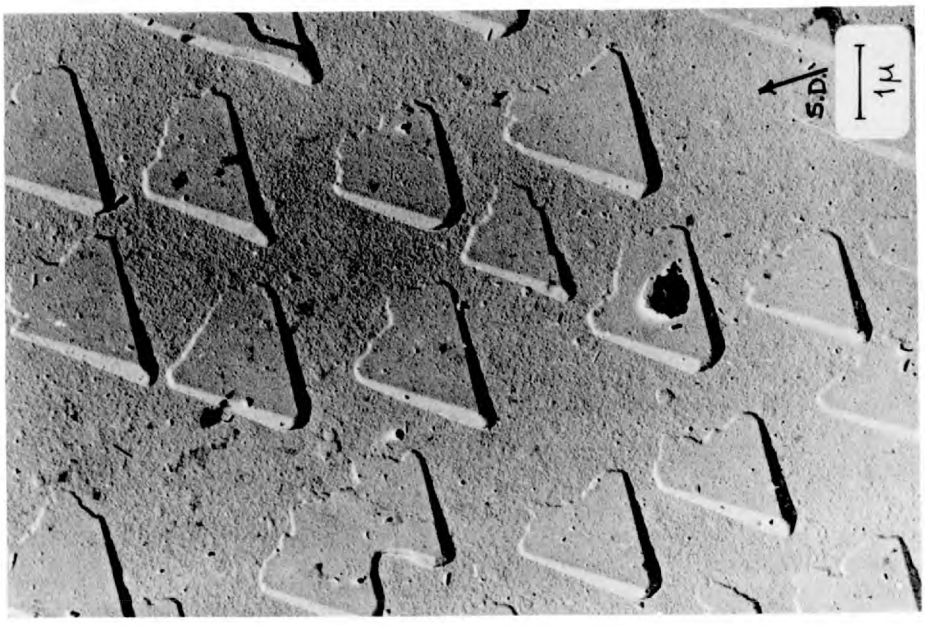
S.D. INDICATES THE SHADOWING DIRECTION



b



c



a

FIG. (4.23) MICROGRAPHS ILLUSTRATING THE MORPHOLOGY OF ETCH PITS AND NUCLEI

a. REPLICA MICROGRAPH OF THE NUCLEI

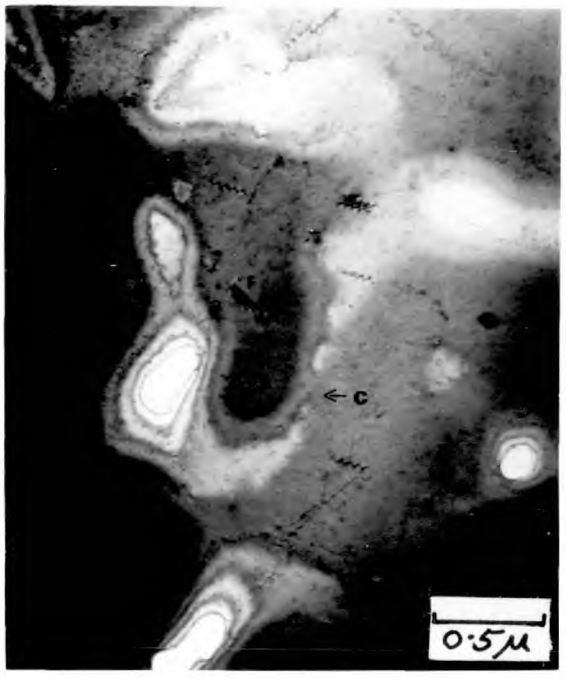
b.) TRANSMISSION MICROGRAPHS OF ETCH PITS IN THE MASK ZONE
c.)



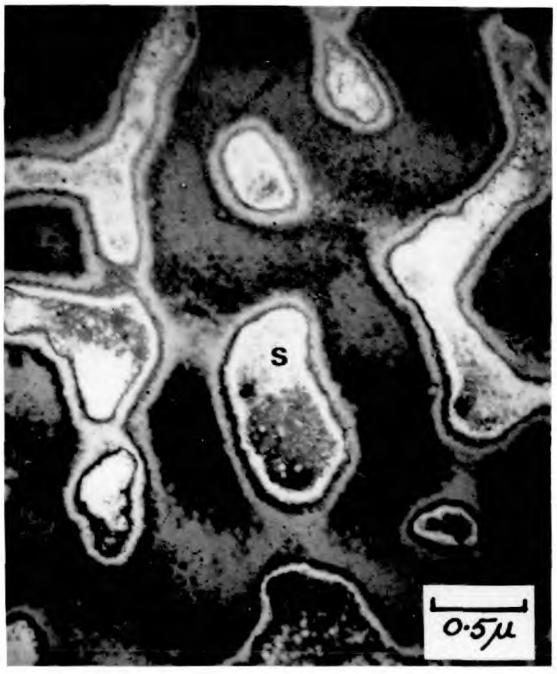
a



b



c

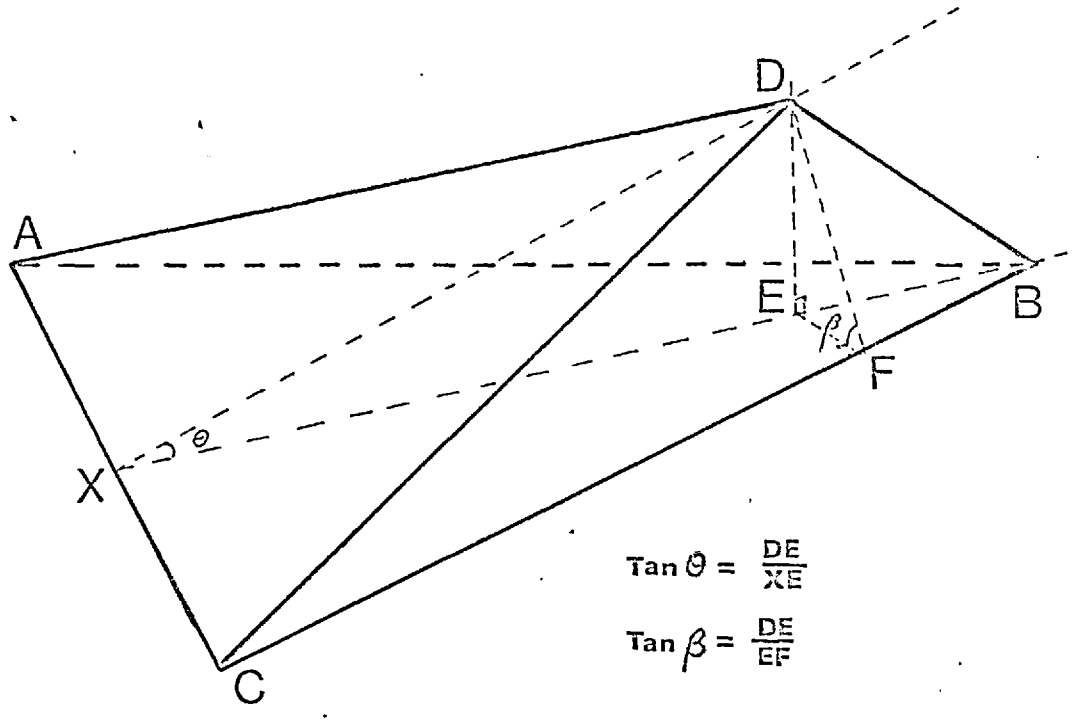


d

FIG. (4.24)

a, b, c TRANSMISSION MICROGRAPHS OF REGIONS IN THE NUCLEATION ZONE, SHOWN AS REPLICA MICROGRAPHS IN FIG. (4.22)

d TRANSMISSION MICROGRAPH OF THE INITIAL COALESCENCE STAGE OF THE NUCLEATION ZONE SHOWN IN FIG. (4.26)



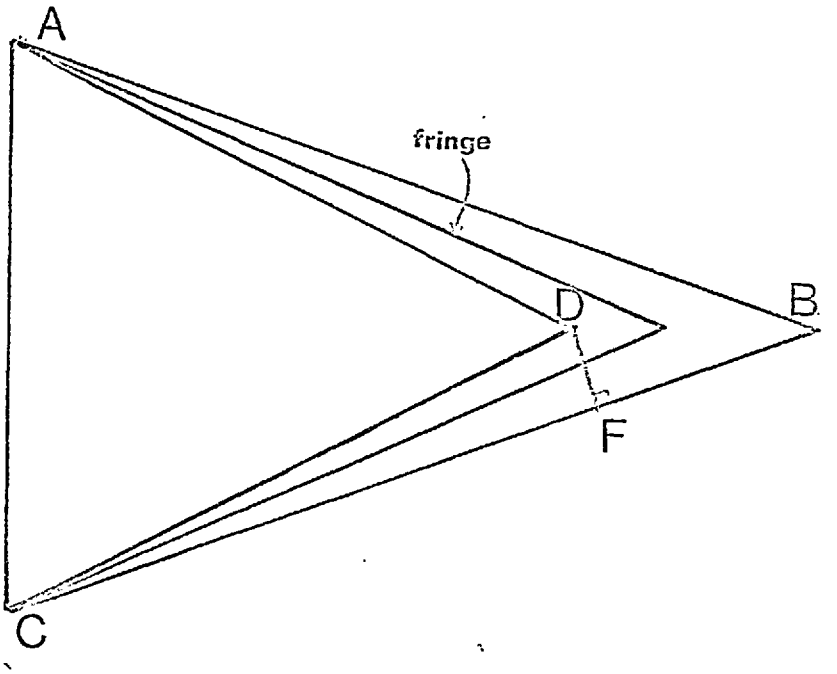


Fig. (4.25)
DIAGRAM SHOWING THE THREE DIMENSIONAL GEOMETRY OF THE GROWTH ISLANDS SHOWN IN THE TRANSMISSION MICROGRAPHS FIGS (4.22) (4.24b)

The fringes also indicate the overall flatness of the top-faces of the nuclei. Using a $\{2\bar{2}0\}$ type reflection, the extinction distance for silicon is 750Å. Thus the tilt angle can be found from the geometry, shown in fig. (4.25).

The value obtained for the tilt of the top face of the nuclei relative to the substrate surface is approximately 3°. The inclination of the side faces of the pyramids can also be found from the geometry of fig. (4.25). The value found is 30° to the substrate surface.

The main source of uncertainty in these values is the plate magnification errors. The magnifications of the plates were deduced from measurements of the image lengths of faults of characteristic length l_D, together with measurements of the thickness of the layer.

The values of inclinations of the side faces of the nuclei to the substrate surface are close to the value of the angle between a $\{111\}$ plane and a $\{311\}$ plane. This indicates that these faces may be $\{311\}$ type planes. This is in accord with the observations of Joyce et al (1967) on the morphology of the growth nuclei observed on (111) oriented substrates.

The value found for the tilt angle of the top faces of the nuclei suggests that the nuclei were in exact (111) orientation, since the substrate surface is missoriented by up to $3\frac{1}{2}^{\circ}$ from the [111] as supplied by the manufacturer.

The etch pits shown in fig. (4.23) confirm that the surface was tilted from an exact crystal orientation.

From fig. (4.22c and d) it can be seen that the nuclei increase in size, whilst maintaining the tilted orientation relative to the substrate. When the nuclei grew large enough to touch, coalescence occurred. The coalescing process appeared to have involved the flow of material between the nuclei so as to produce a discontinuous layer of uniform thickness whose free surface was then parallel to the substrate surface. The stages in this coalescence are shown in fig. (4.22 e,f,g). The layer thickness at the initial coalescence

stage can be estimated from the thickness fringes in fig. (4.24), which is a transmission micrograph of the coalescing nuclei taken using a $\{2\bar{2}0\}$ reflection. The number of thickness fringes at the edges of the nuclei, indicates an initial coalescence thickness of the order of 1000Å - 2000Å. This value is confirmed by the number of fringes visible in the stacking fault indicated at F in fig. (4.24c).

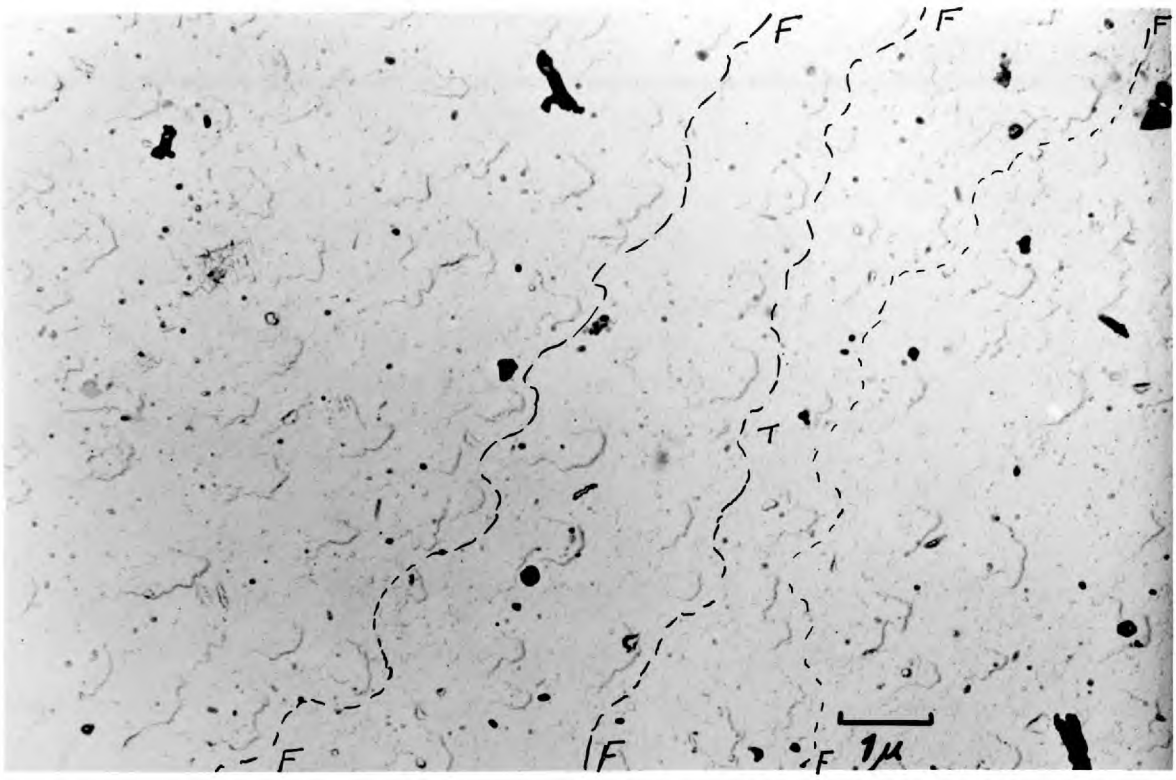
The stacking fault fringe periodicity is $\frac{Eg}{2}$. For $(\bar{2}20)$ in silicon Eg = 750Å, which yields a layer thickness value of about 1000Å.

The later stages of coalescence are shown in the replica micrographs fig. (4.22 f and g) and in transmission micrograph fig. (4.24c) where it can be seen that the layer marked L grew laterally at apparently constant thickness to fill in the bare areas of the substrate; indicated at S in the figure.

Fig. (4.26) shows a replica and a transmission micrograph of a portion of the nucleation zone of a layer grown at 800°C at a pressure of 10^{-8} torr. It can be seen that the nuclei do not have well defined crystallographic shapes, but consist of long terraced growth fronts, F. The terraces, however, show the tilt with the trailing edges, T blending into the substrate surface.

The initial coalescence height in this case was about 750Å, as estimated from the number of stacking fault fringes visible at F in fig. (4.24d).

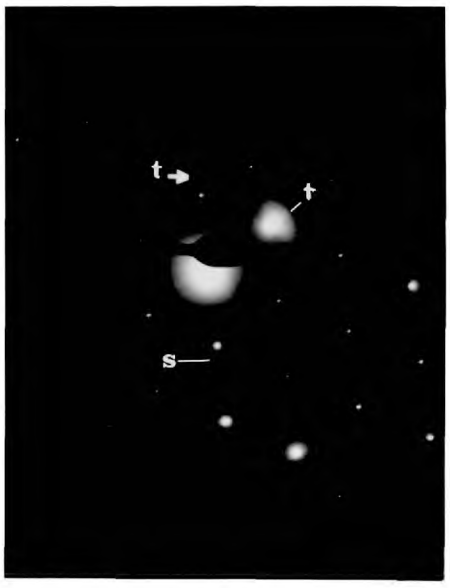
In the replica micrograph, the growth fronts can be seen to be indented; fig. (4.26) shows a transmission micrograph of an indentation. This shows the piling up of the growth front at an obstruction indicated by X in the micrograph. The selected area diffraction pattern of the area X, Fig. (4.26c), showed extra spots; indicated at S and T. The ratios of the radial distances of S, T and the $\{\bar{2}20\}$ matrix spots; from the centre spot, the same as the ratio of the $\{\bar{2}20\}$ plane spacings for silicon and silicon carbide, this suggests that the material present at X is silicon carbide. The occurance of discrete spots rather than a ring also shows the material is a single crystal and is oriented with the silicon substrate.



a



b



c

FIG. (4.26)

a. REPLICA MICROGRAPH OF A REGION OF THE NUCLEATION ZONE OF A LAYER DEPOSITED AT 800° C AT A PRESSURE OF 10^{-8} torr

b. TRANSMISSION MICROGRAPH SHOWING A PINNED GROWTH FRONT

c. SELECTED AREA DIFFRACTION OF AREA X IN b.

Chapter 5. Discussion.

5.1. General Comparisor of the results with Review Data.

From comparison between Fig. (4.1) and Table II, it is seen that the limiting values of epitaxial temperatures and rates obtained in this work are in very good agreement with those obtained by various workers cited in the review. The small differences in values of Rc and Tc observed in this work, are probably due to the higher working pressures, of the order 10^{-8} torr, as opposed to $10^{-10} \sim 10^{-9}$ torr, used by the workers cited in the review.

This close agreement is believed to be due to the very low partial pressure of oxygen present in the residual gases, in the vacuum chamber. Fig. (3.2) shows a mass-spectrum trace of the residual gases presented in the system used in the present work. The mass spectrometer used, an AEI MS 10, detects oxygen at $\frac{M}{e} = 32$, for O_2^+ (singly ionised) and $\frac{M}{e} = 16$ O^+ or O_2^{++} (doubly ionised). The 'cracking pattern' for oxygen (as given in MS10 handbook) shows that the oxygen peak height at 32 $\approx$ 10x peak height at 16. In fig. (3.2) the $[\frac{m}{e}] = 16$ peak is due entirely to methane, CH_4 and it is seen that the $[\frac{m}{e}]$ peak at 32 is indistinguishable from the background level. The noise level for the MS10 is given as 2×10^{-15} amps (MS10 Data Sheet A.5.10). The sensitivity of the MS10 for oxygen is 2.6×10^{-5} amps torr. Thus the minimum detectable pressure of oxygen is $\sim 8 \times 10^{-11}$ torr. From these observations it may be assumed that the partial pressure of oxygen in the system is $\leq 10^{-10}$ torr. This low pressure of oxygen is probably due to two effects: one is the preferential pumping of oxygen by the ion-pump and to a lesser extent by the titanium sublimation pump; the other is the possible gettering effect of the evaporated silicon on the walls of the vacuum chamber, since it was observed that the system pressure fell during depositions.

The delaterious effects of oxygen in the source were shown by the work of Weisberg (1967). In this present work, no special precautions were taken to exclude oxygen from the source; however, since the method of evaporation from a molten pool is used, any oxygen in the source is likely to be 'boiled out' during the source outgassing procedures.

The variation of epitaxial temperature with rate, shown in Fig. (4.1) is seen to be in accord with the trends discussed in the review, in that increasing the deposition rate required an increase in substrate temperature to maintain epitaxial growth.

5.1.(1) Analysis of the Relationship between the Critical Growth Parameters R_c and T_c

If we assume the epitaxial process has an activation energy q ev., then the maximum epitaxial growth rate at a temperature $T^{\circ}K$ will be given by an equation of the form $R = Ae^{-\frac{q}{kT}}$; (assuming a simple first order reaction process) where A is a constant and k is Boltzman's constant. (This form of relationship is termed an Arrhenius equation.) Thus $\log_{10} R = \log_{10} A - \frac{q}{kT} 2.303$. (The factor 2.303 comes from converting to $\log_{10}$.) A plot of $\log_{10} R$ versus $\frac{10^3}{T^{\circ}K}$ will be a straight line whose slope is $[\frac{q \times 10^{-3}}{2.303k}]$ using $k = 8.65 \times 10^{-5}$ ev, then $q = 0.198\ S$ where S is the slope. Fig. (5.1a) is a plot of log Rc versus reciprocal temperature for the data shown in Fig. (4.1). As can be seen, the graph Fig. (5.1a) consists of three straight lines, AB, BC, CD, of different slopes. These indicate different values that processes of different activation energy are occurring. The values of activation energy found from the slopes are as follows: $q_{AB} = 2.3$ ev; $q_{BC} = 0.12$ ev; $q_{CD} = 0.4$ ev.

For comparison, the UHV data of Fig. (2.8) has also been plotted in Fig. (5.1b) as the lines E, F, G, and it is seen that CD is parallel to FE (to within the plotting limits). The activation energies, q_{CD} and q_{FE} found from the slopes are 0.40 ev. and 0.41 ev; the difference is within the plotting errors of the graphs. The activation energies found from the slopes of the logarithmic plots may be interpreted as representing the surface diffusion activation energies as in the work of Sloope and Tiller (1962).

It is seen from Fig. (2.8) that for conditions in which the surface is not clean, as would occur for deposition pressures $\geq 10^{-6}$ torr. the value of surface diffusion activation energy as found from the slope of AB, is of the same order as that of the silicon interatomic bond energy as given in Table V. For clean surface conditions as

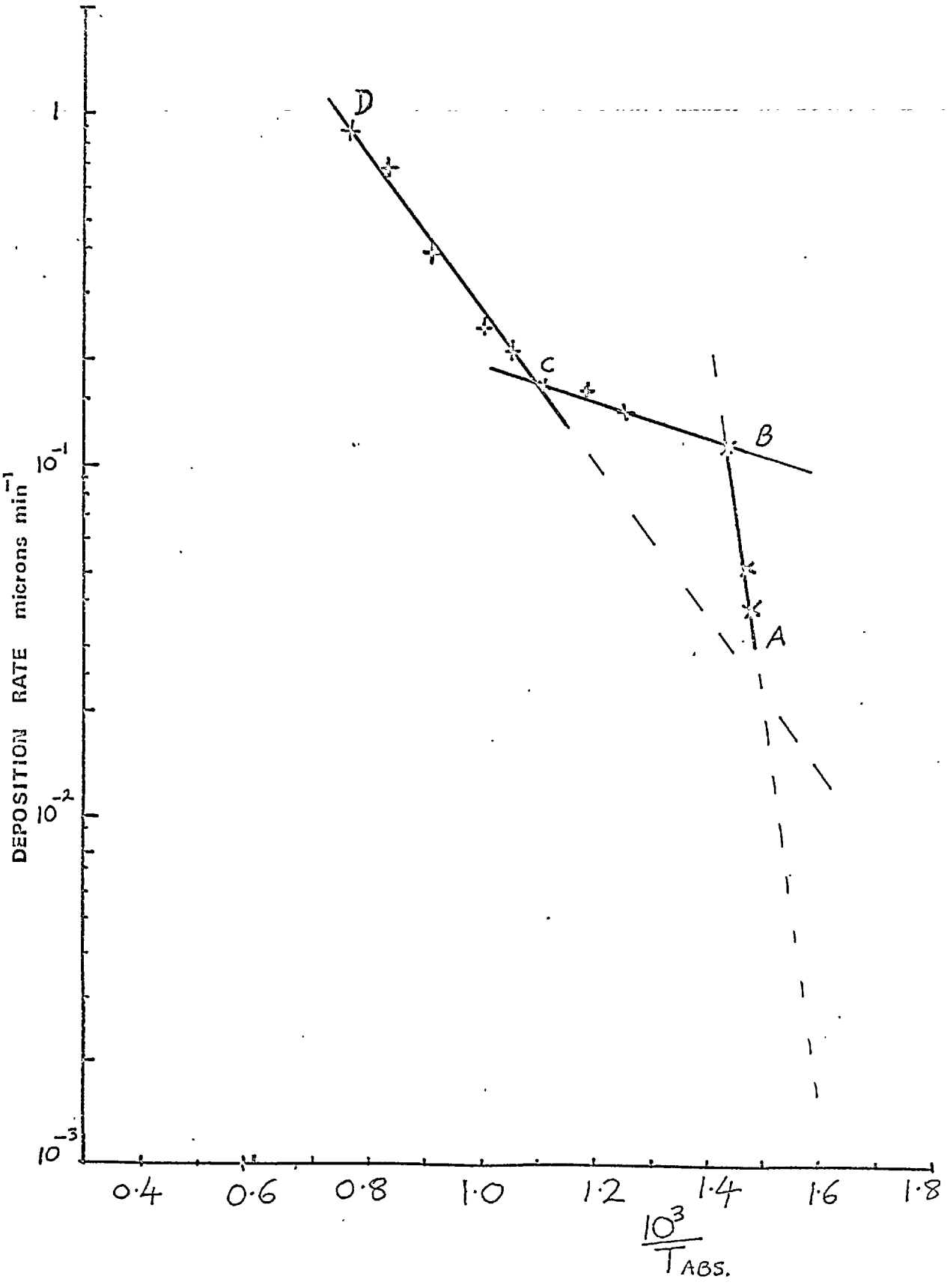
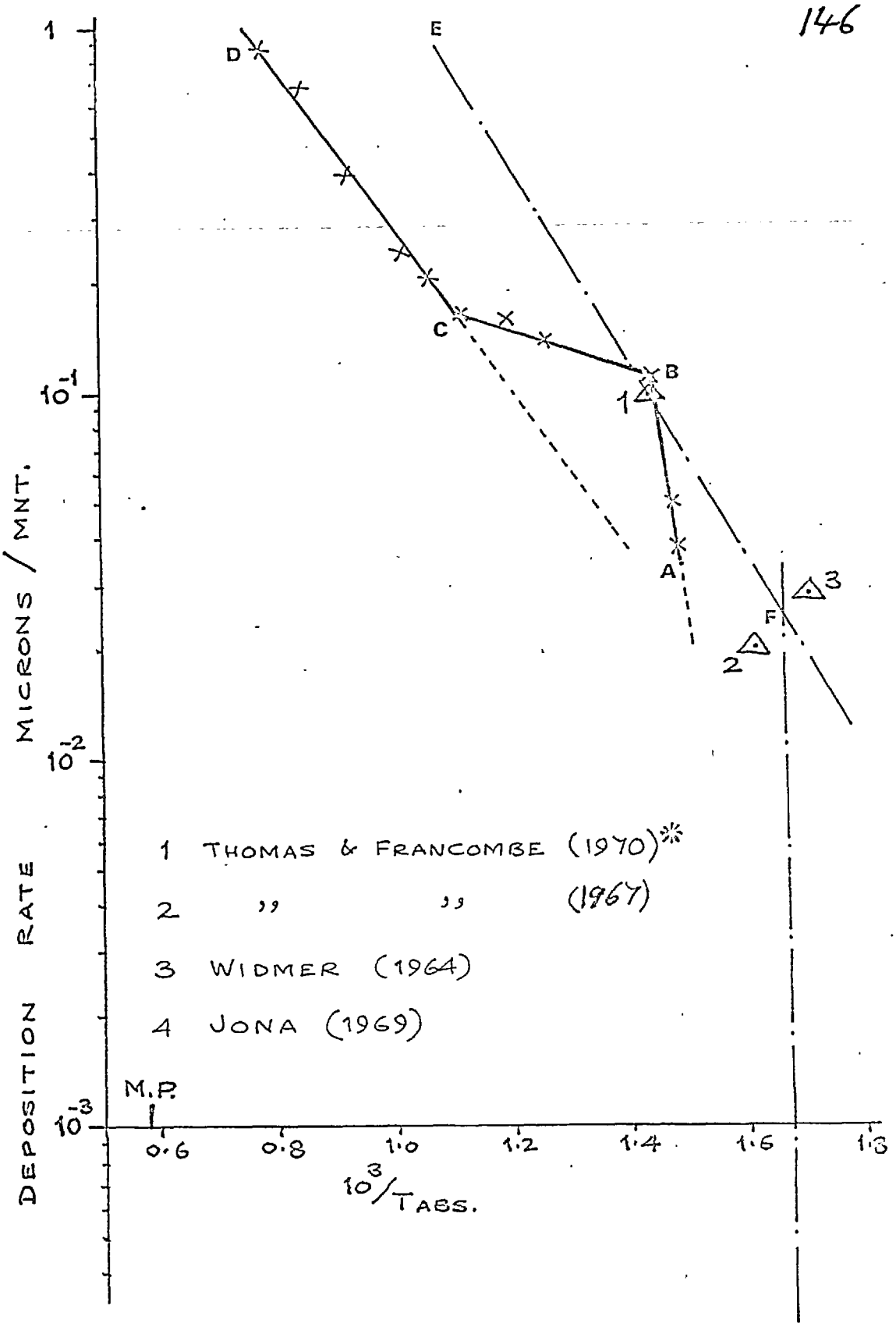


Fig. (5.1a)
GRAPH OF THE DATA OF FIG. (4.1) PLOTTED AS LOG. RATE VERSUS $10^3/T°K$ ACTIVATION ENERGIES DERIVED FROM GRAPH ARE:

AB, q = 2.3 ev
BC, q = 0.12 ev
CD, q = 0.4 ev



DEPOSITION RATE VS. $(\text{EPITAXIAL TEMP.})^{-1}$

* PRIVATE COMMUNICATION

Fig. (5.1b)
PLOT OF FIG. (5.1a) with U.H.V. DATA OF FIG. (2.8) ADDED FOR COMPARISON.

produced in ultra high vacuum, the surface diffusion activation energy is much lower, as shown by the value 0.41 ev found from the slope of E_F in fig. (2.8).

Various values have been obtained for the clean surface diffusion activation energy on silicon surfaces. Allen (1961) deduced a value of 2 ev based on surface motion observed in field emission studies. This value however, includes the energy required to dissociate an atom from a surface step and so may be greater than a mobility energy value alone.

Abbink et al (1968) deduced a value for the surface diffusion activation energy from analysis of the nucleation kinetics. They obtained a value of 0.2 ev for motion on a planar (111) oriented surface.

Joyce et al (1967) using a molecular beam of Silane also found a surface diffusion activation energy. The value they obtained depends on the choice of value of the silicon bond energy. As can be seen from Table V, there is a large spread in the published values. From this data, the results of Joyce et al (1967) indicate a value of surface diffusion activation energy in the range 1.6 to 2.4 ev.

From the review data plotted in fig. (2.8) the ultra high vacuum growth studies show the existence of two distinct activation energies: for growth rates $\geq$ 0.1u min. a value of 0.4 ev. and for growth rates less than this value, the growth rate; temperature data suggest that there is no strong temperature dependence of the deposition rate, however, there is not enough data on growth rates and temperatures in this range, to enable a definite conclusion to be reached.

The activation energies found from fig. (5.1a) - 0.4 ev and 2.3 ev; are in good agreement with the values of 0.4 ev found from the slope of EF in fig. (2.8) and the value of 2.4 ev found from the work of Joyce et al. (1967).

The presence of the region BC, Fig. (5.1a) suggests the presence of a third process of activation energy 0.12 ev. This value is of the same order as the value 0.2 ev, found by Abbink et al (1968).

5.1.(2) Comparison of the Structure and Quality of the Layers grown in this present work with published data.

The structure, crystalline perfection, and defect content of the layers showed considerable variance from the results obtained by other workers which have been discussed in the review and summarised in table IV. Thomas and Francombe (1969) found films grown in their equipment at deposition temperatures $\gtrsim 650^{\circ}$ and for rates of the order of 0.1μ min^{-1} had stacking fault densities less than 10^{+3} per sq. cm. and these only increased rapidly for deposition temperatures below $600^{\circ}C$. In contrast, as can be seen from Fig. (4.4), at a growth temperature of the order $600^{\circ}C$ and deposition rates of 0.1μ min^{-1}, the layers consisted of doubly positioned areas; and as may be seen from Fig. (4.10) the fault density was many orders of magnitude greater, at deposition parameters which were reported in previously published work to produce fault-free layers, as given in table IV. For example Widmer (1965), at a deposition rate of 0.036μ min^{-1} and growth temperature of $800^{\circ}C$, obtained fault-free layers, whereas in this work, for substrate temperatures of $900^{\circ}C$ and growth rates of 0.04μ min^{-1} fault densities of the order $\sim 10^{+6}$ sq. cm. were obtained. As can be seen from Fig. (4.10), the fault density at constant growth temperature increased with increasing deposition rate. Although the fault densities were reliable only to an order of magnitude, the densities observed were several orders of magnitude higher than those reported for similar growth rates and temperatures listed in table IV. The discrepancies are well outside the limits of experimental errors.

The deposition pressures used in this work, were an order of magnitude higher than those used in the works cited in the review, [see table IV] also, the pre-deposition thermal treatment used was of much shorter duration; than those used by the workers discussed above, it is possible that these differences may account for the high fault densities observed. However, as will be discussed below, ion bombardment of the films took place during the deposition, and this could influence the fault density, as it influenced the layer structure, as will be discussed later.

As well as very high fault densities, the faults showed variations of lengths, which indicated that they had nucleated at various times during the layer growth. A variation of fault size was observed by

Nielson and Rich (1964) only in epitaxial layers grown at deposition pressures $\geq 10^{-5}$ torr. This variation of fault size was ascribed to the effects of the high deposition pressure.

In this present work, the deposition pressure varied between 10^{-7} torr and 1×10^{-8} torr, thus it is unlikely that a similar effect is responsible for the results observed. No observations of varying fault sizes have been reported for growth experiments carried in ultra high vacuum (apart from the normal growth interaction effect discussed in section 2).

The major and most significant difference observed between the results presented in this work, and those reviewed is the presence of the background defects in the present films. Examples of these background defects can be seen in all the micrographs shown in the results section of this work, and figs (4.15) to (4.19) in section 4.2.(6) show the variation of the background defect density and structure with deposition rate and growth temperature.

From these micrographs it can be seen that, for temperatures $\geq$ about 600°C and growth rates $\geq 0.1\mu$ min^{-1} the background defects appear as small regions of contrast variation as can be seen in Fig. (4.19), and for deposition rates less than 0.1μ min^{-1} the background defects appeared as small black spots. No contrast variation regions were seen in layers grown at deposition rates $< 0.1\mu$ min^{-1}, and no black spot defects were seen in layers grown at deposition rates $> 0.1\mu$ min^{-1}. Thus each form of background defect had a well-defined domain of existence. The transition occurring at a deposition rate of about 0.1μ min^{-1}.

It is possible that the observed high fault densities and the variation in fault sizes may be due to deposition conditions such as the high partial pressure of water vapour present in the residual gases, or the pre deposition thermal cleaning treatment. It is however, difficult to ascribe the presence of the background defects to these effects since in no studies of the epitaxial growth of silicon were any similar defects observed or reported.

In the stereo-pair, Fig. (4.17c) it can be seen that the contrast variation regions are distributed throughout the foil thickness which suggests that they may be produced during, or by the deposition process.

It is also seen that the deposition rate is a major factor, since not only does the transition from black spot defects to contrast variation regions occur at a deposition rate of about 0.1μ min^{-1}; as can be seen from Figs. (4.15) to (4.19); but, also, the change of slope of the Arhenius plot; shown in Fig. (5.1a); occurs at a value of deposition rate of 0.1μ min^{-1}. It was also found that the change of layer structure from predominately single crystal; [denoted as group II structure in section 4.3.(1)] to predominately twinned material; [denoted as group I structure in section 4.3.(2)]; occurred at deposition rates of the order of 0.1μ min^{-1}. It was also found that both the layer structure transitions defined above; and the background defect transitions were not strongly dependent on temperature, in the temperature ranges over which they occurred.

The similarity of the black spot background defects in these silicon films, to those observed by Pashley and Presland (1961) in thin gold film led to the hypothesis that a similar process might have occurred. Pashley and Presland showed that the black spots observed in the examination of thin gold films by transmission microscopy, were caused by the bombardment of the specimens by ions produced by ionisation of the residual gas in the electron microscope. The ions responsible were found to be negative gas ions which were accelerated by the electron gun voltage (100 kV) and which then impinged onto the specimen. Since in the work reported here, the results were consistent with the idea that the background defects were produced during the deposition, as shown by Fig. (4.17c), it was at first assumed that they might be due to the residual gas being ionised by the electron beam in the furnace, and then bombarding the layer, during the deposition. In order to investigate this possibility, an experiment was carried out to detect and measure the number of ions present in the silicon vapour stream during the deposition.

From Fig. (3.2b) it is seen that the top-plate assembly was insulated by the glass cylinder. During depositions this top-plate and hence the substrate was connected to earth via the secondary of the substrate heater transformer. By grounding the top-plate through a micro-ammeter, the number and charge of any ions hitting the substrate could be found.

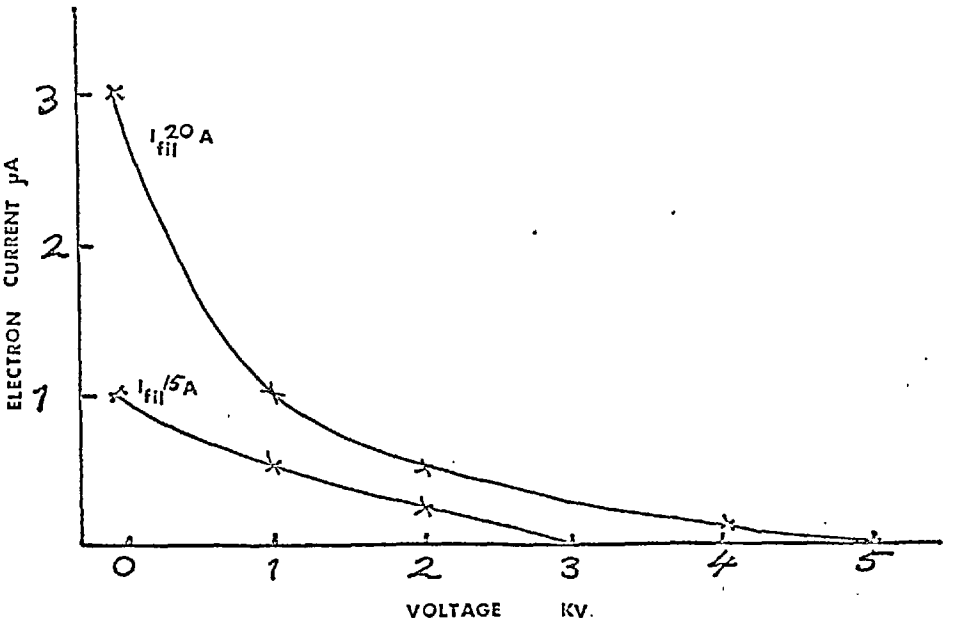


Fig.(5.2a)
VARIATION OF ELECTRON CURRENT AT SUBSTRATE, WITH PEDASTLE VOLTAGE FOR DIFFERENT VALUES OF FILAMENT CURRENT.

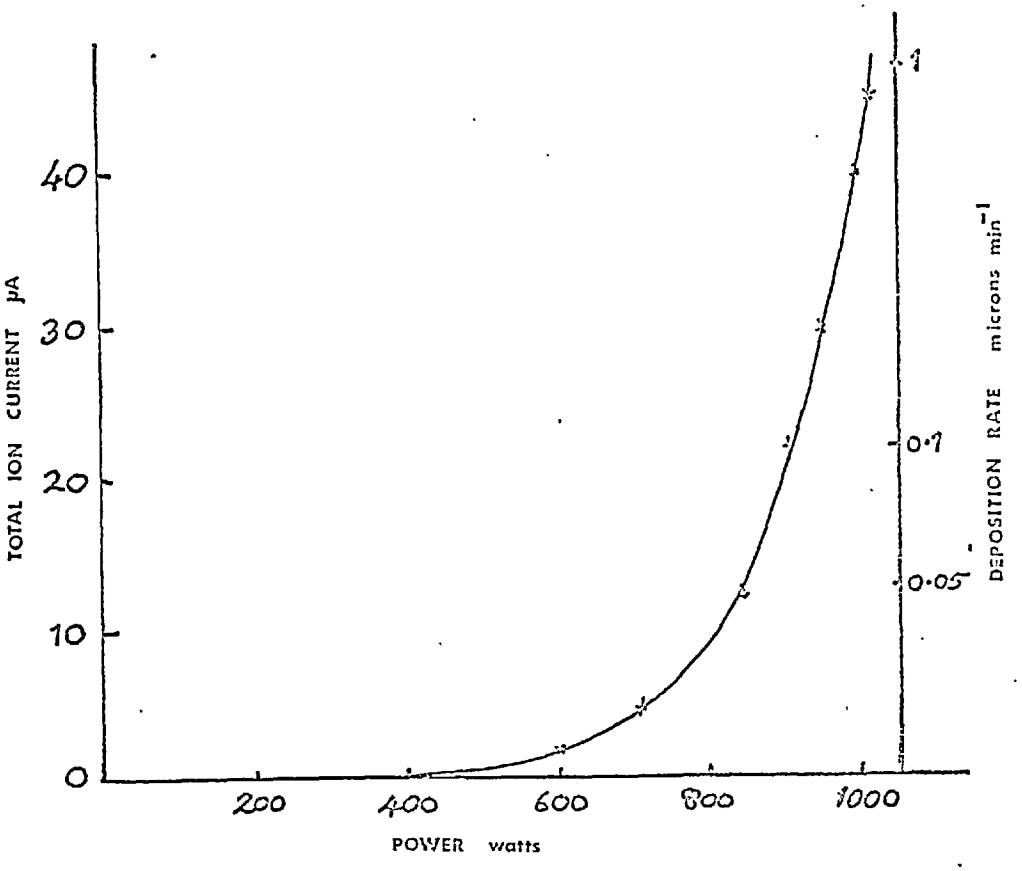


Fig. (5.2b)
VARIATION OF TOTAL POSITIVE ION CURRENT AND DEPOSITION RATE WITH FURNACE POWER AT CONST PEDASTLE VOLTAGE 10 K V.

Fig. (5.2) shows the results of this experiment. As can be seen, the ion current increased rapidly with furnace power, and from the sense of the meter deflection the ions were found to be positively charged. Fig. (5.2a) shows the variation of the number of 'escaping' electrons from the furnace, with variation of the voltage. This indicated that if any negative ions were formed, they are unlikely to escape from the interior of the furnace; thus confirming the ions in the silicon vapour stream to be positively charged.

The strong variation with furnace power, and also the rapid increase in ion current at that value of power at which evaporation commenced, suggested that the majority of the ions were not from the residual gas atoms but were silicon ions. This conclusion was reinforced by the correlation of the ion current with the deposition rate, and the fact that although the chamber pressure was varied from $\sim 10^{-8}$ to $> 10^{-7}$ torr, the ion current stayed constant, for a given furnace power.

The values of ion current given in Fig. (5.2) were measured by the collection of the ions on the underside of the shield. The area of the substrate was found to be about 1 tenth of the area of the patch of deposited silicon on the underside of the shield; thus the fraction of ion current arriving at the substrate is assumed to be one tenth of the total ion current measured.

Correction for secondary electron emission.

In measuring these ion currents, no corrections have been applied for secondary electron emission. Values of the coefficient of secondary electron emission, have been determined by Hagstrum (1960) for 1000 ev Ne^+ ions incident on (111) oriented silicon surfaces. He found values of $\gamma \approx 0.2$. Thus the true ion current will be approximately $\frac{i_m}{1.2}$; where i_m is the measured current. This correction however, does not significantly change the value of the estimated number of ions incident on the substrate.

In order to discuss the effects of the ion bombardment a brief review will be given of the results of ion bombardment studies, to provide background information.

5.2. Review of Radiation Damage

In this section some of the studies of the structure produced by radiation damage in silicon will be reviewed in order to obtain an overall view of the variation of the nature of the damage with radiation dose, and annealing treatments. The nature of the damage will be discussed to allow comparisons to be made with the results obtained in this work.

5.2.(1) Range Energy Relationships

Particles lose energy in passing through solids in two ways: interaction with the electrons and interaction with the nuclei via the coulomb field.

If the particles are not charged, eg. neutrons, then the interaction is only with the nucleus via the nucleon field. The basic work on the energy exchange process was carried out by Bohr in 1948, who showed that the velocity of the incident particle was the dominant factor in determining which energy loss mode occurs.

This work was extended by Lindhard et al. (1969), who developed a theory for the range variation with energy, by dividing the energy losses into two components: electronic stopping and nuclear stopping losses. The results derived by Lindhard et al (1969) refer to the penetration of an amorphous solid.

In studies of radiation damage, an amorphous solid, defined as one whose density is the same as that of the material under consideration;, and which has no crystalline structure. In the case of single crystal target material, the penetration effects are modified by a structure-dependent process called channelling. This process allows the penetration by ions over distances many times those predicted by the Lindhard theory.

Since the channelling process is in general, not associated with the creation of lattice damage, it will not be discussed in detail.

The energy losses are made up of the two components, electronic stopping losses and nuclear stopping losses. The lattice damage is caused mainly by the nuclear collision process. Since both the processes are functions of energy, the damage will depend on the relative

contributions of the processes over the energy range of the ion. Following the procedure of Gibbons (1968) the energy at which the electronic stopping and nuclear stopping processes are equal in magnitude may be calculated. From Gibbons (1968) the nuclear stopping power S_n is given by the equation

$$S_n = 2.8 \times 10^{-15} \frac{Z_1 Z_2}{H^{\frac{1}{3}}} \left[\frac{M_1}{M_1 + M_2}\right] \text{ ev};$$

where Z_1 and M_1 are the atomic number and mass number of the incident particle; Z_2 and M_2 are the atomic number and mass number of the target material; and $H^{-\frac{1}{3}} = [Z_1^{\frac{2}{3}} + Z_2^{\frac{2}{3}}]^{\frac{1}{2}}$.

S_e, the electronic stopping power, is given by the equation $S_e = kE^{\frac{1}{2}}$; where E is the incident particle energy in electron volts. For amorphous silicon, $k = 0.2 \times 10^{-15}$ (Gibbons (1968)). At a certain ion energy E_c, $S_n = S_e$, since S_e is a function of ion energy; and S_n, is assumed independent of ion energy. Thus $S_n = S_e = kE_c^{\frac{1}{2}}$. Substituting for S_n, we have $E_c = \left(\frac{S_n}{k}\right)^2$ electron volts.

Substituting the values for the case of a silicon ion incident on a silicon target: $M_{1,2} = 28$; $Z_{1,2} = 14$. This gives $E_c \approx 160$ KeV.

Thus for the case of a silicon ion incident on a silicon target, if the energy is $\ll 160$ KeV, then nuclear collision processes will dominate. For the energy range $E < E_c$, where nuclear stopping predominates, the range R, in Å is given in silicon by

$$R = 0.7 \times \frac{H^{-\frac{1}{3}}}{Z_1 Z_2} \cdot \left[\frac{M_1 + M_2}{M_1}\right] \times E_{ion} \quad \text{(after Gibbons (1968))}$$

where the symbols have the same meanings as before, and E_{ion} is the incident ion energy in electron volts. Thus for a 10 KeV silicon ion incident on an amorphous silicon target the range is of the order 240 Å. The range calculated using the equation given above, expresses the range as a total path length. Thus to determine the depth of penetration of the ion, normal to a surface, a correction factor must be applied. Schiott (1969) has shown that the depth of penetration P, is given by $P \approx \frac{R}{1.3}$; for $M_1 = M_2$. Thus the penetfation of the 10 KeV silicon ions $\approx \frac{240}{1.3}$ Å units which gives a value of ~ 185 Å.

These values of ranges and penetrations calculated are average values, and a distribution of ranges will exist about the average value.

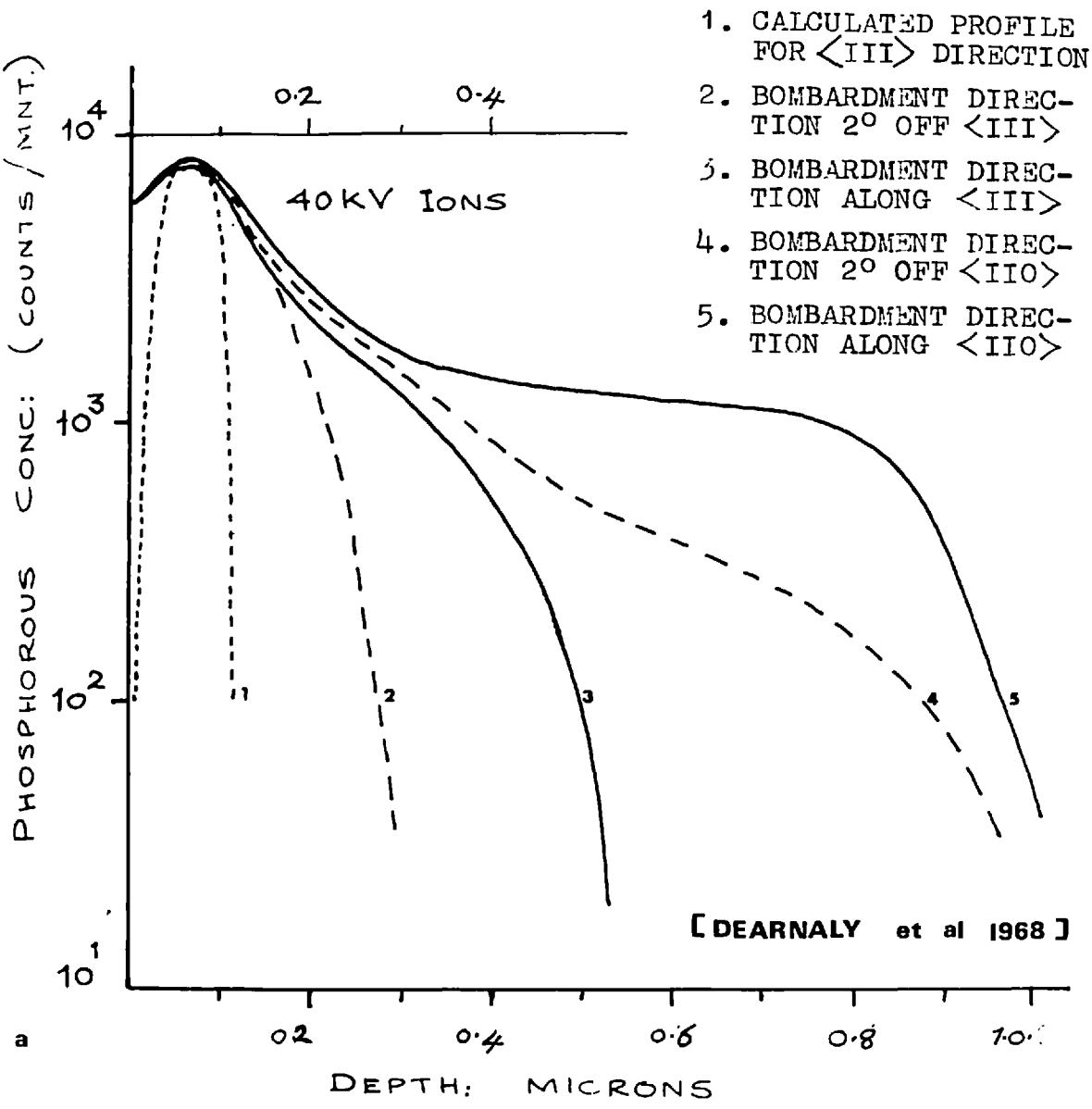
The theory of Lindhard et al (1969) shows that the distribution of ranges about the average value will be Gaussian for both stopping processes.

In the majority of experimental studies of radiation damage in silicon due to ion bombardment effects, the ions used were those of the group III or group IV elements used to dope silicon, eg. boron, phosphorus, etc. As has been shown above, the penetration and range depend on the Atomic and Mass numbers of the bombarding ion and target. Table VI gives these values for various elements and an amorphous silicon target. It is seen that phosphorus and aluminium have atomic and mass numbers close to those of silicon; thus their effects will be similar to those produced by silicon ions, and so may be used for comparison.

Fig. (5.3a) shows the results obtained by Dearnaley et al (1968). By using radio-phosphorus and an anodic stripping technique the phosphorus content at various depths in the silicon target could be found by counting techniques. The theoretical plot of R based on the theory of Lindhard is shown for domparison. The greater penetration in the $< 110 >$ direction is due to channelling in the relatively open structure of the diamond cubic lattice in $< 110 >$ directions as compared with $< 111 >$ directions, as illustrated in Fig. (5.3b,c). The tail of the $< 111 >$ direction results is also assumed to be due to channelling, mainly by scattering into favourable directions.

The effect of small misorientations from the low index directions is to reduce the channelling effect considerably.

The depth of maximum phosphorus content is seen to be approximately 600 Å, for the 40 KeV ions used. The range energy equation previously used shows that for a given $M_{1,2}$: $Z_{1,2}$, the range is proportional to the energy if it is below E_c. (From table VI, E_c for phosphorous $\approx$ 200 KeV); thus in this case the penetration of a 10 KeV phosphorous ion would be $\frac{600}{4} = 150$ Å. This is in excellent agreement with the calculated value of 185 Å for a 10 KeV silicon ion in amorphous silicon, allowing for the differences of M_1, Z_1 for silicon and phosphorous.



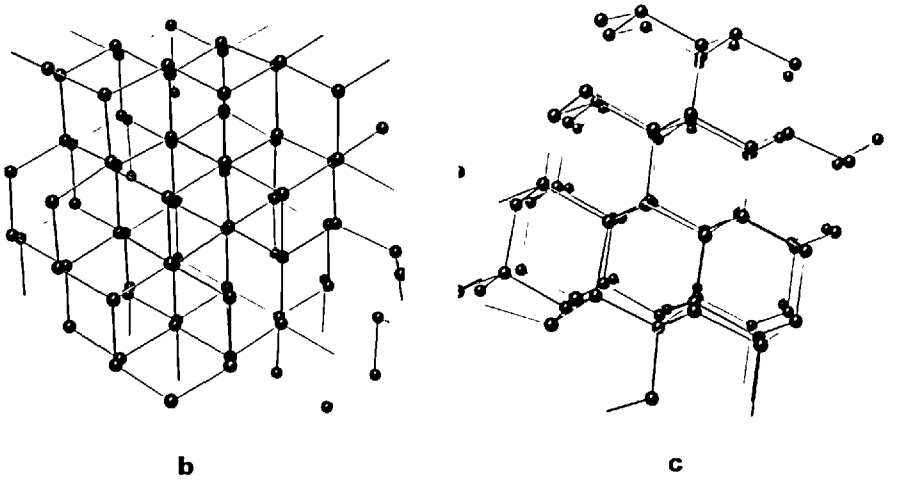


FIG. (5·3)

a. PLOT OF CONCENTRATION OF 40 KV IMPLANTED P^{31} IONS VERSUS DEPTH, FOR DIFFERENT IMPLANTATION DIRECTIONS

b. BALL MODEL OF SILICON LATTICE VIEWED IN <III> DIRECTION

c. BALL MODEL OF SILICON VIEWED IN <IIO> DIRECTION

5.2.(2) The Nature of the Damage

In the energy range where nuclear stopping predominates, the incident ion loses energy by a series of collisions with atoms of the target. In a "collision interaction" the energy transferred may be sufficient to displace the atom from its lattice site. The displaced atom and its vacancy will then form a Frenkel pair. If the displaced atom has sufficient energy, it can in turn displace other atoms, the process continuing until the energy transferred is below the displacement energy, E_d, of the material. This process is called a collision or displacement cascade.

The number of displaced atoms as a function of the energy of the bombarding atom can be estimated using an equation derived by Kinchin and Pease (1955). If the collisions are assumed to be independent of each other, and only involve two atoms, then N(E), the number displaced by the incident particle of energy E, is given by $N(E) = \frac{E}{2E_d}$. For silicon, values of E_d have been found as follows: 14 ev, Novak (1963); 12.9 ev, Loferski and Rappaport (1958). Thus for a 10 KeV incident ion, $N(E) = \frac{10^4}{28} \approx 350$. This value is an approximation; in that directional effects of the target lattice structure are ignored.

More recent work by Marsden et al (1969) using back scattering techniques to examine collision cascades, has shown that for 10 KeV ions incident in silicon in the $< 111 >$ direction the number of displaced atoms $\approx$ 800 per ion.

However, the back-scattering measurement will also detect regions of lattice disorder, and thus the actual number of displaced atoms may be much lower.

From the above review it is seen that the initial damage is the creation of a disordered region by the displacement of a large number of lattice atoms. The final state of the disordered region depends upon the initial distribution of the damage, the temperature during the bombardment, the presence of sinks for the vacancies and interstitials produced and any post-bombardment annealing treatments.

5.2.(3) Variation of Damage with Dose; Distribution of Damage.

The dose is defined as the number of ions received per square centimetre of target during the bombardment time. Using back-scattering techniques, Mayer et al (1968) investigated the variation of lattice disorder with dose for silicon crystal targets. They found that the 'disorder' increased linearly with dose, until a certain dose value, and then remained constant. This dose value was called the saturation dose.

The saturation dose was found to be of the order of 10^{14} ions per square centimetre for 40 KeV phosphorous ions for bombardment at room temperature. A similar value was found by Mazey et al (1967) who observed that the onset of the saturation effect could be detected by the change in visual appearance of the bombarded silicon surface. At the saturation dose the surface became 'milky white'. The colour change was explained by Mazey et al (1967) as being due to Rayleigh scattering by the disordered surface.

These results show that for a certain dose, the surface of the target becomes disordered. For room temperature bombardments, Mazey et al (1967) found the saturation dose for the surface disorder, to be of the order 3×10^{13} ions per square centimetre for silicon using 60 KeV Neon ions.

The saturation effect has been explained by the overlapping of the individual disordered zones, to give a disordered layer which cannot then be further disordered, and which also shields the undisturbed material below from both further damage and from registry as undisturbed material in the examination technique used.

The overlap of the disordered regions will occur at the peak value of the range, as was shown by Sigmund et al (1969) and then spread out on either side as the dose increases. Thus if the range is less than the diameter of the disturbed zone, the surface is immediately affected. If the range R is much greater than the diameter of the disturbed zone a disordered layer will be produced within the target at a mean depth R below the surface, and continued bombardment causes the damage level to rise to eventually intersect the surface.

Gianola (1957) studied the effects of bombardment of (110) oriented single crystal silicon with 30 KeV helium ions. He investigated the nature of the surface damage, using electron reflection diffraction. The electron diffraction data indicated that the surface of the target was severely disturbed, and consisted of amorphous material after doses of 10^{14} - 10^{15} ions cm^{-2}. The diffraction patterns of the bombarded material targets also showed some Kikuchi lines, even when the single crystal spot pattern had been destroyed. These Kikuchi lines were assumed to originate at relatively undamaged material close below the surface.

These results indicate a direct surface damage effect, as opposed to the 'climb' of the damage zone discussed above. Climb of the damage zone as mentioned above would not produce material in a state capable of producing Kikuchi lines. Also, for diamond structured material the $< 110 >$ direction is favourable for channelling as can be seen from Fig. (5.3c), also as shown in table VI, the critical energy for helium ions in silicon is less than 10 KeV, thus for these reasons the zone of damage is likely to be well below the bombarded surface.

The results of Whan and Arnold (1970) have shown that the surface of ion bombarded crystals of silicon is disturbed by the stress field produced by the sub-surface damage layer. Using doses of $10^{13} \sim 10^{15}$ ions per sq. cm., and 400 KeV Xenon ions, they found that after room temperature bombardments, steps and ledges were formed in the surface. These they ascribed to the damage-zone stress field rather than the effect of the implanted Xenon gas atoms.

The range of 400 KeV Xenon ions in silicon is approximately 2000 Å as estimated from the data of Ferber (1963). It is likely that damage regions closer to the surface will have a larger disturbing effect.

From the calculations given in section 5.4.(1) it was shown that the range of the 10 KeV ions was of the order of 150 Å, thus from the above result, there could be appreciable surface stress generated, due to the proximity of the damage region to the surface.

5.2.(4) Variation of the Saturation Dose with Temperature

Mazey et al (1968) investigated the variation of the saturation threshold dose as a function of target temperature using the surface change discussed above as an indication of the transition. Their results are shown in Fig. (5.4). A similar investigation was carried out by Irving (1969) using 100 KeV phosphorous ions and electron reflection-diffraction techniques to examine the surface: his results are also shown in Fig. (5.4). From these results it is seen that at high temperatures a higher dose is needed to disorder the surface. This indicates that annealing is occurring during the bombardment.

From their results, these workers have found the activation energy for the annealing of the disorder. Mazey et al (1968) have found a value of 0.3 ev, and Irving (1969) 0.18 ev. The value of 0.3 ev is close to the activation energy of vacancy migration in silicon, as quoted by Watkins (1963).

The effect of the bombardment temperature for doses less than the saturation value were investigated by Eriksson et al. (1969), who showed that for bombardment temperatures $\geq 300^{\circ}C$ and doses less than the saturation value, the residual damage is very small. This is confirmed by work of Anderson and Wehner (1964) who investigated the temperature dependence of germanium single crystal target sputtering ejection patterns. Above a certain target temperature, ejection patterns characteristic of a single crystal were observed. This suggests that above this temperature the bombardment damage is annealed out rapidly enough for each approaching ion to see a nearly perfect surface.

5.2.(5) Annealing Characteristics of the Damage.

Fig. (5.5) shows the results obtained by Mayer et al (1968) for isochronal annealing of the radiation damage. It is clear that the annealing temperature for the two doses are different, thus showing the effect of the saturation dose. Almost identical results have been obtained for neutron and electron irradiation damage studies, using various measurement techniques; these results have been reviewed by Vook and Stein (1969).

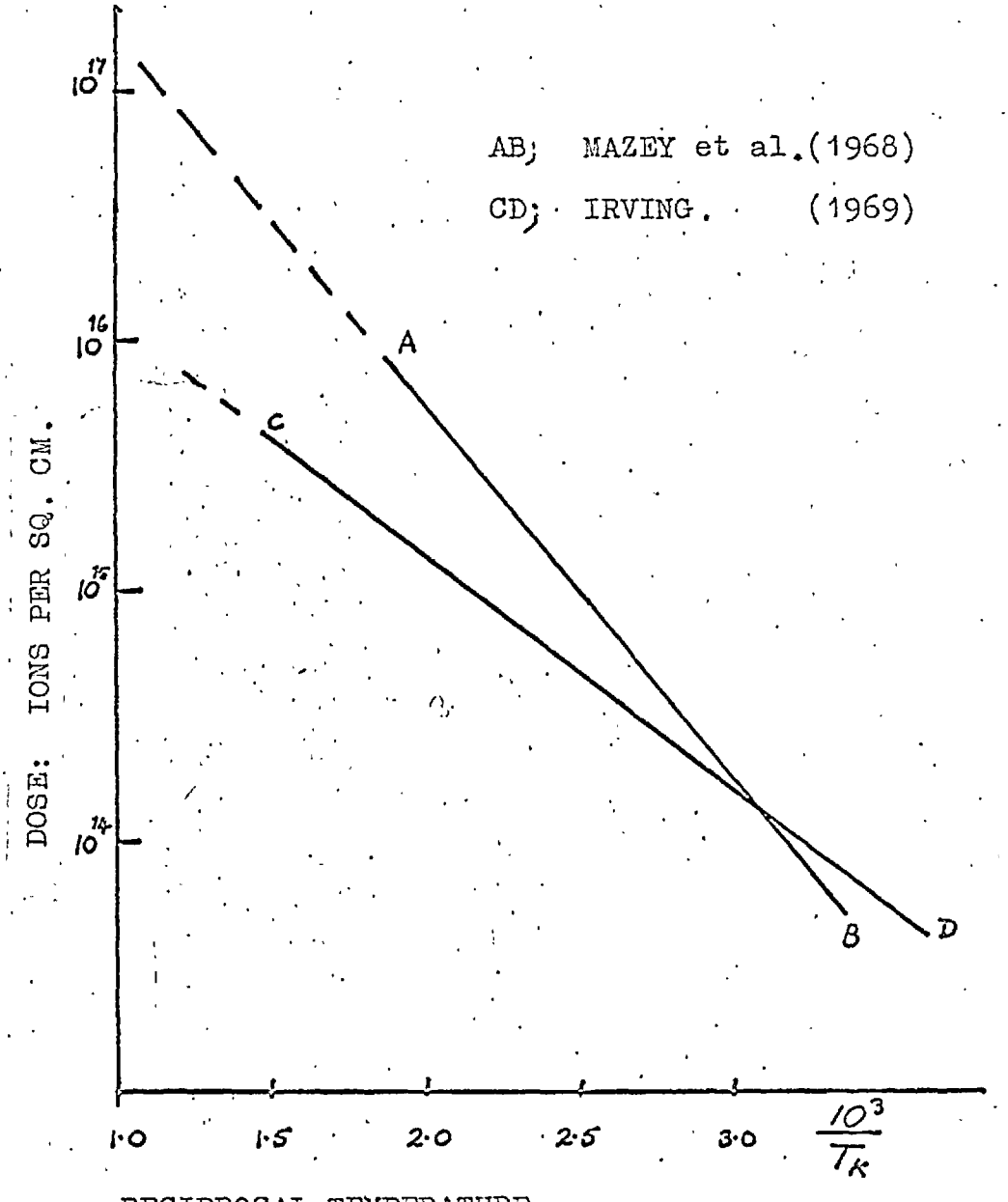


FIG. (5.4) GRAPH OF THRESHOLD SURFACE DISORDER ION DOSE, PLOTTED AGAINST RECIPROCAL TEMPERATURE

	ION	ENERGY KeV	TARGET ORIENTATION	ACTIVATION ENERGY Ev
AB	Ne^+	60	Nominal (III)	0.3
CD	P^+	100	7^o off (III)	0.18

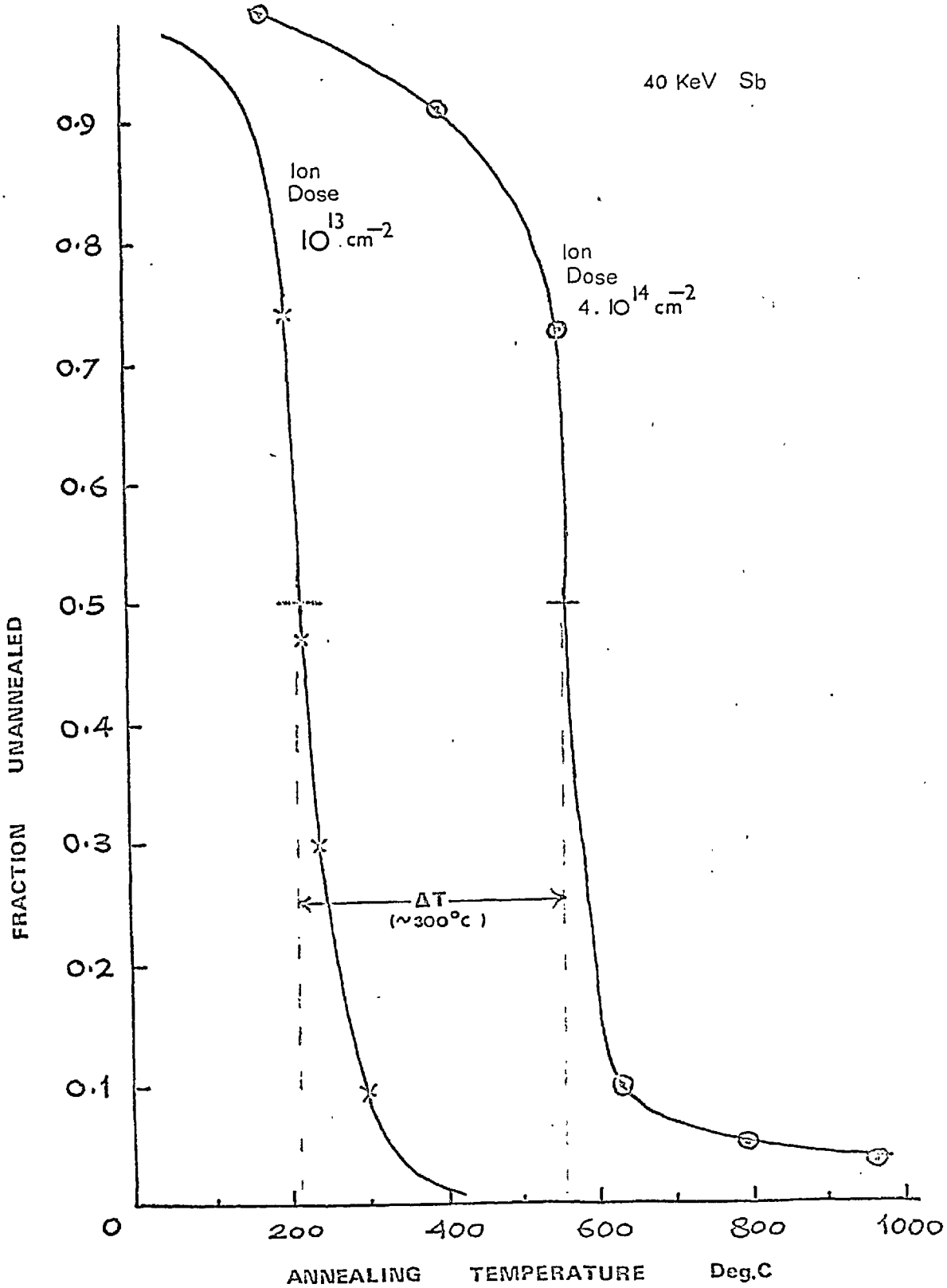


Fig. (5.5)
PLOT OF UNANNEALED DAMAGE VERSUS POST-BOMBARDMENT ANNEALING TEMPERATURE FOR DOSE ABOVE AND BELOW THE SATURATION VALUE. BOMBARDMENT AT ROOM TEMPERATURE. [DATA FROM MAYER ET AL 1968].

The temperature of 600°C for the 100%anneal stage of the saturated damage condition, Fig. (5.5) is in agreement with the value of 630°C found by Mazey et al (1968) for the disappearance of the surface discolouration. This value of 630°C is also close to the temperature of 700°C found by Hasse and Scott (1950) for the crystallisation of thick (~ 1μ) amorphous silicon films deposited on to quartz. Vook and Stein (1969) have shown from analysis of radiation damage data that germanium and silicon which are both diamond structured, have characteristic annealing stages corresponding to doses above and below the saturation dose value. These stages occur at temperatures of 0.31 Tmp and 0.5 Tmp where Tmp is the melting point temperature in deg. K. For silicon these values correspond to 240°C and 550°C, which agrees with the experimental data.

From this brief review it appears that the main results of ion bombardment effects can be summarised as follows:

(a) The effect of bombardment by ions or particles on a crystal is to create a region of disordered lattice by displacement of atoms from their lattice sites. The final size and nature of the disordered region depends upon the n ture and energy of the bombarding particle, and the treatment, especially thermal, during and after bombardment of the target.

(b) A saturation dose exists, which is temperature-dependent.

(c) The damage is cumulative, being proportional to the total dose, for doses less than the saturation value.

(d) The annealing characteristics of the damage vary for doses above and below the saturation value.

5.3. Effect of ion bombardment on the epitaxial growth process.

We must now re-examine the processes occurring during the deposition of the layer since it was shown that the deposition was accompanied by the bombardment of the surface by silicon ions of 10 KeV energy.

From Fig. (5.1) it is seen that the rate of bombardment is proportional to the deposition rate. If it be assumed that the depositing silicon will 'lock-in' the structure of the growth surface, then the resulting structure of the deposited layer, single crystal, or polycrystalline, will depend on the state of the growth surface, and hence on the ion current, as well as on the requirements of the epitaxial growth prodess.

From the results presented in section 4, it is seen that there is a strong bombardment rate dependence of the radiation damage in the present work, as opposed to a dose dependence as reported in the review data. A rate dependence effect can be understood in terms of the relationship between processes which are occurring, one is the rate of damage production by the bombarding ions, the other is the rate of restoration of order in the lattice by the annealing processes.

By considering these two processes, a relationship may be derived linking the substrate temperature, bombardment rate, and resulting crystal structure of the layer. It can be seen that if the bombardment rate R_b > the rate of anneal A, then the number of displaced atoms, and hence amount disordered material increases. Similarly if $R_b < A$, the annealing process will dominate, and an ordered structure will result. If $\frac{dN}{dt}$ is the net rate of increase of damage then we have $\frac{dN}{dt} = R_b - A$, where N is the number of disordered regions. If it is assumed that the rate of annealing A is a function of temperature of the form $A = A_0 \exp [- \frac{a}{kT}]$. Where A_0 is a constant, and a is the activation energy of the annealing process. Thus for zero net increase of damage $\frac{dN}{dt} = 0$, and $R_b = A$. At these values we may put $R_b = R_t$ and $R_t = A_0 \exp [- \frac{a}{kT}]$. Where R_t is the threshold dose rate to amorphise the surface at temperature T. Thus if $R_b > R_t$, the damage builds up and the amorphous or disordered surface state is produced.

Since the epitaxial growth process is likely to be very sensitive to the state of the surface, it is likely that radiation doses much less than the surface amorphisation values discussed in the above review will destroy the epitaxial growth.

The analysis used, above is similar to that of Vook and Stein (1969) who have also considered the effect of the order of the annealing process. The results they obtained for first order annealing were of the same form as the equation derived above. Thus, polycrystalline growth may be caused by either of the following conditions.

(i) $R_b > A_0 \exp [- \frac{a}{kT}]$

or

(ii) $R_g > A \exp [- \frac{q}{kT}]$ where R_g is the growth rate.

and the transition line from polycrystalline growth to single crystal growth will be given by growth parameters satisfying the conditions

$$R_b = A_0 \exp\left[-\frac{a}{kT}\right]; \quad R_g = A \exp\left[-\frac{q}{kT}\right].$$

Since the ion current is proportional to the growth rate, as shown in Fig. (5.2b), the conditions (i) and (ii) above can be written as

$$R_g > A_0' \exp\left[-\frac{a}{kT}\right]$$

$$R_g > A \exp\left[-\frac{q}{kT}\right]$$

where A_0' is a constant.

In the model used to derive these equations, it is assumed that the growth surface is directly affected by the ion bombardment. Whether the mechanism is by the propagation of the strain field of the sub-surface damage layer, as indicated by the results of Whan and Arnold (1970), or direct disordering by the ions, as suggested by the findings of Gianola (1957), is not known, however, both effects will affect the free surface during growth.

From Fig. (5.1a) it is clear that the activation energy changes at point B, at a deposition rate of about 0.1μ per minute and a growth temperature of 400°C. From Fig. (5.2b) it is seen that 0.1μ per minute corresponds to a dose rate of about 2.2μA. Assuming singly ionised silicon ions, this current corresponds to a dose rate of $\simeq 8 \times 10^{14}$ ions per square centimetre per minute. Eriksson et al (1969) showed that for target temperatures $\geq$ 350°C, the disorder for doses of $10^{14} \sim 10^{15}$ ions per square centimetre was below their detection limit. This indicated that for those doses and target temperatures, the rate of annealing during bombardment was fast enough to prevent the formation and build-up of the amorphous layer surface. This result is in accord with the results of the sputtering studies by Anderson and Wehener (1964) cited in the review.

Thus B, Fig. (5.1) represents the value of deposition parameters at which $R_b = A_0 \exp\left[-\frac{q}{kT}\right]$. Fig. (5.1a) shows that AB lies in the range $T > 300^{\circ}C$; $R_g \leq 0.1\mu$ per minute, thus AB represents the growth conditions $R_g \simeq A' \exp\left[-\frac{q}{kT}\right]$ and $R_b < A_0 \exp\left[-\frac{a}{kT}\right]$ and hence the energy found from the slope of the graph represents the activation energy of the epitaxial growth process. For growth rates $\geq$ 0.1μ per minute, the saturation dose rate is reached and the process kinetics change. Thus BC may be interpreted as representing the locus of growth conditions:

$R_b \approx A_0 \exp\left[-\frac{a}{KT}\right]$ and $R_g < A \exp\left[-\frac{q}{KT}\right]$

and the structure of the layer is then controlled by the annealing of the radiation damaged material rather than the process of epitaxy. The slope of BC in Fig. (5.1a) yields a value of 0.12 ev. This may be interpreted as the activation energy of the growth surface reordering process as just discussed.

Vook and Stein (1969) quoted the following values for the activation energies of processes observed in annealing studies of radiation damage in silicon.

Neutral Vacancy motion	0.33 ev.
Divacancy motion	1.2 ev.
Double negatively charged vacancy motion.	0.18 ev.

Swalin (1961) calculated a value for the activation energy of vacancy migration of 1.1 ev for silicon. The value obtained from Fig. (5.1) is low compared with these, but is close to the value found by Irving (1969) given above in Fig. (5.4). It was also found that the difference in temperatures of the points B and C was approximately 250°C which is in good agreement with the difference in temperature $\sim 300^{\circ}C$ of the isochronal anneal plots, shown in Fig. (5.5). This agreement suggests that BC represents the annealing of saturated surface damage.

For temperatures $\gtrsim 600^{\circ}C$ the annealing studies discussed in the review, Fig. (5.5), indicated that complete (post-bombardment) annealing, of the saturated damage state would occur. In Fig. (5.1a) point C occurs at a temperature of about 640°C, which is in good agreement with the value of temperature 630°C found by Mazey et al (1967) for the post bombardment annealing of disordered (111) silicon surfaces.

In view of the dynamic equilibrium between annealing and the radiation damage, and from consideration of the damage annealing data shown in Fig. (5.5), it may be assumed that for temperatures > 650°C no continuous amorphous layer will be produced by the ion bombardment, current levels observed in this work.

The rate limiting effect under these conditions is then again the epitaxial process, and the activation energy found 0.4 ev may be assumed to be that of the epitaxial growth process. This is confirmed by the close agreement with the activation energy of epitaxial growth found from Fig. (2.8) for growth experiments under similar conditions of growth rate and temperature. Thus in Fig. (5.1a) AB and CD represent epitaxial growth process and BC represents the annealing of the radiation damage.

5.4. The Effect of the Radiation Damage on the Structure of the Layers.

The observed variation of layer quality, and defect content with growth rate and temperature can now be correlated with the variation of ion bombardment damage. Fig. (5.6) is a diagrammatic representation of Fig. (5.1a) for growth parameters R,T which lie in the area BQC; it is seen that the growth rate is $\geq$ 0.1μ per minute, and the growth temperature is $< 640^{\circ}C$. Thus the dose rate is greater than the overlap value which occurs at B, but less than the "surface amorphisation" values which lie along the line BC. Thus the crystal structure of the layers grown under these conditions will be dominated by considerable disorder produced by recrystallisation effects.

This can be seen in Figs. (4.3) and (4.4). In Fig. (4.3c) there is evidence of random recrystallisation, as shown by the presence of polycrystalline grains P. Fig. (4.4) indicates a more ordered structure, the double positioning suggesting that the underlying undamaged regions have acted as a seed and the disordered material has recrystallised epitaxially on to the underlying material. This process has been observed by Large and Bicknell (1967) in post bombardment annealing studies of damage in silicon. Twins and included grains have also been reported by both Mazey et al (1968), and Irving (1969) in post-bombardment annealed thin radiation disordered layers in single crystal silicon targets.

For growth rates > 0.1μ per minute, and temperatures $\geq 700^{\circ}C$, corresponding to region PQCD, in Fig. (5.6) the temperature is high enough to prevent formation of the continuous amorphous layer, but since the dose rate is higher than the overlap value, the disordered

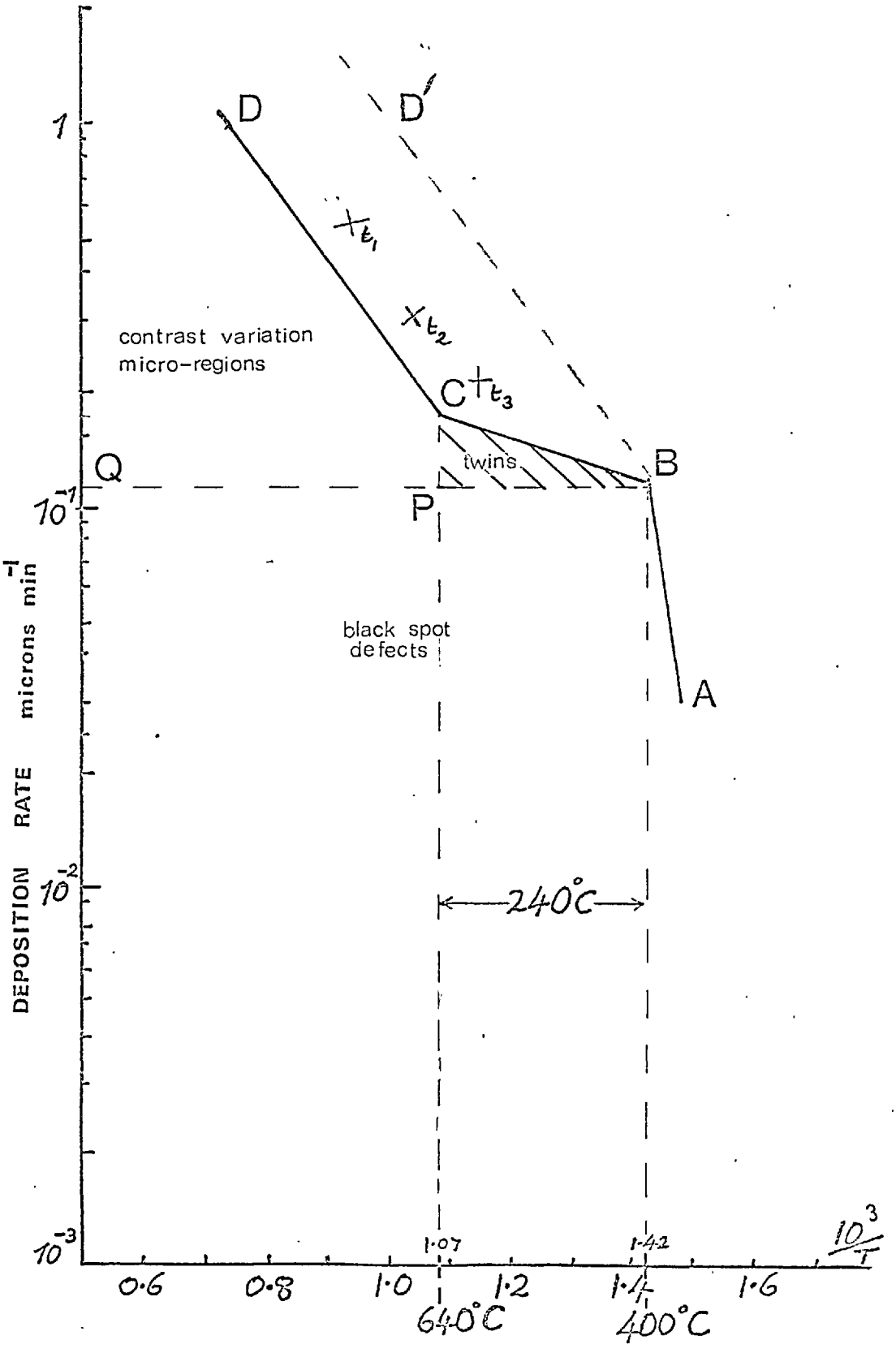


Fig. (5.6)
DIAGRAMATIC REPRESENTATION OF FIG. (5.1a)
SHOWING THE RANGE OF DEPOSITION PARAMETERS AT WHICH
THE VARIOUS TYPES OF BACKGROUND DEFECT OCCUR.

regions are now much bigger because they form from the agglomeration of several overlapped individual damage zones. Since they are larger, they do not anneal out so rapidly; thus they appear as large regions of contrast variations as can be seen in Figs. (4.8), (4.17) and (4.18). The contrast analysis carried out in section (4.3.7) showed that the damage zone E_g^i was greater than the extinction distance E_g of the surrounding crystalline silicon. This result is the same as that found by Parsons (1965) in a study of radiation damage caused by 100 KeV oxygen ions, in germanium. He interpreted this result as indicating that the regions were amorphous germanium of density less than the surrounding crystalline material.

A similar result was also inferred by Mazey et al (1968) from their studies of bombarded silicon by transmission diffraction. They found the transmission electron diffraction pattern of heavily damaged material to consist of diffuse halos, as opposed to the rings produced by polycrystalline material. Figs. (4.15a) and (4.16a) show faint halos passing through the $\{\bar{2}20\}$ and $\{\bar{4}22\}$ spots. The evidence from the stereo pair Fig. (4.17) indicates that the amorphous regions are distributed through the layer.

The diffraction patterns shown in Figs. (4.15) and (4.16) show the presence of fine rings and arced streaks passing through the matrix spots and also through the twin spot positions. These are similar to features observed by Ogilvie and Thomson (1959; 1961) in the diffraction pattern from (111) oriented silver crystals which had been heated and bombarded with 4 KeV argon ions. They found that the small arced streaks could be explained by the presence of small crystallites slightly misoriented from the matrix. The darkfield micrograph Fig. (4.15d) shows the presence of included crystallites similar to those discussed above.

From measurements of the diameters of the ring of $\{\bar{2}20\}$ spots, and the halos, in Fig. (4.16), the interplanar spacing of the material producing the halos was estimated to be between 3.2 and 3.3Å. Mazey et al (1967) quoted a value of 3.28Å for the ~~official~~ effective lattice parameter of disordered silicon. Richter and Breitling (as quoted by Mazey et al 1967) have found a value for the effective lattice parameter of amorphous silicon of 3.22Å. Allowing for the inaccuracies of measurement due to the faintness of the halos; the value of $3.2 \sim 3.3$Å is in good

agreement with these values. This indicates that the diffraction halos were due to the presence of amorphous silicon, as opposed to the presence of a surface layer of hydrocarbon contamination.

5.5. The Nature of the Defects produced by Bombardment Rates less than the Saturation Value.

For growth rates $< 0.1\mu$ per minute the defects observed, consisted of 'black spots' of various sizes as can be seen in the micrographs shown in Section 4.

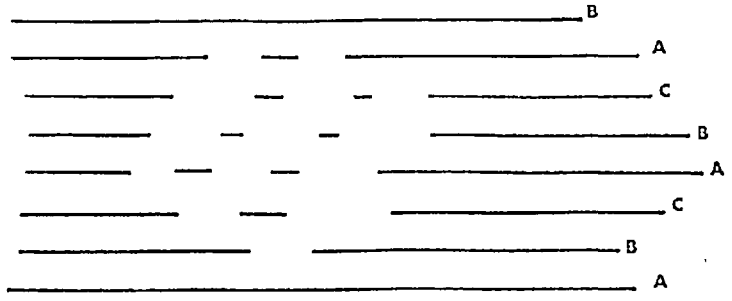
The defects do not have resolvable characteristic shapes, and so they were probably visible by diffraction contrast effects caused by lattice strain. Since the growth rate was less than the overlap bombardment level as given by BP, Fig. (5.6), it may be assumed that each spot represented the damage due to one ion although for doses very near to the saturation value, coalescence of damage zones may have occurred.

The diffraction contrast effects of defects produced by radiation damage in various materials have been investigated by many workers. The results of contrast calculations for the defects, and experimental results of defect analysis have been reviewed in detail by Rühle (1969).

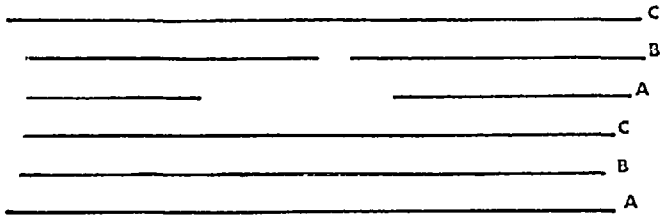
In Fig. (4.19b) it can be seen that the 'black spot' defect contrast vectors $\underset{\sim}{d}$, (whose sense is defined as in Rühle (1969)) make angles of $\sim 30^{\circ}$ with $\underset{\sim}{g}$. This indicated that the defect strain field displacements lay in $< 111 >$ directions, since the projection of a $< 111 >$ direction on to the (111) foil plane will lie in a [112] direction, which is at an angle of 30° to the $< 1\bar{1}0 >$ type directions in the (111) plane.

This result is consistent with the hypothesis that the black spot defects are Frank sessile loops produced by the condensation of vacancies or interstitials on to the $\{111\}$ planes, as illustrated in Fig. (5.7). Such dislocation loops would have Burgers vectors of the form $\pm \frac{a}{3} < 111 >$.

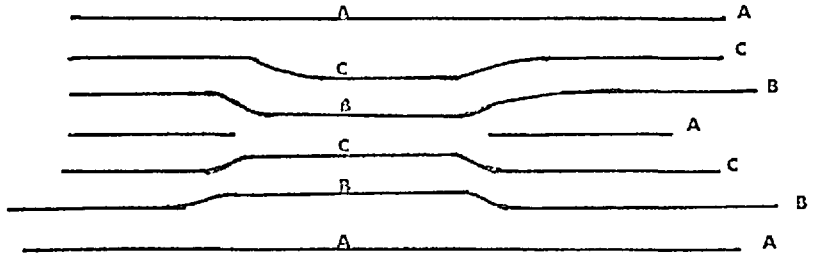
Rühle (1969) showed that the sign of $\underset{\sim}{g}.\underset{\sim}{d}$ (ie. the direction of $\underset{\sim}{d}$ relative to $\underset{\sim}{g}$) for defect images in micrographs taken under two-beam diffraction donditions depends not only on the type of defect, ie. interstitial or vacancy, but also on the depth of the defect within the foil. Thus it is not possible to distinguish between the defects



(i) THE INITIAL DISORDERED REGION



(ii) CONDENSATION OF THE VACANCIES ONTO (111) PLANE TO FORM A VACANCY DISC.



(iii) COLLAPSE OF VACANCY DISC TO FORM THE STACKING FAULTS.

Fig. (5.7)
STAGES IN THE FORMATION OF A STACKING FAULT BY THE COLLAPSE OF A VACANCY RICH REGION.

by the sign of $(\underset{\sim}{g}.\underset{\sim}{d})$ alone, unless the position of the defect within the foil is known.

The bombardment collision process produces equal numbers of vacancies and interstitials. The processes which can then occur are:-

(i) Recombination of the vacancies and interstitials to produce a relatively undamaged area;

(ii) Migration of the defects to other regions and sinks;

(iii) Formation and growth of clusters of defects of like types.

Under the experimental conditions, all of these processes will occur. One may dominate, however, to give the defects observed.

The mobilities of the interstitials and vacancies differ considerably. Rhodes (1964) states that interstitials migrate much faster than vacancies in silicon and germanium, because of the lower lattice distortion caused by interstitials. Moreover, the motion of a vacancy requires the breaking of strong covalent bonds, whereas the interstitial is not strongly bonded into the crystal. The diamond structure also is not close-packed, and has large open tetrahedral channels along $< 110 >$ directions as can be seen from Figs. (1.1) and (5.3b,c). This feature of the silicon crystal structure will enhance the mobility of interstitials considerably.

Theories of the formation of the radiation damage regions by Brinkman (1954) suggest that the regions consist of a central vacancy-rich core, surrounded by a shell of interstitial-filled material. This structure would produce an initial separation of the two types of defects, thus lessening the probability of recombination. Picraux et al (1969) used proton back-scattering measurements to investigate the damage produced by 40 KeV Sb ions. They found that after bombardments at temperatures of $200 \sim 300^{\circ}$ C, and doses less than the saturation value, no interstitial defects were observed. These were specially looked for in back-scattering measurements along the $< 110 >$ directions. The crystal structure of silicon is such that the interstitials, if present, would tend to congregate along $< 110 >$ directions, in the target crystals. From this data, it appears to be possible that the small black spot defects shown in Fig. (4.19b) are vacancy loops, of burgers vectors $\frac{a}{3} < 111 >$, though this point was not investigated in detail, and it was not possible to determine the exact nature of these defects.

5.6. Investigation of Stacking Faults

In section (4.2.(5)) the nature of the stacking faults was investigated and it was shown that the 'line' defects were intrinsic stacking faults and the tetrahedral defects were composed of extrinsic stacking faults.

Booker and Stickler (1963) showed that if it is assumed that the stacking faults are produced by a mismatched region at the substrate-layer interface, then the nature of this initiating defect could be found from the analysis of the resultant stacking fault. Their analysis showed that if the partial dislocation joining the two faults is a $\frac{1}{6} < 110 >$ stair-rod type, and the angle between the faults is acute, then the faults are both of the same type, ie. both intrinsic or both extrinsic.

If the angle between the faults is obtuse, then the faults are of dissimilar types, ie. intrinsic $\sim$ extrinsic, or vice versa. From this it can be seen that the three faults forming a 'tetrahedral' defect must all be of the same type, since they are at acute angles to each other. As can be seen from Fig. (2.6), the faults forming the tetrahedral defects are at obtuse angles to the initiating fault in the growth plane. Thus if the triangular faults are intrinsic, the initiating fault is extrinsic, and vice versa.

The tetrahedral defects in the films grown in the present work were found to be extrinsic. Thus, from the analysis of Booker and Stickler discussed above, it follows that if the initiating stacking fault lay in the $\{111\}$ growth surface, it would be intrinsic in nature.

Booker (1964) found that for both evaporated and chemically deposited layers, the tetrahedral defects consisted of three intrinsic faults. By the analysis of Booker and Stickler (1963) this indicated that the initiating faults were extrinsic in nature. This is in agreement with the mechanism suggested by Finch et al (1963), in which the faults are nucleated by clusters of impurity atoms on the surface.

The line defects examined by Booker (1964) were found to be intrinsic in nature as is the case in this investigation.

The variation of stacking fault densities as shown in the data of Fig. (4.10) may be due to the effects of the ion bombardment during the growth of the layers. This is in line with the observations of

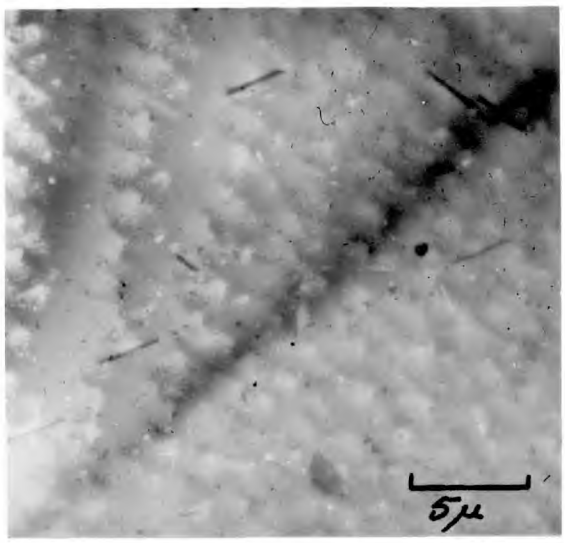
Pearmain (1971), who deposited silicon on silicon epitaxially by a sputtering technique using 10 KeV argon ions. He found that if the substrate was biased positively so as to repel any ions, then the stacking fault density of the layers was considerably reduced. Stacking faults were also observed by Irving (1969) in post-bombardment annealed silicon crystals, which had been implanted with 100 KeV phosphorous ions.

The extrinsic nature of the small tetrahedral defects indicated that the originating defects were intrinsic in nature. This is consistent with growth from vacancy clusters as suggested by Jacodine (1963).

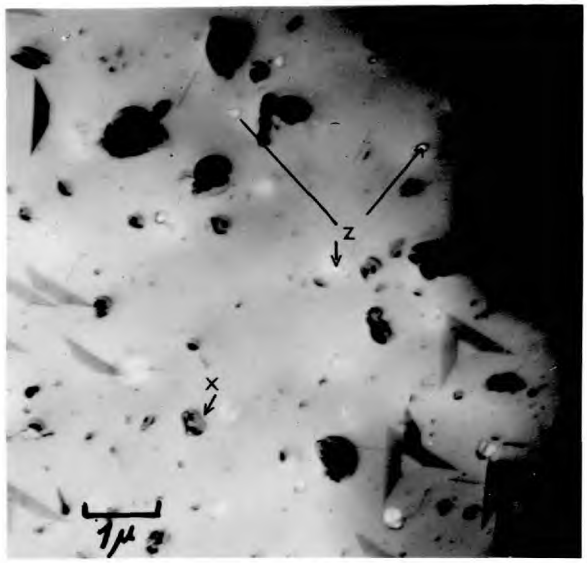
The results in Fig. (4.10) show that the fault density had a strong rate dependence. Whether this is due to deposition rate effects or the associated ion bombardment, which is proportional to the deposition rate, has not been resolved. Fig. (4.11) shows that features at the interface nucleated stacking faults. Since the pre-deposition treatment was maintained constant, it cannot have been responsible for the observed variation of stacking fault density.

It was also found that the coalescence of the nuclei did not produce stacking faults, as can be seen in Figs.(4.24) where the coalescence is seen to take place by a bridging flow of material between the nuclei. Also it is seen that the nuclei do not contain many stacking faults; though this latter fact may be due to the difference in growth conditions in the nucleation zone and the layer as discussed in Section (5.7.2.) The observation that no faults are produced at coalescence is in accord with observations of Thomas and Unvala and Booker, discussed in the review section (2.2.(6)). From the preceding discussion it is clear that the results obtained in this investigation may be interpreted on the basis of the ion bombardment effects. The good correlation between these observations and those reported in studies of ion bombardment phenomena strengthens the argument.

Experimental confirmation of the nature of the ions and of the bombardment effects are seen in Fig. (5.8). Fig. (5.8a) is a micrograph of a layer grown at 800°C and 0.06μ per minute with the substrate at earth potential. The mottled background characteristic of the bombardment effect can be clearly seen. Fig. (5.8b) is a micrograph of a layer grown at the same values of the deposition parameters, but which was deposited with the top plate of the vacuum system linked to



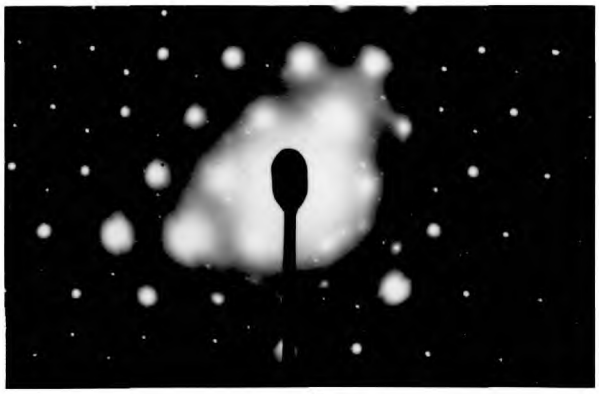
a



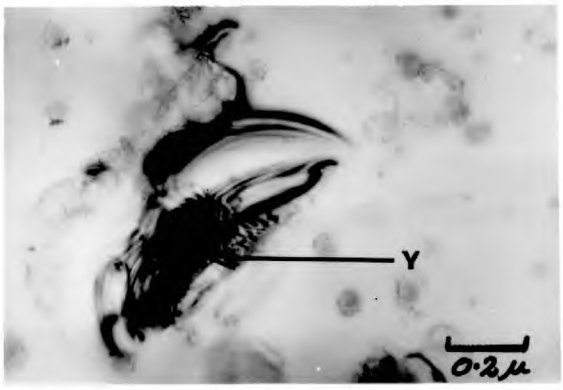
b



c



d



e



f

FIG. (5.8)

a. MICROGRAPH OF A LAYER GROWN AT 800° C, 0.06 μ per minute

b. MICROGRAPH OF A LAYER GROWN AT 800° C, 0.06 μ per minute; SUBSTRATE HELD AT + 10 KeV

c. DIFFRACTION PATTERN OF AREA IN a.

d. DIFFRACTION PATTERN OF AREA IN b.

e. AREA X IN b. AT HIGHER MAGNIFICATION

f. DIFFRACTION PATTERN OF AREA Y IN e.

the pedestal. This maintained the substrate at + 10 KeV. As can be seen, there was no trace of the mottled background, although some large 'black spots' are visible. The diffraction pattern of figure showed several of the $\{\bar{2}20\}$ type spots to be elongated and split. There were also large numbers of random spots in the diffraction pattern. The splitting of the diffraction spots indicated severe lattice strain. Fig. (5.8d) showed one of the black spots at higher magnification. As can be seen, fringes were visible, indicating the object to be crystalline. The bend extinction contours B around the area showed that the foil was severely and locally strained.

The selected area diffraction pattern of figure (5.8e) confirmed the crystallinity of the region and measurements of the spot spacing indicate it to be a small crystal of silicon embedded in the layer. It is concluded that the effect of maintaining the substrate assembly at + 10 KeV had caused the electrostatic attraction of small particles of silicon on to the substrate surface where they were engulfed by the layer. The small holes indicated at Z in Fig. (5.8b) are thought to be the places where these small crystalites or silicon particles have been dissolved by the thinning reagents.

The results of this experiment confirm that the ions were positive, and that they were responsible for the observed variation of the layer structure with growth rate and temperature.

From consideration of the effects of the ion bombardment, discussed in the preceding sections, it is seen that elimination of the ion bombardment would shift the line CD in Fig. (5.6) so that C and B coincide and BD would be parallel to CD. The region BPC would also be removed. Fig. (A2) in the appendix shows the modifications carried out to the apparatus, to allow reversal of the focussing electrode polarity. This polarity reversal eliminates the ion bombardment. Layers grown after these modifications were carried out, at rates and temperatures indicated by points T_1 ; T_2 in Fig. (5.6) were found to be epitaxial, thus confirming the hypothesis developed in sections (5.3), (5.4), and (5.5) of this thesis.

5.7. Nucleation and Growth Experiments

The results on nucleation and growth phenomena were carried out after modification to the electron beam furnace, to reverse the polarity. Thus the results obtained were directly comparable with those in the literature as discussed in the review.

5.7.(1) Analysis of the thermal cleaning process

The results obtained by other workers by heating silicon under various vacuum conditions have been described in the review. The work of Lander and Morrison, Hagstrum, Allen et al, showed that the silicon surface oxide layer could be removed by heating.

Fig. (4.20) illustrates the changes observed in the mass spectrum peak $[\frac{m}{e}] = 44$ during the heating of the silicon substrates.

The gaseous species which are likely to be present and which have $[\frac{m}{e}] = 44$, are CO_2^+ and SiO^+. Both are singly ionised species.

From plots 1 and 2 in Fig. (4.20) it can be seen that the increase in the 44 peak was not due to CO_2 evolved from the tungsten heater, although it was shown by Naber and O'Neal (1968) and a substrate heater of this type produced large quantities of CO_2. It is also unlikely that the peak was due to detection of SiO, since there was no direct line of sight from the substrate to the mass spectrometer, and the vapour pressure of SiO at room temperatures is of the order 10^{-10} torr, so it would have tended to condense on the relatively cold walls of the vacuum system. Thus it may be assumed that the increase observed in the 44 peak was due to CO_2 produced by heating the silicon substrate.

The rapid rise and fall shown in Fig. (4.20) suggested a reactant-limited reaction between the silicon surface and an absorbed layer. The coincident increase in the hydrogen peak, and the detection of silicon carbide on the surface, as shown by the diffraction patterns of Fig. (4.21), suggested that the CO_2 may have been produced by reaction between the clean silicon surface and a hydrocarbon. The fact that the reaction only commenced for temperatures $\geq 800^{\circ}C$ indicated that a clean silicon surface was necessary since this temperature was in the range found by Lander and Morrison (1961) for the thermal generation of an oxide-free surface under conditions of low partial pressures of oxidising gases.

This conclusion is reinforced by the results of the experiments on a heavily oxidised substrate, described in section (4.3.(1)). These results showed that an oxide-free silicon surface was required for the reaction to occur, and that thermal treatment alond would not remove a thick ($\sim 1\mu$) oxide layer.

The observations of silicon carbide on the surfaces of the silicon substrates after thermal processing were discussed in the review in section (2.2.(3)).

The observation of silicon carbide, as found by the workers who used oil diffusion pumped vacuum systems; and pressures of 10^{-1} torr, could be ascribed to contamination by hydrocarbons from the pump oils.

The finding of silicon carbide under oil-free ultra-high vacuum conditions in the present work indicated that a different source for the carbon must have been operative.

As discussed in the review, the possible sources of carbon which have been suggested are, carbon present in solid solution in the silicon, and surface contamination by the reagents used in preparing the surface. The results of Charig and Skinner (1969) discussed in the review confirmed the presence of carbon on the surface of the silicon after certain chemical cleaning processes.

As well as these possible sources of carbon, the residual gas mass spectrum, Fig. (3.2.), showed the presence of methane $[\frac{m}{e}] = 16$, and peaks at $[\frac{m}{e}] = 27, 29, 30$. The latter peaks indicated the possible presence of hydrocarbons of the forms C_2H_5; C_2H_6; C_2H_3. There was also the possibility that C_2H_4 was present as its peak at an $[\frac{m}{e}]$ value of 28 would be masked by the N_2^+ and CO^+ peaks. The peak heights at $\frac{m}{e} = 27; 29; 30$, indicate partial pressures of these gases of the order 10^{-10} torr.

These hydrocarbon compounds may have existed as definite gaseous species, in the residual gases, or they may have been produced in the mass-spectrometer as the "cracking-pattern" of a higher hydrocarbon. The action of the ion-pump would also have tended to crack any hydrocarbons present. Thus only light fragments would have been observed by the mass-spectrometer as was the case. No peaks in the mass spectrometer traces were found for $[\frac{m}{e}]$ values in the range 50-200.

From the results of section(4.3.(1)) it can be concluded that whilst the thermal treatment used removed the silicon surface oxide layer, large amounts of silicon carbide were produced on the surface, although no large crystallites were observed as found by Abbink et al (1968).

The source of the carbon is uncertain, but it may have been due to the presence of the hydrocarbon species discussed above.

5.7.(2) Analysis and Discussion of Nucleation Investigation

The method used to produce the nucleation zone, in Fig. (3.10) showed that the deposition rate varied across the nucleation zone. Thus the conditions in the nucleation zone were deposition at various rates for a constant time. This contrasts with the standard method used in nucleation studies, in which a series of discontinuous layers is grown at a constant rate, and for various deposition times. These nucleation studies usually use growth rates of the order 10 - 100 Å per minute. These low rates enable the deposition thickness to be easily controlled so as to produce discontinuous layers.

Because of the difference between the growth conditions of the layer and those in the nucleation zone, quantitative data on nucleation kinetics could not be obtained. However, the nucleation zone did represent qualitatively the growth processes of the layer.

In Fig. (4.2.(2)) it can be seen that the nuclei consisted of well-formed truncated pyramids slightly tilted, so that the top face blended into the substrate surface.

The variation of size of nuclei was due to the method of generating the nucleation zone as described above. Thus the smallest nuclei were those grown at the lowest rate, since the deposition time was constant over the whole zone. The effect of contamination by background gases may have dominated the nucleation process at this low rate. The areas in Fig. (4.2.(2) e.f.g.) corresponded to higher rates, and it can be seen that the growth of the nuclei is uniform, andthe tilted orientation is maintained until the initial coalescence stage.

Comparison between Figs. (4.2.(2)) and (4.2.(6)) showed that the pressure had a great effect on the morphology of the growth nuclei.

This effect may have been due to the presence of water vapour which, as can be seen from Fig. (3.2) is present in large quantities. Water vapour might have oxidised the surface. Thus the triangular shape might have been caused by the presence of surface oxide.

Joyce et al (1967) observed similar triangular growth islands at much lower pressures $\sim 10^{-9}$ torr. However, the thermal cleaning process they used may not have removed the oxide from the surface. There was some evidence of surface pitting in the micrographs of Fig. (4.2.(4)) which indicated the presence of large quantities of oxidising gases, in this case probably water vapour.

The tilted aspect of both the pyramid and terraced growths is significant. Abbink et al (1968) used substrates whose surfaces were deliberately misoriented by 2° from the exact (111) orientation, but did not observe any tilt effect in the nuclei. They did report that their thermal treatment produced surface steps, which were not operative in the nucleation process, during subsequent deposition.

Whilst the replication techniques used in this work were not sensitive enough to detect surface steps of the size found by Abbink et al, (1968) the tilt of the nuclei suggested that the initial growth commenced at steps in the surface. These steps would be produced as a consequence of the misorientation of the substrate surface as shown in Fig. (5.9a). Fig. (5.9b) illustrates the formation of tilted islands by lateral extension of these steps.

The effect of silicon carbide on pinning the growth fronts as shown in Fig. (4.26) is in agreement with data reported by various workers as discussed in the review, and these present results indicated that the presence of oxide as well as of silicon carbide may affect the initial growth.

It can also be seen from comparison of the range of epitaxial growth parameters shown in Fig. (4.1) with the data in Table III, that the presence of the silicon carbide as observed in this present work does not appear to inhibit epitaxial growth.

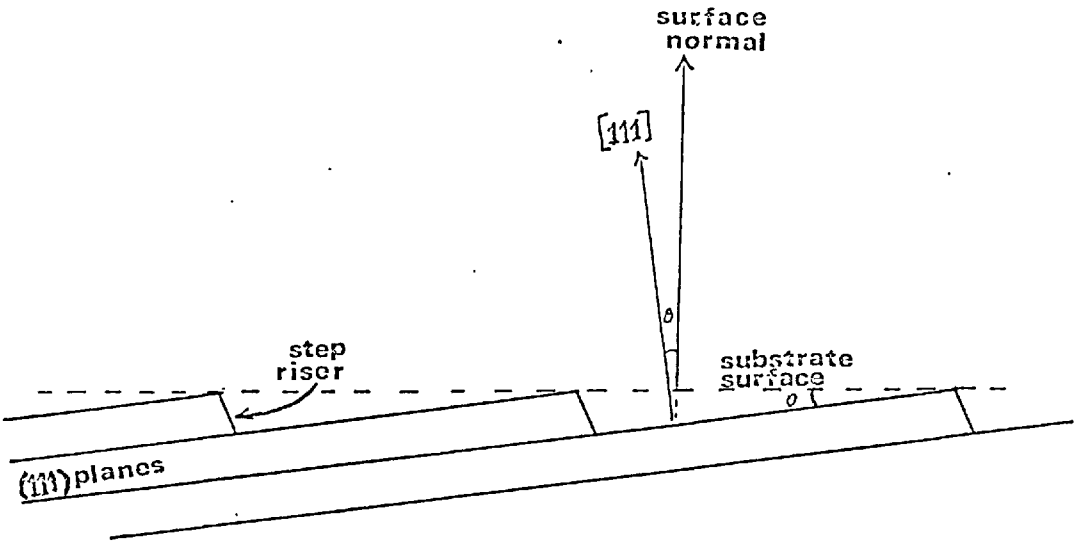


Fig.(5.9)a. SURFACE STEPS PRODUCED BY THE INTERSECTION OF THE (111) PLANES WITH THE SUBSTRATE SURFACE

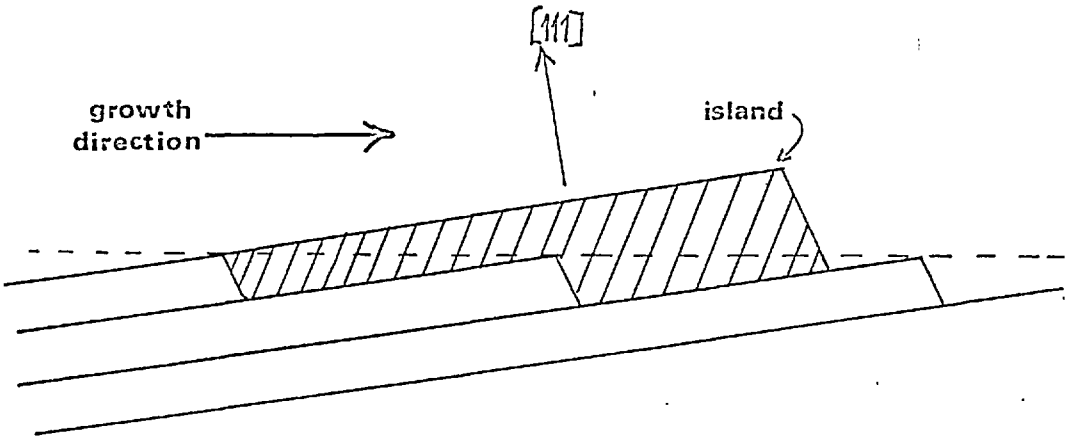


Fig.(5.9)b. EXTENSION OF THE SURFACE STEPS BY ADDITION OF MATERIAL AT THE RISER TO PRODUCE THE TILTED ISLANDS OBSERVED IN Fig.(4.24)

CHAPTER 6. ELECTRICAL MEASUREMENTS

The majority of the work presented in this thesis has been concerned with studies of the variation of the structure of the layers with the deposition rate and growth temperature.

Some experiments were carried out to measure some of the electrical properties of the layers. In this section, the experimental techniques which were used will be described, and the results discussed with reference to the structure of the layers as found from the transmission electron microscopy studies.

6.1. Introduction: Experimental Techniques.

The electrical properties of the epitaxial layer which are of interest, are carrier mobility and concentration. The former can be related to the crystalline perfection of the layer, and the latter to the dopent transfer mechanism between source and layer. The electrical properties which are manually measured are the Hall mobility μH and the resistivity σ. For a material in which both electrons and holes are active in the conduction process, the resistivity is given by the equation $\rho = [n_e e\mu_e + n_h e\mu_h]^{-1}$ where n_e and n_h are the concentrations of electrons and holes, and $\mu_e \mu_h$ are their respective mobilities. For specimens which show extrinsic behaviour, the conduction process is controlled by the impurity doping effects; and the resistivity $\rho = (n_c e\mu_c)^{-1}$ where n_c is the carrier concentration and μ_c the carrier mobility.

Resistivity measurements on samples of the geometry of those used in this work may be best carried out by means of four point probe technique as described by Valdes (1954) and Smits (1958). Uhlir (1955) has tabulated various correction factors relating the specimen dimensions and the geometry of the probe array.

The main difficulty in measuring the resistivity of epitaxial layers of silicon deposited onto silicon substrates, of the same conductivity type is the shunting effect of the substrate, which is electrically in parallel with the layer. This difficulty can be overcome by the use of substrates of the opposite conductivity type to the layer; and using the reverse biased junction so formed to electrically isolate the layer from the substrate.

In the work reported here, the majority of layers grown were of N type material deposited onto N doped substrates. Because of this, no junction isolation was possible, and Hall mobility studies could not be performed. The layer resistivity measurements were carried out using the technique described by Mazur and Dickey (1966), which does not require electrical isolation of the layer. This method is based on the measurement of the spreading resistance of a point probe, in contact with the surface of a 'semi-infinite' body. By combining this technique with bevel lapping of the layer, the vertical resistivity profile of the layer was investigated; by measurements of the spreading resistance as a function of probe position along the bevel.

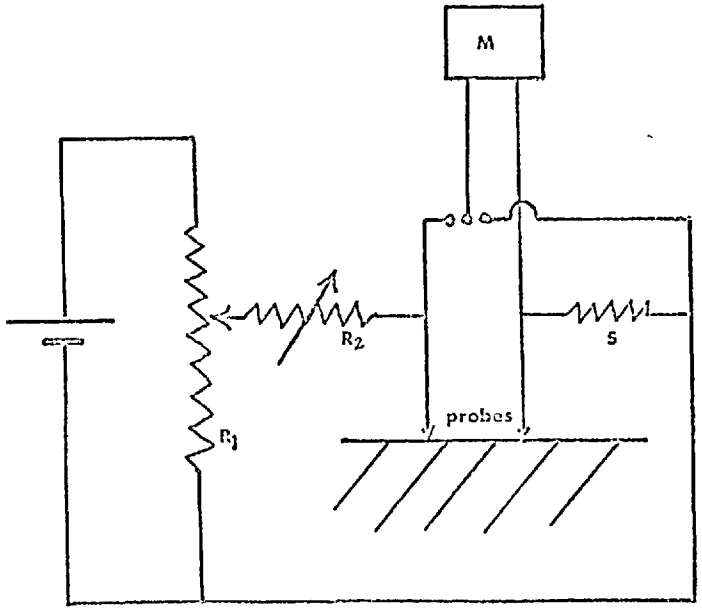
6.1.(1) The Spreading Resistance.

For a hemispherical contact of radius r embedded in the surface of a semi-infinite block of material of resistivity ρ, the resistance between the contact and the block is given by $R = \frac{\rho}{2\pi r}$.

The contact interface between a plane surface, and a probe of radius r, loaded by a force F, has been shown to be a circular disc of radius a, where a is given by the equation

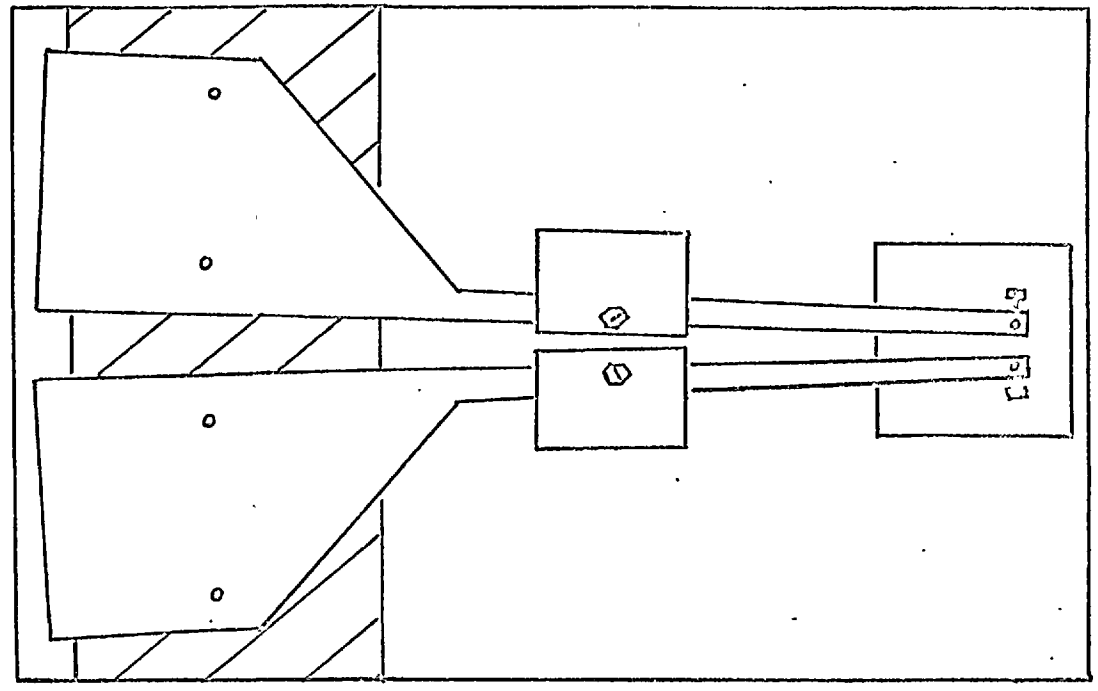
$a = 1.1. \left\{\frac{Fr}{2}\left[\frac{1}{E_1} + \frac{1}{E_2}\right]\right\}^{\frac{1}{3}}$: Bowden and Tabor, (1950). E_1 and E_2 are the Youngs moduli of the probe and surface materials.

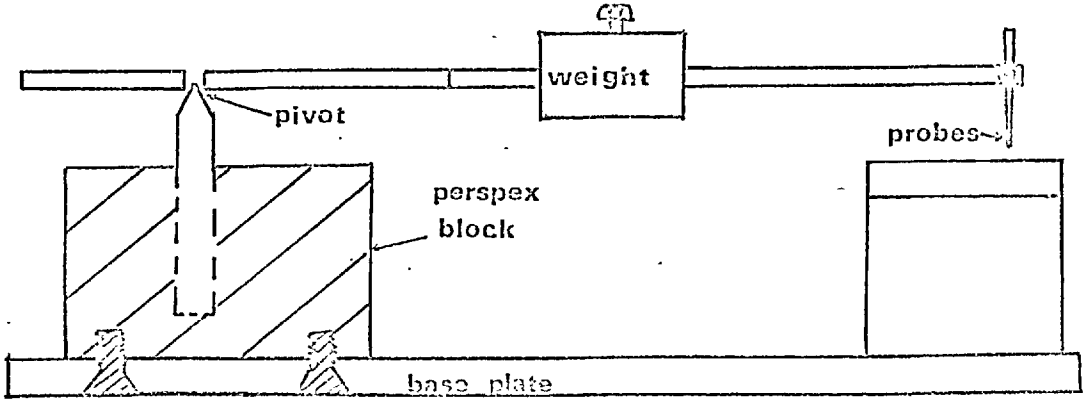
For this probe surface contact geometry, the spreading resistance $R_s = \frac{\rho}{4a}$; Shive (1959). Metal semiconductor contacts are non-ohmic because of the difference in band structure. Mazur and Dickey investigated the effects of probe voltage on carrier injection and showed that for probe voltages less than $\frac{kT}{e}$, [k = Boltzmans conts, e = electronic charge; T = temperature Deg. K], the carrier concentration and mobility in the material in the region of the probes was not appreciably disturbed and carrier injection does not occur. Mazur and Dickey also showed that for reproducibility of measurements, the specimen surface condition and probe loading and tip geometry must remain constant to ensure the same value of contact interface geometry. The apparatus used for the measurement of the resistivity profiles, is shown in Fig. (6.1). It consists of two osmium tipped probe needles, mounted on two arms, which were loaded to give the required probe force.



a

Fig. (6.1a)
ELECTRICAL CIRCUIT OF 2 POINT PROBE.
R_1 = 10K Ω R_2 = 50K Ω S = 1000 Ω 0.1%





b

Fig. (6.1b)
DIAGRAM SHOWING CONSTRUCTION OF THE
2 POINT PROBE.

The pivots for the probe arms were hardened steel points, which engage in holes bored in the arms, as shown in Fig. (6.1). This form of pivot prevents lateral motion of the probe tips. By making the probe arms convergo, the probe tip spacing was reduced to 1.5 mm. The probe loading was set to 50 gram weight by means of the adjustable weights, using a ballance to measure the loading. To raise and lower the probes onto the specimen surface, a cam operated lever was used. The probe needles were mounted into small bushes at the ends of the arms, and secured by grub screws. Electrical connections were soldered directly to the probes. Fig. (6.1b) shows the electrical circuit. The voltage across the probes was set to 10 mV using the variable resistors R_1 and R_2. The current flowing through the probes was measured by connecting the voltmeter across the standard resistor S, which is in series with the probes. The resistance between the probes, $Rp = \frac{10S}{V_s}$ where V_s is the voltage measured across the resistor S. If R_s is the spreading resistance of the probe contact, then $Rp = 2 R_s$, since the probes are in series. The voltmeter used was a high impedence type to avoid the shunting effect of the input impedence, since as can be seen from Fig. (6.1b), this impedence is in parallel with Rp.

6.1.(2) Callibration of the two point probe.

The results of Mazur and Dickey (1966) showed that the linear relationship indicated by the equation $R_s = \frac{\rho}{4a}$ varied with the conductivity type of the specimen. This effect they showed was due to metal-semiconductor contact effects. Because of this effect, a callibration of the two point probe was carried out using both P and N type substrates, whose resistivities were measured with a four point probe.

These substrates were beveled as described below, to produce a surface finish which would be the same as that on specimens to be examined. Fig. (6.2) shows the callibration curve obtained. The observed difference between P and N type materials is in accord with the findings of Mazur and Dickey.

6.1.(3) Bevelling Procedure.

The bevels were produced by lapping the specimen on a glass plate using a 1 degree or 3 degree bevelling tool.

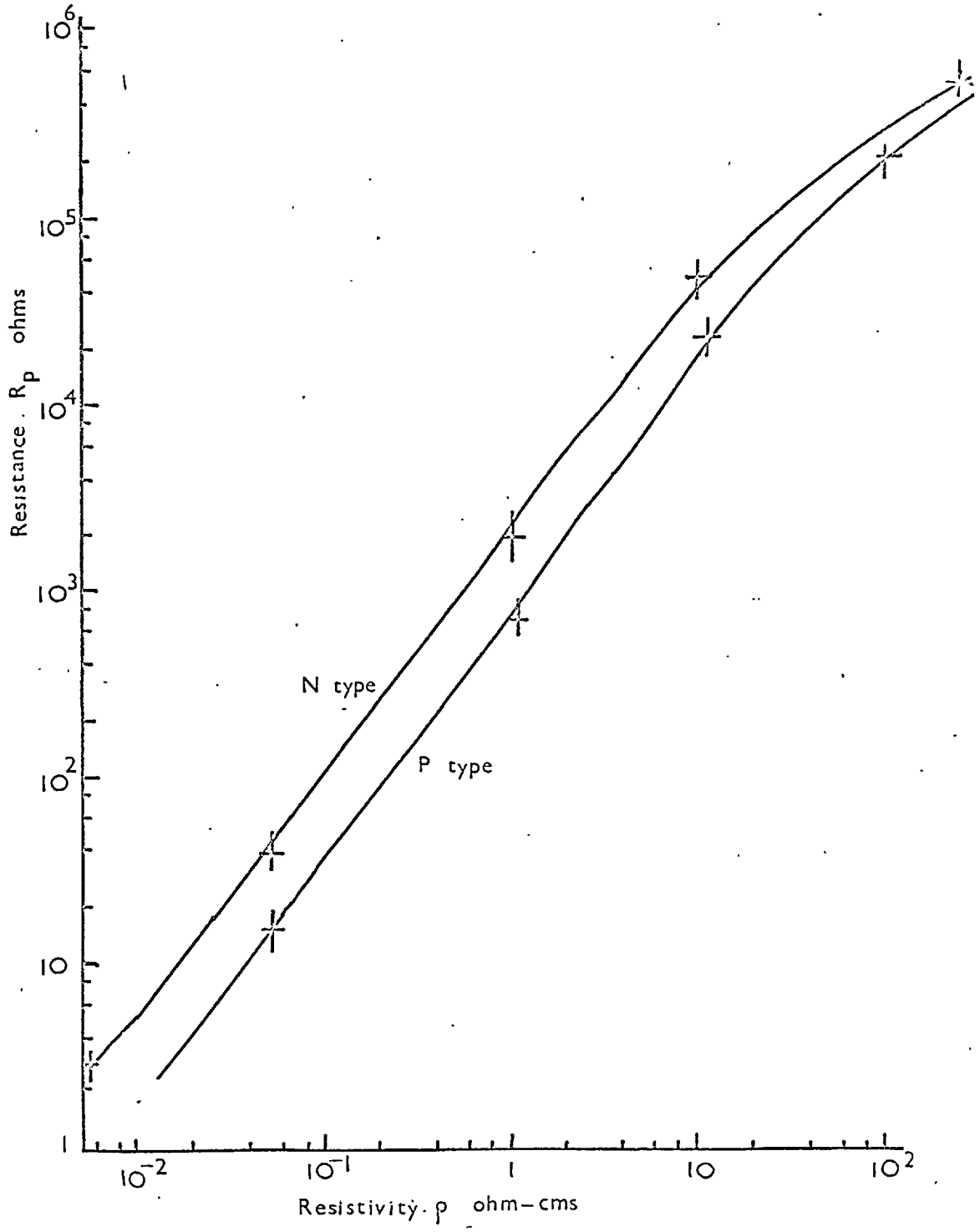


Fig. (6.2)
CALIBRATION GRAPH FOR 2 POINT PROBE.

The lapping process was carried out using 20μ diamond paste for 10 min. after which, the specimen was washed then lapped for a further 10 mins. using 7.5μ diamond paste. Before the resistivity measurements, the specimen was chemically polished using a solution of 5:3:5: Acetic Acid: Hydrofluric acid:nitric acid, for 1 minute. The bevel angle was measured using a 'Talysurf'.

6.1.(4) Other Electrical Measurements.

The conductivity type of the layer, was determined by the Thermal probe technique as described by Shive (1959).

As well as resistivity profiles measurements properties of PN junctions were also investigated, and experiments were also carried out, using a scanning electron microscope to investigate the electrical properties of the layers.

Conductivity Inversion.

Changes of conductivity type were observed by Allen (1959) who found that a thin P type skin formed on N type material after heating in vacuum. This effect was found due to boron transferred from the 'pyrex' glass walls to the silicon by residual water vapour.

In this present work, no traces of inversion were found. However, it was found that layers grown after long source use were P type although the source was initially N type.

6.2.(1). Results of Measurements of Resistivity Profiles.

Fig. (6.3.(i)(ii)) and (6.4) show resistivity profiles of layers grown at different substrate temperatures and rates. The source used was antimony doped N type material of initial resistivity 30 Ω cms.

Fig. (6.3(i)) shows the resistivity profile of an N type layer deposited at 600°C 0.1μ min^{-1}, onto an N^+ type substrate of nominal resistivity, 0.005 Ω cms.

It is seen that the profile is not a step as would be expected from the relatively low growth temperature. In comparison, Fig. (6.3(ii)) shows the resistivity profile of a layer deposited at 900°C; 0.1μ min^{-1} onto a substrate of nominal resistivity 0.005 Ω cms. It is seen that

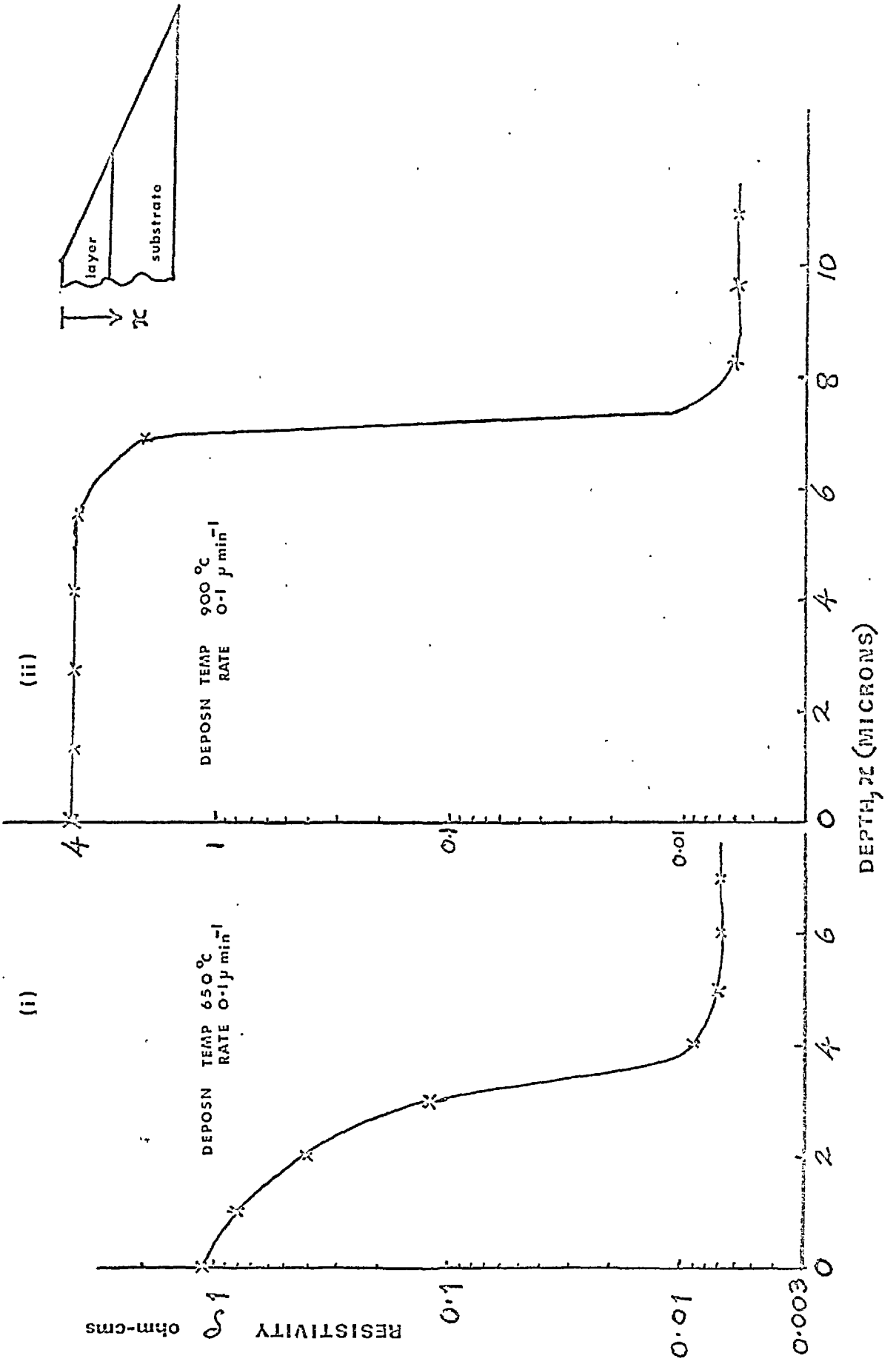


Fig. (6.3)
RESISTIVITY PROFILES OF N TYPE LAYER DEPOSITED ONTO N TYPE SUBSTRATES.

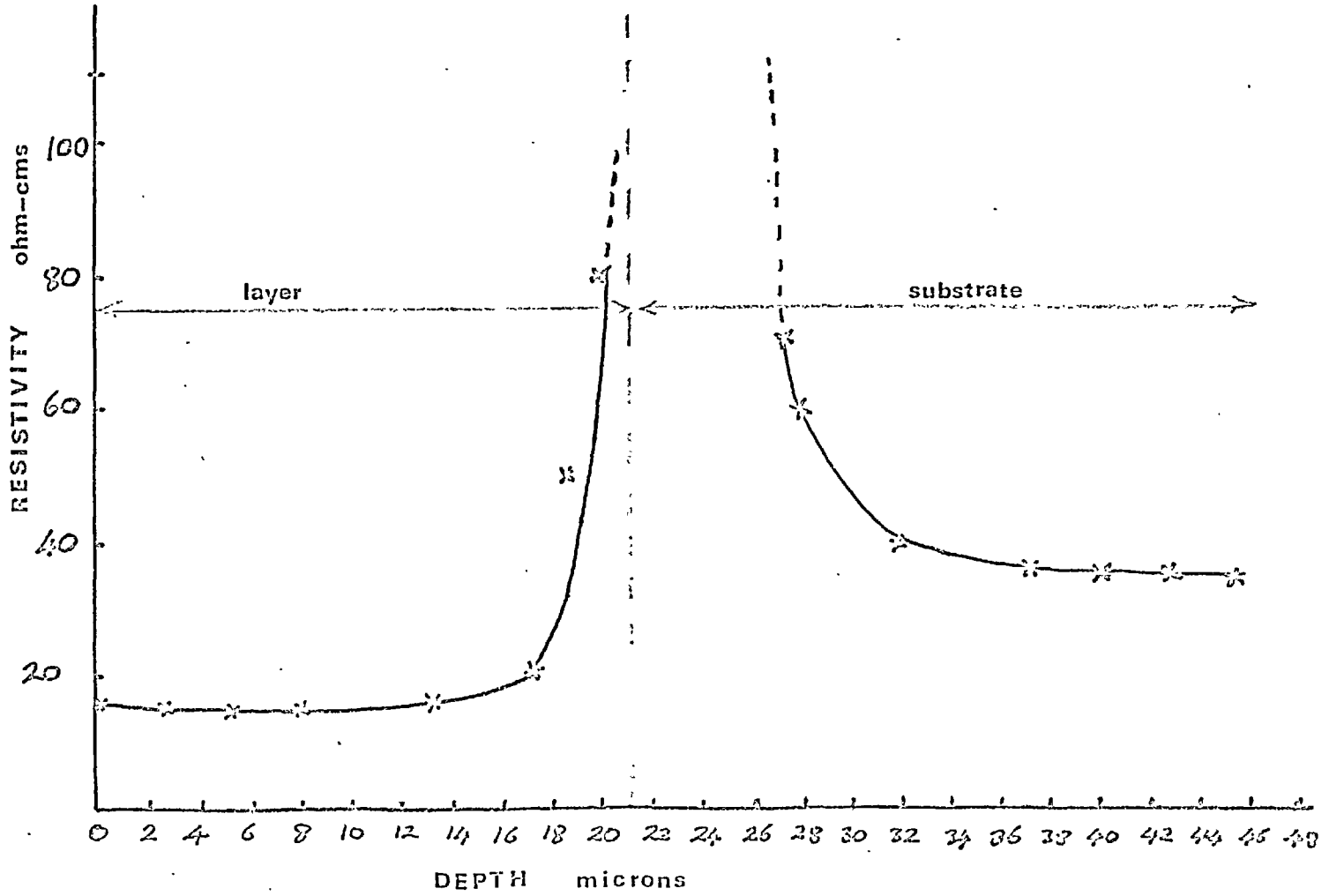


Fig. (6.4)
RESISTIVITY PROFILE FOR N TYPE LAYER DEPOSITED ONTO P TYPE SUBSTRATES.

the profile is a sharp step to within the limits of resolution of the probe arrangement used.

Fig. (6.4) shows the resistivity profile of an N type layer deposited at 850°C 0.15 μ min^{-1}, onto a nominal 35 Ω cm P type substrate.

6.2.(2) Measurements of I-V Characteristics of a P.N. Junction.

Fig. (6.5) shows the current-voltage characteristic of a PN junction produced by the deposition of N type material onto a P type substrate at deposition temperature of 850°C, and growth rate 0.15μ min^{-1}. [The 2 point probe resistivity profile of this layer is shown in Fig. (6.4).] The measurements of current and voltage were carried out on a mesa structure, whose dimensions are shown in the inset in Fig. (6.5). Contact lands on the N type layer, were made by the evaporation of antimony doped gold (0.1% Sb) onto the layer, thru a mask. These dontacts were then diffused in to produce ohmic contacts. The mesa was mounted on a standard transistor header, which provided an electrical contact to the substrate. Contacts to the layer were made by thermo-compression bonding to the evaporated gold lands, using 0.001" diam. gold wire.

The current-voltage characteristic shows the junction has good rectifying properties. The forwards slope resistance is however high. This may be due to the high resistivity of the materials used, - viz. substrate; 35 Ω cms, - layer; as found from 2 point probe measurements Fig. (6.4); - 15 Ω cms. The reverse biase characteristic shows a high leakage current, and breakdown occurs at about 40 volts. The high leakage current may be due to surface leakage at the edge of the mesa. This could be caused by traces of moisture at the exposed junction.

The reverse bias breakdown voltage observed is lower than is expected, from considerations of the thickness of the layer and resistivity. For these values in this specimen 20μ and 10 - 15 Ω cms, Runyan (1965) quotes a breakdown voltage of the order of 100 volts for an abrupt junction. A possible reason for this discrepancy will be discussed in Section 6.3.(1).

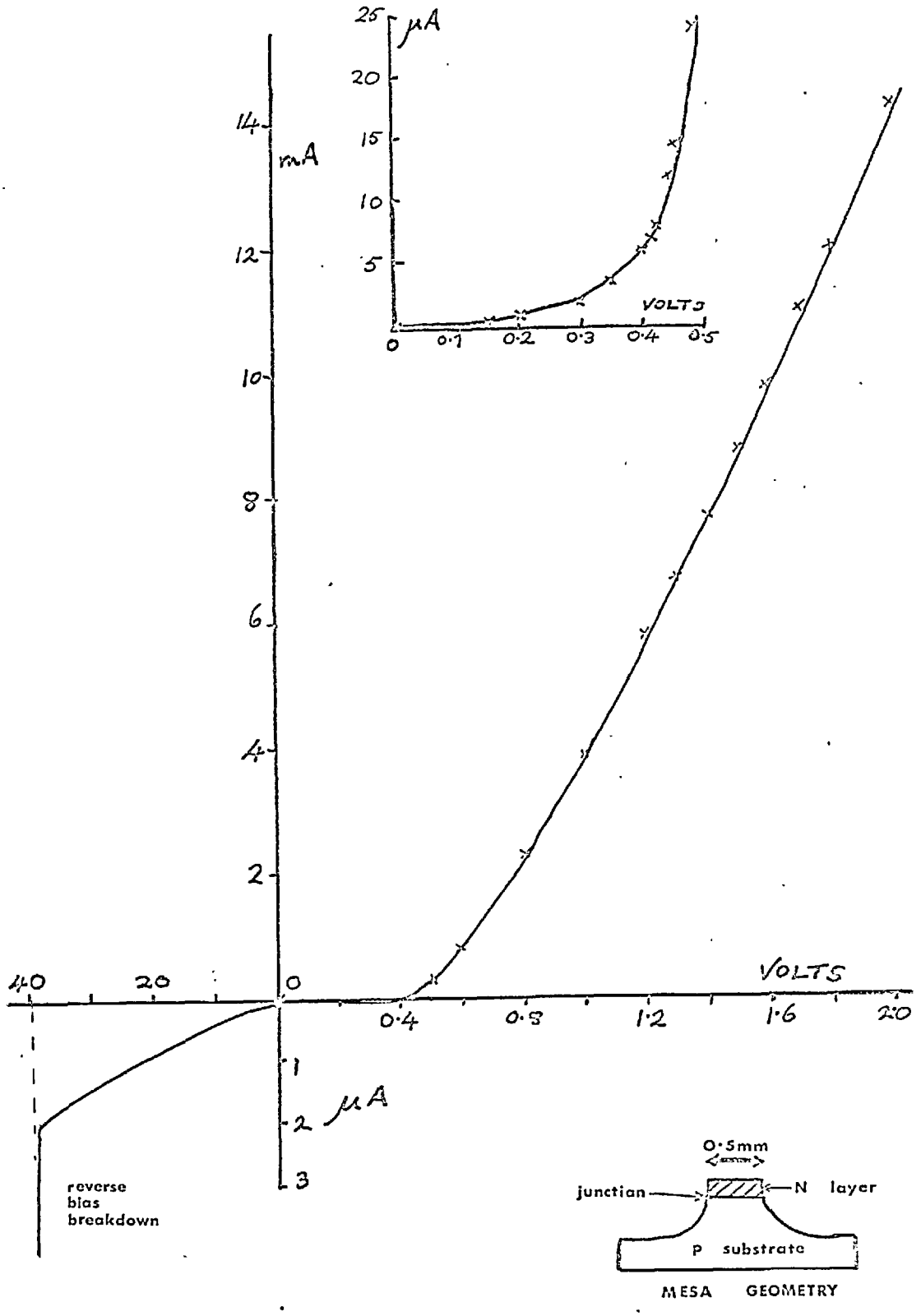


Fig. (6.5)
IV CHARACTERISTIC OF A PN JUNCTION GROWN AT 0.15 μ MIN^{-1}; 850°C.

6.2.(3) Scanning Electron Microscope Investigation of a P.N. Junction.

Fig. (6.7(i) and (ii) show S.E.M. micrographs of a cleaved edge of a P.N. junction. The specimen was the same as that whose I/V characteristic is shown in Fig. (6.5).

Fig. (6.7(i)) is a micrograph taken in the emissive mode. In this mode of operation, the micrograph contrast is controlled by specimen surface effects, such as surface electric fields or surface topography. This latter effect can be seen in the sharp deliniation of the cleavage steps along the edge of the specimen.

Electrically active regions such as P.N. junctions can be displayed by using the electron-hole pair current produced by the incident beam, to control the contrast of the C.R.O. display. The P.N. junctions appear as regions of strong contrast variation. This mode of operation of the S.E.M. is called the charge collection mode. Fig. (6.7(ii)) shows the same area as Fig. (6.7(i)); using the short circuit charge collection current to control the micrograph contrast. The experimental arrangement is shown in Fig. (6.8(i)). Electrical contacts to the specimen were made by springing wires against the sides of the specimen.

In Fig. (6.7(ii)) the P.N. junction is clearly seen as a bright line indicated by d in the micrograph. This line indicates the position of the junction depletion region. The depth of the junction from the surface of the N layer is of the order of 22μ. This is in good agreement with the thickness of the layer≈2μ as measured by the step profile method using the Tallysurf. The junction is also seen to be uniform over a distance of 300μ along its length.

By scanning the electron beam across the specimen in a line perpendicular to the P.N. junction, and measuring the electron- hole pair current produced; as a function of the scanning beam position, the minority charge carrier diffusion lengths may be found, by the method described by Thornton (1969).

If the electron-hole pairs are produced at a distance ℓ from the junction, which acts as a collector for the charge carriers; the number of carriers diffusing to the junction is proportional to $\exp\left[-\frac{\ell}{Ln}\right]$; where Ln represents the diffusion length of the minority carriers under consideration, ie. electrons on the P side of the junction; holes on the N. side of the junction.

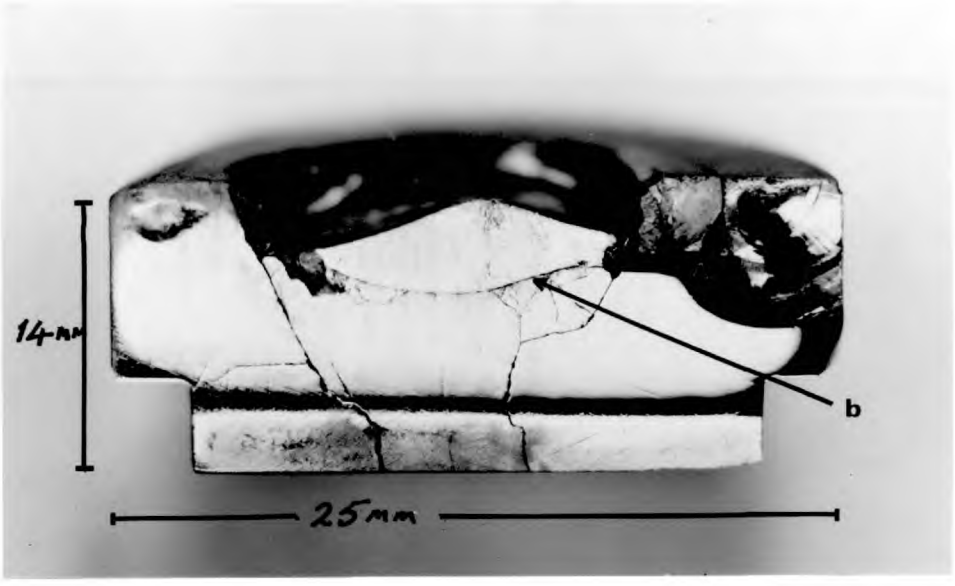


FIG. (6.6) POLISHED CROSS-SECTION OF A USED SOURCE, SHOWING MOLTEN ZONE BOUNDARY, b



i ii

FIG. (6.7) SCANNING ELECTRON MICROGRAPH OF AN N-TYPE LAYER DEPOSITED ON A P-TYPE SUBSTRATE AT 850° C; 0.15µ $min.^{-1}$

(i) BACK SCATTER CONTRAST MODE

(ii) S.C. SPECIMEN CURRENT CONTROLLED CONTRAST MODE

Fig. (6.8(ii)) shows a plot of the amplifier output; which is proportional to the charge collection current; as a function of the scanning beam position. This data is replotted in Fig. (6.8(iii)) as Log $\left[\frac{I(x)}{Imax}\right]$ versus x; where x is the distance of the beam impingement point from the junction. [The junction position, x = 0 is assumed to coincide with the value of current Imax.] From the simple theory given above, the plot, Fig. (6.8(iii)) should be two straight lines of slopes $\frac{1}{L_e}$ and $\frac{1}{L_h}$; where L_e and L_h are the diffusion lengths of electrons and holes respectively.

For the substrate side of the junction the plot shows a distinct curvature. A.B. represents a line of mean slope of the plotted points. The non-linearity of the variation of photo-voltaic currents with distance of the light spot from the junction has been analysed by Van Roosbroek, (1955). He has shown the non-linearity to be due to carrier recombination effects at the surface. Since the mechanisms of carrier generation, recombination and transport in photo-voltaic effects are similar to those pertaining in this experiment, it is thus possible that the observed non-linearity is due to this same effect.

The values of minority carrier diffusion lengths obtained from the graph, are $L_h \simeq 2 \times 10^{-4}$ cms.

$L_e \simeq 15 \times 10^{-4}$ cms.

As can be seen from these figures, the carrier diffusion length in the deposited layer is much smaller than that in the substrate, reflecting the effects of the ion bombardment on the layer structure. Fig. (4.18) is a transmission electron micrograph which shows the structure of a portion of the layer whose electrical properties are discussed above.

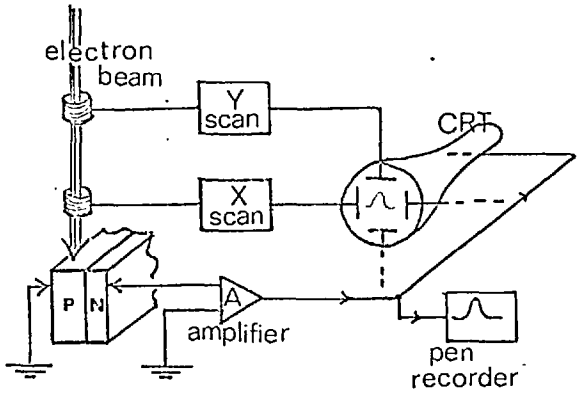
6.3. Discussion of the Results of Electrical Measurements Experiments.

The analysis of the layer structure, section (5.3), has shown the layer structure to be dependent on deposition temperature and ion bombardment rates. From this it is expected that structure dependent properties of the layers such as electrical conductivity will be similarly affected, and show a deposition rate, growth temperature dependence.

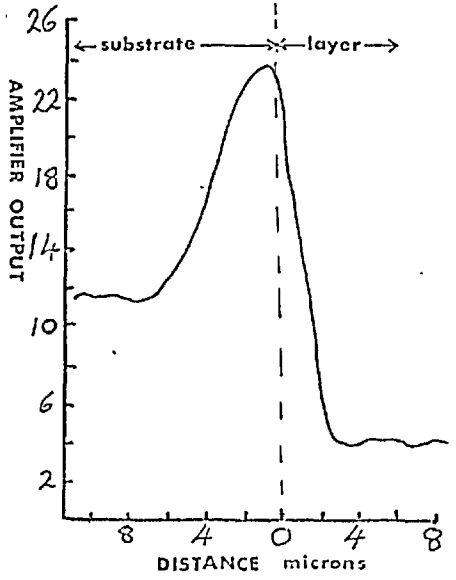
Fig. (6.8)
(i) EXPERIMENTAL ARRANGEMENT FOR CHARGE COLLECTION CURRENT MEASUREMENTS USING A SCANNING ELECTRON MICROSCOPE.

(ii) PLOT OF AMPLIFIER OUTPUT AS A FUNCTION OF ELECTRON BEAM POSITION.

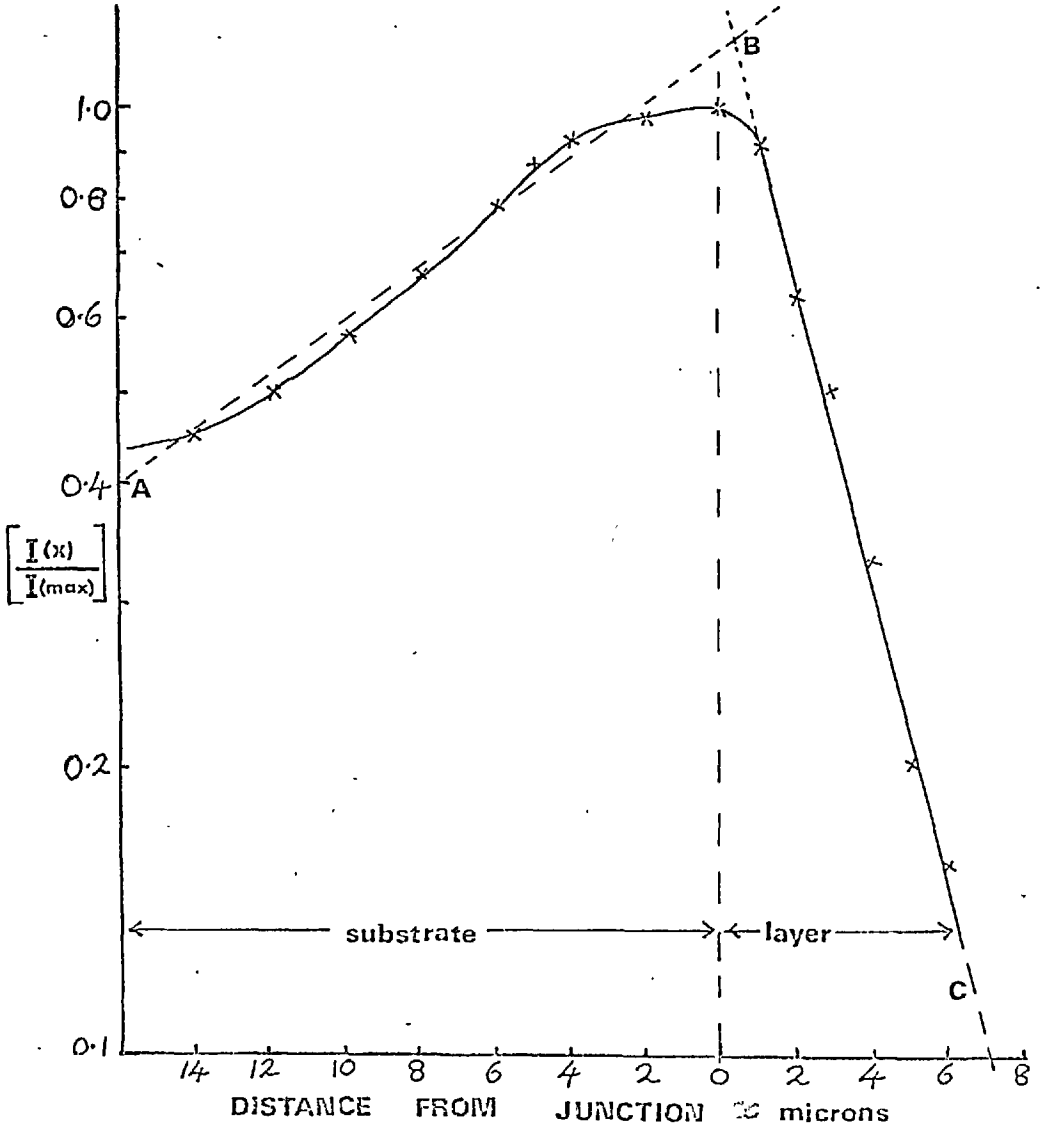
(iii) AMPLIFIER OUTPUT PLOTTED AS $\log\left[\frac{I(x)}{I_{max}}\right]$ VERSUS x, THE DISTANCE FROM THE JUNCTION.



(i)



(ii)



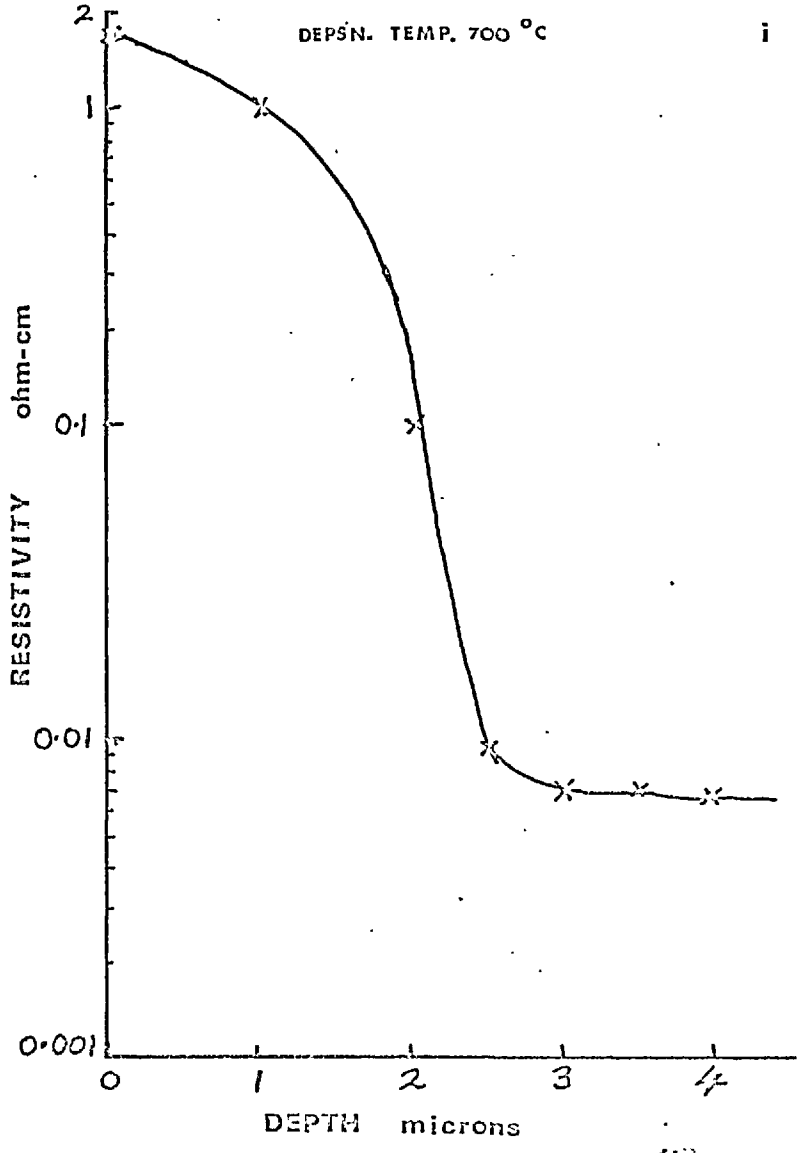
(iii)

The large body of literature on experimental investigations of radiation damage effects on the electrical properties of semiconductors have been reviewed by various authorities. Crawford and Cleland (1957), Billington and Crawford (1961), Crawford (1964), Corbett (1966), Mayer and Marsh (1968). The results of the experiments show that the effects vary with the nature of the radiation, the temperature during bombardment and the post-bombardment annealing treatment.

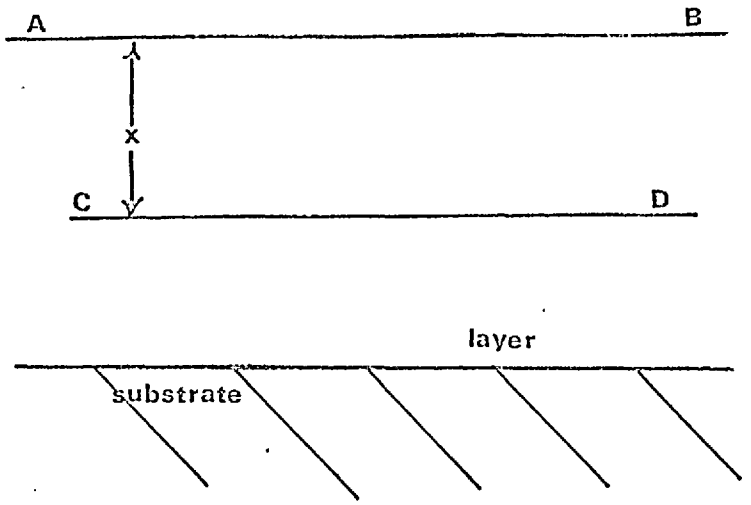
The main observed effects in radiation damaged silicon are as follows:
(i) Decrease of carrier life-time caused by the formation of trapping centres associated with the radiation damage.
(ii) Increase in resistivity caused by the reduction of the carrier concentration due to the production of donor and acceptor levels in the forbidden energy gap. These energy levels are associated with the interstitials, which show donor characteristics, and vacancies which have acceptor characteristics. Energy levels are also produced by combinations of these defects, ie. divacency and trivacency clusters, also vacency impurity combinations, for example vacancy-oxygen pairs.
(iii) The carrier mobility is also reduced by lattice disorder scattering.

6.3.(1) Analysis of the Resistivity Profiles.

From Fig. (6.4(i)(ii)) it is seen that the resistivity profile of the layer grown at the higher temperature 900°C, is sharper than that grown at 600°C. This variation cannot be due to diffusion of dopent between layer and substrate, since if this were the case, the profile exhibited by the 900°C growth would show a greater deviation from a step profile than the 600°C profile, since diffusion coefficients increase exponentially with temperature. Thus the variations of resistivity shown in the profiles can be attributed to the effects of the ion bombardment during the deposition of the layers. This is confirmed by comparison of Figs. (6.4(i)) and (6.9(i)), which shows the resistivity profile of a silicon epitaxial layer, grown by an ion bombardment sputtering technique; Unvala and Pearmain (1970). As can be seen, the profiles are very similar in shape. These profiles can be analysed by means of a simple model analogous to that used in analysing the structural variations of the layers as discussed in section (5.3).



(i)



(ii)

Fig. (6.9)
(i) RESISTIVITY PROFILE OF A SILICON LAYER DEPOSITED BY ION BEAM SPUTTERING.

(ii) CROSS-SECTION THROUGH A LAYER.

Fig. (6.9(iii)) represents a section through a layer. AB is the free surface, and CD represents a layer δx thick at a depth x below the surface AB. Since the bombardment accompanys the growth, the bombardment disorder in layer CD was a maximum when CD was the free surface. After coverage of CD by deposited material, no further disordering occurs, but since growth continues at the deposition temperature T, annealing of the damage in layer CD will also continue. Thus the resistivity profiles can be interpreted as representing isothermal anneal profiles of the radiation damage, with the depth x, proportional to the annealing time.

For the layer CD, the disorder remaining after annealing may be described by the equation

$$\text{Disorder} = a[R_b - \int_{t_1}^{t_2} A\, dt]$$

Where a is a contant. R_b is the rate of bombardment, A, the rate of damage anneal, t_1 the time at which CD was the growth surface, t_2 the total growth time of the layer. It is assumed that the rate of annealing is proportional to time. Since the effects of the radiation damage are to increase the resistivity, as discussed above, in section (6.3), it is assumed that the measured resistivity of a radiation damaged sample is equal to the sum of the unirradiated resistivity ρp; and a component ρD which is proportional to the net disorder in the sample. ie. ρD and $a[R_b - \int_{t_1}^{t_2} A\, dt]$

We may then put ρCD; the measured resistivity of the layer CD, equal to $\rho p + \rho CD$

$$\therefore \rho CD = Ka[R_b - \int_{t_1}^{t_2} A\, dt] + \rho p.$$

Rg, the growth rate $= \frac{dx}{dt}$. therefore $dt = \frac{dx}{Rg}$.

$$\therefore \rho CD = Ka[R_b - \int_{o}^{x} \frac{A\, dx}{Rg}] + \rho p$$

where x is the depth of the layer CD. Integrating, we may put

$$\rho(x) = Ka[R_b - \frac{Ax}{Rg}] + \rho p.$$

At x = O; corresponding to the surface layer, we may put $\rho(x)_o = \rho max$. Then $\rho max = KaRb + \rho p$. Thus we may write $\rho(x) = \rho max - \frac{KaAx}{Rg}$

Hence $[\rho max - \rho(x)] = \frac{KaAx}{Rg}$

Thus if the simple model used is correct, a plot of $[\rho max - \rho(x)]$ versus x, the depth will be a straight line of slope $[\frac{KAa}{Rg}]$. Fig. (6.10)

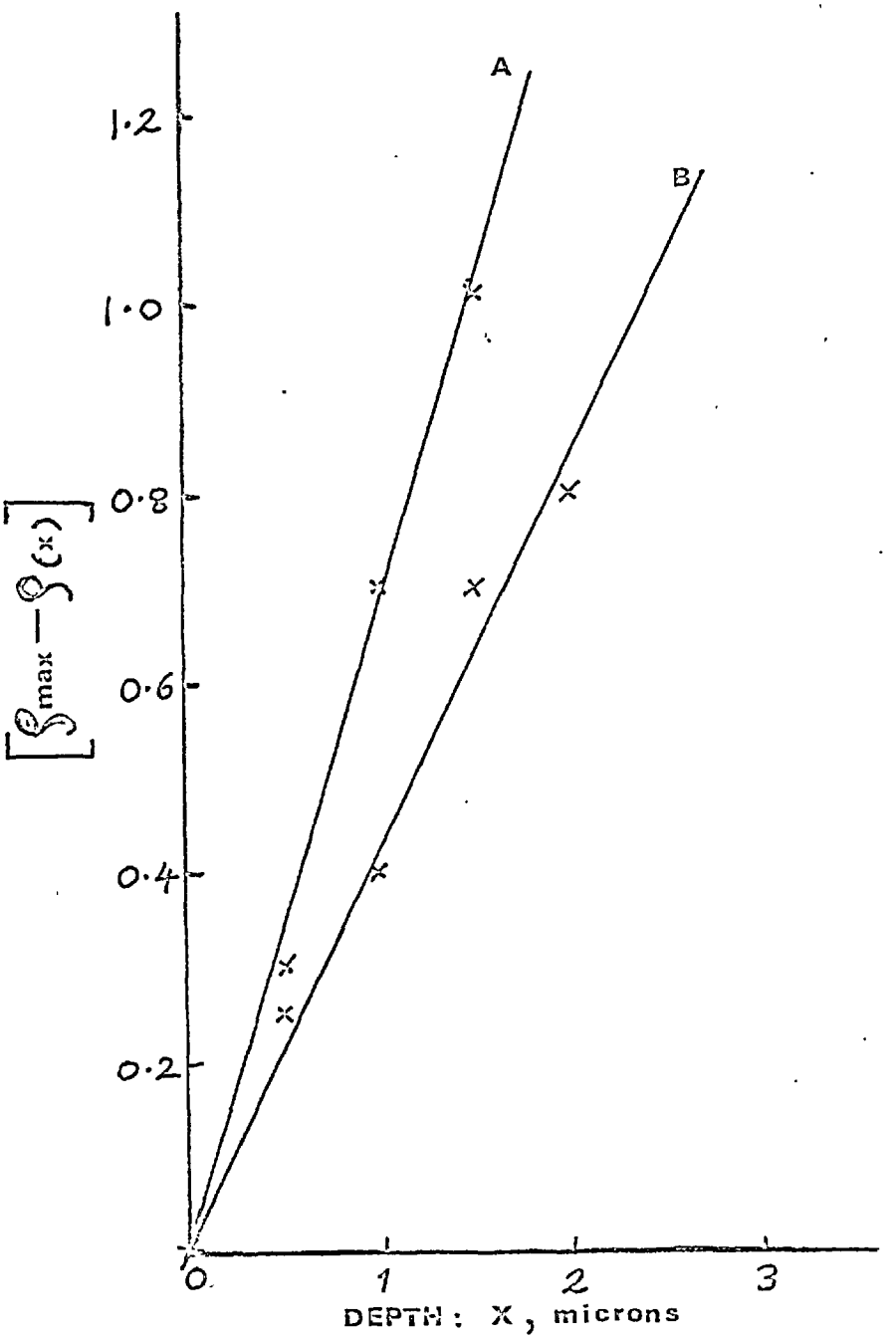


Fig. (6.10)
PLOT OF [ρ max - ρ (x)] VERSUS DEPTH IN LAYER; x: FOR PROFILES SHOWN IN FIGS.(6.3) AND (6.9).

shows plots of $[\rho_{max} - \rho(x)]$ versus depth x for the profiles shown in Fig. (6.3(i)) and (6.9(i)). OA is obtained from the profile in Fig. (6.9(ii)).

As can be seen, the plots are straight lines indicating the validity of the model. It is possible to extend the analysis to estimate the activation energy of the annealing process. The slopes S_i of the plots in Fig. (6.10) are given by $S = \frac{KAa}{Rg}$. If it is assumed the annealing process is of a simple first order type, then the rate of anneal A may be put as $A_0 e^{-\frac{q}{KT}}$, where A_0 is a constant and q is the activation energy of the annealing process, and T the anneal temperature in deg. absolute. Thus $S = \frac{Ka}{Rg} \cdot A_0 \exp[-\frac{q}{KT}]$. taking logariths; $\log_{10} S = \log[\frac{A_0 Ka}{Rg}] - \frac{q}{2.3KT}$ then $\frac{\partial}{\partial(1/T)} \log S = -(\frac{q}{KT})$.

ie. $\left\{\frac{\log S_1 - \log S_2}{1/T_1 - 1/T_2}\right\} = \frac{q}{2.3k}$.

From this equation and the values of temperatures and slopes from Fig. (6.10), q has a value in the range 0.3 - 0.4 ev. Davies and Roosild (1971) have examined the high temperature annealing processes of radiation damage produced by doses of 10^{14} cm^{-2} 1MeV carbon ions. They found for temperatures $\geq$ 700°C, several annealing processes occurred, of which the two major processes detected had activation energies of 0.32 and 0.38 ev, the value found in this present work is thus in good agreement with these values.

The resistivity, $\rho = [ne\mu]^{-1}$ where n is the number of charge carriers, and μ is the mobility. The observed variations in resistivity discussed above, could be caused by either variation of carrier concentration or mobility. The results obtained in this work, do not enable these alternatives to be distinguished.

The work of Davies and Roosild (1971) indicates that for anneal temperatures $\geq$ 600°C, for the dose specified above, the mobility is restored to its pre irradiation value. From this it is possible that the resistivity variations observed in this present work may be due to variations in carrier concentration caused by trap annealing. The quoted temperature of 600°C, Davies and Roosild (1971) corresponds to the overlap disorder annealing stage as discussed in Section (5.1).

The structure of the layers whose deposition parameters lie in region BPC in Fig. (5.6), as deduced from the micrographs in Figs. (4.15), (4.16), (4.17), (4.19a) is shown in Fig. (6.11). The layer consists of regions of vacancy rich material, V, distributed in a matrix of relatively good crystal material the matrix would alsl contain a large number of small defect clusters, C. This structure would exhibit a mobility characteristic of the matrix material, with a large number of traps, associated with the interfaces of the defect disorder regions and the silicon crystal matrix. A similar structure was postulated by Gossick (1959) to explain the effects of neutron irradiation on the lifetime of charge carriers in silicon. This form of structure would also have similar properties to the SiO_2 precipitate model discussed by Shockley (1961) to explain some aspects of P.N. junction reverse vias breakdown. It is possible that the carrier trap sites associated with interfaces of the vacancy regions V, and the silicon crystal matrix would have similar effects to those associated with the SiO_2 precipitates, thus causing the low value of reverse bias breakdown voltage shown in Fig. (6.5).

As discussed above, the general effect of radiation damage is to increase the resistivity. Thus the fact that the values of $\delta(max)$ observed in Figs. (6.3) are very much less than the source resistivity, indicated that the dopent was evaporated preferentially, as was observed by Hale (1953). This was confirmed by a thermal probe investigation carried out on a used source. Fig. (6.6) shows a polished crossection through a used N. type source. (Use time estimated at about 5 hours) The molten pool boundary is seen, indicated in the figure by b. It was found that whilst the rest of the source had remained n type, the molten pool region was strongly p type.

The antimony dopent has a much higher vapour pressure than silicon $\left(\left.\frac{P_{sb}}{P_{Si}}\right|_{1800^\circ C} \simeq 10^{7}\right.$ as given by the R.C.A. vapour pressure data$)$ thus it would tend to evaporate more rapidly than the silicon, leaving any low vapour pressure dopents such as boron in the molten pool. Boron has a lower vapour pressure than silicon $\left(\frac{P_B}{P_{Si}} \simeq 10^{-4}\right)$ and thus the molten pool would tend to become boron rich. This effect could account for the observation of N type source material producing P type layers.

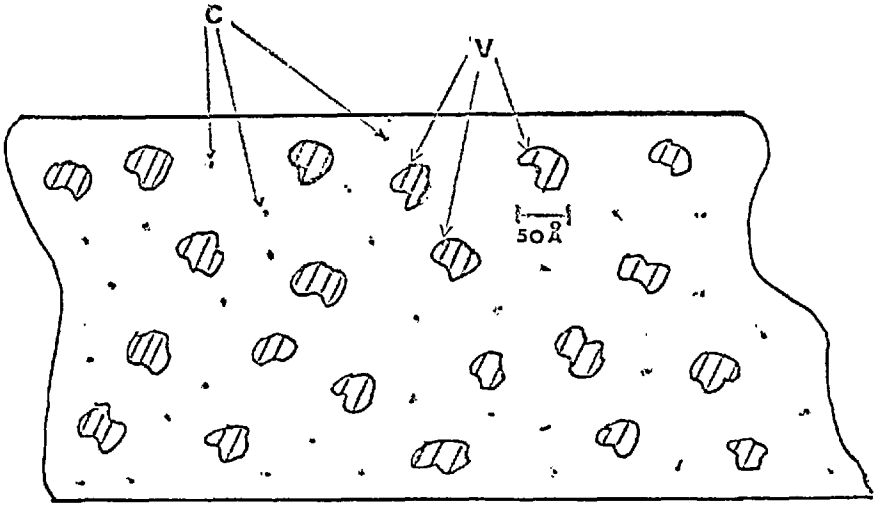


Fig. (6.11)
STRUCTURE OF LAYER GROWN AT
$T > 650^{\circ}C$; $R > 0.1\mu$ MIN.
AS DEDUCED FROM TRANSMISSION MICROSCOPY AND ELECTRICAL MEASUREMENTS.
V = VACANCY RICH REGION.
C = SMALL DEFECT CLUSTER.

Summary

From the analysis of the electrical measurements data, it is seen that the electrical properties of the layers were controlled by the structure produced by the effects of the ion bombardment.

However, the resistivity profiles suggest that elimination of the ion bombardment, will enable sharp step junctions to be grown. The sharpness of the profiles which can be produced is aided by the predeposition thermal treatment, described in Section 3., which produces negligible dopant depletion from the substrate surface.

Chapter 7. Suggestions for Future Work.

The work reported in this thesis has shown that the variation of epitaxial temperature with deposition rate, and the layer structure, were controlled by the effects of the ion bombardment, which accompanied the deposition.

It has also been shown that these delaterious effects can be removed by reversal of the furnace electrode polarity as discussed in the appendix.

The future work using the evaporation technique for the production of epitaxial layers can be divided into two parts, (i) structure and growth, (ii) electrical properties.

(i) Structure and Growth Studies.

The examination of the variation of epitaxial temperature with rate, especially for temperatures and rates around the values of 400°C; 0.1μ min^{-1}; where as can be seen from Fig. (2.8) there is a change in the activation energy of the growth process. Also investigation at deposition rates and temperatures below 400°C; 0.1μ min^{-1} where there is little reported data.

The investigation of fault densities as a function of growth rate temperature and surface treatment, would throw light on the processes of fault nucleation, and hence on treatments to avoid the formation of stacking faults.

(ii) Electrical Properties.

The electrical measurements carried out have shown that the low growth temperatures can produce sharp resistivity profiles, but the 'pool depletion' effect allows little control of the layer resistivity. Control of resistivity could be achieved by the use of intrinsic material as a source, and the co-evaporation of the dopent or the introduction of the dopent as a background gas.

By the grwoth of layers of opposite conductivity type to the substrate, the electrical properties of the layers could be studied by using the reverse biased junction to isolate the layer. This technique would enable Hall mobility studies to be carried out on

the variation of the mobility with deposition parameters. These results could also be correlated with the structure as observed by electron microscopy.

TABLE (I)

Pressure Torr.	Number of Molecules Hitting 1 sq. cm. per sec.	Number of Monolayers Absorbed per sec. [for sticking coefficient of unity.]
10^{-2}	3.8×10^{18}	4.4×10^{3}
10^{-4}	3.8×10^{16}	4.4×10^{1}
10^{-5}	3.8×10^{15}	4.4×10^{0}
10^{-7}	3.8×10^{13}	4.4×10^{-2}
10^{-9}	3.8×10^{11}	4.4×10^{-4}
10^{-10}	3.8×10^{10}	4.4×10^{-6}

TABLE (II) PROPERTIES OF SILICON CRYSTAL PLANES.

Plane	Area of Unit Cell in Plane	No. of Atoms in Area	No. of Available Bonds in Area	Atoms per sq.cm. $\times 10^{14}$	Available Bonds per sq. cm. $\times 10^{14}$
(111)	$\frac{\sqrt{3}\, a^2}{2}$	2	3	7.85	11.8
(110)	$\sqrt{2}\, a^2$	4	4	9.6	9.6
(100)	a^2	2	2	6.8	6.8

TABLE (V) VALUES OF SILICON-SILICON BOND ENERGY.

Energy [ev]	Reference
3.51	Steele and Stone (1962)
2.03	Gun and Green (1961)
2.17	Kleinberg et al (1960)
2.2	Honig (1954)
3.78	Kubechewski, Alcock and Evans (1958)
3.24	Drowert et al[¤] (1958)

TABLE (VI) VALUES OF $E_c^{¤}$ FOR VARIOUS IONS AND A SILICON TARGET.

Element	Atomic No. Z	Mass No. M	E_c (in Si) (^{c}See Text) KeV
Boron	5	10	7.6
Phosphorus	15	31	201
Arsenic	33	75	1380
Antimony	57	121	4000
Silicon	14	28	162
Aluminium	13	27	138
Germanium	32	72	1280
Copper	29	63	1020
Helium	2	4	0.325

[¤]Values calculated from the data of Gibbons (1968).

APPENDIX I

Radiation Heating

The model on which the calculations are based consists of two close-set parallel planes of large area, so that edge effects can be ignored. If the emissivities of the planes are e_1 and e_2, and they are at temperatures $T_1\,^{o}K$ and $T_2\,^{o}K$, then the energy radiated by unit area of plane 1 is $W_1 = e_1 sT_1^4$, where s = Stephans constant.

If a fraction, $e_2 W_1$ is absorbed by unit area of plane 2, and the rest reflected back towards plane 1, then by considering the multiple reflections, at each of which a fraction e_2 of the incident energy is absorbed, we have the net amount of energy transferred from plane 1 to plane 2: $q_{1,2}$ is

$$q_{1,2} = e_1 sT_1^4\left[1 - \frac{e_1(1-e_1)}{(1-z)}\right] - e_2 sT_2^4\left[\frac{e_1}{(1-z)}\right] \quad \text{where}$$

$$z = (1 - e_1)(1 - e_2).$$

At temperature T_2, plane 2 will radiate to the surroundings which are at temperature $T_0\,^{o}K$. Then if $q_{2,0}$ is the rate of radiation of energy to the surroundings, at equilibrium $q_{1,2} = q_{2,0}$.

$q_{2,0} = e_2 s(T_2^4 - T_0^4)$; since T_0^4 is small with respect to T_2^4, we may put $q_{2,0} \approx e_2 sT_2^4$.

Substituting for $q_{1,2}$ we have:-

$$e_1 sT_1^4\left[1 - \frac{e_1(1 - e_1)}{(1 - z)}\right] = s\, e_2\, T_2^4\left[1 + \frac{e_1}{(1 - z)}\right]$$

$$\text{Therefore } T_2^4 = \frac{e_1[(1 - z) - e_1(1 - e_2)]}{e_2[(1 - z) + e_1]}\, T_1^4 \quad \ldots\ (i)$$

where T_2 and T_1 are in degrees Kelvin.

However, if the fraction of the radiation which is not absorbed by Plane 2 is transmitted by it, with negligible reflection, then we may write for the equilibrium of plane 2, $e_2 W_1 = s\, e_2(T_2^4 - T_0^4)$. Then neglecting T_0^4, and substituting for W_1 we have: $e_2 e_1\, sT_1^4 = .s\, e_2 T_2^4$ which yields $T_2^4 = e_1 T_1^4$ .... (ii).

Since silicon is relatively transparent to a wavelength range of 2 - 15μ [Donovan and Burger (1969)], it is likely that this latter state will occur.

It is seen that both the equations derived predict the linear relationship between the temperatures, but equation (ii) is independent of e_2 - the emissivity of silicon.

Jona and Wendt (1966) report that the temperature of a silicon wafer heated by radiation was independent of the surface finish, ie. polished or lapped, for temperatures up to 700°C. From Fig. (3.8b) it is seen that a substrate temperature of 700°C corresponds to a heater temperature of 1150°C.

From Wiens' displacement law - $T\lambda_{max} = 0.289$. For T = 1150°C; $\lambda_{max} = \frac{0.289 \times 10^4 \mu}{1450} = 2.06\mu$.

This is in excellent agreement with the lower wavelength limit of the pass-band of silicon as given above.

For substrate temperatures higher than 700°C the heater colour temperature as given by λ_{max} in the Wien equation shifts out of the pass band of silicon, hence the emissivity, which will depend on surface finish, will affect the temperature.

APPENDIX II

Construction of Water Cooled Heat Shield.

The heat shield consists of a box-shaped structure, made by brazing together five pieces of $\frac{1}{4}$" thick copper plate. The brazing was carried out in an atmosphere of forming gas (95% N_2; 5% H_2), using R.F. heating. The brazing alloy used was Ag/Cu eutectic melting point 790°C.

This method of brazing is flux free and the heat treatment also removes any volatile impurities likely to be present in the commercial grade of copper used. (Commercial-grade copper usually contains traces of zinc and cadmium.) The copper box was jigged together using 6 B.A. mild steel screws. Since the forming gas contains a small amoung of water vapour, the steel screws are oxidised, and thus not wetted by the braze. Any copper oxide, however, is reduced by the hydrogen. After the brazing, the steel screws were removed by unscrewing them. Two turns of $\frac{1}{4}$" bore copper pipe were brazed to the box by the same method. The pipe was partially flattened before wrapping around the box, to give a large contact area. The ends of the pipe were brazed into holes bored through a 1" diameter copper rod 3" long. This braze was also carried out with Ag/Cu since these joints would also be in vacuum.

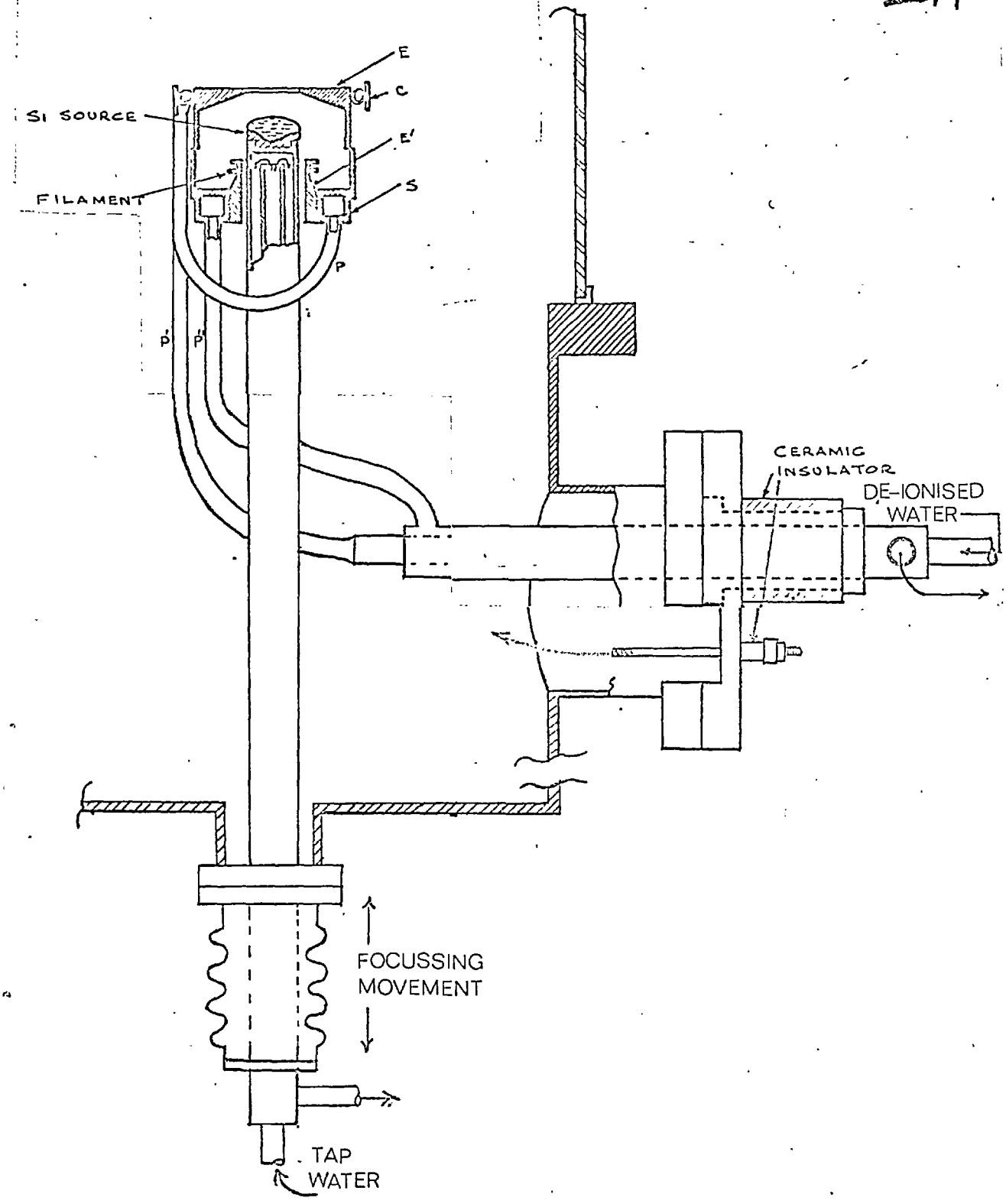


Fig. A2
DIAGRAM SHOWING STRUCTURAL MODIFICATIONS TO THE ELECTRON BEAM FURNACE, TO ALLOW REVERSAL OF FOCUSSING ELECTRODE POLARITY. [COMPARE WITH FIG. 3.4].

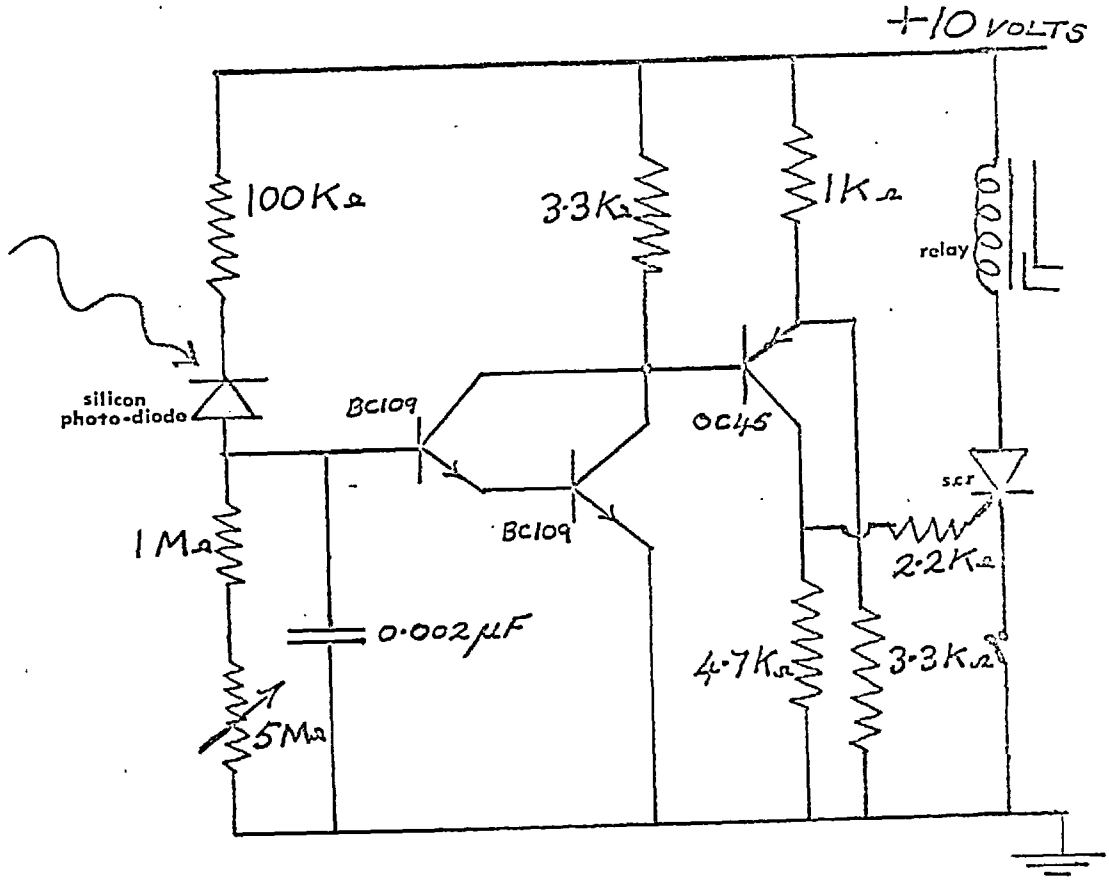


Fig. A.2
CIRCUIT DIAGRAM OF PHOTO-ELECTRIC DETECTOR USED IN JET THINNING.

List of References in Alphabetical Order.

Abbink, H; Broudy, R; McCarthy, G; J. App. Phys. 39, (1968) p.4673.

Allen, F.G., J. App. Phys. 28, (1957) p.1510.

Allen, F.G.; Eisinger, J; Hagstrum, H.D.; Law, J.T., J. App. Phys. 30, (1959) p.1563.

Allen, F.G., J. Phys. Chem. Sol., 19, (1961) p.87.

Allen, F.G.; Buck, T.M.; Law, J.T., J. App. Phys., 31, (1960) p.979.

Anderson, G.S. and Wehner, G.K., Surface Sci., 2, (1964) p. 367.

Archer, R.J., J. Electrochem. Soc., 104, (1957) p.619.

Arizumi, I; Nishinaga, T.N.; Kakehi, M.; Shimokawa, R., J. Cryst. Growth, 3, (1968) p.226.

Arts, A; Gevers, R.; Amelinckx, S., Phys. Stat. Sol., 3, (1963) p.979.

Ashby, M.F. and Brown, L.M., Phil. Mag., 8, (1963) p.1083; 1649.

Bassett, G.A.; and Pashley, D.W., J. Inst. Metals, 87, (1958) p.449.

Batdorf, R.L. and Smits, F.M., J. App. Phys., 30, (1959) p.259.

Batsford, K.O. and Thomas, D.J.D., Micro Electronics and Reliability, 3, (1964) p.353.

Bean, K.E., and Gleim, P.S., Proc. I.E.F.E., 57, (1969) p.159.

Bickley, J., Electrical Comm., 38, (1963) p.373.

Billington, B.S. and Crawford, J.H., Radiation Damage in Solids, Oxford Press, (1961), p.312.

Blau, H.H. and Fischer, H. eds. Radiative Transfer from Solid materials, Macmillan (1962) p.88.

Bohla, S.R. and Meyer, A., R.C.A. Review, 24, (1963) p.511.

Bonsels, W. and Lambert, J.L., Semiconductor Silicon; Edited by R.R. Haberecht and E.L.Kern, Pjblished by Electrochemical Society Press (1969) p.89.

Booker, G.R., Trans. Faraday Soc., 38, (1964) p.298.

Booker, G.R. and Stickler, R., J. App. Phys. 33, (1962) p.3288.

Booker, G.R., and Stickler, R., App. Phys. Letters, (1963) 3, p.158.

Booker, G.R. and Joyce, B.A., Phil. Mag., 14, (1966) p.289.

Booker, G.R. and Howe, A App. Phys. Letters. 3, (1963) p.156.

Booker, G.R. and Stickler, R., Brit. J. App. Phys., 13, (1962) p.446.

Bowden, F.P., and Tabor, D., Friction and Lubrication of Solids. Clarendon Press, Oxford, 1950.

Booker, G.R. and Unvala, B.A., Phil. Mag., 11, (1965).

Booker, G.R. and Unvala, B.A., Phil. Mag., 8, (1963) p.1597.

Bradley, D.E., Brit. J. App. Phys., 10, (1959) p.198.

Brinkman, J.A., J. App. Phys., 25, (1954) p.961.

Burton, W.K., and Cabrerra, N., Disc. Faraday Soc., No. 5, (1949).

Burger, R.M., and Donovan, R.P., editors, Fundamentals of Silicon Integrated Circuits and Device Technology, Vol. I. Prentice Hall, (1969).

Bylander, E.G., J. Electro Chem. Soc., 109, (1962) p.1171.

Cabrerra, N. and Vermilyea, Proc. Conf. Crystal Growth, (1958) ed. Doremus.

Charig, J.H., and Joyce, B.A., J. Electro. Chem. Soc., 109, (1962) p.957.

Charig, J.H.; Joyce, B.A.; Stirland, D.J.; Bickness, R., Phil. Mag., 7, (1962) p.1847.

Charig, J.H., and Skinner, D.K., Surface Sci., 15, (1969) p.277.

Chu, T.C. and Gruber, G.A., J. Electro Chem. Soc., 114, (1967) p.522.

Chu, T.C. and Tallman, W., J. Electro Chem. Soc., 111, (1964)

Cullity, B., Elements of X-ray Diffraction, Published McGraw Hill, (1953)

Corbett, J.W., Electron Radiation Damage in Metals and Semiconductors, Academic Press (1966).

Crawford, J.H., in Interaction of Radiation with Solids. Ed. by Strumane, R.; Nihoul. J.; Gewers, R. and Amelinckx, S. Proc. Summer School, Mons. (1963), North Holland Press (1964) p.421.

Crawford, J.H., and Cleland, J.W., (1957), Progress in Semiconductors, Vol. 2, Eds. Gibson et al. Pub. Haywoods. p.67.

Davies, D.E., and Roosild, S.A., App. Phys. Lett., 17, (1971) p.107.

Davies, D.E., and Roosild, S.A., App. Phys. Lett., 18, (1971) p.550.

Dearnaly, G.; Freeman, J.H.; Gard, G.A.; Wilkins, M.A., Can. J. Phys., 46, (1968) p.586.

Dillon, J.A., and Farnsworth, H.E., J. App. Phys. 29, (1958) p.1195.

Drower, T.J.; Demaria, G.; Ingham, M., J. Chem. Phys., 29, (1958) p.1015.

Eriksson, L.; Davies, J.A.; Johansson, N.; Mayer, J.W., J. Appl Phys. 40, (1969) p.842.

Farnsworth, H.E.; Shlier, R.E.; Dillon, J.A., J. Phys. Chem. Sols., 8, (1959).

Farnsworth, H.E.; Shlier, R.E.; Dillon, J.A., Solid State Electronic., 1, (1960).

Ferber, R., I.E.E.E. Trans. Nucl. Sci., 10, (1963) p.15.

Finch, R.H.; Queisser, H.J.; Thomas, G., and Washburn, J., J. App. Phys., 34, (1963) p.406.

Frank, F.C., Disc. Faraday Soc., 5, (1949) p.3153.

Frank, F.C., Conf. Crystal Growth, ed. by Doremus. (1958).

Gasson, D.B., as reported in Newman (1964).

Gevers, R.; Arts, A.; Amelinckx, S., Phys. Stat. Sol. 3, (1963) p.1563.

Gianola, U.F., J. App. Phys., 28, (1957) p.868.

Gibbons, J.F., Proc. I.E.E.E., 56, (1968) p.295.

Glang., R. and Wajda, E.S., Proc. Met. Soc., Conf., 15, ed. by J.B. Schroeder, (1962).

Gossick, B.R., J. App. Phys., 30, (1959) p.1204.

Grove, A.S.; Roder, A.; Sah, C.T., J. App. Phys., 36, (1965) p.802.

Gun, S.R. and Green, L.G., J. Phy. Chem. 65, (1961) p.779.

Hagstrum, H.D., Phys. Rev. 119, (1960) p.940.

Hagstrum, H.D., J. App. Phys., 32, (1961) p.1020.

Hale, A.P., Vacuum, 13, (1963) p.93.

Handelman, E.T. and Povilonis, E., J. Electro Chem. Soc., 111, (1964) p.201.

Hasse, G. and Scott, N.W., J. Phys. Rad., 11, (1950) p.394.

Holland, L., Vacuum Deposition of thin films; Chapman-Hall (1956).

Honig, R.E., J. Chem. Phys., 22, (1954) p.1610; 126.

Hornstra, J., J. Phys. Chem. Solids, 5, (1958) p.29.

Hirsh, P.B.; Howie, A.; Whelan, M.J.; Nicholson, R.B. and Pashley, D.W. Electron Microscopy of thin Crystals. Pub. Butterworths (1965).

Hass, G., and Thun, R.E., eds. of Physics of Thin Films Vol. 5, (1969).

Irving, S.M., in Semiconductor Silicon, Eds. Haberecht, R.R. and Kern, R. Pub. Electro Chemical Soc. Press (1969) p.433.

Jaccodine, J., App. Phys. Lett. 2, (1963) p.201.

Jona, F., Surfaces and Interfaces, Vol. I., Proc. Sagamore Army Materials Research Conf., Ed. by J.L. Burke, N.L. Reed, V. Viess (1968) p.399.

Jona, F., and Wendt, H.R., J. App. Phy. 37, (1966) p.3637.

Joyce, B.A.; Bradley, R., and Booker, G.R., Phil. Mag., 14, (1966) p.301.

Joyce, B.A.; Bradley, R., and Booker, G.R., Phil. Mag., 15, (1967) p.1167.

Joyce, B.A., and Bradley, R.R., J. Electro Chem. Soc., 110, (1963) p.1235.

Joyce, B.A., Neave, J.H. and Watts, B., Surface Sci., 15, (1969) p.1.

Kagdis, W., J. Electro Chem. Soc., 109, (1962) p.71.
Kahn, I.H., and Summergrad. R.N., App. Phys. Letts., 11, (1967) p.12.
Kinchin, G.H., and Pease, R.S., Rep. Prog., Phys., 18, (1955) p.1.
Kleinberg, J., Inorganic Chemistry, Pub. Heath, (1960) p.104.
Kubechewski, O.; Alcock, C.B., and Evans, E., Metallurgical Thermochemistry, Pergamon Press, (1967) (1958).
Lander, J.J. and Morrison, J., J. App. Phys., 33, (1962) p.2089.
Lander, J.J., and Morrison, J., J. App. Phys., 34, (1963) p.1403.
Lander, J.J., and Morrison J., J. Chem.Phys. 37, (1962) p.729.
Lander, J.J.; Morrison, J., and Gobeli, G.W., J. App. Phys., 34, (1963)
Lang, G.A., and Stavish, T., R.C.A. Rev., 24, (1963) p.488.
Large, L.N., and Bicknell, R.W., J. Matl. Sci., 2, (1967) p.589.
Lawrence, J.E., J. Appl. Phys., 36,(1965) p.360.
Lever, R.F., I.B.M. J. Res. Devel, 8, (1964) p.460.
Lewis, B., and Campbell, D.S., J. Vac. Sci., and Tech., 4, (1967) p.209.
Li, C.H., Phys. Stat. Sol., 15, (1966) p.3; 419.
Litton, F.B., and Anderson, H.C., J. Electrochem. Soc. 101, (1954) p.287.
Lindhard, J., and Scharff, M., Phys. Rev., 124, (1961) p.128.
Lindhard, J.; Scharff, M., and Schiott, H.E., as reported in Applied Solid State Science, Vol. I. Ed. by Wolfe, R., Academic Press (1969)
Loferski, J.J., and Rappaport, P., Phys. Rev., 111, (1958) p.432.
Marsden, D.A., Bellavance, G.R., Davies, J.A., Martini, M., and Sigmund, P. Phys. States Solidi., 35, (1969) p.269.
Matthews, J.W., Phil. Mag., 8,(1960) p.1017.
May, J.E., J. Electro Chem. Soc., 112, (1965).
Mayer, S.E., and Shea, D.E., J. Electro Chem., 111 (1964) p.550.
Mayer, J.W., and Marsh, O.J., in Applied Solid State Science, Vol. I of Advances in Materials and Device Research, Ed. by R. Wolfe, Published Academic Press, (1969).
Mayer, J.W., Ericksson, L., Picraux, S.T., and Davies, J.A., Can. J. Phys., 46, (1968) p.673; 663.
Mazey, D.J., Nelson, R.S., and Barnes, R.S., Phil. Mag., 17, (1968) p.1145.
Mazur, R.G., and Dickey, D.H., J. Electro. Chem. Soc., 113, (1956) p.285.
Mendelson, S., J. App. Phys., 35, (1964) p1570.
Miller, K.J., and Grieco, M.J., J. Electro Chem. Soc., 110, (1963) p.1252.
Miller, D.P., Watelski, S.B., and Moore, C.R., J. App. Phys. 34, (1963) p.2813.

Miller, R., and Haneman, D.J., Surface Sci., 19, (1969), p.49.

Mills, B.D., Elec. Comm., 38, (1963) p.363.

Naber, C.T., and O'Neal, J.E., Trans. Met., Soc., A.I.M.E., 242, (1968) p.470.

Nakanuma, S., I.E.E.E., Trans. Electron Devices, Ed. 13 (1966) p.478.

Nannichi, Y., Nature, 200, (1963) p.1087.

Nelson, R.S., and Mazey, D.J., Can. J. Phys., 46, (1968) p.689.

Newman, R.C., Micro Electronics and Reliability, 3, (1964) p.121.

Nielson, S., and Rich, G.J., Micro. Electronics and Reliability, 3, (1964), p.165; 171.

Notis, M.R., and Conrad, G.P., J. App. Phys., 35, (1963), p.695.

Novak, R.L., Bull. Amer. Phys., Soc., 8, (1963).

Ogilvie, G.J., J. Phys., Chem., Sols., 10, (1959) p.222.

Ogilvie, G.J., and Thompson, A.A., J. Phys. Chem. Sols., 17, (1961) p.203.

Parsons. J.R., Phil. Mag., 12, (1965) p.1159.

Pashley, D.W., Advances in Physics, 14, (1965). p.327.

Pashley, D.W., and Stowell, M.J., Phil. Mag., 8, (1963) p.1605.

Pashley, D.W. and Presland, A.E.B., Phil. Mag., 6, (1961), p.1003.

Pearmain, K., Thesis London University (1971).

Picraux, S.T., Westmorland, J.E., Mayer, J.W., Hart, R.R., and Marsh, O.J., App. Phys. Lett., 14, (1969) p.7.

Pinsker, Electron Diffraction, Butterworths (1953).

Pomerantz, D., J. App. Phys., 38, (1967) p.5020.

Queisser, H.J., and Goetzberger. A., Phil. Mag., 8, (1963) p.1063.

Queisser, H.J., Finch, R.H., and Washburn, J., J. App. Phys., 33, (1962) p.1536.

Rawlings, T.G.R., and Brosselard, L.E., Trans. Met. Soc., A.I.M.E., 236, (1966), p.286.

Resvez, A.G., and Evans, R.J., Trans. Met. Soc., A.I.M.E., 230, (1964) p.581.

Rhodes, R.G., Imperfections and Active Centres in Semiconductors, Pergamon Press, (1964).

Richman, D., and Arlette, R.H., in Semiconductor Silicon, ed. by. R.R. Haberecht and H. Kern, Electrochem. Soc. Press., (1969) p.200.

Royer, M.L., Bull. Soc., France Mines., 51, (1932) p.7.

Rundle, P.C., Int. J. of Electronics, 24, (1969) p.405.
Runyan, W., Silicon,Semiconcuctor Technology, Pub. McGraw Hill (1969).
Rymer, Electron Diffraction, Pub. Methuen (1969).
Rühle, M., Radiation Damage in Reactor Materials, Vol. I.
Proceedings of Vienna Conf., (1969) p.113.
Sangster, R.C., J. Electro Chem. Soc., 104, (1957) p.317.
Schink, O., Solid State Electronics, 8, (1965) p.767.
Schlier, R.E., and Farnsworth, H.E., J. Chem. Phys., 30, (1959) p.4.
Schwuttke, G.H., J. App. Phys., 33, (1962) p.1538.
Sedgwick, T.O., J. Electro Chem. Soc., 111, (1964) p.1381.
Seitz, F., Disc. Faraday Soc., 5, (1949) p.271.
Shive, J.N., Properties, Physics and Design of Semiconductor Devices.
Pub. Van Nostrand, (1959).
Shockley, W., Solid State Electronics, 2, (1961) p.35.
Sigmund, P., Schiedler, G.P., Roth. G., reported in Mayer and Marsh.
Silcox, J., and Hirsh, P.B., Phil. Mag., 4, (1959), p.1356.
Sloop, B.W., and Tiller, C.O., J. App. Phys., 32, (1961) p.1331.
Sloop, B.W., and Tiller, C.O., J. App. Phys., 33, (1962) p.3458.
Sloop, B.W., and Tiller, C.O., J. App. Phys., 37, (1966), p.887.
Steinmayer, W., Phillips Resch. Reports., 18, Feb. 1963.
Swalin, R.A., J. Phys., Chem. Sols., 18, (1961) p.290.
Theurer, H.C., J. Electro. Chem. Soc., 108, (1961) p.849.
Thomas, R.N., and Francombe, M.H., App. Phys. Letters, 11, (1967) p.108.
Thomas, R.N., and Francombe, M.H., App. Phys. Lett. 11, (1967) p.134.
Thomas, D.J.D., Phys. Stat. Sol. 13, (1968) p.359.
Thomas, R.N., and Francombe, M.H., Solid State Electronics, 12, (1969) p.719.
Toombs, N.C., and Welch, A.J.E., J. Iron and Steel. Lond. 172, (1952) p.69.
Toombs, N.C., Comer, J.J., Fitzgerald, J.F., Solid State Electronics.,
8, (1965) p.839.
Thornton, P.R., Scanning Electron Microscopy: Applications to Materials
and devices. Chapman and Hall, (1968).
Tung, S.K., J. Electro Chem. Soc., 112, (1965) p.185.
Unvala, B.A., and Booker, G.R., Phil. Mag., 11, (1964) p.691.
Unvala, B.A., Le Vide, 104, (1963) p.109.
Uhlir, A., Bell Syst. Tech. Jn. 34, (1955), p.105.
Unvala, B.A., and Pearmain, K., J. Matl. Sci., 5, (1970) p.1016.

Valdes, L.B., Proc. I.R.E., 42, (1954) p.420.

Van Roesbroek, J., J. App. Phys., 26, (1955) p.380.

Vook, F.L., and Stein, H.J., Radiation Effects 2, (1969) p.23.

Watkins, G.D., in Electron Radiation Damage in Metals and Semiconductors by Corbett, (1966).

Weisberg, L., J. App. Phys., 38, (1967) p.4537.

Whan, R.E., and Arnold, G.W., App. Phys. Lett., 17, (1970) p.71.

Widmer, H., App. Phys. Lett., 5, (1964) p.108.

Wood, E.A., J. App. Phys. 35, (1964) p.1306.

ACKNOWLEDGEMENTS

The author would like to thank Professor J.G. Ball for providing research facilities; the S.R.C. for financial support; Dr. B.A. Unvala for encouragement and guidance; the author's colleagues for their advice and useful discussions; Mrs. G. Murray for the many hours of spare time devoted to the typing.

The author would also like to thank his parents for their continuous help.